Characterization of the coastal dynamics and turbulent dispersion in the Gulf of Tonkin from HF radar measurements and modeling : the effect of fine-scale dynamics on the spatial structuring of phytoplankton

Manh Cuong Tran

▶ **To cite this version:**

Manh Cuong Tran. Characterization of the coastal dynamics and turbulent dispersion in the Gulf of Tonkin from HF radar measurements and modeling : the effect of fine-scale dynamics on the spatial structuring of phytoplankton. Ocean, Atmosphere. Université du Littoral Côte d'Opale; Université de Hanoi – Vietnam, 2022. English. NNT : 2022DUNK0626 . tel-03988218

HAL Id: tel-03988218

https://theses.hal.science/tel-03988218

Submitted on 14 Feb 2023

HAL is a multi-disciplinary open access archive for the deposit and dissemination of scientific research documents, whether they are published or not. The documents may come from teaching and research institutions in France or abroad, or from public or private research centers.

L'archive ouverte pluridisciplinaire **HAL**, est destinée au dépôt et à la diffusion de documents scientifiques de niveau recherche, publiés ou non, émanant des établissements d'enseignement et de recherche français ou étrangers, des laboratoires publics ou privés.

Thèse de Doctorat

Mention : Sciences agronomiques et écologiques
Spécialité : Sciences de la Mer : Océanographie physique

présentée à *l'Ecole Doctorale en Sciences Technologie et Santé (ED 585)* **de**
l'Université du Littoral Côte d'Opale
et
l'Université des Sciences, Université Nationale du Vietnam

par

TRAN MANH CUONG

pour obtenir le grade de Docteur de l'Université du Littoral Côte d'Opale

Caractérisation de la dynamique côtière et de la dispersion turbulente dans le golfe du Tonkin à partir de la courantographie radar HF et de la modélisation: effet de la dynamique à fine-échelle sur la structuration spatiale du phytoplancton

Thèse dirigée par **Alexei SENTCHEV et Kim-Cuong NGUYEN**

Soutenue le 10 novembre 2022, après avis des rapporteurs, devant le jury d'examen :

M. Hubert Loisel, ULCO, LOG, France	**Président**
M. Francesco d'Ovidio, CNRS, LOCEAN, IPSL, France	**Rapporteur**
M. Alejandro Orfila, UIB-CSIC, IMEDEA, Espagne	**Rapporteur**
M. Simone Cosoli, UWA, Oceans Graduate School, Australie	**Examinateur**
Mme. Anna Rubio, AZTI-Marine Research, Espagne	**Examinatrice**
M. Alexei Sentchev, ULCO, LOG, France	**Directeur de thèse**
M. Kim-Cuong Nguyen, HUS, Vietnam	**Co-encadrant**

THESIS

Mention: Sciences of agriculture and ecology
Specialty: Ocean sciences - Physical oceanography

presented at *the Doctoral School of Sciences, Technologies and Health (ED 585) of*
the Université du Littoral Côte d'Opale
and
the University of Science, Vietnam National University

by

TRAN MANH CUONG

in order to obtain the degree of Doctor of the Université du Littoral Côte d'Opale

Characterization of the coastal dynamics and turbulent dispersion in the Gulf of Tonkin from HF radar measurements and modeling: the effect of fine-scale dynamics on the spatial structuring of phytoplankton

Thesis directed by **Alexei SENTCHEV et Kim-Cuong NGUYEN**

Defended on 10 November 2022, for the dissertation committee composed of :

Mr. Hubert Loisel, ULCO, LOG, France	**President**
Mr. Francesco d'Ovidio, CNRS, LOCEAN, IPSL, France	**Reporter**
Mr. Alejandro Orfila, UIB-CSIC, IMEDEA, Spain	**Reporter**
Mr. Simone Cosoli, UWA, Oceans Graduate School, Australia	**Examiner**
Mrs. Anna Rubio, AZTI-Marine Research, Spain	**Examiner**
Mr. Alexei Sentchev, ULCO, LOG, France	**Supervisor**
Mr. Kim-Cuong Nguyen, HUS, Vietnam	**Co-supervisor**

Acknowledgment

I owe my sincere gratitude to my advisor, Alexei Sentchev, who hosted me at the beginning of my doctoral journey and has given me tremendous time and support ever since. Many thanks to his encouragement, guidance, and patience that enables me to complete this work. It was my privilege to be part of your team and to learn how to be a scientist. Additionally, I want to show my deep appreciation to my co-advisor, Nguyen Kim Cuong, for encouraging me to continue the research and helping me to progress my work since the time I was a master student.

I thank the members of the dissertation committee, Marine Herrmann and Cedric Jamet, for their constructive comments and suggestions to improve the study. I am also thankful to the jury members, Hubert Loisel, Francesco d'Ovidio, Alejandro Orfila, Simone Cosoli and Anna Rubio, for evaluating this work and giving many interesting questions during my defense which are important for my future study.

I would like to acknowledge the financial support from the University of Littoral Côte d'Opale and the Région "Hauts-de-France" PhD fellowship to finish this thesis. Additionally, I would like to express my sincere thanks to the administrative members of the Laboratory of Oceanography and Geosciences (LOG) and the Doctoral School of the Université du Littoral-Côte d'Opale for their helpful support with the paperwork during my stay in France.

I am very grateful to have my colleagues and friends in the Remote sensing and hydrodynamics team at LOG, Daniel, Gabi, Roy, Sara, Carina, Kien, Manh, Son, Thinh, Tu, Huyen, Yang. Together, we have a lot of fun and relaxing moments and, also, learned a lot from each other.

And finally, I owe endless gratitude to my dearest wife, Mai, and my daughter, An, who have always been there and supported me unconditionally during my difficult time.

Contents

List of abbreviations

2dVar: Two-dimensional Variational interpolation

ADCP: Acoustic Doppler Current Profiler

AWAC: Acoustic Wave and Current Profiler

CODAR: CODAR Seasonde radar system

CMEMS: Copernicus Marine Systems

ECMWF: European Centre for Medium-Range Weather Forecasts

ENSO: El Niño Southern Oscillation

EOF: Empirical Orthogonal Function

FFT: Fast Fourier Transform

FMCW: Frequency Pulsed Continuous Waveform

FSLE: Finite-Size Lyapunov Exponents

GDOP: Geometric Dilution Of Precision

GoT: Gulf of Tonkin

HFR: High-Frequency Radar

LS: Least Square fit

LCSs: Lagrangian Coherent Structures

MUSIC: Multiple Signal Classification algorithm

OMA: Open-boundary Mode Analysis

RRD: Red River Delta

SEA: Southeast Asia

SNR: Signal-to-Noise ratio

SSS: Sea Surface Salinity

SST: Sea Surface Temperature

WERA: WERA radar system

VASI/MONRE: Vietnam Administration of Seas and Islands/ Ministry Of Natural Resources and Environment

VHF: Very-High Frequency

VNES/SCS: Vietnam East Sea (or the South China Sea)

Résumé

Le golfe du Tonkin (GoT), situé sur le plateau continental dans la partie nord-ouest de la mer orientale du Vietnam / mer de Chine méridionale (VNES/SCS), est très riche en ressources naturelles. Malgré sa situation stratégique, la dynamique régionale et les échelles de sa variabilité sont encore très mal documentées, ce qui empêche une avancée dans des études environnementales. Le manque d'observations systématiques est probablement la principale raison qui rend difficile la compréhension du schéma global de la dynamique dans ce bassin. Pour combler le manque d'observations océanographiques, un réseau de radars Haute Fréquence (radar HF) a été déployé dans la région permettant la télédétection des courants de surface en continu. Les séries temporelles de vitesses de courants, longues de deux ans et demi, ont été utilisées pour caractériser la variabilité de la dynamique régionale dans une large gamme d'échelles et pour identifier les processus physiques régissant cette variabilité. Il a été démontré que la marée explique une grande partie (60%) de cette dernière. A l'échelle saisonnière, les apports d'eau douce des fleuves affectent fortement l'écoulement en modifiant la polarisation des ellipses des courants de marée et en produisant l'intensification du courant côtier, en fin d'été et en automne. Le vent de mousson régit la dynamique à grande échelle et contrôle l'extension spatiale du courant côtier. Les schémas du transport de traceurs passifs et les régimes de la dispersion turbulente ont été étudiés dans un cadre lagrangien en utilisant les champs de vitesses issues des mesures radar et des simulations numériques (modèle SYMPHONIE à haute résolution). Les diagnostics lagrangiens utilisés (dispersion relative et exposants de Lyapounov) ont permis de mettre en évidence un changement significatif dans le régime de la dispersion et dans les propriétés du transport engendré par le vent de mousson et les apports d'eau douce. L'effet de la turbulence et de mélange horizontal sur la distribution de matière a été trouvé particulièrement important dans quatre régions du golfe. Nos analyses ont révélé que la variabilité à petite échelle des courants marins joue un rôle déterminant dans la structuration de la distribution spatiale du phytoplancton dans ces régions.

Mots-clés: Circulation côtière ; Variabilité multi-échelles ; Dispersion relative ; Turbulence; Radar HF; Golfe du Tonkin

Abstract

The Gulf of Tonkin (GoT), located on the shelf in the northwestern part the Vietnam East Sea, / South China Sea (VNES/SCS), is very rich in natural resources. Despite its strategic location, the regional circulation and scales of its variability are only poorly understood preventing a progress in environmental studies. A limited knowledge of the circulation in the Gulf is tightly related to the lack of observations. To make up the gap, a network of High-Frequency (HF) radars was deployed in the region providing with an opportunity to monitor the coastal circulation continuously via the remote sensing of surface currents. The 2.5-year-long velocity time series, derived from radar measurements in the southern Gulf, allowed characterization of the flow variability and identification of key process governing this variability. It was shown that tidal motions account for a major part of this variability (60% of the total variance). The freshwater input strongly affects the seasonal variability of currents by modifying the polarization of tidal current ellipses and causing the coastal current intensification in late summer and autumn. The monsoon wind controls the large-scale dynamics and modulates the spatial extension of the coastal current. Transport patterns of passive tracers and turbulent dispersion regimes were investigated in the Lagrangian framework using the velocity fields from radar measurements and high-resolution SYMPHONIE model simulations. Lagrangian diagnostics (relative dispersion and Finite Size Lyapunov Exponents), revealed a significant change in dispersion rate and transport pathways caused by the monsoon wind and freshwater input. The effect of turbulence and horizontal steering on particulate material distribution was found particularly strong in four regions of the gulf. It was shown that fine-scale dynamics plays a major role in structuring the phytoplankton distribution there.

Keywords: Coastal circulation; Multi-scale variability; Relative dispersion; Turbulence; HF radar; Gulf of Tonkin

Introduction Générale

Situées à l'interface entre l'atmosphère, le continent et l'océan ouvert, les mers côtières (appelées parfois régions océaniques côtières) constituent des environnements dont la dynamique complexe peut évoluer selon une vaste gamme d'échelles spatio-temporelles. Ces espaces sont soumis à de nombreuses pressions anthropiques, liées aux activités industrielles, de pêche ou de tourisme. Ils sont également soumises à des forçages naturels divers, allant des aléas extrêmes (tempêtes, surcotes, tsunamis) aux phénomènes naturels d'érosion. Le changement climatique induit également un impact sur ces milieux en favorisant par exemple l'élévation du niveau de la mer, ou l'augmentation de la fréquence de tempêtes.

Ces zones de *continuum* terre/océan représentent un ensemble de problématiques scientifiques où se confrontent à la fois des phénomènes liés à de longues échelles de temps et d'espace, comme les variations du climat, et des effets liés aux causes plus locales et de courte échelle de temps, tels que les facteurs anthropiques ou les évènements météorologiques. La compréhension des processus physiques et biogéochimiques qui régit l'environnement physique et les écosystèmes dans les mers côtières est donc fondamentale pour mener efficacement une politique de gestion durable de ces espaces.

La compréhension de l'état présent de ces espaces et de sont évolution future nécessite une approche multi-méthodes, telles que des mesures *in situ*, la télédétection, des modélisations numériques et physiques, ou le relevé de différents types d'indicateurs biogéochimiques.

Cette approche repose sur une compétence pluridisciplinaire, faisant intervenir des savoirs issus de la physique, des études hydrodynamiques (variabilité des courants), ou encore de la biologie, de l'écologie et des sciences humaines et sociales. Enfin, cette compréhension doit également être multi-temporelle, depuis l'observation de l'instantané jusqu'à l'approche de phénomènes se déroulant sur plusieurs dizaines d'années (milliers d'années pour certaines disciplines).

Les études menées dans le cadre de cette thèse adoptent cette approche pluridisciplinaire faisant intervenir des compétences principalement en sciences physiques: en télédétection des courants marins et de couleur de l'eau, en modélisation eulérienne et lagrangienne, en mesures *in situ* et en traitement du signal, et, très modestement, en océanographie biologique.

Les processus physiques et (à titre d'exemple) biologiques, abordés dans cette étude, évoluent selon une gamme d'échelles spatio-temporelles assez étendue, allant du jour à l'année et du kilomètre à la

centaine de kilomètres. L'attention particulière a été portée à la problématique d'interaction d'échelles ce qui a requis l'emploi d'outils et de techniques d'analyses différents.

La zone géographique choisie pour cette étude est le Golfe du Tonkin – une mer épicontinentale située intégralement sur le plateau nord-ouest de la mer orientale du Vietnam / mer de Chine méridional, dont l'acronyme anglais est VNES/SCS (Vietnam East Sea, or South China Sea).

Ce bassin semi-fermé en forme de croissant s'étend sur environ 500 km du nord au sud et de 270 km d'ouest en est. Il échange avec la mer VNES/SCS principalement par la grande entrée sud et aussi par un détroit étroit et peu profond - le détroit de Hainan (ou Qiongzhou) à l'est. Le golfe lui-même est peu profond. Sa bathymétrie (Fig. 0.1) augmente progressivement depuis la côte pour atteindre environ 70 m dans la partie sud, avec le maximum, 100 m, situé à l'entrée principale du sud. La ligne des côtes est assez complexe, en particulier dans la zone proche du delta du fleuve Rouge (RRD), où se trouvent environ 2000 petites îles qui font le charme le la baie de Ha Long. Le golfe reçoit des apports d'eau douce de plusieurs fleuves sur les côtes vietnamiennes et chinoises dont le plus important est le fleuve Rouge (Fig.0.1). Son débit annuel est d'environ 3500 m^3 s^{-1} mais il peut atteindre 30 000 m^3 s^{-1} en période de pluies.

La circulation complexe dans le golfe résulte d'un forçage macro-tidale, d'un important apport d'eau douce des fleuves et d'une forte variabilité saisonnière des forçages atmosphériques. Ces derniers incluent le forçage climatique de mousson, avec une nette distinction entre vent saisonnier et précipitations. Certaines particularités des côtes (la présence de grands fleuves et d'estuaires, le plateau continental étendu et le petit fond) et les forçages atmosphériques extrêmes multiplient les interactions à l'interface terre-mer-atmosphère et sur l'ensemble du golfe rendant ainsi l'étude de la dynamique de cette région difficile.

Situé dans une zone stratégique, potentiellement exposée aux conflits géopolitiques avec la Chine, ayant de riches ressources en gaz, en pétrole, une grande diversité d'espèces marines commerciales, la région n'a suscité qu'un intérêt limité pour les études scientifiques. L'hydrodynamisme du bassin ne fait pas l'exception. La circulation générale, sa variabilité aux différentes échelles d'espace-temps n'a été documentée que dans très peu de publications en anglais, qui se basent en majeur partie sur la modélisation.

Dans ce contexte, il paraît indispensable d'acquérir la connaissance des interactions entre les composantes physiques, géologiques et biologiques de l'environnement marin côtier au Vietnam et en particulier dans le golfe du Tonkin, soumis à une forte pression anthropique.

Le manque d'observations systématiques dans cette région est probablement la principale raison qui empêche une bonne compréhension du schéma global de la dynamique dans ce bassin. Cela induit

notamment le débat sur la variabilité saisonnière de la circulation (par exemple, circulation cyclonique/anti-circulation en été) et sur le rôle de processus physiques contrôlant cette variabilité (Ding et al., 2013; Gao et al., 2013; Sun et al., 2001; Wang, 1998; Xia et al., 2001; Zu, 2005).

Pour combler le manque d'observations océanographiques dans la zone, un réseau de radars océanographiques haute fréquence (radar HF) a été déployé le long des côtes ouest du golfe du Tonkin en 2012 (plus précisément, en décembre 2011) pour la mesure des courants de surface et des vagues. Ce réseau, devenu opérationnel assez rapidement, est opéré par l'Administration Vietnamienne des Mers et des Iles (VASI, MONRE). L'emplacement des stations radar dans le golfe est indiqué sur la Figure 0.1 par les cercles verts et la couverture spatiale par les mesures - par les segments de cercle. Figure 0.2 montre à quoi ressemble la station radar installé à Dong Hoi (DHOI), Vietnam.

Il convient de préciser que radar HF est un instrument très performant de télédétection des courants en zone côtières. Les mesures de la vitesse des courants par radar ont été utilisées massivement dans de nombreuses études de la dynamique régionale côtière. Elles ont contribué au développement d'outils d'océanographie opérationnelle mis en place dans un certain nombre de pays (e.g., Kohut et Glenn, 2003; Abascal et al., 2009; Paduan et Washburn, 2013).

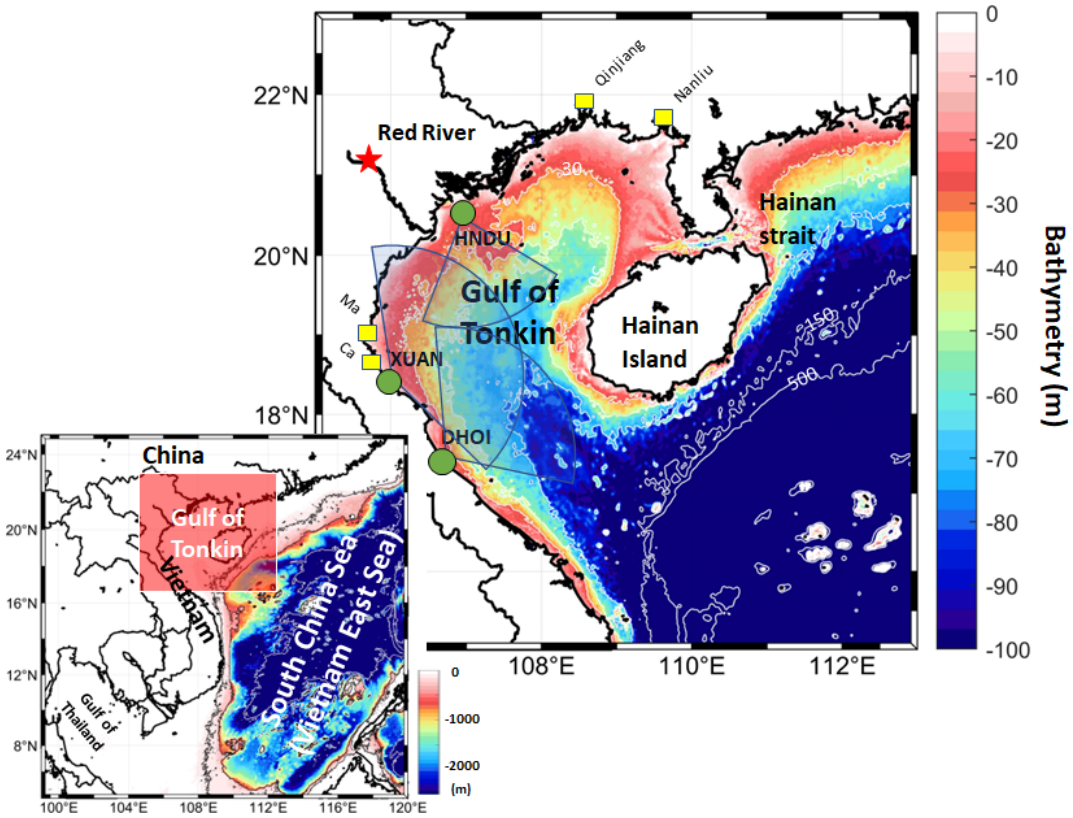

Figure 0.1 : Région d'étude - le golfe du Tonkin avec bathymetrie (figure de droite) et sa position géographique (figure de gauche). Emplacements des embouchures de principaux fleuves sont indiqués par des carrés jaunes. L'étoile rouge marque le Fleuve Rouge. Les sites radar sont indiqués par des cercles verts. La couverture spatiale de chaque radar est montrée en bleu clair.

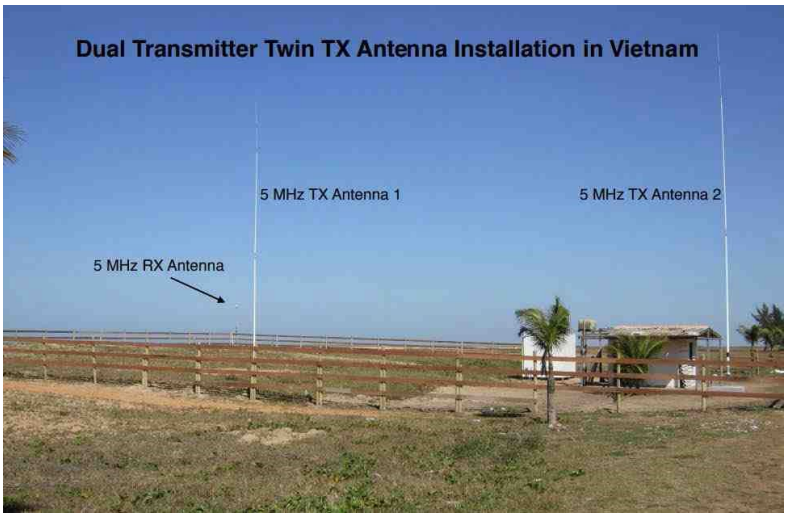

Figure 0.2. Radar HF Seasonde de CODAR installé à Dong Hoi (DHOI), Vietnam.

Ainsi, **le premier objectif** de la thèse vise à développer une approche méthodologique innovante de la caractérisation de la dynamique océanique régionale à partir d'observations des courants marins par radars, installés dans le golfe du Tonkin. La technique de la mesure et surtout les méthodes efficaces de traitement de données que nous avons mises en œuvre ont permis de constituer des séries longues de vitesse des courants superficiels. Cette base de données a été utilisée pour effectuer l'analyse de la variabilité des courants dans une large gamme d'échelles spatio-temporelles.

Nous somme allés plus loin dans l'utilisation de mesures radar et nous avons étendu le champ d'application de la télédétection des courants à la problématique de la caractérisation du transport et de la dispersion turbulente dans le GoT en utilisant une approche lagrangienne. Cette approche fait intervenir des particules virtuelles (petits volumes d'eau étiquetés) advectées dans le champ de vitesse des courants mesurés par radar.

Très vite nous nous sommes confrontés à une limitation sérieuse qui est la couverture spatiale limitée des observations radar dans le golfe. L'utilisation d'un modèle de circulation est apparue indispensable pour la poursuite des études. Le deuxième outil d'investigation que nous avons employé était donc le modèle numérique à haute résolution - modèle SYMPHONIE.

La validation du modèle et l'évaluation de ses performances a constitué **le deuxième objectif** visé dans ce travail de thèse. L'ensemble des mesures radar a été comparé au modèle. Cette vérification a conforté la validité des résultats de la modélisation. Elle a permis également l'utilisation du modèle pour étudier les processus de transport lagrangien à l'échelle du golfe. A notre connaissance, cette problématique scientifique n'a pas encore été abordée dans cette région géographique et même dans la région plus vaste de l'Asie du sud-est.

Il convient de préciser que ce modèle de circulation régionale a été mis en œuvre dans le golfe du Tonkin pour la première fois par Piton et al. (2020, 2021). Puis il a été beaucoup amélioré par Nguyen-Duy et al. (2021), dans le cadre de sa thèse au LEGOS. Ces améliorations et un raffinement du maillage du modèle ont permis de reproduire des structures dynamiques à fines échelles dans l'écoulement et plus particulièrement au voisinage des côtes vietnamiennes. Ces structures, caractérisées par des échelles spatiales allant d'un à cent km et des échelles temporelles allant du jour à la semaine, affectent fortement le transfert d'eau et de matière via le mécanisme de dispersion turbulente.

Le troisième objectif de la thèse consistait à caractériser l'effet de la dynamique à fine-échelle dans le golfe sur la structuration de la distribution spatiale du phytoplancton. Les mécanismes impliquant les variations conjointes des quantités physiques et biologiques dans la région ne sont pas encore bien documentés. Pour combler le manque de connaissances dans ce domaine, nous avons étudié les impacts potentiels de la dynamique, de la turbulence et des processus de mélange horizontal sur la répartition spatiale de chlorophylle-a observée depuis l'espace, c'est-à-dire en utilisant des produits couleur de l'eau.

En conformité avec ces trois objectifs, la structure de cette thèse est la suivante :

Le chapitre I fournit une description de la région (caractéristiques géographiques, forçages physiques, processus hydrodynamiques), détaille les connaissances existantes sur la dynamique du golfe du Tonkin et les limitations associées, et enfin identifie les principales questions ouvertes sur la variabilité de la dynamique.

Dans le chapitre II, nous présentons le principe du fonctionnement des radars HF, les méthodes de traitement et d'analyse de données utilisées dans cette étude. La comparaison des mesures radar HF et des mesures de vitesse *in-situ* ainsi que le problème de la prévisibilité lagrangienne sont également abordés dans ce chapitre.

Le chapitre III présente les résultats de l'application de la télédétection des courants par radar dans le golfe. Les différentes échelles de la variabilité des courants de surface, allant de l'échelle de la marée à l'échelle annuelle ont été examinées. Les processus physiques à l'origine de cette variabilité ont été caractérisés. Un article scientifique intitulé «Multi-scale variability of circulation in the Gulf of Tonkin from remote sensing of surface currents by high-frequency radars» a été publié en 2021 dans la revue Ocean Dynamics (https://doi.org/10.1007/s10236-020-01440-x).

La question du transport lagrangien et de la turbulence dans le golfe sont abordées dans le chapitre IV. Les vitesses des courants mesurées par radar et celles issues de la modélisation à haute résolution sont utilisées pour étudier la dispersion turbulente des traceurs passifs. Nous avons caractérisé l'effet des

zones frontales générées par l'interaction multi-échelle de l'écoulement turbulent sur la distribution spatiale des traceurs passifs dans le golfe. Les résultats présentés dans ce chapitre ont été publiés en 2022 dans Continental Shelf Research : «Assessment of relative dispersion in the Gulf of Tonkin using numerical modeling and HF radar observations of surface currents» https://doi.org/10.1016/j.csr.2022.104784.

Dans le chapitre V, nous analysons conjointement la distribution spatiale des structures cohérentes lagrangiennes (LCS) et des quantités biologiques (concentrations de chlorophylle-a mesurés depuis l'espace). Nous discutons le rôle qui joue l'advection horizontale et le mélange turbulent dans la structuration des champs biologiques dans le golfe.

Le chapitre VI résume les principaux résultats de cette étude. Les questions restant ouvertes et des perspectives sont également abordées dans ce chapitre.

Chapter I. Introduction

1.1. Preamble

Between the continents and the deep open oceans, there are shallow bodies of water lying on the continental shelf up to 200 meters deep compared to the thousands of meters deep in the open ocean. In the course of history, humans have utilized these regions, including coastal waters and the adjacent seas, for a wide range of benefits. These shallow regions are productive areas, which contribute about 90% to the world's fisheries consumption that directly provide food for humanity as well as for natural resources, maritime commerce, scientific, industrial and recreational activities. As a strategic position between the land and the ocean, the shelf region is extensively used for marine transport and trade ports for global business. Thus, despite making up only a small fraction of roughly 9% of total areas of the world's oceans, they are trivial to humankind as being home to 40% of the population living within 100 km of the shoreline (Simpson and Sharples, 2012). The oceanographic characteristics of the shelf sea regions are somehow different from that of the deep seas and degrees of variety are respected with the location. The main reason why the dynamics of the shallow seas are different from that of the deep sea is the water properties and general circulation in these shallow water zones are largely modified by the shallow topography and their regional settings, i.e., surface wind, river discharge, heat flux, precipitation, etc., that set the unique ocean dynamics among them. More importantly, the shelf region is the part of the ocean that is mostly affected by pollution from human activities.

Lying over the shelf of the Vietnam East Sea, or South China Sea (VNES/SCS), the Gulf of Tonkin (GoT) accounts for a very special role in the social and economic spheres. The attractiveness of the coasts, spanning many levels (economic, commercial, tourist, etc.), has made the area a highly populated territory, i.e., the Red River Delta (RRD) is one of the highest population densities in the world (~1000 inhab km^{-2}), and exposed to growing anthropogenic pressure. As part of the Southeast Asian (SEA) waters, the GoT shares similarities in characteristics with the VNES/SCS region. The monsoonal climatic forcing, in particular, the distinction between seasonal wind and precipitation, induces a strong variation in dynamics. Certain particularities of the coasts (i.e., the presence of large rivers and estuaries, the extended continental shelf and the shallow bottom, extreme atmospheric forcing, etc.) multiply the interactions at the land-sea interface thus making the study of the dynamics

of this region difficult. A dramatic event (Formosa steel event), which occurred in 2016 not far from the Vietnamese coast and caused massive pollution of coastal waters, livestock farms, and beaches, gives a fair example of the vulnerability of the marine environment. The event revealed the shortage in the response procedure to marine hazards and diagnose the extent of the phenomenon and its evolution. This failure is also linked to the lack of sufficient knowledge of the dynamics of the environment, the processes governing this dynamics, and modeling tools.

Despite the GoT having an important geographical location, great diversity in commercial species, and rich in gas, and oil resources as well, the region attracted only limited interest in scientific studies. In this context, it is fundamental to improve the understanding of the interactions between the physical, geological, and biological components of the coastal marine environment in the northern part of Vietnam and in particular in the Gulf of Tonkin which is subject to strong anthropogenic pressure.

Since late 2011, an operational data acquisition network has been set up in the north of Vietnam to cover the existing gaps in the knowledge of the regional hydrodynamics and oceanographic processes. A coastal radar network was established by the Vietnam Administration of Seas and Islands (VASI, MONRE) along the western coast of the GoT for ocean surface currents and wave monitoring. HF radar data are used massively in the study of regional coastal ocean dynamics and the development of operational oceanography tools which were previously established in a number of regions (e.g., Kohut and Glenn, 2003; Abascal *et al*., 2009; Paduan and Washburn, 2013). The technique of measurement provides an opportunity for investigating the interaction of oceanic processes at a regional scale. This is the main focus of the PhD thesis which aims to develop an innovative methodological approach for characterization of the regional coastal ocean dynamics using observations of surface currents by a network of oceanographic radars (HF radars) installed along the coast in the GoT.

The modern processing techniques are applied to radar data to build long time series of ocean current velocities in the northern part of Vietnam. Methods for analyzing current maps, non-linear and non-stationary evolution of velocities were implemented and applied to identify the major circulation patterns and to quantify the temporal variability of coastal dynamics in a wide range of frequencies: from the semi-diurnal to seasonal period. This database has a large spatial coverage and is continuously renewed. It is used to respond to the concerns of many local studies aimed at understanding the complexity of coastal dynamics, developing of methods for characterizing the ecological state of the marine environment, the transport and dispersion of material in the water (Lagrangian transport). Based on our research, an innovative approach of analysis was built for the first time in Vietnam and the SEA region. This observing system and method of analysis help to understand and forecast the evolution of short-term coastal dynamics. They will be made operational in the nearest future.

In the first chapter, the study region and the current state knowledge of the regional dynamics based on previous research are present. The description of the GoT geography, the circulation, and the forcing that drive the surface dynamics are summarized in the following subsections. Based on this overview, we identified the scientific issues that remain to be investigated and determined the objects of the research.

1.2. The study region and environmental conditions

1.2.1. The Gulf of Tonkin (GoT)

Between the coast of Vietnam and China, the GoT (16°10' – 21°30'N and 105°30' – 111°E) lies on a shelf in the northwestern part of the VNES/SCS (Fig.1.1). This crescent shape, semi-enclosed gulf extends about 500 km long and 270 km wide, exchanges waters with the open sea mainly through the large southern entrance and partly through the Hainan (or Qiongzhou) strait in the east. The strait is narrow, only about 30 km wide, but it is quite deep in the middle part (~50 m depth). The gulf covers an area of about 115000 km² and is characterized by shallow depth. The bathymetry of the gulf (Fig. 1.1) gradually increases from a few meters on the coast to about 70 m in the southern gulf with the largest depth of about 100 m in the main entrance. The topography along the coastline is rather complex, especially in the area close to the Red River Delta (the RRD). There are about 2000 small islands in the gulf, sometimes no bigger than a few hundred square meters, and the majority of them are scattered in the RRD. The gulf is also fed by several rivers on the Vietnamese and Chinese coasts while the largest being the Red River (Fig.1.1). Its annual freshwater discharge is about 3500 $m^3 s^{-1}$, and it carries out a large volume of sediments (Vinh et al., 2014).

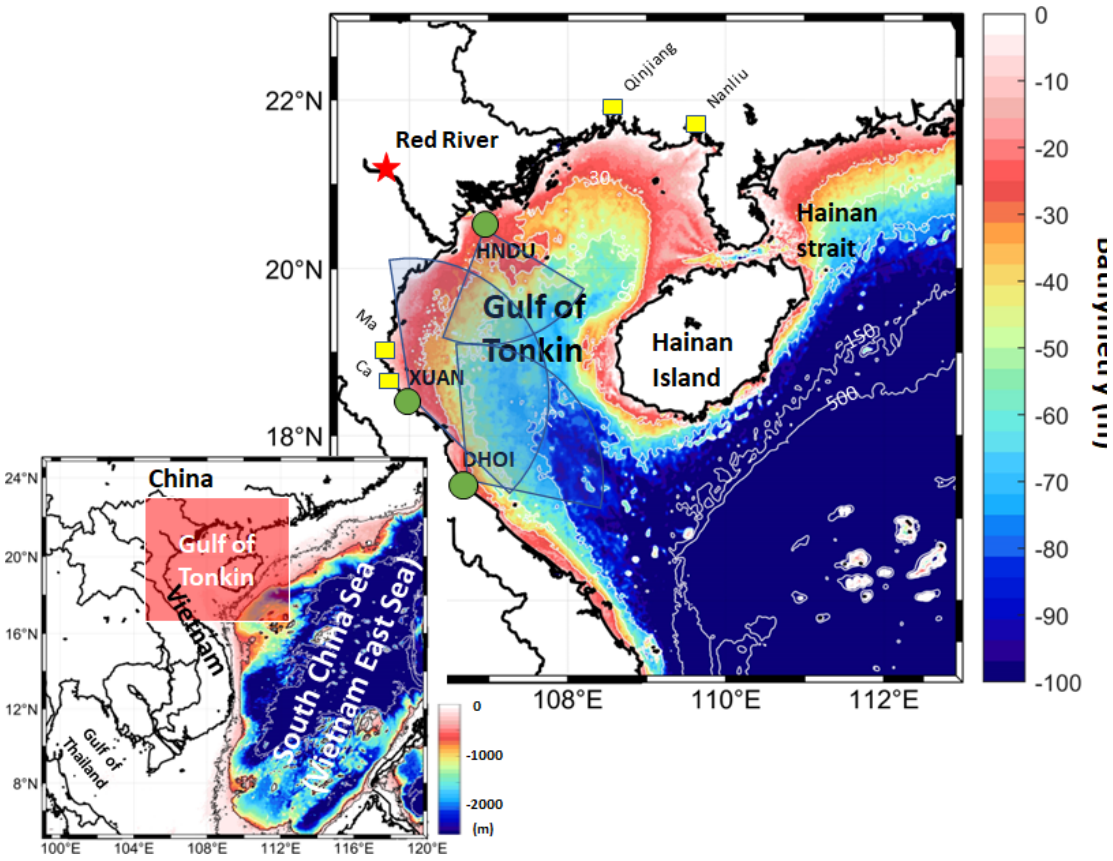

Figure 1.1: Location of the study region, the Gulf of Tonkin. The main river mouth locations are shown by yellow squares. The red star marks the location of the Red River. The radar sites are shown by green circles. The typical coverage of each radar site is shown as blue shade color.

1.2.2. Meteorological conditions

- **Monsoon wind**

As part of the South East Asian (SEA) region, the climate of the GoT is largely influenced by large-scale seasonal reversal of wind regimes of the Asian monsoon system (Wyrtki, 1961). The monsoon weather system is a result of large land-sea temperature differences caused by solar radiation, in which the landmass in the northern hemisphere is larger and warmed greater than in the south (Huffman et al., 1997). This monsoon condition features a high seasonal variability of climate conditions, in particular, precipitations and winds. Two monsoon regimes can be distinctly recognized as the northeast (NE) monsoon (winter, or dry season) and the southwest (SW) monsoon (summer, or wet season). A review of the Asian monsoon can be found in Loo et al. (2015). The annual cycle of the surface wind direction and magnitudes is shown in Fig. 1.2.

The NE monsoon season lasts about six months from mid-October to March and fully develops during mid-January. During this period, the northeast wind is strong and periodically blows from the Siberian

High towards the tropics, thus, bringing cold and dry air to the SEA region. The intensity of the wind in this period is the highest during the year. Inside the GoT, the wind speed decreases due to the constraints of land topography with an average magnitude of about 6-8 m s^{-1} (Fig. 1.2a). The SW monsoon usually takes place from the beginning of May and lasts until September with quite persistent western to southwestern wind (Fig. 1.2c). Originating from the southwest Pacific and the Indian Ocean, the SW wind brings warm and humid air over the GoT. In between each season, there are two transitional periods: Spring (April – May) and Fall (September to mid-October). During Spring, the wind is low, prevailing from the east, and is typically weakest during April (the average wind speed of about 2-3 m s^{-1}, Fig. 1.2b). Whereas in September, the predominant wind changes to NE direction (Fig. 1.2d). However, the SW wind is still strong. Thus, the conflict between the SW wind and periodically strong NE wind leads to large variations in the wind forcing.

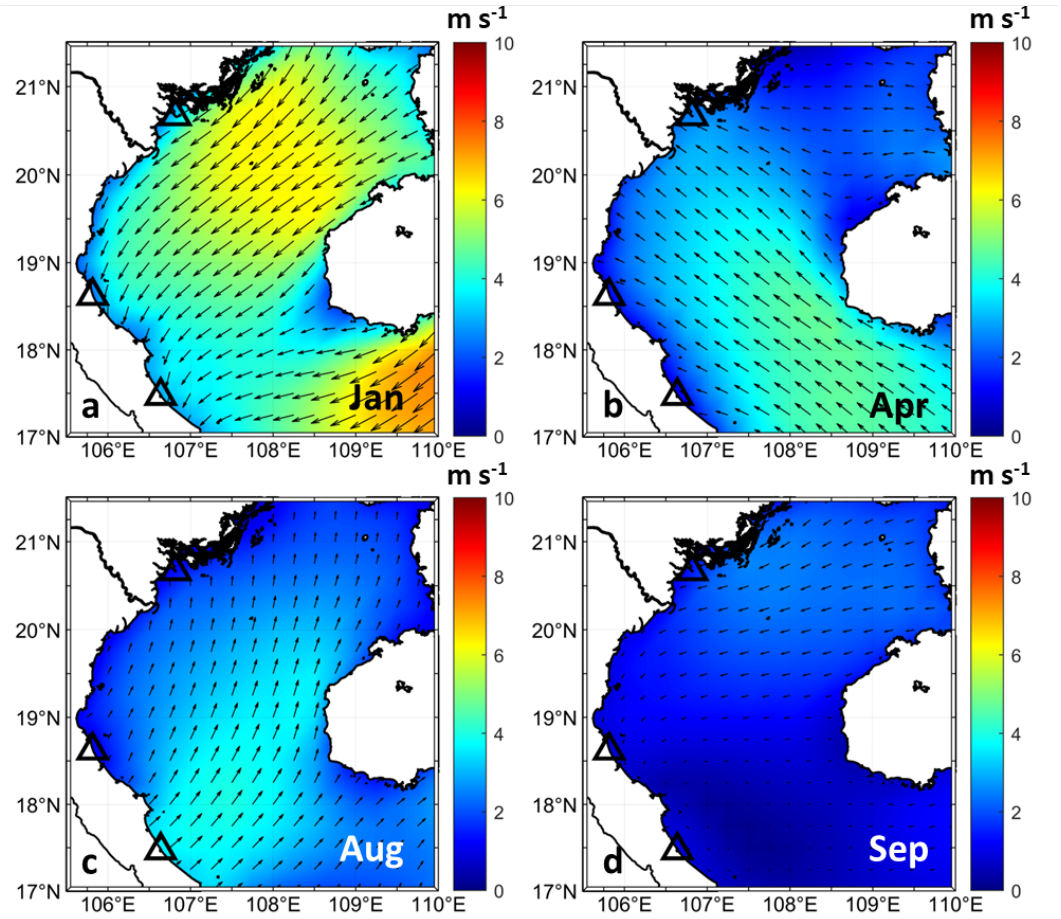

Figure 1.2: Monthly average wind fields for four months from Era5 reanalysis dataset at 10 m above sea level in the GoT during the period from 2000 to 2020. The wind magnitude is shown by color shading.

- **Surface heat flux and precipitation**

The surface heat flux does not directly inject momentum into the upper ocean, however, the seasonal cycle of heat energy exchange adjusts the density of water parcels and modifies the stratification of the water column. This process leads to an unequal distribution of heat energy and generates density gradients which in turn, drive the circulation. To justify the annual cycle of heating and cooling in the GoT, Fig. 1.3 represents the monthly mean net heat flux averaged for a 20-year long period from 2000 to 2020 over the whole domain. During the year, the net heat flux is positive from February to September with a large amount of solar energy of 44 W m^{-2} on average and the maximum heat gain is during April (Fig. 1.3). With the onset of the NE monsoon and large cloud coverage, the net heat flux during winter is negative and the sea surface is vastly cooling.

Similarly, the input of freshwater input constitutes an important second source of mechanical forcing which injects the potential energy via buoyancy gradients. The freshwater gained through rainfall indeed leads to a lower sea surface salinity (~1 lower) for the VNES/SCS than the surrounding ocean (Qu et al., 2009). Rainfall in the GoT demonstrates a large seasonal variation. The rainy season in the GoT starts from May until mid-winter and accounts for about 85 – 95% of the total annual rainfall (Loo et al., 2015). The average net freshwater flux during summer is about 2.3 mm $days^{-1}$. From autumn to early summer, due to the cold and dry conditions brought by the northeast monsoon wind, the rain intensity is low and the evaporation exceeds the precipitation during this period (Fig. 1.3).

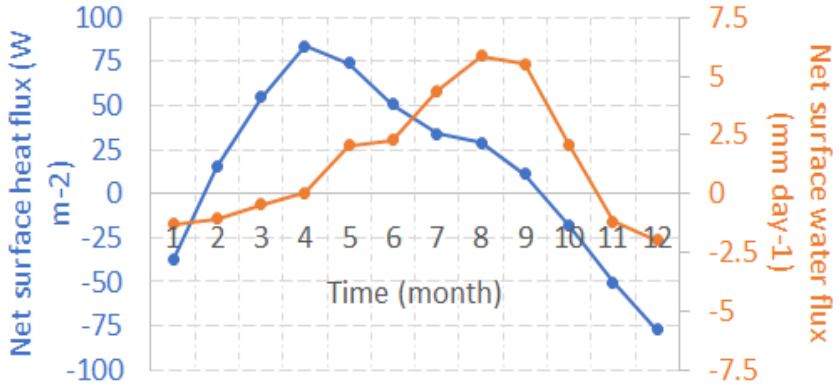

Figure 1.3: Climatological heat and net freshwater flux averaged over the GoT from Era5 reanalysis during the period from 2000 to 2020.

- **Episodic forcing**

The SEA climate, environment, and society are also experienced a strong influence from extreme events, including tropical cyclones (or tropical typhoons). The conventional typhoon season typically spans from summer to fall, extending for several months from May to November. Tropical cyclones can sometimes form beyond this period. About five to six storms affect the Vietnamese coastline every

year, mostly occurring in August and September (Nguyen et al., 2019). Not only causing severe impacts on human and economic losses, tropical storms also induce a strong momentum, heat, and water fluxes exchange between the ocean and atmosphere at a short timescale. In the VNES/SCS, the effects of tropical cyclones on the ocean have been investigated in several studies, e.g., the typhoon Ernie (1996) triggered significant SST cooling and sea surface depression in the wake of the storm (Chu et al., 2000). Another can be named, such as typhoon Pabuk (2007) which largely intensified the near-bottom current along its route (from the Luzon Strait to the Hainan Strait) (Liu et al., 2011). Wang et al. (2014) also observed a strong deep SCS circulation induced by typhoon activities which suggests that the effects of typhoons can penetrate the deep ocean. By examining 4 strong typhoons during the year 2013, Piton et al. (2021) have demonstrated that the typhoon, depending on their direction and intensity, can significantly alter the general circulation by rapidly generating water fluxes that can be up to 400 times larger than the climatological fluxes, and their influence can last for several days before and after the storm passes the region.

- **Large-scale phenomena**

Additionally, at interannual time scales, the VNES/SCS region is influenced by the El Niño Southern Oscillation (ENSO) phenomenon. ENSO indicates an irregular variation in winds and sea surface temperature over the tropical eastern Pacific Ocean that can influence the global atmospheric circulation. The phenomenon consists of two opposite phases, known as the warming phase of the sea temperature, El Niño, and the cooling phase, La Niña. There are a number of studies that targeted the inter-annual variability of the VNES/SCS region due to ENSO, in particular, the sea surface temperature (Huynh et al., 2016; Liu et al.,2014; Yang et al., 2015: Wang et al., 2006), sea level (Peng et al., 2013; Rong et al., 2007), surface winds (Huynh et al., 2016), precipitations (Juneng and Tangang 2005; Vinh et al., 2014; Räsänen and Kummu, 2013; Räsänen et al., 2016), cyclone frequency occurrences (Camargo and Sobel, 2005; Wu et al., 2005), river runoff (Räsänen and Kummu, 2013; Xue et al., 2011) and upwelling variability (Da et al., 2019). Furthermore, many studies suggested that the summer monsoon is modulated by ENSO such that El Niño/La Niña phases weaken/strengthen the summer monsoon with later/earlier onset (Chou et al., 2003; Liu et al. 2012; Dippner et al., 2013). Nevertheless, the Madden Julian Oscillation (MJO) and the Indian Ocean Dipole (IOD) also influence the VNES/SCS interannual variability, and thus possibly the GoT dynamics inter-annual variability. MJO contributes to larger than 10% of the intra-seasonal anomalous precipitations over the VNES/SCS in summer (Zhang et al., 2009) while the IOD may impact the onset of the summer monsoon during non-ENSO years (Yuan et al., 2008).

In a recent study by Piton et al. (2020), it is argued that the ENSO event influences the seasonal circulation in the GoT by adjusting the strength of the monsoon wind. During the El Niño event, the winter circulation is weakened in response to the reduction of the northeastern wind while it is

strengthened during summer as the southwestern wind intensifies. However, the assessment of their impacts is still limited in the GoT.

1.2.3. River runoff

River input provides a significant amount of freshwater, sediments, and nutrients into the sea. From the north to the south, the freshwater is distributed into the gulf through several river mouths. Among the five main river sources in the GoT (Fig. 1.4), the Red River is the largest in terms of freshwater and sediment discharge. The Red River originates from the Yunnan River in southern China. When flowing into Vietnam, the main river branch receives waters from two major tributaries: the Da and Lo rivers before discharging into the GoT. Downstream, the river separates into several distributaries in the low elevated area and forms the large Red River delta with an area of 15,000 km². The river, which is 1150 km long and contains a total amount of 169,000 km² of watersheds, is the second-largest river system in Vietnam after the Mekong River system (Vinh et al., 2014). The climatological Red River discharge demonstrates a seasonal modulation that is largely controlled by the monsoon regime (Fig. 1.4). It is shown that the high river discharge period occurs during summer (June to early October), which is associated with the rainy season, and the low river discharge period spans from November to May. The discharge during the rainy season brings about 71-79% of the total annual input. The annual peak river discharge during the rainy season is at the rate of about 12,000 $m^3 s^{-1}$ (Fig. 1.4) and the maximum discharge rate was observed in 1976, about 23,000 $m^3 s^{-1}$ (Vinh et al., 2014).

Although little is known about other rivers in the GoT in terms of freshwater discharge, the climatological data suggest that their contribution is by far smaller than that of the Red River. In the north of the GoT, the annual peak river discharge of two rivers: Nanliu and Qinjiang, are about 500 $m^3 s^{-1}$ from June to August. In the southern gulf, the flooding period occurs from late September to October, one month later compared to the northern rivers. The maximum discharge rate of the Ca River attains the rate of about 1900 $m^3 s^{-1}$ (Fig. 1.4). The higher discharge rate of the southern rivers can be caused by large excessive rainfall at the end of the rainy season and the occasional occurrence of tropical cyclones. Moreover, the short and steep slope of the river drainage basin leads to an increase in the peak flow of these rivers.

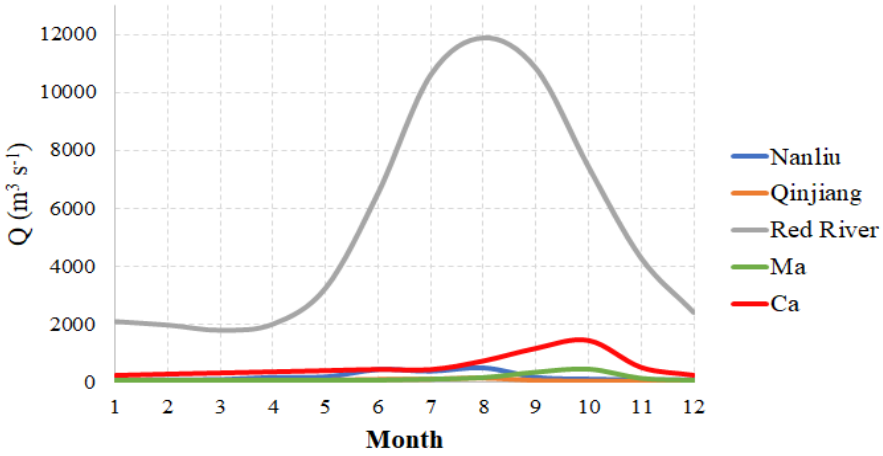

Figure 1.4: Climatological freshwater discharge from five main rivers in the Gulf of Tonkin (data from Global Runoff Data Centre (GRDC) (https://portal.grdc.bafg.de))

1.3. Existing knowledge of the GoT hydrodynamics

1.3.1. Ocean climatology

In a recent study, the variability of ocean dynamics in terms of surface current kinetic energy, sea surface temperature (SST), and salinity (SSS) in the GoT was documented (Loisel et al., 2016). Overall, the water dynamics in the GoT exhibit a strong seasonal variability due to the impact of monsoonal conditions (Fig.1.5). During the NE monsoon (winter), a combined effect of surface heat flux and northeastern cold wind blowing over the shelf induces a vast cooling and densification of surface water (Fig.1.5b). The water over the shallow region is cooling faster than the offshore region, thus, leading to the formation of a cold tongue along the northwest coast of the gulf and a difference of about 4°C between the offshore and nearshore regions (Fig.1.5b). Consequently, the densification of surface water and the minimum precipitation and river discharge results in strong vertical mixing down to the bottom depth in almost all the regions (Fig.1.5a). The seasonal contrast in vertical mixing is observed during the summer when the warm and wet weather conditions kick in. The sea surface heating and the weak southwest wind thus result in strong stratification and weak vertical mixing in the GoT as shown by the mixed layer depth (MLD) which penetrates down only to about 20 m below the surface (Fig.1.5d).

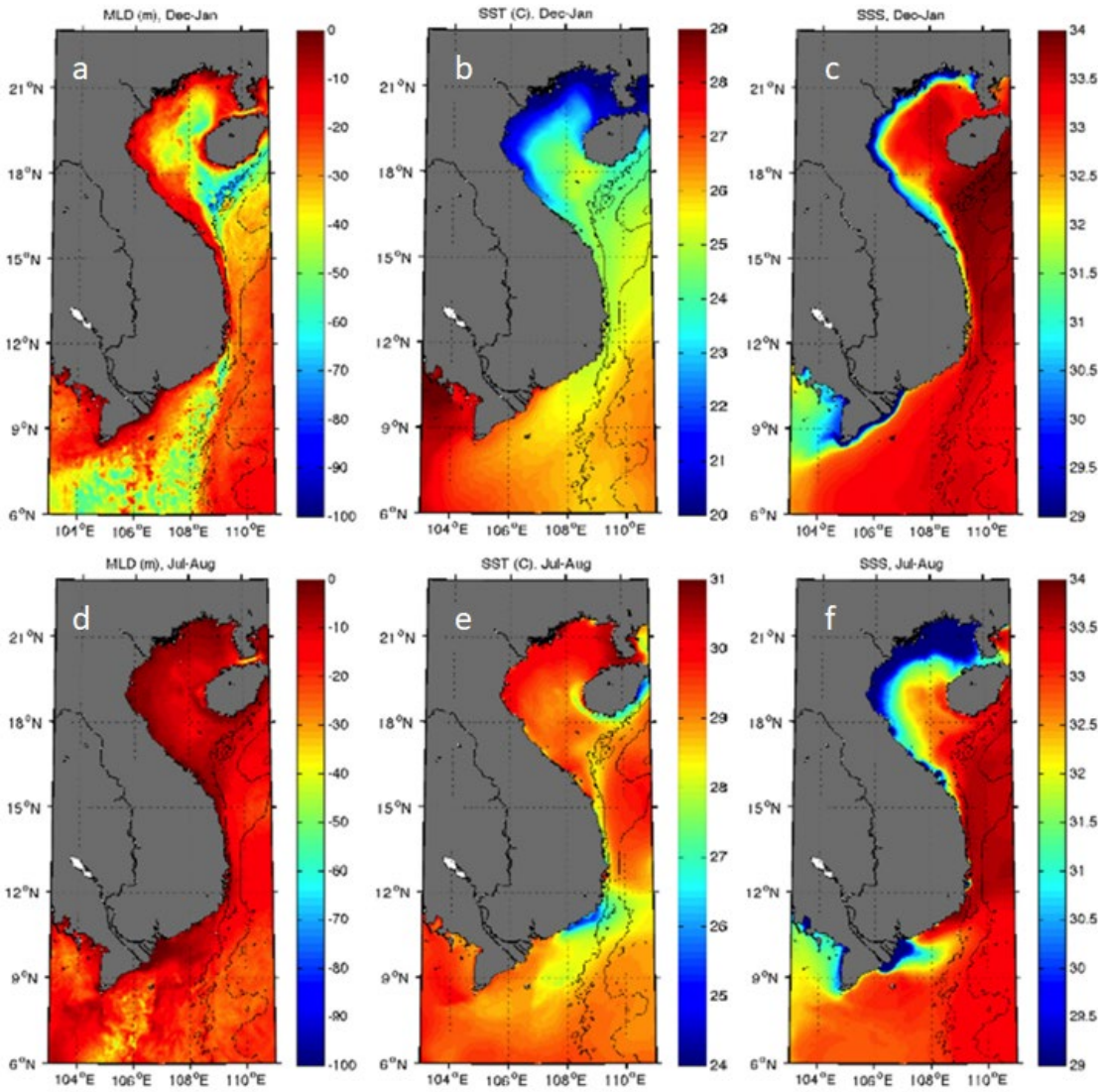

Figure 1.5: Distribution of mixed layer depth (MLD) (a, d), sea surface temperature (SST) (b, e) and sea surface salinity (SSS) (c, f) from numerical model between July 2013 and January 2016 (adapted from Loisel et al. (2016))

1.3.2. Surface circulation in the GoT

The VNES/SCS circulation has been focused on in many studies (Xu et al., 1982; Chu and Li 2000; Fang et al., 2002). The dynamics of this region as well as in the GoT are largely driven by the atmospheric monsoon wind systems. While the VNES/SCS oceanic circulation is largely studied and understood, the GoT circulation has attracted only limited attention from researchers over recent decades and remains a topic of debate in the literature. A most up-to-date review on the modeling and observation-based studies of the GoT circulation can be found in (Gao et al., 2017).

Winter circulation

Besides a general agreement on a gulf-scale cyclonic circulation in winter, four different structures of the regional winter circulation have been proposed:

1) The gulf-scale cyclonic circulation consists of two cyclonic gyres: one in the southern GoT and one in the middle of the northern GoT (Tan 1987, results based on one-year long observations) (Fig. 1.6a).

2) The gulf-scale cyclonic circulation with a small cyclonic gyre enclosed in the northern GoT (Yu and Liu, 1993, based on historical in-situ observations) (Fig. 1.6b).

3) The gulf-scale cyclonic circulation consists of two cyclonic gyres: one in the southern GoT and one in the northern GoT, with a southward current following the Vietnamese coast and a southwestward current following the northwestern coasts of Hainan (Manh and Yanagi, 2000; Xia et al., 2001; Sun et al., 2001, all based on 3D modeling) (Fig. 1.6c).

4) The circulation consists of a northern enclosed cyclonic gyre and a southern anticyclonic gyre (Yuan and Deng, 1999; based on the 3D model). Despite these discrepancies in proposed circulation patterns, all of the above-mentioned studies suggested that winter monsoon winds are the primary drivers of winter surface circulation. However, the results of Gao et al. (2014b), based on numerical modeling, demonstrated that density-driven currents are the most relevant factor that influences winter circulation (Fig. 1.6d).

Summer circulation

Due to the combined effect of wind, heat flux, and river discharge, the circulation structure during summer is complex and can be generally characterized by three patterns:

1) A gulf-scale anticyclonic circulation (Sun et al., 2001, based on 3D modeling) (Fig. 1.6e)

2) A gulf-scale cyclonic circulation (Ding et al., 2013; Xia et al., 2001, using numerical modeling) (Fig. 1.6f)

3) A two-gyre structure circulation: one cyclonic gyre enclosed in the northern GoT and one anticyclonic gyre at the southern GoT boundary (Yang et al., 2003, based on field observations; Gao et al., 2013, based on 3D modeling) (Fig. 1.6g)

In addition, driving mechanisms are still under discussion as some studies suggest that the summer circulation is mainly driven by density gradients (Xia et al., 2001; Yang et al., 2003, based on 3D modeling) while others show that the circulation is dominated by the monsoon winds (Manh and Yanahi, 2000; Sun et al., 2001).

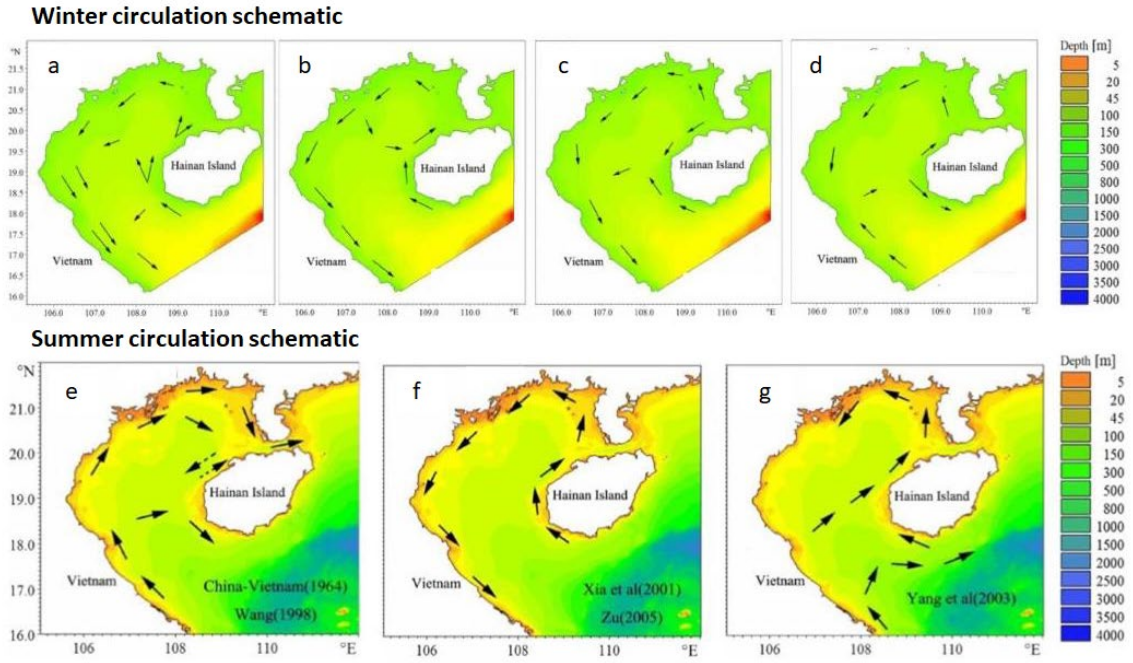

Figure 1.6: Different schematics of the Gulf of Tonkin surface circulation during winter (a, b, c, d) and summer (e, f, g) (adapted from Gao et al. (2017))

1.3.3. Tides

In shallow water regions as in many shelf sea regions, tides are the largest mechanical forcing that drives the circulation. It is an important driving force for coastal sediment transport and mixing in the river mouths. In fact, most of the tidal energy input to the shelf seas does not come directly from the action of the tidal generating force due to the small area, instead, it is delivered to the shelf from the open ocean. The tide-generating force acting over the large extent of the ocean basins drives the deep ocean tides which travel around the oceans in the form of long waves. Tides in the VNES/SCS were first described in Wyrtki (1961) who documented a general pattern of four main tidal constituents (K1, O1, M2, S2) in the region. Later, a more complete picture of tidal magnitudes and phases in the area was assessed by Ye and Robinson (1983) by using the numerical model.

In the earlier studies (e.g., Nguyen Ngoc Thuy, 1984; Fang et al., 1999; Manh and Yanagi, 2000; Shi et al., 2002; van Maren et al., 2004; Chen et al., 2012a; Minh et al., 2014), tidal motions in the GoT have been assessed with specific emphasis on coastal circulation and estuarine dynamics. In the GoT, as well as in the VNES/SCS region, diurnal tides (period close to one day) largely dominate the semi-diurnal tides (period close to 12 h). The tidal energy flux in the GoT is maintained primarily through the large southern entrance where the diurnal tide amplitude is already larger than the semi-diurnal (Hu et al., 2001; Shi et al., 2002; Minh et al., 2014). From the south to the north of the gulf, the diurnal tidal amplitudes (O1 and K1) gradually increase, reaching the maximum of about 1 m in the northeastern part of the gulf (Fig. 1.5a, b). The M2 tidal amplitude while almost equal in the southern gulf, appears to be about half of the magnitude of the diurnal tides in the northern Gulf (Fig. 1.5c). For

the S2 tidal constituent, the tidal magnitude is reduced by a factor of 8 compared to the diurnal tides (Fig. 1.5d). The GoT is one of few basins in the world where the tidal regime is mesotidal (tidal range of 2 – 4 m), or even locally macrotidal (tidal range -larger than 4 m) (van Maren et al., 2004).

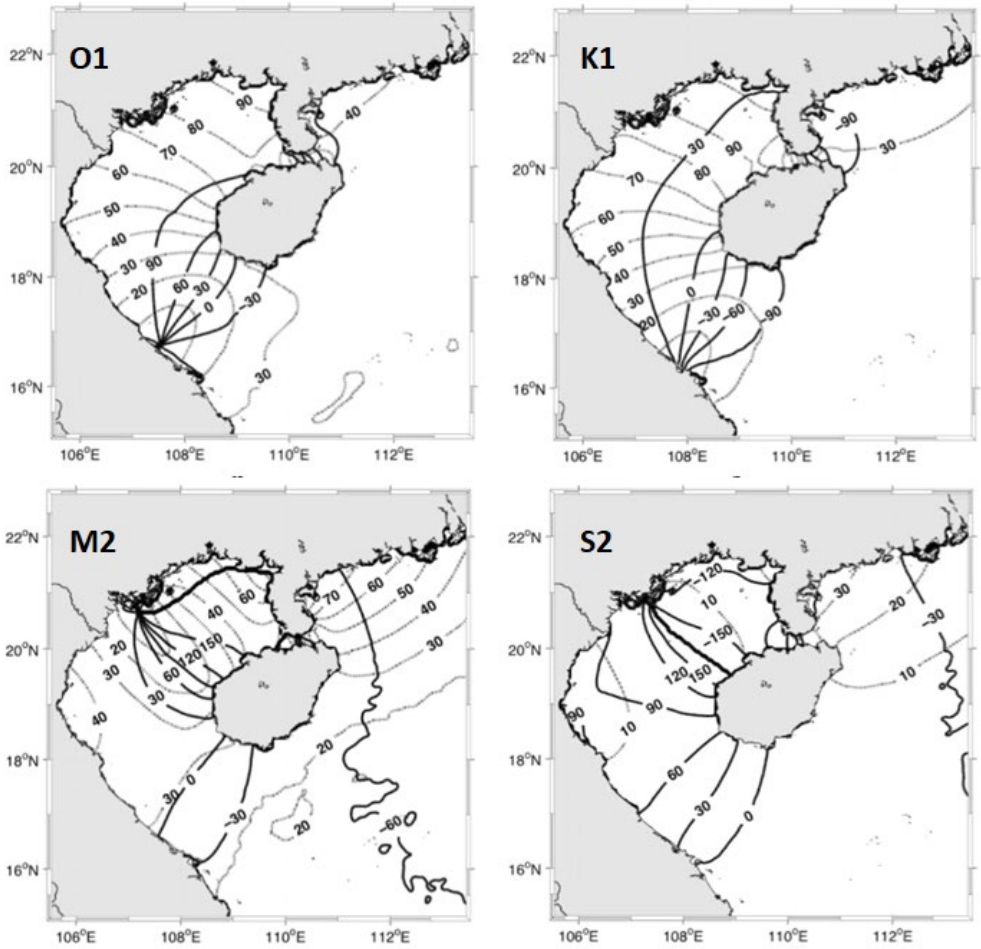

Figure 1.7: Co-tidal chart for four main tidal constituents in the Gulf of Tonkin referred to GMT+7. Solid lines represent tidal phase-lag in degree, dashed line represents tidal amplitude in cm (Minh et al., 2014)

In the previous modeling studies (Nguyen Ngoc Thuy, 1984; Fang et al., 1999; Manh and Yanagi, 2000; Shi et al., 2002; van Maren et al., 2004; Chen et al., 2012a; Minh et al., 2014), the tidal prediction reveals large discrepancies compared to observations. The limitation often comes from the coarse resolution and poorly resolved bathymetry in the numerical model, especially in the coastal area (Minh et al., 2014). Also, the uncertainties in the boundary forcing or due to a poorly resolved bathymetry can play a major role in tidal simulations (Piton et al., 2020).

Moreover, to the best of our knowledge, the tidal currents were only documented in a few studies since most of them relied on observations by the coastal tidal gauges and in-situ current measurements in the gulf, which are limited in time. In these studies, a quite close behavior to the Kelvin wave in an enclosed basin (Taylor, 1922) has been found. Shi et al. (2002); Chen et al. (2012a, b) argued that the

tidal currents are generally weak in the interior of the gulf but are rather strong near the Chinese coast, around Hainan Island, and in the Hainan strait. From mooring observations in the middle of the northern gulf, Ding et al. (2013) found that the tidal ellipses are flat and symmetric in the north-south direction with a small magnitude (25 cm s^{-1} for the K1 and O1 constituents and 15 cm s^{-1} for the M2). However, they also indicated that the tides were more energetic under stratified summer conditions than during winter vertical mixing. In addition, the dynamics of the southern part of the gulf was not assessed because of the lack of observations. This reveals the need for further investigation to better understand the tidal motions in the GoT and to better improve the model simulations.

1.3.4. Influence of the river discharge

The coastal rivers release a significant amount of freshwater into the sea. The low salinity water flow is constrained by the Coriolis force and tends to be trapped at the coast to establish a flow parallel to the coast, namely the coastal current. This current, balanced by the bottom friction and the Coriolis force, has the same direction as a propagating Kelvin wave (Simpson and Sharples, 2012). Away from the outflow region, coastal current can be characterized as bottom trapped, in which most of the flow structure is in contact with a sloping bottom (Lentz & Helfrich, 2002), or surface advected, where the surface layer is detached from the bottom (Mazzini & Chant, 2016). Several coastal current dynamics have been documented in the literature, such as the Norwegian Coastal Current (Mork 1981), the Delaware Coastal Current (Münchow and Garvine 1993), and the Oregon coastal current (Mazzini et al., 2014).

Coastal currents play an important role in the transport of freshwater, nutrients, larvae, pollutants, sediment, etc. They contribute to the along-shore transport of materials from the estuary to the sea which can propagate for a long distance. The formation of sharp density fronts between the low salinity region and ambient ocean water often acts as barriers prohibiting the exchange processes between the regions inshore of the front and the adjacent ocean waters offshore. These fronts can significantly impact the marine ecosystems by controlling the along- and cross-shore transports and modifying the ocean stratification (Hickey et al. 2010). In addition, the change in stratification may allow or modify internal motions and also affect small-scale processes such as turbulence and mixing (Mazzini et al., 2014).

In the GoT as well as in the VNES/SCS region, very few studies were focused on assessing the impact of the river on large-scale circulation. Using a numerical model, Chen et al. (2012a, b) argued that the freshwater discharge from the Red river induces a buoyant current along the Vietnamese coast. This flow could extend toward the middle of Vietnam and joins a tidally rectified current from the south in central Vietnam inducing a seaward extension in this region. Ding et al. (2013) elevated this idea and suggested that the river plume interacts with the southwest monsoon significantly intensifying the surface cyclonic circulation in summer. The dynamics of the river plume is largely controlled by the

buoyancy input, the surface wind, and tides. The changes in the balance between stratification and mixing occur on a variety of time scales: from seasonal through monthly and fortnightly down to one day or shorter. The seasonal variability of the river plume is more extreme in the tropical regions which exhibit monsoonal cycles, and the freshwater discharge is the largest during the wet summer (Simpson and Sharples, 2012). In the GoT, the seaward extension of the river plume can exceed 150 km from the coast during the high runoff in summer while under low runoff in winter, it is confined to a narrow region and is almost diminished (Nguyen-Duy et al., 2021). Along-shore wind forcing can also alter the speed and the structure of the river plume as it moves along the coast, thus, largely affecting the dynamics of the coastal area in the southern GoT (Rogowski et al., 2019).

1.3.5. Turbulent motions

The GoT circulation is asserted to be complex in response to the highly variable forcing conditions mentioned above. The turbulent motions, spanning a wide variety of spatial and temporal scales, are directly connected to the transport of heat and salt, dispersion of pollutants, nutrients, etc., especially in marginal ocean areas with more complex geography and bathymetry. In-situ observations are generally too sparse to provide comprehensive information about turbulent motions. Using satellite observations of Chl-a distribution at the sea surface, the complex dynamics was revealed which include numerous swirling and filamentary patterns as a result of the interaction of multi-scale motions (Fig. 1.8). Characterizing these dynamics is important as it helps to improve the study of horizontal transport and mixing and how they affect, for example, the marine ecosystems, carbon cycle, etc.

The term “fine scales” represents the dynamics of the ocean with spatial scales of roughly 1-100 km and temporal scales of days to weeks. These scales of motion are of practical importance because it is associated with a peak in the energy spectrum of ocean turbulence (Ferrari & Wunsch 2009) and emerge as dominant factors that determine the water parcels’ trajectories (Lehahn et al., 2018). At the same time, it is difficult to separate mesoscale motions, O(~ 10 – 1000 km), from the nearby submesoscale structures, which are often referred to as fronts and small eddies with O(~ 1 – 10 km). The study of transport and dispersion processes in the flow is often performed in the Lagrangian framework, focusing on the flow evolving along the water trajectories. This approach is similar to describing the property of the flow following an object (water parcels) that does not have active motion and therefore drifts along current trajectories (Lehahn et al., 2018). Lagrangian statistics based on the availability of observational drifter data (i.e., Balwada et al., 2020; Berti et al., 2011; Schroeder et al., 2011, 2012; van Sebille et al., 2015) or from the advected virtual particles (e.g., Berti & Lapeyre, 2021; Foussard et al., 2017; Haza et al., 2010) have allowed accessing the stirring operated by turbulent flow at different scales. In addition, the Lagrangian approach allows to understand the mechanisms behind the distribution patterns of oceanic tracers using the theory of geometric structures, or the identification of Lagrangian Coherent Structures (LCSs) (i.e., D’Ovidio et al., 2004;

Haller & Yuan, 2000; Hernández-Carrasco & Orfila, 2018). However, turbulence and dispersion properties are not generally conclusive and vary from region to region (Berti & Lapeyre, 2021) as well as the physical processes acting at the submesoscale require further investigation (Lévy et al., 2018).

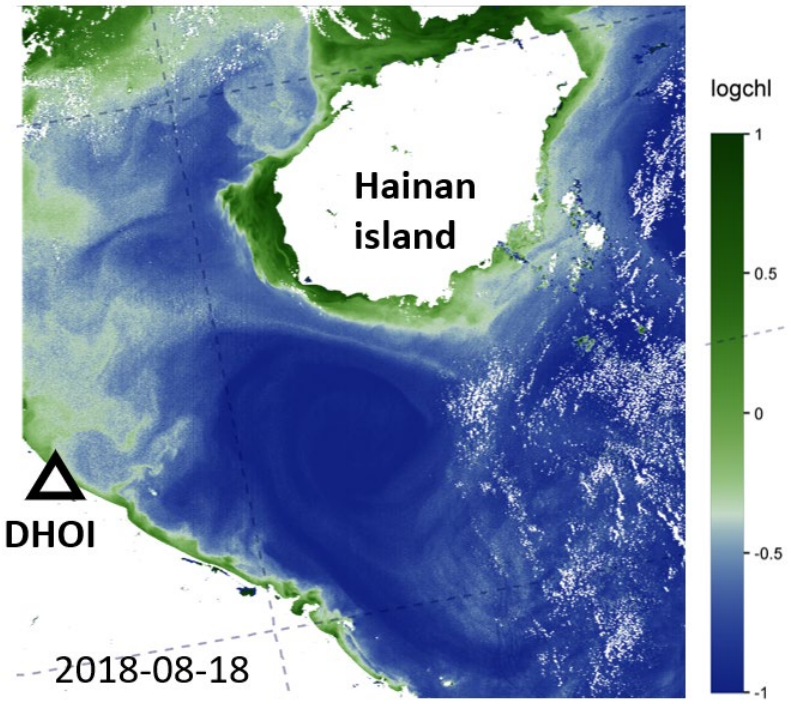

Figure 1.8: A cloud free snapshot of Chlorophyll-a concentration from MODIS/AQUA satellite on 18-August-2018 captures an extensive bloom in the region

1.4. Advantages of HF radar technology

Quantifying the ocean currents is important from certain points of view regarding ecological and economic reasons, however, it raises a challenge in oceanographic research since the ocean surface exhibits a wide range of temporal and spatial variability. There are several ways for achieving this task. For example, the surface current velocity can be measured using surface drifters (Lumpkin et al., 2017), or in situ current measurements throughout the water column at a static point or along a vessel track by towed Acoustic Doppler-based instruments (ADCP/AWAC) (Sentchev et al., 2020); or recently by sea glider (e.g., Miles et al. (2017). The drawbacks of these techniques are a short life time of the surface drifter while the use of ADCP, or gliders can provide measurements only in limited size regions. Observations made by the satellite altimetry, through providing instantaneous measurements over a large area, are not designed to capture reliable information in the coastal regions and their temporal resolution is low thus preventing capturing the evolution of small-scale motions there.

In this context, during the last decades, the remote sensing of surface currents using land-based radar technology has become a powerful tool for the study of coastal circulation and variability of surface currents. In particular, the radar data were used in many studies of tidal dynamics (Kaplan et al., 2005;

Lopez et al., 2020; Sentchev et al., 2009, 2013; Yoshikawa et al., 2007), wind-induced currents (Dzwonkowski et al., 2009), or quantification of the variability of coastal currents at different scales (Kim et al., 2010, 2013). Tidal current patterns were validated and observed in many places around the world, such as in the Iroise Sea and the English Channel where the tidal flow speed can be attained as high as 4 m s^{-1} (Sentchev et al., 2013). The authors also noted that the HF radar provided observations that cannot be done using traditional techniques due to extreme weather conditions and powerful tidal streams. In addition, the high temporal coverage of the radar data allows analyzing the evolution of river plumes, the fate of freshwater, and pollutants released from land to the ocean (i.e., Chant et al., 2008; Rogowski et al., 2019). The real-time data were also used for assessment of the anomalies of surface circulation triggered by extreme atmospheric conditions, i.e., surface current responses to the typhoons in the Taiwan strait (Fujii et al., 2013), or the detection of tsunamis, recently gaining much interest (Barrick and Lipa, 2011; Dzvonkovskaya et al., 2011; Guérin et al., 2018; Grilli et al., 2017).

For a long-term period of time, radar measurements can also be used in conjunction with in-situ measurements, providing a more complete description of the seasonal and inter-annual variation of ocean dynamics. For example, HF radar data were used to assess the inter-annual variation of Soya Warm currents (Ebuchi et al., 2006), and seasonal shifts in the coastal current along the United States west coast (Garcia-Reyes and Largier, 2012). Other applications of HFRs are also possible, targeting marine environment monitoring (biological transport, fisheries management, water quality monitoring), human activities at sea (port management, industries, offshore farms, marine renewable energies), wind/wave interaction (Shen et al., 2012), ship detection (Grosdidier, 2010; Roarty et al., 2013) and also other possible applications which will not be detailed in this study.

In a broad sense, motions in the ocean and associated processes are characterized by the interaction of multiple scales spanning both space and time, which greatly affect the state of the ocean and marine life in it. Fig. 1.9 shows the whole spectrum of motions in the ocean and a part of it that can be assessed using remote sensing of currents by HF radars. Due to the high potential of remote sensing of surface currents for oceanographic research, in the last two decades, coastal radar has been recognized as an important part of the coastal monitoring system which serves the purpose of coastal protection and management. Globally, the HF radar network has expanded and grown steadily at the regional and national levels. Actually, there are approximately 400 radar stations currently operating around the world (Roarty et al., 2019). Global efforts have been made to collaborate and promote radar technology as well as to exchange the data usage. Vietnam also contributes to the joint effort. Its HF radar network has been set up in the GoT and includes three radar sites operating since 2012 (Fig. 1.1).

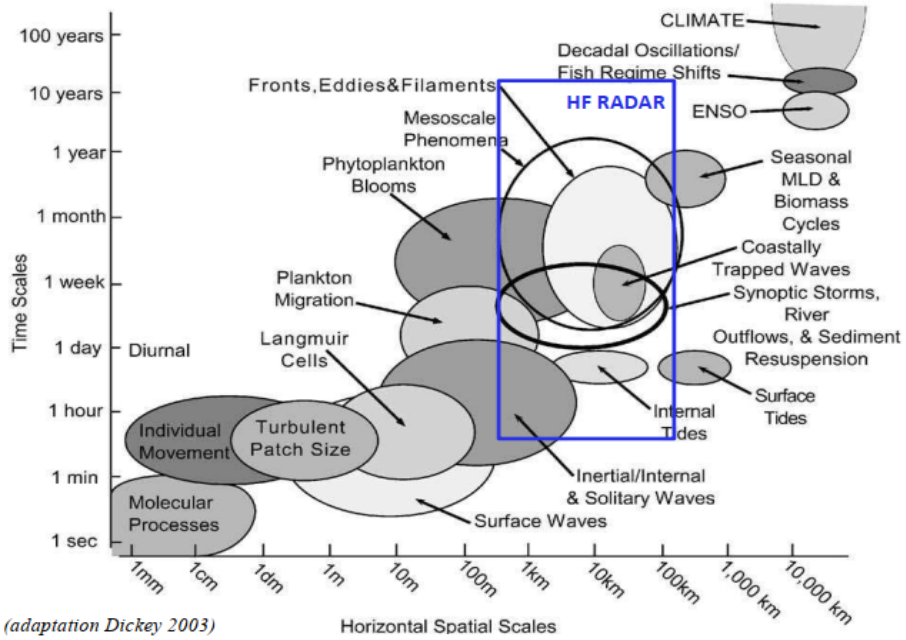

Figure 1.9: Scales of oceanic motions. The blue box represents processes in coastal ocean environment which can be captured by HF radar measurements. Diagram adapted from Dickey (2003)

1.5. Overview and objectives of the thesis

As described in sections 1.2 and 1.3, the previous studies have provided insight into dominant physical processes that govern large-scale circulation in the GoT. The surface circulation shows a high spatial and temporal variation linked to the variability of different forcing (local and remote). However, the results of modeling studies reported above also show limitations, i.e., the inputs were often idealized (homogeneous density, climatological forcing, etc.) or focused on a particular physical process or a single period. Thus, they were not sufficient to fully characterize the circulation in the GoT and investigate the mechanisms that govern its variability.

For this reason, the availability of coastal radar data, with high spatial and temporal coverage, is expected to help respond to the concern of many local studies aimed at understanding the complexity of coastal dynamics in the GoT. Therefore, we have identified three main objectives in this thesis:

(1) Using the HF radar velocity measurements and the advanced techniques of data processing, we built an extended database of current velocities which allowed us to characterize the coastal water dynamics, transport, and dispersion processes in the GoT extensively.

(2) The velocity dataset was used for extensive validation of the high-resolution numerical model (SYMPHONIE model) of circulation in the GoT. The validation exercise increased the confidence in modeling results and allowed to use the model for assessing the Lagrangian transport processes.

(3) The detailed mechanisms involving co-variations of physical and biological variables in the region are still not well documented. To fill the lack of knowledge in this field, we explore potential impacts of (sub)mesoscale features of circulation and lateral mixing on the variability of biological materials, in particular, the surface chlorophyll-a observed from satellite.

Following these objectives, the structure of this thesis is as follows:

In Chapter II, we present the basic knowledge of HF radar technology, data processing, and the methods of analysis used in this study. The validation of HF radar measurements with the *in-situ* measurements in the Eulerian framework as well as the problem of Lagrangian predictability is also discussed in this chapter.

Chapter III reports the results of application of the HF radar data in analyzing the variability of the surface circulation in the GoT. In particular, we examine in detail the surface current velocity variability at various scales, spanning from tidal to annual scale, and from that we investigate physical processes driving the variability. The research paper entitled "Multi-scale variability of circulation in the Gulf of Tonkin from remote sensing of surface currents by high-frequency radars" containing the results of our investigation was published in Ocean Dynamics. https://doi.org/10.1007/s10236-020-01440-x.

The issue of Lagrangian transport in the GoT is discussed in Chapter IV. Here we focus on turbulent properties of the flow field and multi-scale variability of coastal ocean motions. Relative dispersion of virtual particle pairs was assessed during two seasons (winter and summer). In this chapter, both current velocities derived from radar data and high-resolution numerical model are used for investigating the turbulent dispersion of passive tracers. We demonstrated the effect of frontal zones generated by the multi-scale interaction of turbulent motions on the spatial distribution of tracers in the GoT. The results present in this chapter were published in Continental Shelf Research: "Assessment of relative dispersion in the Gulf of Tonkin using numerical modeling and HF radar observations of surface currents". https://doi.org/10.1016/j.csr.2022.104784".

In Chapter V, we analyze a joint distribution of Lagrangian Coherent Structures (LCSs) and biological materials (satellite-derived chlorophyll-a concentrations) and discuss their variability. We discuss the role of horizontal advection and turbulent stirring in structuring the biological fields in the GoT.

Chapter VI summarizes the key results and findings obtained during this study. Questions remaining to be explored in future work are also discussed.

Chapter II. Materials and Methods

2.1. Remote sensing of currents by High-Frequency radar

A coastal radar system consists of transmitter and receiver antennas that are capable of transmitting electromagnetic radio waves of the frequency 3 - 50 MHz and capturing the signals backscattered from the moving ocean surface (Paduan & Graber 1997). Since the first land-based oceanographic HF radar was developed by Barrick in 1978, the radars have been recognized as a cost-effective means to expand the existing ocean observing system. HF radars are able to cover the gaps that other observation techniques (satellite or in-situ measurements) have in the fields. Installed along the coast, the radars can measure the ocean surface currents up to 200 km from the seashore and are capable of resolving the data with high spatial resolution (100 m – 6 km) in near-real-time (up to 20 minutes sampling rate). In this part of the thesis, we will focus on the key elements required for understanding the principles of current velocity measurement by HF radars and applications of this technology in oceanographic studies.

2.1.1. Description of HF Radar technology

2.1.1.1. Principle of surface current velocity measurements

The principle of current velocity measurement by HF radars is based on the radio waves backscattering from the moving rough sea surface. In the ocean, the sea waves act as a large diffraction grating for the transmitted electromagnetic radio waves. Under a known resonant condition, the transmitted radio waves of the wavelength λ_r are largely reflected back to their source whenever they encounter the trains of surface gravity waves traveling radially to the radar antenna and the wavelength of exactly half of the transmitted wavelength (Barrick et al., 1978) (Fig. 2.1). This phenomenon is called Bragg scattering by the ocean surface gravity wave which was firstly discovered by Crombie (1955). The resonant Bragg condition is given by:

$$\lambda_B = \frac{\lambda_r}{2cos\,(\theta)} \approx \frac{\lambda_r}{2} \qquad \text{(Eq. 2.1)}$$

Where θ is the incident angle between the transmitted radio wave and the reflected ocean surface. Assuming that the radar is placed close to the sea surface such that the incident angle is small, thus, $cos(\theta) \approx 1$.

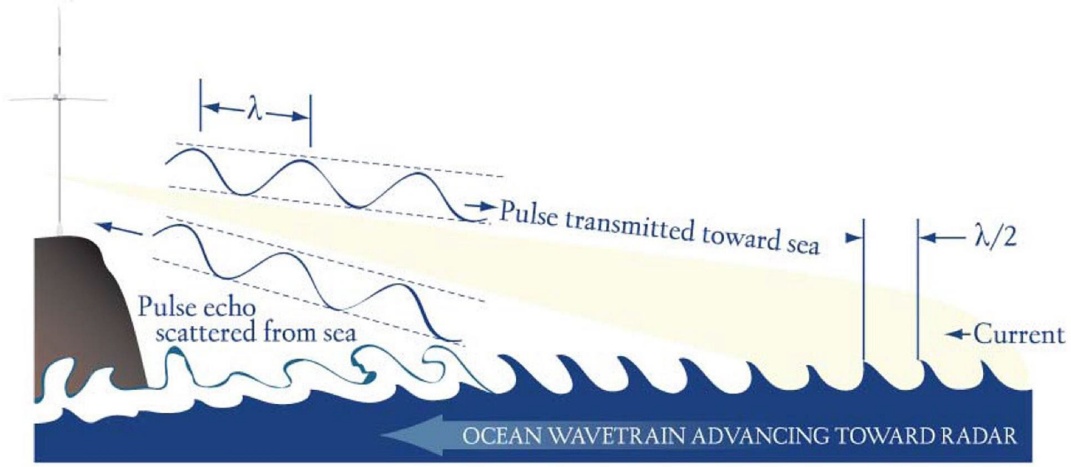

Figure 2.1: Principle of monitoring ocean surface currents and waves by HF radar. Adapted from Roarty et al. (2019)

The relationship between the radio signals backscatters and the ocean wave characteristics has been explored previously in the works of Barrick et al. (1971a, b; 1972). It was found that the Doppler frequency shift of the transmitted and backscattered radio waves agreed well with that predicted from the known phase speed of surface gravity waves traveling radially toward or away from the source. The spectra analyzed from the backscattering features two strong, narrow peaks due to the Bragg scattering (referred to as Bragg peaks or the 1st order peaks) arranged on either side of the operating frequency f_0 and surrounded by the lower energy peaks on the spectrum (Fig. 2.2). Crombie showed that these Bragg peaks came from two separate sources moving at a constant speed and can be utilized to express the speed of the moving sources as a function of the Doppler shift f_B. The continuum in the energy spectra appearing next to the Bragg peaks is considered the 2nd order and can be used to estimate the surface wave parameters. Using the resonant condition and the known transmitted wavelength, the Doppler shift of the Bragg peaks can be precisely identified (Barrick et al., 1977). Theoretically, in the case of no currents, these Bragg peaks are symmetric with respect to the Bragg frequency f_B offset from the origin:

$$f_B = \pm \frac{2v_B}{\lambda_r} \qquad \text{(Eq. 2.2)}$$

In this equation, f_B is shifted above or below the transmit frequency (shown at zero in Fig. 2.2), which represents the ocean wave advancing or receding toward the antenna respectively. The equation is

based on the assumption of the ocean waves travelling in the deep water, thus, the surface wave celerity (velocity), v_B, can be expressed by the dispersion equation ~~relation~~ of water waves in the linear wave theory:

$$v_B = \frac{\omega}{k} \approx \sqrt{\frac{g}{k} tanh(kh)} \qquad \text{(Eq. 2.3)}$$

Where g is the acceleration of gravity (9.81 m s^{-2}) and $k = \frac{2\pi}{\lambda_B}$ is the wave number. The shift of the Bragg peaks in relation to the transmitted frequency depends not only on the velocity of the resonant ocean surface wave but also on the velocity of the current that the ocean wave is riding (Stewart & Joy, 1974). When the ocean wave propagates over a current field, the propagation speed of the resonant ocean surface wave is now adjusted by the underlying current velocity component oriented toward the radar site. It can be expressed as $v = v_B + v_r$, where v_r is the radial surface current velocity. In this case, the Doppler peaks are no longer symmetric and are shifted with respect to the frequency f_B by an additional quantity Δf accounting for the underlying surface current (Fig. 2.2). The offset frequency Δf is expressed as:

$$\Delta f = \frac{2v_r}{\lambda_r} \qquad \text{(Eq. 2.4)}$$

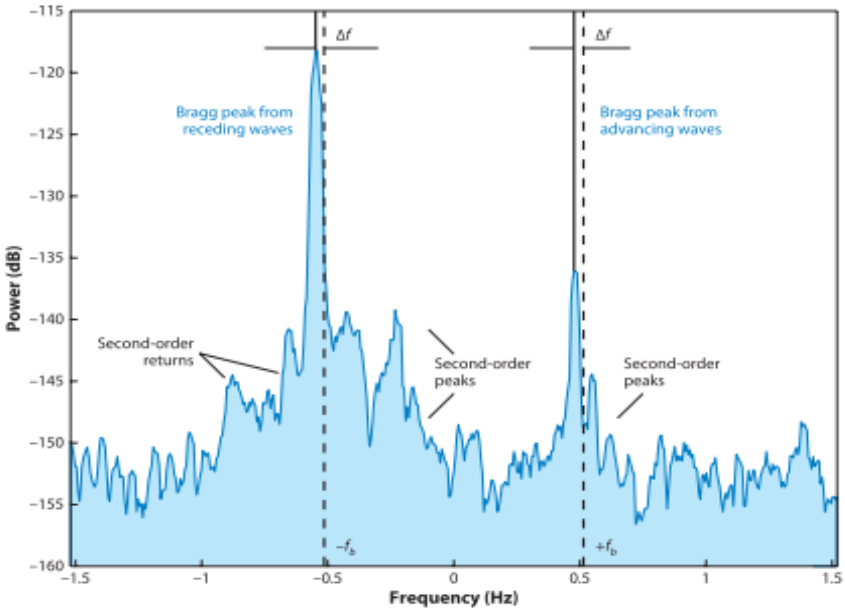

Figure 2.2: Doppler Spectrum retrieved from Ocean Surface Current Radar system in North Carolina, US. The dash lines at the positive (negative) frequency bands represent the predicted first-order peaks frequency based on theoretical phase speed formula of the Bragg-resonant surface waves approaching (receding) from the radar. The surface current components are then determined from the shift of the Doppler peak (Δf) (Paduan & Washburn, 2013).

By measuring this offset Δf from the Doppler spectrum, the surface current velocity in the radial direction v_r can be computed. The radial velocity v_r is designated positive if the ocean waves move toward the antenna or becomes negative if waves move away from the source. The current velocities measured by HF radar are depth-averaged. The effective depth of velocity measurement d below the surface varies as the function of transmitted wavelength (Stewart & Joy, 1974):

$$d = \frac{\lambda_r}{8\pi} \quad \text{(Eq. 2.5)}$$

Thus, the radar operating at a frequency of 5 MHz measures the current velocity within the water depth $d = 2\ m$ while the radar with the frequency of 15 MHz has the effective measurement depth $d \sim$ 1 m below the surface.

For mapping the surface currents, the radars provide three parameters: the magnitude, direction and distance to the measurement. While the magnitude of the surface current is obtained by analyzing the Doppler spectrum mentioned above, two additional pieces of information are determined by different approaches according to different HF radar systems.

The “target” direction is referred to as the angle of a return signal to the radar or the bearing of the measurement point. The extraction of the signal bearing requires a specific configuration for the radar receiver antenna. On the commercial ocean radar market, two different radar configurations exist. The first is the phased-array antenna, which is implemented by WERA company in Germany and several other systems. This system requires a linear array of at least 4 receiver antennas separated by half of the transmitted wavelength (Helzel et al., 2006). The second radar type uses the compact crossed-loop receiving antenna. It is fabricated by the CODAR company, USA (Barrick et al., 1977). For the case of the CODAR system, the compact form receiving antenna is configured with a three-elements system that simultaneously collect the data: one omnidirectional (monopole antenna) and two crossed-loop antennas placed 90° degree to each other (Fig. 2.3). The compact design allows the Seasonde CODAR radar to be set up in a small ground space which is convenient for the temporal deployment, for example, in case of maritime accident. In this configuration, simultaneous data from three antennas are reprocessed by a “direction-finding" method, namely Multiple Signal Classification (MUSIC), to extract the bearing angle to the scattering source.

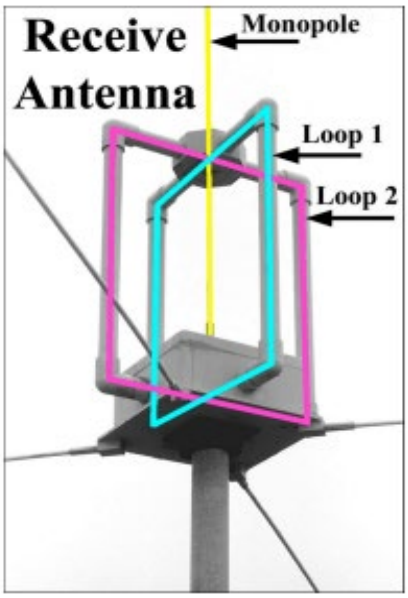

Figure 2.3: Configuration of the crossed-loop Seasonde CODAR receiver antenna (adapted from CODAR Seasonde applications manual).

In order to extract the signal bearing information, the data processing requires azimuthal resolving techniques (or direction-finding methods) which are categorized into two groups. The first one uses "beam-forming" (BF) technique which accurately identifies the signal origin by comparing the amplitudes and phases of individual antenna receivers from a linear phase array configuration (Helzel et al., 2006). The second method implements the MUSIC algorithm which allows the determination of the source of the signal using closely spaced antenna elements and is gaining much interest (Fujii et al., 2013). While the BF technique is often used in radar operation and is more accurate in identifying the signal direction even in the case of high noise (Wang & Gill, 2016), the angular resolution resolved from this technique heavily relies on the number of antennas which is limited in the installation space. Several comparisons between two azimuthal resolving techniques have been done in the past (e.g., Gürgel et al., 1999a, b; Essen et al., 2000). For example, a study carried out by Sentchev et al. (2013) in the Iroise Sea compared the BF and MUSIC techniques using the WERA radar system. They demonstrate both methods performed well and indicated a similar pattern in the velocity maps during the period of study. However, the authors noted that the velocity map reconstructed from the BF technique was smeared in azimuth and it was difficult to recognize small scale spatial structures in the velocity field. The DF, on the other hand, provided by the MUSIC algorithm yields much more details in the velocity field, however, inherently introduces noise and gaps (Fig. 2.4). Therefore, the application of the DF technique requires an efficient method for gap-filling and noise level control.

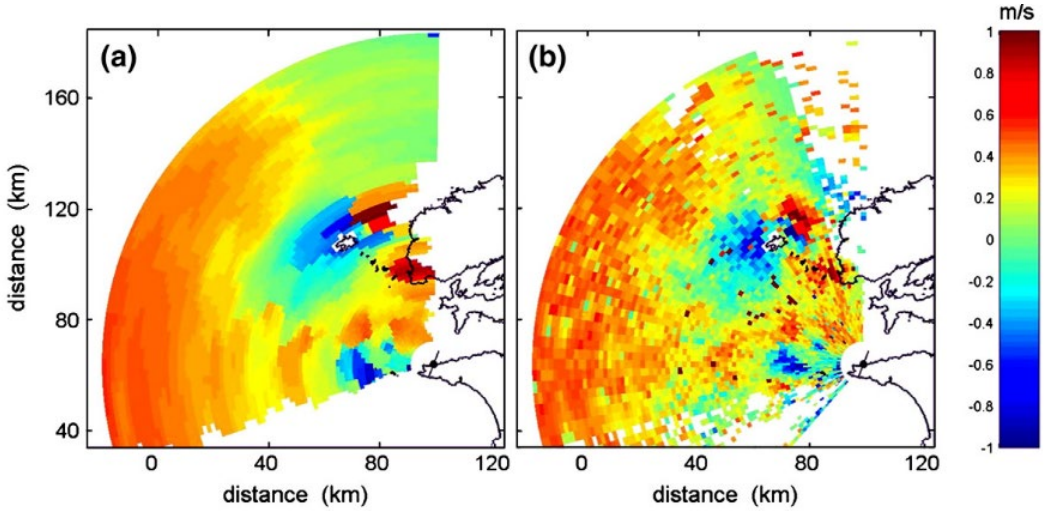

Figure 2.4: Radial velocity field derived from beam forming (BF) (a) and MUSIC (b) method of data processing in the Iroise Sea (Sentchev et al., 2013)

Lastly, determining the distance from the radar site to the point of radial velocity measurement is done by modulation of the emitted signals. Specifically, the radar transmits an electromagnetic wave in a frequency-swept pulse signals, in which the transmitted frequency increases linearly in the upper end of the pulse signal. The time lag between the transmitted electromagnetic radio waves and the returned signals are recorded. This time delay between each receiving period is used for the determination of the "target" range. The higher frequency of the transmitted and received signals, the larger distance from the radar to the "target" range. The spectral analysis of the returned signals is sorted into different bins which range from the closest to the furthest distance from the radar site.

Depending on the configuration of the radar, its ability to measure the surface current velocity varies. For the case of spatial resolution of velocity processing in each range cell from the radar, it is defined by the type of signals emitted by the radar. As for the CODAR radar type, it utilizes the Frequency Modulated Interrupted Continuous Wave with linear varying frequency (FMICW waveform). The radial resolution is constrained by the duration of the pulse signal and is approximately identified by the relationship with the signal bandwidth B (or the frequency interval in a swept):

$$\Delta r \approx \frac{c}{2B} \qquad \text{(Eq. 2.6)}$$

Where c is the speed of light. The radar with a higher frequency can monitor the surface current velocity with higher spatial resolution, i.e., the radar operating at a very high frequency (VHF) can measure the current velocity field with up to 300 m resolution. However, the radial resolution used in the real deployment is often smaller than this theoretical approximation. Depending on the transmitted

wavelength and the swept frequency of the signals, the width of the range cell typically ranges from 300 m to 6 km (http://www.codar.com/intro_hf_currentmap.shtml). Besides, the signal attenuation of the transmitted radio wave increases with the increase of transmitting frequency (Shay et al., 2002) which means that the signal with a higher frequency largely reduces its signal strength during transmission. A higher range of about 200 km is obtained for a 5 MHz system and a lower range of 30 – 40 km can be measured with the 45 MHz system. Thus, it gives a fair tradeoff that the low frequency radar system with low spatial data resolution can have a larger observation range and vice versa.

In other applications of the radar, the ocean surface waves can be empirically estimated from Doppler spectra using the integral information contained in the second order region and fitting with the ocean wave spectrum (Lipa et al., 2005). The wave parameters, i.e., wave height, period and direction or even the full directional spectrum, can be obtained depending on the quality of the radar data and the capability to identify the second order spectrum above noise level (Wyatt et al., 2011). The capability to probe the ocean surface wave is determined by the operating frequency of the radar as well. The lower the frequency is, the higher wave height can be measured. Above the maximum threshold for each radar frequency used, the first-order peak merges with the second-order one and the interpretation of the spectra becomes impossible with existing methods (Roarty et al., 2019). The example of different radar configurations and their associated measurement ability are given in Table 2.1.

Table 2.1: Characteristics of typical radar configurations and their associated solutions of surface current mapping (adapted from CODAR Seasonde applications manual)

Radar Frequency f_c(MHz)	Radar Wavelength λ_r(m)	Ocean Wavelength λ_B(m)	Effective depth of measurement d (m)	Typical Bandwidth B (kHz)	Typical Resolution Δr (km)	Typical Observation Range (km)	Upper Wave Height Limit $H_{1/3}$ (m)
5	60	30	2	15-30	6-12	175-220	25
12	25	12.5	1-1.5	25-100	2-5	60-75	13
25	12.5	6	0.5-1	50-300	1-3	35-50	7
48	6	3	<0.5	150-600	0.25-1	15-20	3

2.1.1.2. Surface current mapping by HF radar

A single radar measures a projection of the current velocity vector on the radar beam (radial velocity component, or the radials) in a polar coordinate system. The radial velocity field is divided into a number of range cells separated by range resolution Δr extending circularly from the radar site and azimuthal beams from 0° – 360° incremented every 1-5°. This signal processing technique requires several steps. At the first step, the raw signals are run through Fast Fourier transform (FFT) to acquire the Range Series data. Second FFT is applied to the Range Series to get Doppler Calculations. The final product of this process is the unaveraged cross spectra data (CSQ file). Each CSQ file covers a

relatively short period of time centered on a timestamp. For an individual long range CODAR radar operating at 5 MHz and sweep rate (frequency of each transmitted pulse) of 1 Hz, the CSQ files are written every 17 minutes using 2048-points FFT. Then, three consecutive CSQs (covering 51 minutes average) are run through a moving average for removing spikes and artificial ship echoes in the spectrum and create the averaged CSSs every 30 minutes with 15 minutes of overlapping between previous and following spectra. Then, the radial velocity field at a central time is processed by the average of five consecutive CSSs which is an average of approximately 3 hours. In the case of a higher frequency radar, the observation range is shorter, which requires less time for collecting spectral information at far ranges, thus, producing data with higher temporal resolution. The radar settings are configured depending on the radar type and the purpose of the application.

Since an individual radar site provides the surface current velocity in the radial direction with respect to the radar, the reconstruction of the surface velocity map requires at least two or more radars within a common footprint. A conventional method for combining radial velocities in a total velocity field is the Least Square fit (LS) method, suggested by Lipa & Barrick (1983). The surface current velocity is processed in each grid point, two or more radial vectors in the overlapping zone between radars are required for obtaining the total current vectors (Fig. 2.5). The velocity information at each grid point within a pre-defined radius is combined by minimizing the sum of deviations to generate u- and v-components of the surface currents. This method is quite straightforward and does not require any assumptions in the field.

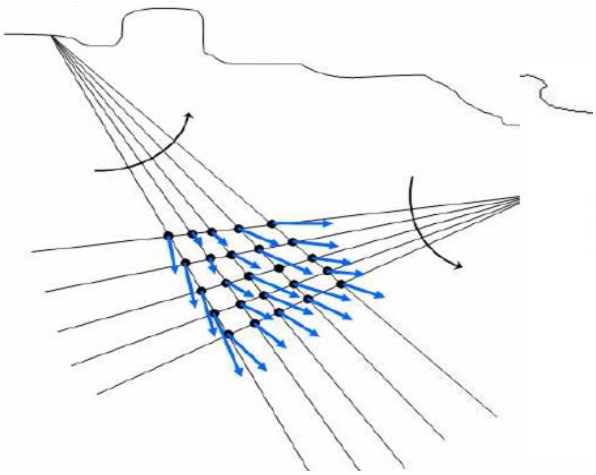

Figure 2.5: Schematic of total surface current velocity combination from two radar sites.

However, radial velocities are often sparse, and the vector current fields are incomplete most of the time. The gaps in the total velocity further restrict the use of radar data in analyzing the oceanic processes, i.e., identification of the coherent structures (Lekien et al., 2005) or limit the prediction of Lagrangian trajectories (Hernández-Carrasco et al., 2018). To overcome this drawback, several

interpolation techniques capable to extend the spatial coverage were proposed. The Optimal interpolation technique (OI), suggested by Kim et al. (2008), uses the empirical error covariances deduced from observations. However, since the idealized covariances implicitly drawn from the data, the method can perform poorly if large gaps are present in the observations. Another more sophisticated method to obtain the constant coverage of the vector fields is "Open-boundary modes analysis" or OMA (Kaplan & Lekien, 2007). The approach is based on the dynamical constrain of the divergent and rotational components of the 2D vector field. In this method, boundary conditions (free slip at the land boundary and zero gradients at the open boundary) are taken into account. The decomposition into different eigenfunctions allows the velocity field to be reconstructed using a certain number of characteristic modes.

At nearly the same time, Yaremchuk & Sentchev (2009) proposed a variational approach for reconstructing the kinematically constrained velocity fields (2dVar). This method uses the cost function representing the difference between the observed and interpolated current velocity and penalizes the divergence and curl of the surface current field. This method has been used for studying the tidal dynamics in the English Channel (e.g., Sentchev et al., 2011) and assessing the Lagrangian predictability of HF radar measurement in the Gulf of Mexico (Yaremchuk et al., 2013). The method was further extended by Yaremchuk & Sentchev (2011) to include the EOF-based iterative interpolation of radial velocity time series. The combined EOF/2dVar method includes four consecutive steps:

(a) EOF analysis of the spike-removed radial velocities,

(b) Estimation of the inverse of velocity error covariance and signal-to-noise separation,

(c) Filling of gaps in radial maps

(d) Interpolation of the surface current velocities on a regular grid using a variational method (2dVar) and current vector map generation.

An assessment of the performance of EOF/2dVar method in the case of radar measurements in the GoT is given in detail in Appendix C.

2.1.2. HF radar measurements in Vietnam

2.1.2.1. Description of the HF radar network in Vietnam

The coastal radar network in Vietnam, which currently consists of three CODAR-manufactured HF radars, has been set up and operating in the GoT since 2012 to date (Fig. 2.6a). Two southern radar sites, located at Nghi Xuan (XUAN) and Dong Hoi (DHOI), are installed with dual-transmitting

configurations, which consist of two transmitter antennas working simultaneously for extending the monitoring range and one receiver antenna. The northern site (HNDU) was set up and joined the network later. The site operates in low-power mode due to the power shortage of Hon Dau Island, i.e., transmitting signals at half of the peak energy. The remote area conditions and the difficulties in maintaining and operating causes the loss of observations at the HNDU site, which only shows an effective coverage of 30% by the data (Fig. 2.6b). The radars were configured to retrieve the radial velocities of the surface currents at the resolution of 5.8 km along the beam and azimuthal spacing of 5°. The temporal resolution was set to 1 h. Table 2.2 provides the specific configuration of the HFR system in Vietnam. The long-range configuration allows the radar system to cover a wide area up to 250 km, theoretically about one-third of the GoT, in trade-off the spatial resolution. The surface total current velocity is then mapped from the radial velocity on a regular grid of 6 km spacing.

2.1.2.2. HF radar data

After installation, the radar network in Vietnam operated in an experimental regime until 2014. Fig. 2.6b shows the data available from 2014 to mid-2020 for each of three radar sites in the GoT. The data are not uniformly available during the study period as the HNDU radar site covers only a small portion of the operation time due to several technical failures. During the same period, the two remaining radars perform much better except for some interruptions due to technical failures or maintenance stops. In our study, the analysis of the GoT circulation mostly relies on the period from April 2014 to October 2016 which was selected also for the numerical modeling. Generally, during the study period, the data coverage by two southern radars is good accounting for 91% (XUAN) and 87% (DHOI) of the expected coverage, respectively.

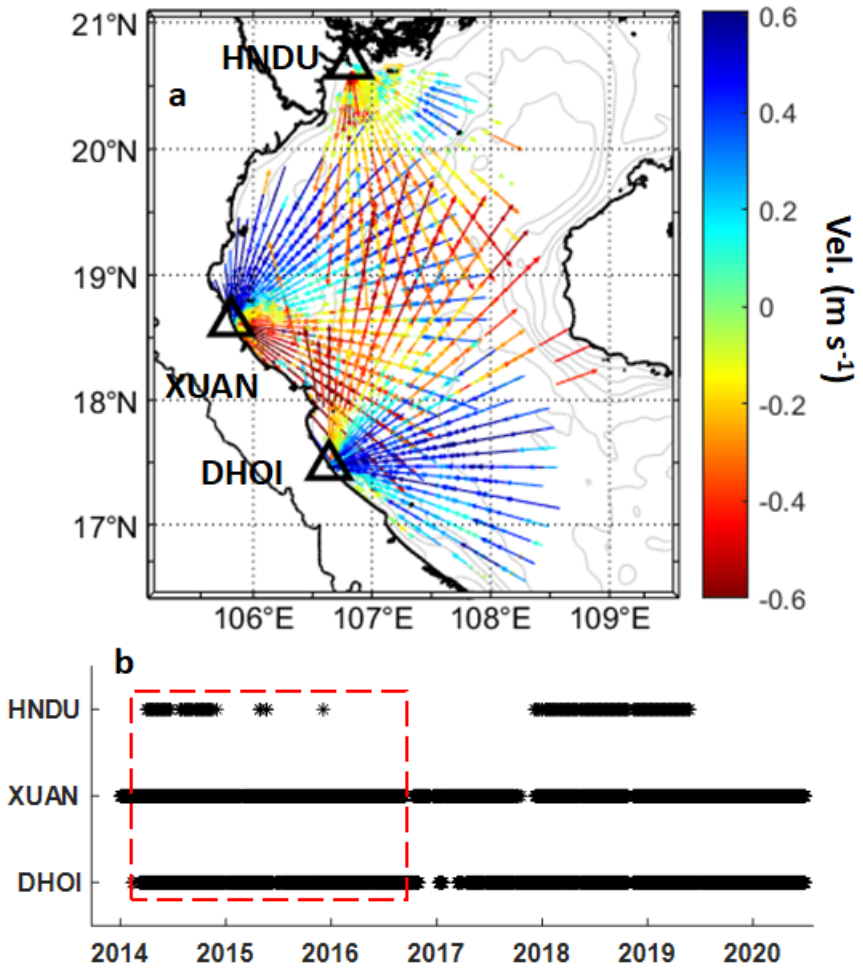

Figure 2.6: (a) Map of radial velocities derived from radar measurements in Vietnam. The radar site locations are shown by triangles. Blue (Red) vectors denote the current toward (away from) the radar. (b) Time history of data acquisition by three radars in Vietnam during the period from 2014 to 2020 (asterisks). Red square shows the period chosen for the study.

Table 2.2: Configuration and settings of CODAR Seasonde HF Radar systems in Vietnam

Parameters	Settings
Transmit frequency (MHz)	4.65 (Configured to 5.625 MHz in late 2018)
Transmit sweep rate (Hz)	1
Transmit Bandwidth (kHz)	25.734
Measurement Spectral Doppler bins	1024
Measurement Cycle (min)	17.1
Nominal range resolution (km)	5.825
Nominal Bearing resolution (°)	5°
Transmitted HF radar wavelength l (m)	64.5 (53.3 m for the frequency of 5.625 MHz)
Bragg scattering wavelength λ_B (m)	32.2 (26.6 m for the frequency of 5.625 MHz)
The effective depth of HF Bragg scatter (m) ($\lambda_B/(4\pi)$)	2.4 (2.1 m for the frequency of 5.625 MHz)
Transmitted waveform	Frequency Modulated Interrupted Continuous Wave (FMICW)
The technique of azimuthal resolution	MUSIC

During the operation, the quality of radar data varies. The gaps present in the data may originate from many sources: from software such as MUSIC used for directional processing, the noise in the signals that prohibits the detection of the Bragg peaks (interference due to the hardware power supply or from the surrounding environment). The quality of observations is thus affected by a poor SNR which causes sudden drops of radials counts and the observation range (Fig. 2.7b). The saturation limit for the receiver antenna is detected at roughly 25 dB whenever the SNRs in all antennas are below this threshold. Thus, the maximum observation range drops by more than 50% during the period of noisy signal (Fig. 2.7c). Moreover, the meteorological conditions also affect the radar measurements in the GoT. Fig. 2.7a indicates the variation of wind obtained in the XUAN radar site. A change in the data return is observed when the wind fluctuated, thus, leading to a drop of about 30% in the mean data availability. A possible explanation could be that the fluctuation in wind does not favor the full development of surface waves in this low-energy environment and is responsible for the drop in observation distance. However, more investigations are needed to understand the driving mechanism of similar failures.

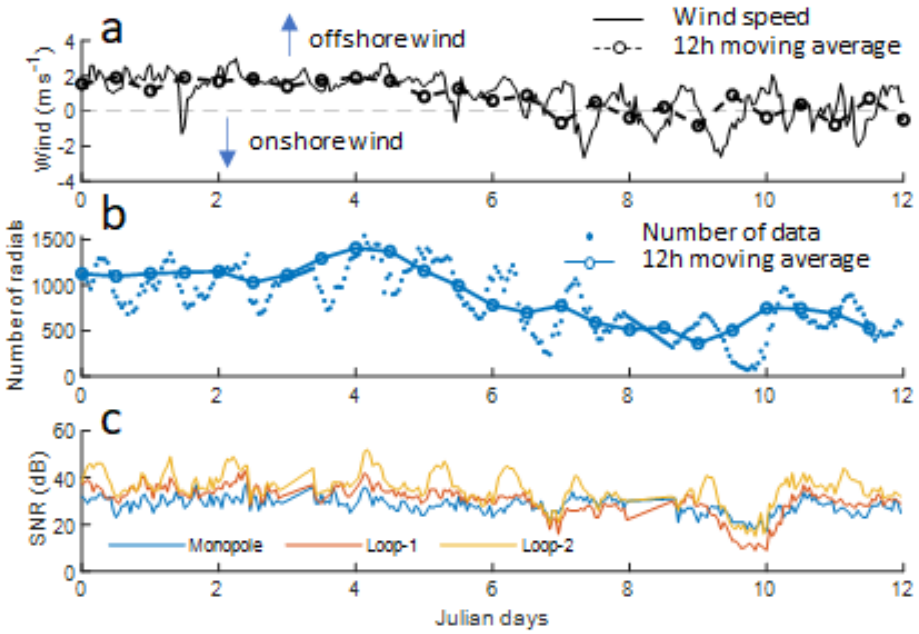

Figure 2.7: Evolution of wind (a) and radar data returned (b) from the XUAN radar site during January 08 – 22, 2018 and the Signal-to-Noise ratio (SNR) at the receiver antenna (c) during the same period.

Fig. 2.8a, b, and c show the portion of data available from each radar site compared to the total amount of data during the study period (April 2014 – October 2016). The sea state within the GoT appears to be less energetic than that at many other HF radar sites (e.g., Kohut et al., 2006; Kim et al., 2008), thus, limiting the radial coverage by the radar observations (Liu et al., 2008). Considering the area of more than 50% of data return, it is shown that the coverage at the XUAN radar site was more stable over the time than that at the DHOI site. Additionally, the data return from XUAN shows a better coverage range than that of the southern site. On the other hand, the region of high data availability from DHOI seems to extend further southward (Fig. 2.8b). A possible explanation of the difference in data acquired at two sites could be related to the antenna pattern distortion affecting the accuracy of signal retrievals in the southern sector. However, the use of operating frequency (5 MHz) could be another factor. In the low energy coastal environment such as in the GoT, the maximum coverage of radar observations is limited by the low frequency signal (Emery et al., 2004; Liu et al. 2010).

The geometric dilution of precision (GDOP) represents the spatial error when combining the radial velocities the total vectors. GDOP instability is computed from the inversion of beam angle covariance and varies with the available data and distance from the radar site. The error distribution increases drastically when the angle of the beam intersection becomes small or moves away from the site (Fig. 2.8d). In the region of high GDOP (~3), the errors in current vector magnitudes are significantly amplified (Kokkini et al., 2014). For the "best" estimation of the surface current vector fields, the

defined grid is chosen approximately inside the region with the GDOP threshold lower than 2.5 and the data coverage of greater than 50% (Fig. 2.8d).

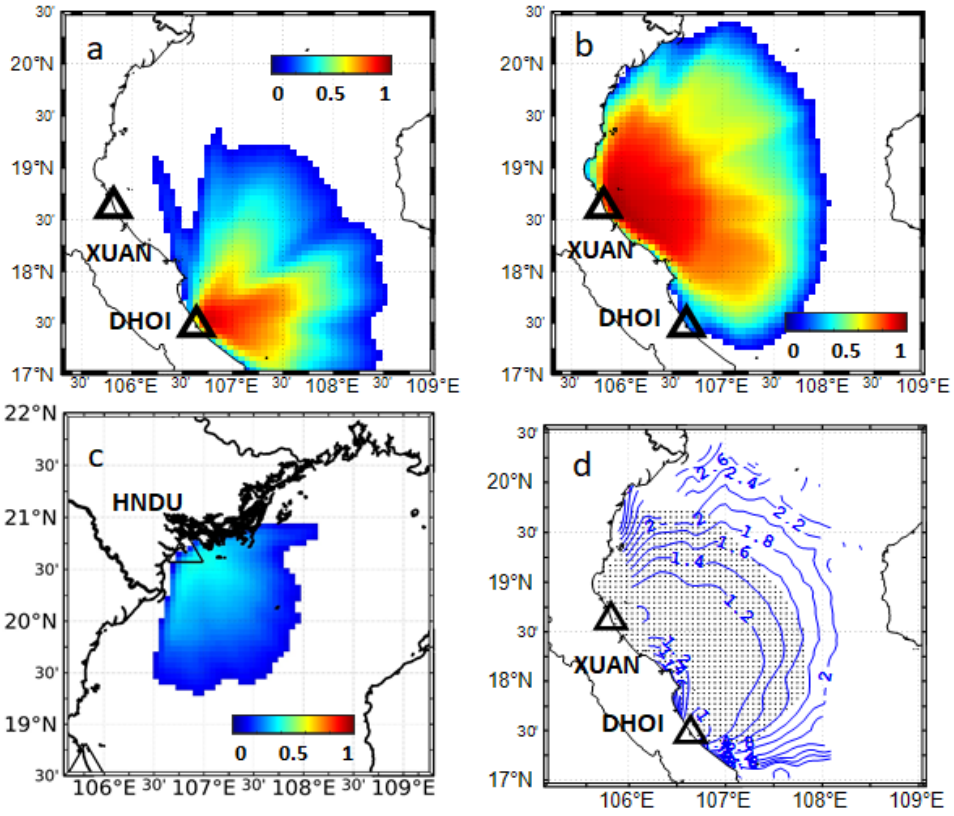

Figure 2.8: Ratio of temporal coverage by observations for three radars (a, b, c). Location of HFR stations is given by black triangle. (d) Average Geometric Dilution of Precision (GDOP) (contourlines) and location of grid points selected for processing the surface current velocities.

2.1.2.3. Surface current velocity maps

For analysis and processing of the radar data, we use the Matlab toolbox "HFR_Progs" (https://github.com/rowg/hfrprogs). The toolbox is open-source and widely used across the HFR worldwide community and contains various functions for visualizing and manipulating radar data.

In this study, a combination of the EOF/2dVar method is implemented for reconstructing the surface current velocity maps from radar measurements. The gaps present in the radial velocity fields are filled by the iterative Empirical Orthogonal Functions (EOF) based method. The covariance matrix of the dataset with nearly continuous space-time coverage can be approximately estimated from the radial velocities. On this basis, the leading EOF modes are computed, and the missing radial velocity data are filled in using these EOF modes (Alvera-Azcárate et al., 2005; Yaremchuk & Sentchev, 2011). This technique has been used in various applications for filling gaps in the gridded SST images

(Alvera-Azcárate et al., 2005; Barth et al., 2020) and also for the HF radar-derived velocities (Kokkini et al., 2014; Lopez et al., 2020; Sentchev et al., 2013; Yaremchuk & Sentchev, 2011).

In the present study, the iterative EOF method was applied to the radial velocity time series with 1-hour resolution. The method works well for the period of two to four months of hourly data within an area of higher than 30% data coverage. About 86 EOF modes, which accounts for more than 80% of explained variability of the initial data, were used to build the reconstructed velocity field. Fig. 2.9 represents the raw and the reconstructed field in October 2015. Being reconstructed from truncated EOF modes, the resulting fields are smoother than the original. In general, the reconstructed radial velocities are in a reasonable agreement with the raw data with the slightly lower values. The error of interpolation was less than 5 cm s^{-1} on average. The details of the interpolation method and cross-validation of the reconstructed velocity fields are given in Appendix B.

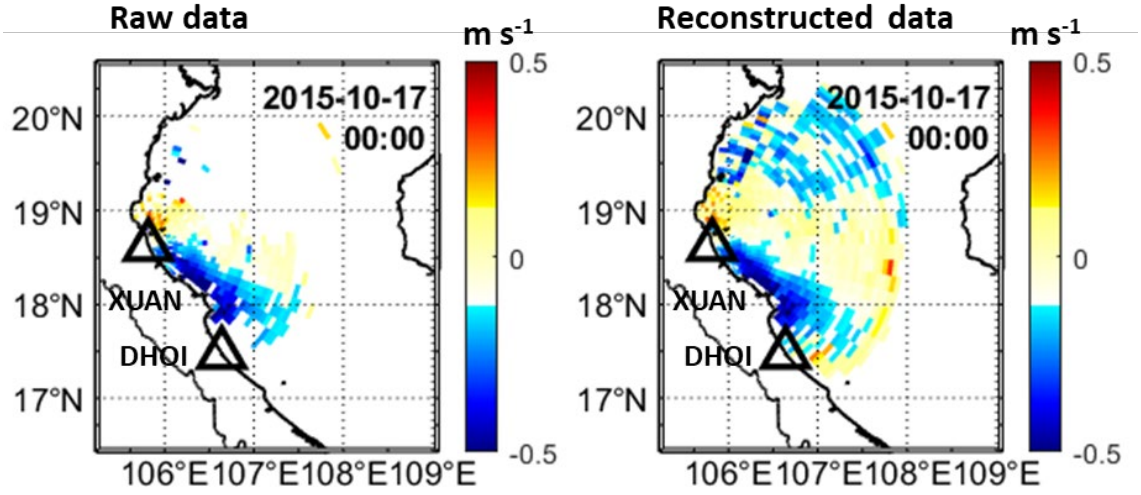

Figure 2.9: Snapshot of the raw data (left) and the reconstructed radial velocities after the application of iterative EOF-based gap-filling technique in XUAN radar site (right).

In the last step, the surface current vectors are interpolated on a regular grid using the variational method (2dVar) (Fig.2.10). Compared to the local method such as Least Square fit (LS) which uses only the data in the overlapping zone, the EOF/2dVar takes into account all the available data when interpolating the velocity into a grid point. Therefore, it appears more efficient in reconstructing the current velocity field when the coverage of one radar is low. Moreover, 2dVar is more flexible than OMA (also a non-local interpolation method) in the choice of regularization. The 2dVar method uses three basic parameters for penalizing the difference between the resulting velocity and observations and enforcing the smoothness of the interpolated field. In OMA, the choice is limited to the minimum number of cutoff length scales. Kinematic constraints (zero flux on the rigid boundary), incorporated

into 2dVar, appear particularly useful in regions with a complex shoreline and islands located inside of the interpolation area.

For verification of the accuracy of the surface current velocity vector reconstruction from radar measurements, we investigated the differences between the velocity measurements by AWAC and the HFR total current velocities reprocessed by EOF/2dVar based on optimal statistical indicators. Details of the comparison are given in Appendix C. Quantitatively, the mean error between the AWAC and HFR measurements is about 0.03 m s^{-1} for the zonal velocity component and less than 0.06 m s^{-1} for the meridional velocity component. The root-mean-squared error is found to be less than 0.14 m s^{-1} for both components (Fig.2.11). The comparison of the total current vector using a complex correlation indicator (Kundu et al., 1976) revealed a good agreement as well. The absolute correlation value (α) was larger than 0.7 and the phase difference (θ) for each of the three cases was less than 3° (Appendix C). The radar-derived surface currents demonstrate a rotation to the right of the AWAC-derived current vector.

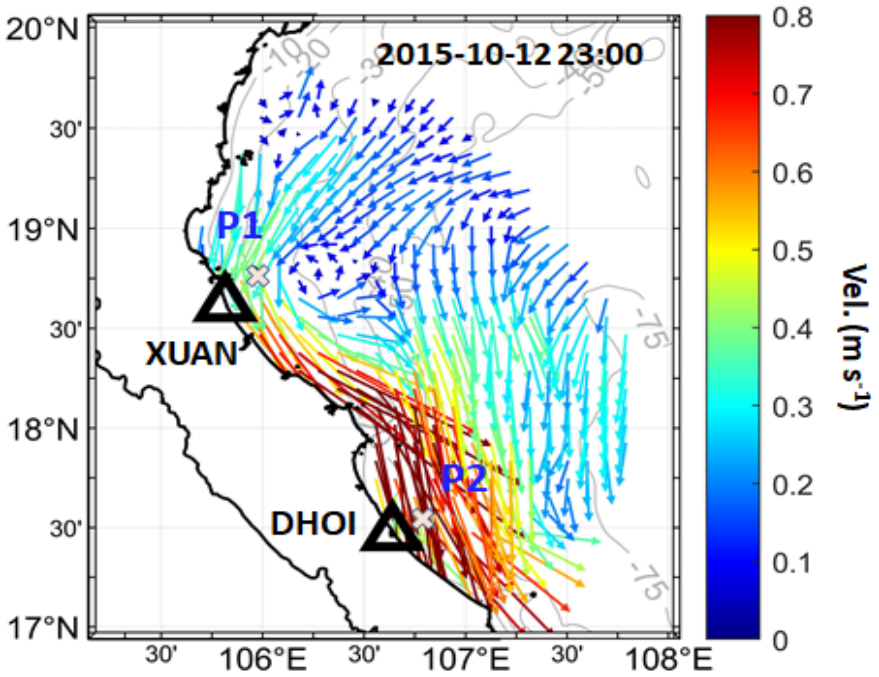

Figure 2.10: Snapshot of surface current velocity processed by EOF/2dVar method. The current vectors are plotted every 10 km for visualization. Location of two AWAC (P1 and P2) is shown by white crosses. AWAC measurements were used for validation of radar derived velocities.

In addition, the quality of radar velocity measurements was assessed following the Lagrangian prediction (LP) methodology. Basically, it consists of a comparison between the real drifter trajectories and the synthetic drifter trajectories when the drifters are advected in the radar-derived velocity field. Here we used the trajectories of seven drifters released close to the XUAN radar site

from April 2017 to January 2018 for the comparison (Appendix C). An example of the comparison is shown in Fig. 2.12a. Generally, the synthetic drifter trajectories processed by two methods (OMA and 2dVar) follow closely their real counterparts though some discrepancies can be noticed (Fig. 2.12a). Quantitatively, the assessment of the differences between the real and the synthetic drifter location indicates an increase in the mean separation with the integration time due to the cumulative errors growing for longer advection. In the shorter integration time, the RMSE between the real drifter and the synthetic drifter separation distance grows almost linearly in time, as can be expected, with the mean rate of about 13 km during the first 24h (Fig. 2.12a). This error is slightly smaller than 17 km / 24 h in case of NCOM numerical model in the VNES/SCS region (Huntley et al., 2011). However, it is larger than a typical value (5 – 10 km/24 h) found in other coastal regions of the Atlantic Ocean and Mediterranean Sea (e.g., Kaplan et al. (2005); Ullman et al. (2006); Molcard et al. 2009). After 2 days of advection, the separation distance between the synthetic and real drifter reached the value of 24 km, then grew up to 35 km after 4 days of simulation in the 2dVar case. Compared to OMA, the 2dVar method reduced the difference by about 17% for both mean separation and standard deviation (Fig. 2.12b).

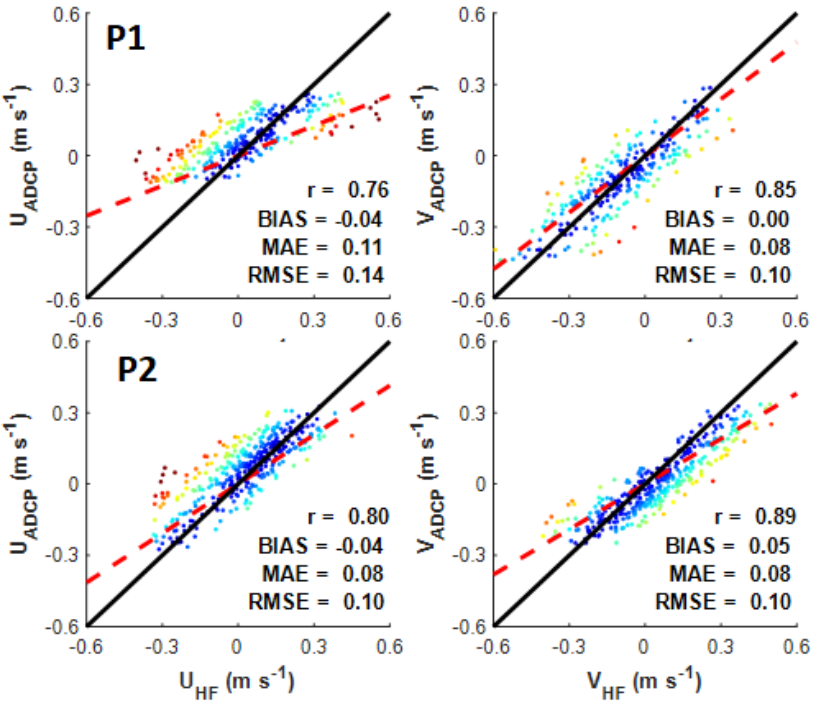

Figure 2.11: Comparison of surface current velocities measured by AWAC and HFR, after reprocessing by 2dVar method, in P1 (upper panel) and P2 (lower panel).

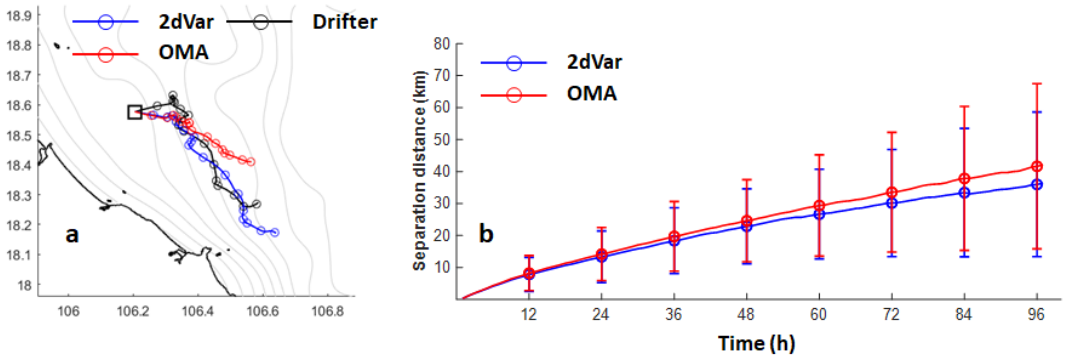

Figure 2.12: (a) Real drifter trajectory (black line) and synthetic drifter trajectories in the radar velocity field after application of 2dVar (blue) and OMA interpolation method (red). The release point is shown by black square. The drifter positions every 6 h are shown by circles. The bathymetry is plotted every 5 m.
(b) Mean separation distance between the real and synthetic drifter advected in radar velocity field. The velocities are obtained by 2dVar (blue) and OMA interpolation method.

2.2. SYMPHONIE numerical model

Numerical modeling is an important and very useful tool allowing to adequately visualize the ocean state in space-time dimensions and characterize the involving physical processes. Nowadays, with the development of high-performance computing which supports the improvement of precision and reduces computational time, the number of studies using ocean numerical modeling has been particularly increased.

In the present study, we use the numerical simulations of the circulation in the GoT made with the SYMPHONIE model. SYMPHONIE is a hydrostatic numerical model which solves the primitive equations on a curvilinear bipolar Arakawa C-grid with regular sigma vertical levels (Marsaleix et al., 2006, 2008). The model was developed by the SIROCCO group (LEGOS, CNRS, IRD, Université de Toulouse, France) and has been used to simulate the hydrodynamic conditions in the Mediterranean Sea region (e.g., Reffray et al., 2004; Herrmann et al., 2008; Ulses et al., 2008) and the VNES/SCS region (Rétif et al., 2014; Piton et al., 2020, 2021; Nguyen-Duy et al., 2021).

For the application in the GoT, the model grid covers the whole gulf with the horizontal resolution varying from ~300 m, near the Red River delta, to ~4500 m close to the open boundaries. The water column is discretized onto 20 sigma levels. The bathymetry is reconstructed from GEBCO 2014 database combined with other sources and field surveys in order to characterize properly the complex topography, with many islands and islets located within the region, especially in the coastal area adjacent to the Red River delta (Piton et al., 2020). Intertidal areas are simulated with a wetting and drying scheme. The k-ε turbulence closure scheme is implemented as in Michaud et al. (2012).

Tidal motions at the open boundaries are prescribed from the sea surface elevation and barotropic currents of 9 tidal constituents from the FES2014 atlas (Lyard et al., 2021). The tidal astronomical potential is also considered at every grid point of the model. In addition, the 1/12° spatial resolution, daily averaged sea surface height (SSH), velocity components, temperature, and salinity, provided by the Copernicus Marine Systems (CMEMS) global model is also used at the boundaries.

At the sea surface, the boundary conditions extracted from the Operational ECMWF product, include the 3-hourly data for wind, precipitation, solar energy, atmospheric temperature, and pressure. The fluxes of momentum, heat, and freshwater are computed internally in the model using the bulk formulation of Large and Yeager (2004).

In the present study, the river discharge from 16 rivers is introduced in the model (Fig. 2.13) and configured as realistically as possible according to the method described in Nguyen-Duy et al. (2021). Daily freshwater runoff is used from the main seven distributaries of the Red River. For other rivers, climatological data are used. An additional configuration without the river discharge (GoT-noriv configuration, see Nguyen-Duy et al., 2021 for details) is used to assess the effect of river discharge on turbulent dispersion properties.

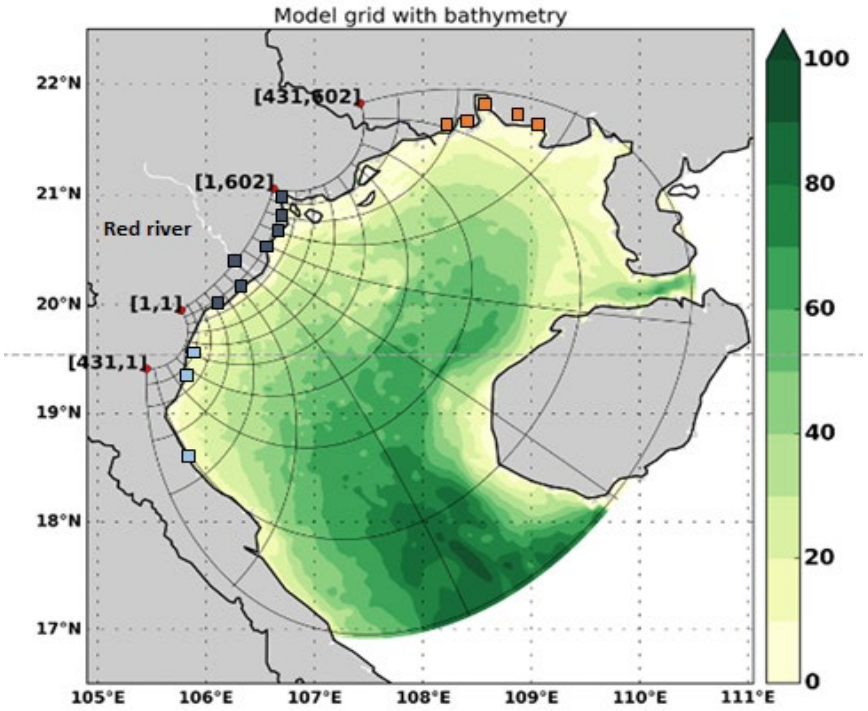

Figure 2.13: The GoT domain in the SYMPHONIE model with interpolated bathymetry (unit: m). The model resolution is increased by the factor of 50. Locations of river estuaries used for freshwater input in the model are indicated by the squared boxes. The red River main distributaries are shown in dark grey.

2.3. Lagrangian applications

2.3.1. Lagrangian tracking model

Lagrangian tracking is a useful tool for studying ocean circulation and dispersion processes. Accurate tracking is important in many applications, including search and rescue missions, accident localization via backward tracking of debris, or optimization of the protective missions in response to environmental disasters. Trajectories of virtual particle advected explicitly in the HFR-derived or from the numerical model velocity field are successfully used in numerous studies, e.g., search and rescue operations (Ullman et al., 2006); predicting and mitigating the spread of oil spill or other pollutants (Lekien et al., 2005; Shadden et al., 2009); understanding the impact of transport and mixing properties on relevant biogeochemical properties such as the primary production by phytoplankton (Cianelli et al., 2017; Hernández-Carrasco et al., 2018b); and tracking the drifted materials, fish larvae (Lacroix et al., 2013; Sciascia et al., 2018); etc. Fig. 2.14 shows an example of drifter trajectories released in Martha's Vineyard (Rypina et al., 2016). An ensemble of drifter trajectories can be useful for the validation of radar data and model assessment.

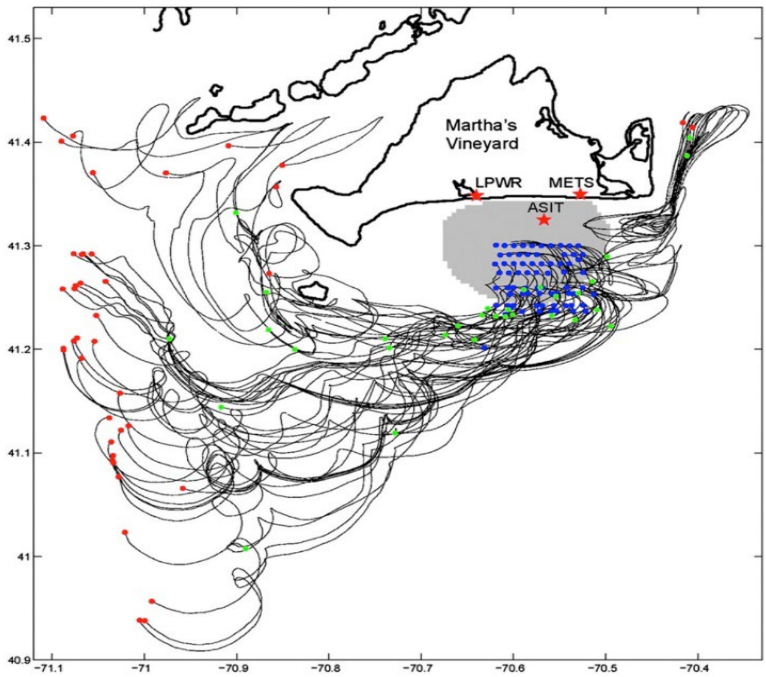

Figure 2.14: Spaghetti plot of drifter trajectories from the drifter study in Martha's Vineyard (Massachusetts, USA). Gray shaded area shows the HF radar footprint, red stars show positions of the three HF radar sites, and thick black curve indicates land (Rypina et al., 2016).

In this study, we used the OceanParcels framework (https://oceanparcels.org/) for Lagrangian tracking of virtual particles in the velocity field provided by SYMPHONIE model simulation. The framework is written in Python which aimed to explore a novel approach for the Lagrangian tracking of a very

large number of particles. The code is built to form a flexible framework and is easy to implement and coupled into the existing forecast model (van Sebille et al., 2018). The input velocity is bilinearly interpolated onto the particle position. The integration in time utilizes the 4th order Runge Kutta scheme. The transport module of the framework thus determines a new position $\boldsymbol{X}$ at time $t+\Delta t$ by integrating the velocity $\boldsymbol{v}$ following the equation:

$$X(t+\Delta t) = X(t) + \int_t^{t+\Delta t} v(x(t),t)dt \qquad \text{(Eq. 2.7)}$$

2.3.2. Lagrangian diagnostics for assessing the turbulent dispersion

Relative dispersion

Turbulence in the ocean can be thought of as the processes involving the transfer of energy from large-scale motion to smaller scales through a series of successively smaller eddies (Kolmogorov, 1941). Characterization of energy distribution across different scales can be inspected by the spectrum of energy as the function of horizontal wave number k. In a steady state, the turbulence kinetic energy, E(k), has a general equilibrium form for a part of the wave number range where the energy is transferred from the largest to an adjacent smaller scale (Fig. 2.15a).

In practice, the measurement of turbulent velocity is rather difficult in spatial coordinates. Alternatively, the nature of oceanic turbulent flows and their related transport can be investigated by means of the Lagrangian statistics involving the average of particle positions and/or their velocities (LaCasce, 2008). Of interest, we consider how a "cloud" of particles moves and spreads in a turbulent flow field. One of the useful Lagrangian metrics is the variance of particle separation distance. In practice, the dispersion of a pair of particles is commonly used. The statistics using particle pairs can be used to assess the mean drift of the cloud and the spread rate around the center of mass. Theoretically, the separation rate of particle pairs is controlled by the kinetic energy spectrum of the underlying flow field and depends on the separation distance. Assessment of relative dispersion is often used to check the consistency of quasi-geostrophic turbulent theory, chaotic advection, and mean shear (Koszalka et al., 2009; LaCasce, 2008).

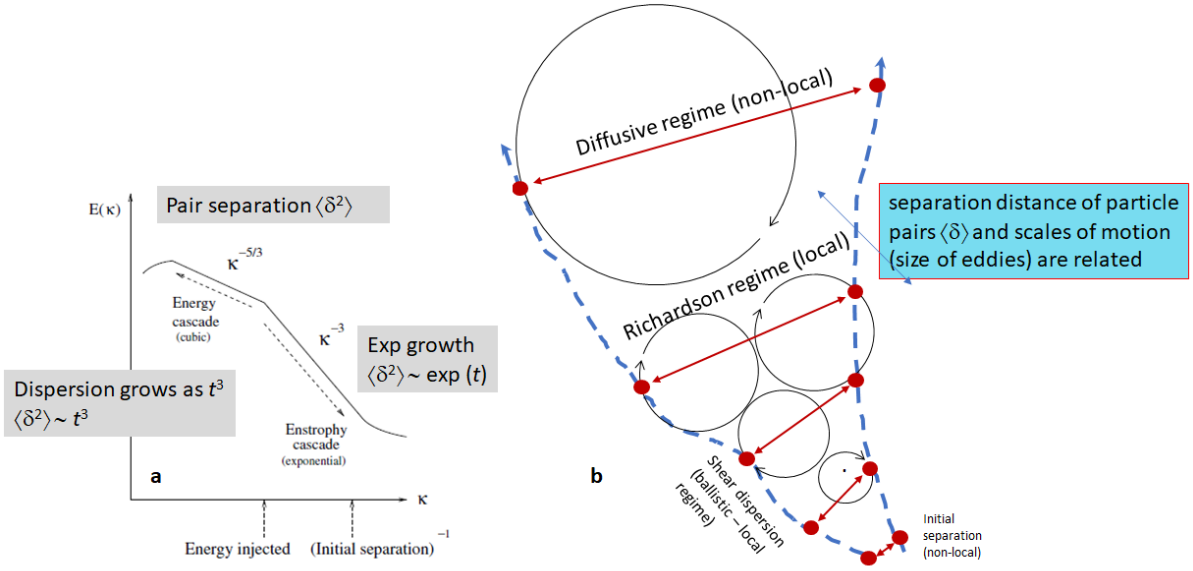

Figure 2.15: Double cascade diagram in the turbulence kinetic energy E(k) as the function of (horizontal) wavenumber k (a) (LaCasce, 2012). Diagram of the behavior of a particle pair in a turbulent flow (b)

One of the Lagrangian quantities used for the investigation of turbulent flows is the relative dispersion δ^2, which is estimated as:

$$\delta^2(t) = \frac{1}{N(N-1)} \sum_{ij}^{N} \|\overrightarrow{x_i}(t) - \overrightarrow{x_j}(t)\|^2 \qquad \text{(Eq. 2.8)}$$

where N is the told number of particles and $\overrightarrow{x_i}$ and $\overrightarrow{x_j}$ are the spatial coordinates of particles. The rate of relative dispersion depends on the shape of the given kinetic energy spectrum, E(k), which assumed to follow the power law, $E(k) \simeq k^{-\beta}$. Here, we first define the terms "local" and "non-local" dispersion regimes. The "local" dispersion occurs if the dispersion at a particular length scale depends only on flow statistics at that length scale while in the "non-local" regime, the separation is caused by the largest dominant scale of the fluid motions (Foussard et al., 2017). At the early stage when the particle pair separation is small ($\beta > 3$, the regime is non-local), the relative dispersion grows exponentially. Otherwise, if $1 < \beta < 3$, relative dispersion is local and scales as a power law $\delta^2 \simeq t^{\frac{4}{(3-\beta)}}$ (Foussard et al., 2017). Richardson superdiffusive regime corresponds to $\delta^2 \sim t^3$ where the pair separation is controlled by eddies with a size similar to the separation distance of particles (Fig. 2.15b). When the particle separation reaches scales much larger than the largest characteristic flow scale, the relative dispersion in this case is expected to scale as $\delta^2 \simeq t$, corresponding to a diffusive behavior.

Another quantity used in the analysis is the relative diffusivity, κ. It represents the growth rate of the average squared separation. This quantity is defined as the time derivative of relative dispersion,

$$\kappa = \frac{1}{2}\frac{d\langle\delta^2(t)\rangle}{dt} \quad , \qquad \text{(Eq. 2.9)}$$

In the turbulent flow, $\kappa(\delta)$ scales as δ^2 for the non-local dispersion regime and as $\delta^{4/3}$ (when $\beta = 5/3$) for the local dispersion.

The third quantity, the Finite Size Lyapunov Exponent (FSLE), is estimated by measuring the time τ, averaged over all particle pairs, needed to separate particles in a pair from a distance δ_k to a distance $\delta_{k+1} = r\,\delta_k$, with $r > 1$:

$$\lambda = \frac{ln(r)}{\langle\tau\rangle} \qquad \text{(Eq. 2.10)}$$

If λ is constant over a range of separation distance classes, the e-folding timescale is constant which is equivalent to an exponential growth of pair separations. Also, FSLE is useful to study the growth of separations which is not exponential, we can use scaling arguments to relate the FSLE power law function. In the case of local dispersion ($\beta < 3$), FSLE scales as $\lambda^{-2/3}$ for Richardson regime, λ^{-1} for ballistic regime, and λ^{-2} for diffusive regime.

Lagrangian Coherent Structures (LCSs) from Finite Size Lyapunov Exponents

In addition, the study of mechanism of turbulent transport involves the characterization of the coherent structures in the flow field. The development of turbulent coherent structures in the flow (such as jets and eddies) is driven by the intrinsic spatial and temporal variability and also by the external forcings (such as wind or freshwater input) interacting with it. These dynamical structures, even though exhibiting a slow decay with respect to the flow field variability dictate much of the transport characteristics (Haza et al., 2008). Estimation of the FSLE for characterization of the flow field allows to identify these transport structures on the basis of the relative dispersion of particles (Berta et al., 2014). It also provides the information about the stirring and mixing in the flow (d'Ovidio et al., 2004; Hernandez-Carrasco et al., 2012). This method allows identifying the LCSs that organize the transport in a flow field, localizing regions in the flow that evolve with time scales different from the temporal variability of the surrounding field. Usually, these characteristic LCSs appear to be surrounded by the lines of large FSLE values, which are also called the ridge lines.

FSLE is computed forward in time to identify the lines of particle divergence while the one computed backward in time demonstrates the compression. The intersection of the lines computed forward and backward in time identifies a so-called hyperbolic point where particles undergo a strong separation (Fig. 2.16). Particles moving toward the hyperbolic point spread along the repelling line (stable manifolds) and compress along the attractive line (unstable manifolds) while moving away from the point. The particle trajectories cannot cross these lines as they form barriers, or so-called in this

context, Lagrangian fronts, which greatly impact the dispersion of oceanic tracers (Lehahn et al., 2007). In the region surrounding the hyperbolic point, a strong density gradient is maintained in the cross direction of the filaments and possibly promotes the frontogenesis and small-scale eddies (Siegelman, L. et al., 2020).

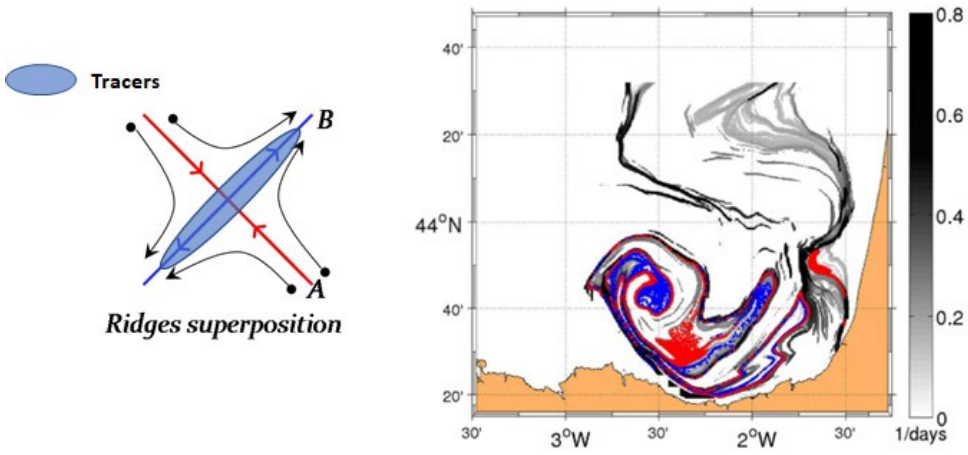

Figure 2.16: (Left) Schematic of how the particles are diverged from the forward FSLE (red lines) and compressed along the backward FSLE (blue lines). (Right) Map of backward FSLEs to illustrate the evolution of the mesoscale eddy in the Bay of Biscay. Particles in red demonstrate the shelf water while the one in blues represent the evolution of water in the eddy core. The largest FSLE values lines mark a physical transport barrier for drifting particles (Rubio et al., 2018)

It is possible to perform mapping of FSLEs by considering the space-time evolution of relative dispersion of particles released in the velocity field. By analogy with Eq. 2.10, we define the exponential growth rate of particle pairs separation distance, $\lambda(x)$:

$$\lambda(x) = \frac{1}{\tau(x)} ln\left(\frac{\delta_f}{\delta_i}\right) \qquad \text{(Eq. 2.11)}$$

Where δ_f and δ_i represent the final and initial separation of the particle pairs respectively. Particles leaving the area before reaching the final distance are removed from the analysis. The optimum choice for the spatial FSLE amplification factor $r = \delta_f/\delta_i$ was discussed in previous studies (Haza et al., 2010; Berta et al., 2014). Generally, $r > 2$ is typically used for computation of the spatially local FSLE. If r is too small, the LCSs cannot be identified while if r is too large, then almost no particles are able to reach the final distance. Thus, in oceanographic applications, r is often chosen between 7 and 10 (Berta et al., 2014). In our study, we compute the spatial FSLE from the initial separation $\delta_i \simeq$ 1.86 km and δ_f = 13 km which adequately allows the visualization of relevant coherent structures and transport patterns associated with small-scale processes.

Chapter III. Surface circulation in the Gulf of Tonkin as revealed by HF radar observations

3.1. Introduction

Motivation for the article

The complex hydrodynamics of the GoT results from a combination of powerful forcings: tides, monsoon wind, large river discharge (Shi et al., 2002; Chen et al., 2012a, b), and remote forcing which can be episodic and potentially very strong (Piton et al., 2021). In the previous studies, the circulation in the GoT has not been fully characterized since most of the studies were based on model simulations, which were often idealized, i.e., used the homogeneous density, climatological forcing, or neglected the freshwater discharge. At the same time, the available observations covered only a few limited-size geographic areas or short periods of time. For this reason, the dominant circulation patterns and modes of variability at different time scales in response to external forcing were only poorly understood. The lack of systematic observations is assumed to be the main reason that prevents further analysis of the water dynamics in this basin, especially leading to the debate on the seasonal variability of the flow field (e.g., cyclonic/anti-cyclonic circulation in summer) and the role of physical processes controlling this variability.

In this context, a network of HF radars, deployed in the GoT and operating since 2012, provides a real opportunity for performing a comprehensive analysis of coastal water dynamics and its space-time variability. Additionally, the surface current velocity measurements by coastal radars can be potentially used for assessing the hydrodynamic model performance and characterizing processes controlling the transport and dispersion of materials in the region.

We took the advantage of continuous data acquisition by HF radars in the GoT in order to come forward in oceanographic research and improve the knowledge of the coastal water dynamics in this wide, semi-enclosed, shallow water basin, surrounded by Vietnamese and Chinese territories with high-density population and economic infrastructure. To reach this objective, we used the radar data of

a 2.5-year-long period (April 2014 – October 2016), characterized by the largest coverage and a rather stable operation condition. Long-time series of surface current velocities allowed assessment of the spatio-temporal variability of the surface circulation in the study area at different scales, spanning from the tidal and sub-tidal frequencies to the annual scale.

Methods of analysis

Despite the undeniable advantages of HF radars to provide nearly real-time observations of a surface circulation at large spatial scales, the radar measurements are always affected by uncertainty related to instrumental errors, the coverage decrease with distance, hardware failure, etc. To acquire the most accurate current velocity maps for a large period of time, we implemented the variational approach (EOF/2dVar) for radar data processing. This non-local, kinematically constrained interpolation method, proposed by Yaremchuk & Sentchev (2011), is capable of producing a continuous, gap-free dataset and particularly effective in case of radar failure during short periods (1 ~ 2 days of one radar malfunction). The performance of the EOF/2dVar method was evaluated by comparison with the *in-situ* measurements of surface current velocities and Lagrangian drifter trajectories available in the study area. A good agreement is found between different sources of data and the results of the comparison are quite consistent with those documented in previous studies performed in other coastal ocean regions (e.g., Liu et al., 2014; Molcard et al., 2009; Yaremchuk et al., 2016). 2dVar interpolation technique was also compared to OMA, routinely used by the "CODAR community", and demonstrated better performance. This increased our confidence in using HF radar data (and data processing method) for investigating *surface circulation in the GoT.* Different methods of analysis, including rotary spectral analysis (RSA), principal component analysis (PCA), and tidal harmonic analysis, were applied to the radar-derived velocity time series in order to identify the characteristic patterns and dominant processes governing the surface current variability.

Results

The results of HFR data analysis revealed the dominant role of tides and monsoon wind in controlling the variability of circulation. The tidal motions account for about 60% of the overall total velocity variability. The diurnal tidal magnitude (K1 and O1) is larger than that of the semi-diurnal, M2 and S2 tidal constituents, by the factor of 4 and 8 respectively. At the seasonal scale, surface circulation in the GoT exhibits a strong seasonal variation controlled by the Asian monsoon system. The seasonal current variability follows closely the reversal of wind forcing. The spectral analysis of the hourly velocity time series indicated the energy transfer from large-scale (low-frequency) variability, in winter, to low-scale (higher frequency) variability, in summer. For instance, the wind-induced variability of the surface currents at the diurnal frequency was found to be amplified in summer by the sea breeze. The relative contribution of river discharge to circulation variability was also assessed. The

freshwater input from the Red River discharge modified the polarization of the tidal ellipse in the near-shore region, namely the "tidal cross-shore straining" phenomenon. Also, the buoyancy-driven current peak, occurring during the autumn to early winter, combined with strong alongshore wind stress causes the intensification of the nearshore current along the Vietnamese coast.

In summary, the radar measurements allowed assessing the GoT circulation at a level of detail that was not previously documented and complemented the knowledge on the surface hydrodynamics in the GoT. The results of the study can be useful for further investigation of coastal circulation in the GoT, i.e., for the improvement of numerical models and management of the marine coastal environment.

Different aspects of the study, briefly presented above, were developed in more detail in the research article: "Multi-scale variability of circulation in the Gulf of Tonkin from remote sensing of surface currents by high-frequency radars" published in Ocean Dynamics journals.
https://doi.org/10.1007/s10236-020-01440-x.

3.2. The article

Ocean Dynamics (2021) 71:175–194
https://doi.org/10.1007/s10236-020-01440-x

Multi-scale variability of circulation in the Gulf of Tonkin from remote sensing of surface currents by high-frequency radars

Manh Cuong Tran[1,2,3] · Alexei Sentchev[1] · Kim Cuong Nguyen[3]

Received: 8 June 2020 / Accepted: 28 December 2020 / Published online: 8 January 2021
© Springer-Verlag GmbH, DE part of Springer Nature 2021

Abstract

The sea surface velocity measurements obtained during the period of 2014–2016 using two high-frequency radars (HFR), which were installed on the northern coast of Vietnam, were reprocessed by using a variational approach (EOF/2dVar) to provide an extended dataset. The high temporal resolution of measurements and large spatial coverage of the radar data enabled the assessment of the surface circulation in the data-poor region of the southern Gulf of Tonkin (GoT) and the characterization of its temporal variations in a wide range of scales: from tidal frequency to annual cycle. It was found that tidal motions account for a large percentage (approximately 60%) of surface current variability in the GoT. The temporal variability of the kinetic energy of the surface currents is tightly correlated with wind variations in the monsoon-dominated atmospheric circulation system. Stratification, induced by the discharge of the Red River, also affects the tidal currents within the coastal region (~ 40 km wide) by modifying the tidal ellipses polarizations. Close to the shore, the prominent coastal flow experiences large temporal variations in response to wind and buoyancy forcing. The seasonal variability of the zonal wind component was found to play a significant role in coastal flow speed variations through the cross-shore mass exchange. The Red River freshwater discharge controls the seaward extension of the coastal flow and causes asymmetry in the seasonal variability of flow velocity. The data obtained and analysis results could be useful for the improvement of the regional circulation models, for further studies of the physical and biological processes in the GoT, and for marine resource management.

Keywords HF radar · Gulf of Tonkin · Surface circulation · Multi-scale variability

1 Introduction

In recent years, the land-based high-frequency oceanographic radars (known as HF radar or "HFR") have been extensively used to monitor surface currents in numerous coastal areas. The HFR observing systems, which are capable of providing information on both the spatial and temporal variabilities of ocean currents within the top few meters, are largely used in oceanographic research and coastal water management. Datasets from HFR observations for the last two decades have enabled a better understanding of the physical processes in nearshore waters and significant advances in the study of the coastal ocean. For example, Bassin et al. (2005) analyzed the HFR data and demonstrated that the bottom-generated vorticity acts on the prevailing westward current on the inner shelf of the Southern California Bight and supplies nutrients to the shallow water zones via the cross-shore transport. Using the data obtained from two mooring sites and the HFR measurements, Yoshikawa et al. (2007) evaluated the wind-driven flow and estimated the Ekman transport through the Tsushima Strait. On the basis of the HFR observations, extreme complexity and variability of the surface circulation in two tide-dominated regions (The English Channel and Iroise Sea) have been revealed by Sentchev et al. (2009, 2013), Thiébaut and Sentchev (2017). In the Iroise Sea, which is characterized by powerful tidal motions with velocities exceeding 3 m s^{-1}, high waves, and wind, the HFR provides a unique possibility for current monitoring (Sentchev et al. 2013). Recently, HFR measurements were obtained from the Alderney Race (Channel Islands region), where the tidal

Responsible Editor: Pierre De Mey-Frémaux

✉ Kim Cuong Nguyen
cuongnk@hus.edu.vn

[1] Laboratory of Oceanology and Geosciences, CNRS UMR 8187, Univ. Littoral Côte d'Opale, Univ. Lille, IRD, 62930 Wimereux, France

[2] Center for Oceanography (CFO), Vietnam Administration of Seas and Islands (VASI), 8 Phao Dai Lang, Dong Da, Hanoi, Vietnam

[3] VNU University of Science, Vietnam National University, 334 Nguyen Trai, Thanh Xuan, Hanoi, Vietnam

current velocity is among the largest in the world (in excess of 5 m s^{-1}) (Lopez et al. 2020). HFR measurements have been used to assess the local hydrodynamics, tidal stream resource variability, and wave-current interaction prior to the deployment of tidal energy converters in this region (Furgerot et al. 2020).

With the rapid development of sea-based activities in Asian countries (including marine transportation, fishery, and harbor constructions), the demand for near real-time observation has increased in recent decades, particularly along the western Pacific Ocean periphery. This led to the development of HFR-based observation networks in numerous Asian countries, such as Taiwan, South Korea, Japan, and the Philippines (Fujii et al. 2013). The Gulf of Tonkin (hereafter referred to as the GoT), which is a shallow semi-enclosed marginal sea located in the northwestern Vietnam East Sea (internationally known as the South China Sea or SCS), is one of the regions where monitoring of such currents by the HFR has been conducted since 2012. This highly populated, tourist-attractive region is exposed to a wide range of natural and anthropogenic risks. For instance, the northern sector of Vietnam and the GoT are often affected by tropical storms every year (IMHEN and UNDP 2015). In recent decades, several powerful typhoons, i.e., Wutip (September 25 to October 1, 2013) and Doksuri (September 10–16, 2017), swept through the region and caused significant damages to the coastal areas. Furthermore, the area is exposed to risks related to climate change. In this region, the sea level is expected to increase by about 0.6 m at the end of this century, which results in the inundation of about 5.9% of the coastal areas in the Red River delta (IMHEN and UNDP 2015). The increase in rain and storm intensities can also result in more frequent flooding, higher storm surges, land erosion, etc. Besides, an extreme hazardous event in the GoT caused by human activities occurred during mid-2016. Toxin waste, which was illegally discharged from the Formosa steel factory (Vung Ang Economic zone near the XUAN radar site) to the seawater, caused severe degradation of the marine environment and heavily impacted the fishing and tourism industry in four central provinces of Vietnam. Due to the potential natural and anthropogenic risks, a robust environmental monitoring network, and, to a great extent, better knowledge of the hydrodynamic processes are important to promote sustainable development.

Despite its privileged geographic location and economic importance, the GoT attracted a few oceanography studies. The general features of the GoT circulation have often been deduced from larger scale studies of SCS dynamics (Wyrtki 1961; Gan et al. 2006; Chern et al. 2010). In the previous studies focusing on the dynamics of the GoT (Ye and Robinson 1983); Manh and Yanagi 2000; Ding et al. 2013; Gao et al. 2013, 2015), tides and wind were found to be the dominant factors controlling the regional circulation. The tidal dynamics of the GoT have been studied since the 1960s and have been fairly well documented by Wyrtki (1961), who identified the role of four main tidal constituents (K1, O1, M2, and S2) in the tidal regime of the SCS. During the 1980s, Ye and Robinson (1983) explored the contribution of K1 and M2 tidal constituents to the water dynamics in the GoT using their two-dimensional nonlinear hydrodynamic model. More recently, the major characteristics and variability of the tidal currents in this region were assessed by Ding et al. (2013) using the Global-FVCOM model. Nguyen et al. (2014) explored the resonance of the diurnal tides in the GoT using the high-resolution numerical model (ROMS at 1/25°). Piton et al. (2020) used the flexible mesh model (T-UGOm) to demonstrate the influence of the model bathymetry and the bottom shear stress parameterization on the simulation accuracy of the tidal dynamics in the GoT. These studies have provided an overview of the tidal dominant processes. In addition, the effects of seasonal wind on the current pattern have been documented in the modeling studies of Manh and Yanagi (2000), Ding et al. (2013), and Gao et al. (2015) and confirmed that the wind plays a significant role in the current variability in the GoT. These studies provided insight into the understanding of the dominant physical processes and mechanisms that govern the large-scale circulation.

However, the model-based studies mentioned above were insufficient to fully characterize the circulation in the GoT and investigate the mechanisms that govern its variability. First, the studies were often focused on a particular physical process or a single time period. Thus, the inputs were often idealized, i.e., homogeneous density, climatological forcing, and the neglect of riverine freshwater discharge with an inaccurate coastal bathymetric dataset. In the most recent modeling study, Piton et al. (2020) addressed a key challenge in the simulation of the tidal dynamics of the GoT as the complex topography and particularly in the shallow water zone. The lack of available observations in the area prevents a detailed characterization of the circulation and model validation. The first systematic survey of the gulf was conducted by China and Vietnam in the early 1960s and was followed years later by several sparse surveys, which were often limited to the northern and eastern sides of the GoT (Gao et al. 2017). The circulation pattern in the GoT, especially in summer (gulf-scale cyclonic or anti-cyclonic), still remains a topic of debate. Numerous scientists, such as Liu and Yu (1980) and Manh and Yanagi (2000), reported that the wind-induced current is the most important component of the circulation and that the pattern of the surface current in summer is anti-cyclonic. However, other researchers believe that the density-driven current significantly contributes to and strongly affects the circulation of the GoT in summer (Gao et al. 2017). Based on the data from a 1-year-long mooring dataset in the northern gulf, Ding et al. (2013) found that the sub-tidal current is highly correlated with the surface wind in winter but not in

summer. This suggests that the anti-cyclonic pattern of wind-driven circulation in the GoT is not realistic. Gao et al. (2015) analyzed the current structures in the GoT using the POM model and reported that in summer, the circulation in the northern part is cyclonic and is mostly being driven by the wind stress curl, whereas in the southern part, the circulation is anti-cyclonic and is largely affected by the SCS water intrusion. In the modeling study, Rogowski et al. (2019) argued that the current pattern in the GoT is gulf-scaled cyclonic, even without the river input. The controversy in the characterization of the circulation of the GoT often comes from the lack of recent field measurements, mostly in the western section of the gulf. Remote sensing of the currents at a large scale of the gulf by HFR seems particularly suitable for the investigation of the water dynamics of the GoT.

Rogowski et al. (2019), who combined the HFR measurements, satellite altimetry, ocean color data, and numerical modeling, provided insight into the seasonal variability of the circulation in the GoT. In our study, we used the HFR observations to investigate the multi-scale variability of water dynamics in the southern GoT: from tidal to annual scales. The remainder of this paper is organized as follows: In Section 2, the location of the study area and physical forcing that controls the water dynamics are presented, and the data available, the configuration of the HFR system in Vietnam, and the analysis methods are described. We also evaluated the performance of the HFR data by comparing it with the in situ current measurements using an acoustic wave and current profiler (AWAC). The comparison is briefly described in the subsection of Section 2. In Section 3, the results are presented. Finally, the discussion and conclusions are provided in Sections 4 and 5, respectively.

2 Data and methods

2.1 Study area and environmental forcing

The GoT is a shallow, semi-enclosed, crescent-shaped marginal sea that lies between 17 and 22° N in the northern part of the SCS (Fig. 1). The gulf is 270 km wide and is bordered by the Vietnamese coast in the west, the Chinese coast in the north including the Leizhou Peninsula, and Hainan Island (China) in the east. The gulf is connected to the South China Sea mainly through the southern entrance, which is 230 km wide and 100-m deep. Another entrance is the shallow and narrow Hainan Strait (18 km wide and 50-m deep) in the east. The bottom topography of the gulf is rather complex. There are about 2000 small islets inside the gulf, which are mostly concentrated in the northwestern area. The northern part of the gulf is very shallow and characterized by a slight decrease in depth from 10 to 30 m. The southern part of the gulf is deeper (depth about 40 to 70 m). Large bathymetry gradients are observed along the Hainan Strait and in the southern part, especially along the coastline.

Tidal motions are generated in the GoT by progressive surface gravity waves coming from the open ocean. The tidal wave enters the gulf mainly through the southern entrance and progresses along the western coast of Hainan Island (Nguyen et al. 2014). Conversely, the Hainan Strait is a region with the strongest tidal energy dissipation, thus leaving little energy of tidal flux entering or escaping the gulf (Nguyen et al. 2014). The tidal regime in the northern gulf is predominantly diurnal. In the southern part of the gulf, the tidal regime is mixed diurnal. The amplitude of the dominant constituents K1 and O1 reaches 80 and 90 cm, respectively (Piton et al. 2020). At the southern entrance of the gulf, the diurnal components already dominate the semi-diurnal components. Here the diurnal tidal energy fluxes (K1 and O1) are three times larger than that of M2 tide and 20 times larger than that of S2 tide (Nguyen et al. 2014). Inside the gulf, the resonance of the diurnal tidal waves due to the basin topography and the degeneration of semi-diurnal components creates a unique diurnal tidal regime.

Located within the East Asian monsoon system, the circulation in the GoT is largely controlled by the Asian monsoon system, which is characterized by two distinct seasons: northeast (NE) monsoon and southwest (SW) monsoon (Wyrtki, 1961; Nguyen et al. 2014). The surface circulation in the GoT experiences a large seasonal variability and is strongly influenced by the two dominant climatic conditions. The NE monsoon (occurs in late fall to the end of winter, or dry season) lasts from October to February and is characterized by prevailing strong north and northeastern wind. The SW monsoon (in summer or wet season) lasts from May to August and is influenced by persistent southwestern wind. Tropical typhoon often occurs during this time. Between these climatic conditions, two transition periods are observed: early March to April, when the northeast wind gradually slows down and reverses to the southeastern wind, and September to the beginning of October, with a relaxation of southwesterly wind (Nguyen et al. 2014). The monthly variability of the wind is demonstrated in Fig. 3.

Buoyancy forcing is dominant in the western region of the gulf, which is related to the seasonal advection of the Red River discharge in the northern part of Vietnam (Rogowski et al. 2019). The Red River (Fig. 1), which originates from China, is fed by two major rivers in the north of Vietnam (Da and Lo) before flowing seaward. The average discharge rate of the Red River is 3500 $m^3\ s^{-1}$ through nine distributaries along the 150-km coastline (Vinh et al. 2014). The peak discharge rate can exceed $1.0 \times 10^4\ m^3\ s^{-1}$ during some wet years (Chen et al. 2012; Ding et al. 2013). The discharged freshwater is confined to the Vietnamese coast and advected southward along the coast. In summer, under persistent southwesterly winds, the freshwater can move northward in a

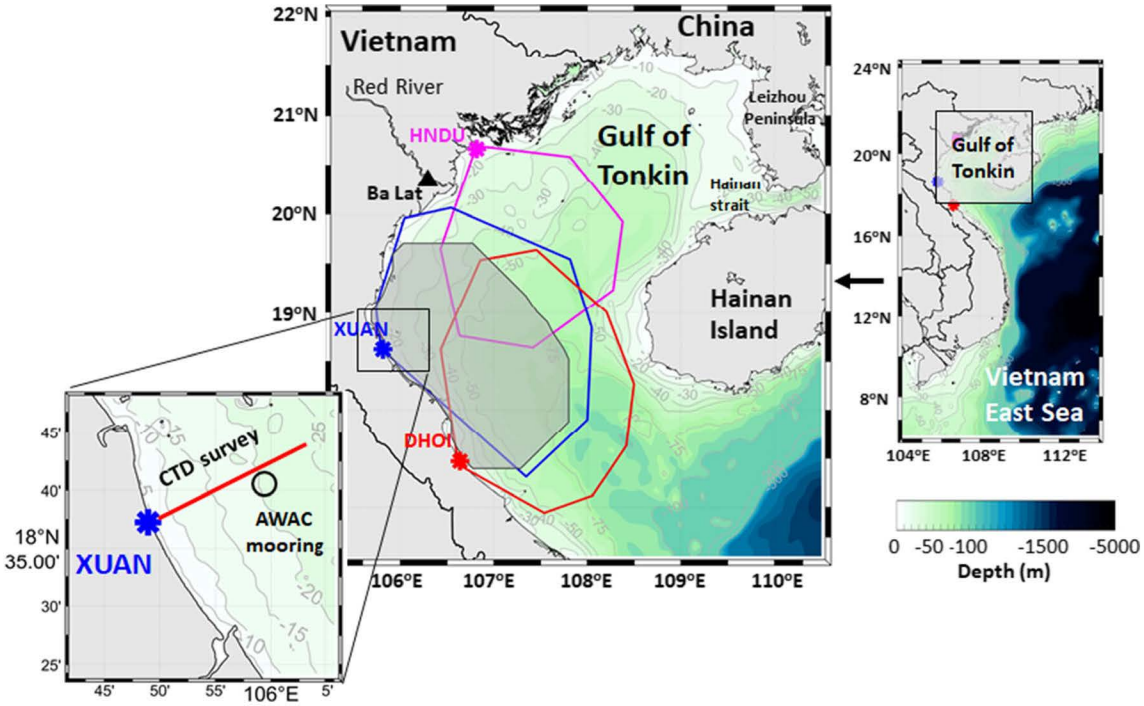

Fig. 1 Location of the Gulf of Tonkin and radar sites (color stars). Individual radar coverage is given in the color line. The study area where analysis of the radar-derived current velocities is performed is shown by gray shading. Also shown is the location of the AWAC mooring site (circle), monthly CTD transects (red line), and hydrological station at Ba Lat (triangle). The bathymetry is shown by color shading with bathymetry contours given by gray lines. Geographic names used in the text are also shown

counterclockwise motion and is described as "trapped" (Ding et al. 2013; Rogowski et al. 2019). Given the large contribution of freshwater discharge to the local dynamics, this GoT region is considered a complex region of freshwater influence (ROFI).

2.2 Data

2.2.1 HFR data

HFR system is land-based systems providing near synoptic observations of surface current for cost-effective operation complementary to traditional ship-based and moor-based stations, which are logistically challenging and expensive (Fujii et al. 2013). HFRs measure the ocean surface currents using the "Bragg scattering" principle. The resonant backscattering (Bragg scattering) results from the coherent reflection of the transmitted wave by the ocean waves which wavelength is half of that of the transmitted one. Although referred to as "radar," HFR systems operate at much longer wavelengths (normally ranging from 10 to 100 m). The electromagnetic wave transmitted from the radar is scattered off by ocean waves and is returned to its source. Through the Doppler spectrum analysis, radial velocities can be inferred in the direction toward or away from the radar. At least two radars are normally used to reconstruct a total vector from each site's radial components. The readers may refer to Paduan and Washburn (2013) for a thorough discussion on oceanographic HFR theory, development, and applications.

The HFR network in Vietnam is operated by the Center for Oceanography, Vietnam Administration of Sea and Islands (CFO, VASI). Individual sites are located at the Hon Dau Island (HNDU, 106.81° E, 20.67° N), Nghi Xuan (XUAN, 105.82° E, 18.62° N), and Dong Hoi (DHOI, 106.64° E, 17.47° N) (Fig. 1). The long-range HFRs are configured to operate at a frequency of 4.625 MHz (which was changed to 5.25 MHz in 2018). The radial velocity components are measured by the radar at an effective depth of 2.4 m. This effective depth is determined as $\lambda_R/8\pi$, where λ_R denotes the radio wavelength (Stewart and Joy 1974). The following configuration has been used at each radar site to retrieve the radial velocities of the surface currents: 5.8 km along the beam and azimuthal spacing 5°. The temporal resolution was set to 1 h.

In this study, hourly HFR radial velocities were obtained at XUAN and DHOI radar sites for more than 2 years (from April 2014 to October 2016) and mapped using EOF/variational interpolation methods (described in Section 2.3). The data from the HNDU site were neglected, because the site suffered from numerous hardware failures during this period. Figure 2 presents the temporal coverage of the XUAN and DHOI sites. Conversely, the spatial coverage was highly sensitive to the conditions of the sea state. The coverage was found to be larger during winter and spring (October to the end of April). During summer (May to September), the HFR

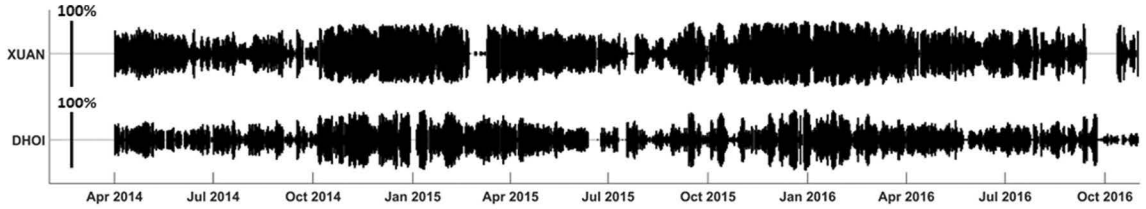

Fig. 2 Time history of the data return for two individual radars from April 2014 to October 2016. The height of each line matches the percentage of data availability. The scale bar on the left represents the maximum coverage (the maximum data return)

records exhibit a gradual drop in the coverage area of the obtained data. During summer, the wind direction reverses from northwest to southeast (onshore to offshore wind); thus, the ocean waves (Bragg waves with a wavelength of 30 m) do not gain sufficient fetch. During this period, a lower sea state results in lower coverage by coastal radars (Rogowski et al. 2019).

2.2.2 In situ velocity measurements

In 2015, a bottom-mounted current profiler AWAC, which operates at 600 kHz, was deployed offshore the XUAN radar site (105.97° E, 18.68° N) at a depth of 20 m and provided data for roughly 14 days (from October 16 to October 30, 2015). The instrument was configured to measure the current velocity profiles at 0.5-m vertical resolution and temporal resolution of 30 min.

2.2.3 Reanalyzed wind data

To evaluate the influence of wind on the surface currents, the wind data were obtained from the European Centre for Medium–Range Weather Forecasts (ECMWF) reanalysis model with a time step of 6 h and spatial resolution of 0.125° (https://www.ecmwf.int/en/forecasts/datasets/reanalysis-datasets/era-interim). The 3-year reanalyzed wind data (from 2014 to 2016) were used to demonstrate the variability of the winds by the wind rose plots in Fig. 3. Wind stress was calculated using the formula of Large and Pond (1981): $\overrightarrow{\tau} = \rho C_d |w| \overrightarrow{w}$ with $C_d = 1.15 \times 10^{-3}$. The wind speed and direction were then interpolated on the HFR grid.

2.2.4 Monthly CTD surveys and climatological river discharge

Monthly CTD surveys were conducted off the coast of the XUAN radar site during the period from September 2015 to August 2016. The transect extends 25-km offshore, with measurements spaced every 2.5 km (Fig. 1). Temperature and salinity profiles were obtained by boat-based, hand-deployed RBR Concerto CTD sampling at 16 Hz. The freshwater discharge data, available at the Ba Lat station, located 11-km inland from the river mouth, do not cover the whole period of observations. Thus, we used the climatological data to demonstrate the evolution of the river plume. These data were obtained in the framework of a collaboration project between the Vietnamese institutes (CFO, VASI) and the US institutes (Scripps Institution of Oceanography, Oregon State University, and Rutgers University).

2.3 Methods for data processing and analysis

2.3.1 HFR data processing and interpolation

After the quality control, the gaps in the radar data were filled in. The issue of filling the missing values in the HFR records has been explored over a long time. Several techniques have been investigated, such as the open-boundary mode analysis (OMA) by Kaplan and Lekien (2007), optimal interpolation

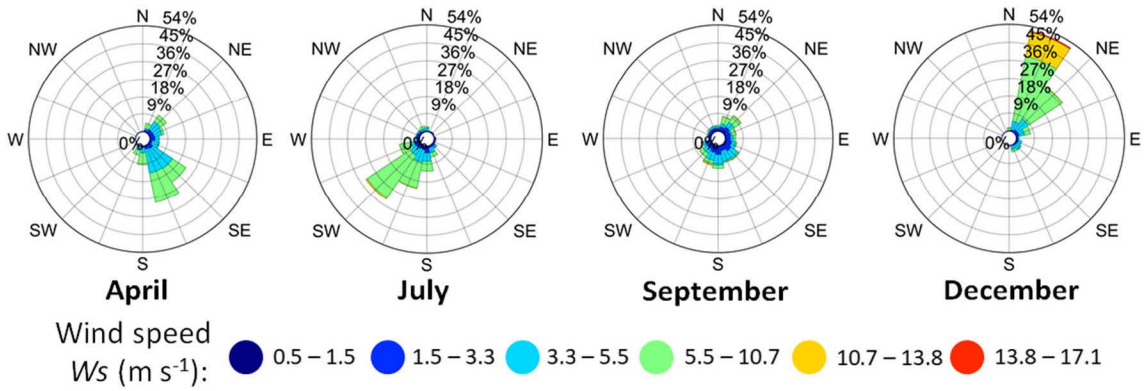

Fig. 3 Wind roses for four climatic conditions: NE monsoon (in December), SW monsoon (in July), and two transition periods: from NE to SW monsoon (in April) and from SW to NE monsoon (in September). The reanalyzed wind data were used from 2014 to 2016

(OI) by Kim et al. (2008), and EOF/variational interpolation (EOF/2dVar) by Yaremchuk and Sentchev (2011). The 2dVar method has several advantages compared to other techniques of radar data interpolation. 2dVar is a non-local and kinematically constrained interpolation method. It uses a combination of all measured velocities to reconstruct the velocity vector in one location and therefore, it creates a surface current velocity map. The 2dVar method is more flexible than OMA (also non-local interpolation method) in the choice of regularization. The smoothness of the interpolated vector field is enforced by penalizing the squared Laplacian of the velocity and also of its curl and divergence, thus providing the algorithm with adjustable and efficient control of smoothness. Kinematic constraints (zero flux on the rigid boundary), incorporated into 2dVar, appear particularly useful in regions with a complex shoreline and islands located inside of the interpolation area. Moreover, at the pre-processing step, the 2dVar method can use the iterative EOF-based technique for filling the gaps in the radial velocity time series. This makes the method particularly effective in case of radar failure or malfunctioning during short periods.

In our study, we used the EOF/2dVar method proposed by Yaremchuk and Sentchev (2011) to map the surface currents from the HFR measurements. The method is decomposed into four consecutive steps: (a) EOF analysis of the spike-removed radial velocities, (b) estimation of the inverse of velocity error covariance and signal-to-noise separation, (c) filling of gaps in radial maps, and (d) interpolation of the surface current velocities on a regular grid using a variational method (2dVar) and current vector map generation. Although both OMA and 2dVar are found to be capable of filling the gaps in space, the EOF/2dVar method is also capable of filling the gap in the HFR records, both at the spatial and temporal scales. The method had demonstrated the ability to fill the gaps up to 2 days, depending on the optimum number of EOF modes used in the decomposition of the time series. The detailed descriptions of the method are presented in the study by Yaremchuk and Sentchev (2011).

2.3.2 Principal component analysis, rotary spectral analysis, and tidal harmonic analysis

We conducted rotary spectral analysis (hereafter referred to as RSA) of the HFR data to retrieve prominent frequencies of surface current variability in the GoT. The method was used to process a 2.5-year-long HFR data and reanalyzed wind from April 2014 to October 2016. In addition, we analyzed a 3-month-long cumulative time series during summer (June to August) and winter (November to January) to evaluate the effect of seasonal variability of wind on currents.

The principal component analysis (PCA) technique was used for the HFR-derived velocities to access tidal motions. This technique enables us to estimate the contribution of all tidal constituents to the observed currents. PCA provides the parameters of synthesized tidal current ellipses: the orientation and magnitude of the dominant currents. The drawback of the PCA is that it does not provide information on the sign of current vector rotations. Therefore, the rotary coefficient was estimated from the RSA of the surface current velocities. The RSA exhibits pronounced peaks in the energy spectrum $S(f)$ at diurnal frequencies (K1 and O1) and semi-diurnal frequency (M2) corresponding to both clockwise (*cw*) motion S_- and counterclockwise (*ccw*) motion S_+ of the current vector rotations. The rotary coefficient, which is defined as $r = (S_+ - S_-)/(S_+ + S_-)$, was estimated at every grid point from these peak values. The value of r ranges from -1, for *cw* rotation, to 1, for *ccw* rotation.

The harmonic analysis was applied to the 1-year-long time series of surface current using the T_tide package (Pawlowicz et al. 2002). Nodal corrections were included in the analysis of tidal currents.

2.3.3 Seasonal variability of coastal water stratification

To evaluate the seasonal variability of stratification in the coastal zone generated by the freshwater discharge variations in the Red River, we used the potential energy anomaly (PEA) index ϕ proposed by Simpson et al. (1990):

$$\Phi = \frac{1}{h}\int_{-h}^{\eta} gz\left(\overline{\rho} - \rho\right) dz$$

Here, h denotes the water depth in meters; η is the sea surface height with respect to depth; ρ is the potential density at depth z; $\overline{\rho}$ is the vertically average potential density; and g is the gravitational acceleration. The value of Φ indicates the amount of required energy per unit volume to completely mix the water column. Thus, it represents the strength of the water column stratification. Zero value means the column is fully mixed and it increases with stratification. In this study, we consider that values smaller than 5 J m^{-3} represent mixed conditions, while values greater than 10 J m^{-3} corresponds to highly stratified conditions, and the values in between correspond to weakly stratified conditions. The intermediate values, between 5 and 10 J m^{-3}, correspond to weakly stratified conditions. The CTD profiles were obtained along the transection off the coast of the XUAN radar site and limit to the upper layer 26 m thick. Therefore, the analysis of the time evolution of water stratification in this study is limited to the subsurface layer.

2.4 Validation of the HFR data and assessment of the data interpolation techniques

To assess the overall performance of the HFR observations, we compared the HFR-derived current velocities with in situ current measurements by AWAC, following the method proposed by Liu et al. (2014). The first complete bin of AWAC-

derived current velocities below the surface at a depth of 2 m was compared with that derived from HFR. The skill metrics include bias, root mean square error (RMSE), and complex correlation analysis between HFR-derived velocity and AWAC velocity time series (Kundu 1976). We investigated both the differences between the AWAC current meters and the HFR total current processed using the OMA solution and the EOF/2dVar method. Three sets of radar-derived velocity were compared with the AWAC data: (1) the radial velocities reprocessed by the OMA method; (2) the velocities after the gap filling by EOF and reprocessed by the OMA method; and (3) the velocities reprocessed by the EOF/2dVar with gap-filling capability. The results, which are presented in Table 1, reveal that all methods provide a good complex correlation between the AWAC and radar velocities. The absolute correlation values (α) are larger than 0.7. The phase difference (θ) for each of the three cases is less than 3° and demonstrates a rotation of the HFR-derived current vector to the right of the AWAC-derived current vector. Quantitatively, the bias between the AWAC and HFR is about 0.03 m s^{-1} for the zonal components for the three cases and less than 0.06 m s^{-1} for the meridional component. In terms of RMSE, the differences are found to be less than 0.14 m s^{-1} for both components. Generally, the radar-derived velocities processed by EOF/2dVar exhibited a slightly better agreement with the AWAC measurements than those processed by the OMA method (Table 1).

3 Results

3.1 Spectral analyses of wind speed and current velocity

Figure 4 presents the rotary power spectral density (PSD) of the wind speed while Fig. 6 presents the PSD of the surface current velocities. The PSD of the wind speed shows the energy cascading from large to small scales (the spectral slope is a − 5/3). It also shows well-defined peaks at the diurnal, semi-diurnal, and third-diurnal peaks. The wind spectrum in winter exhibits notable peaks in the sub-diurnal band (0.0205 and 0.0085 cph), which are related to the strong northeasterly wind often varying the intensity with a period of 2–5 days (Fig. 4b). The prominent diurnal peak in Fig. 4c could be due to the so-called sea breeze, which is supported by higher energy level in wind variability at diurnal frequency in summer. The energy at the diurnal frequency of the wind is larger by an order of magnitude than that at semi-diurnal frequencies, especially in summer. This is due to the large differences in the land-sea temperatures at this period. For example, on June 11, 2019, the temperature observed from Ha Tinh and Dong Hoi provinces, which are the locations of the XUAN and DHOI radar sites, respectively, exceeded 43 °C. The difference in the land-sea temperature in these areas could reach 15 °C (data retrieved from Vietnam National Center of Hydrological and Meteorological Forecast: *www.nchmf.gov.vn*).

Three prominent peaks at diurnal (O1, K1) and semi-diurnal (M2) frequencies are identified in the current velocity spectrum (Fig. 5a). The energy of the diurnal tidal constituents is higher than that of the semi-diurnal constituents by an order of magnitude (1.5 10^{-2} and 1.6 10^{-3} m^2 s^{-2} cph^{-1} respectively), indicating that diurnal tide dominates the tidal dynamics in the GoT. Smaller peaks in Fig. 5 correspond to the third-diurnal shallow-water tidal constituents (SK3, MK3, MO3) (Pawlowicz et al. 2002). These higher order tidal harmonics are generated by nonlinear interactions of the main diurnal and the semi-diurnal tidal constituents in the shallow waters. However, the magnitude of these nonlinear tidal harmonics is extremely low (less than 0.02 m s^{-1}) compared to that of four main tidal constituents.

Both the ccw and cw motions have similar energy level at the diurnal frequency (the peaks at K1 and O1 in Fig. 5a). This suggests that, for these two harmonics, the tidal current is reversive, i.d. the current vector variation is rectilinear. However, the energy of the cw motion at the semi-diurnal frequency (M2) is higher by half an order of magnitude than that of the ccw motion, thus resulting in a more circular shape of the tidal current ellipses.

The influence of the wind on the surface current is also visible at the inertial frequency of 0.026 cph (period of 38 h). The cw motion is greater than the ccw component by half an order of magnitude (Fig. 4).

Considering the seasonal change in the surface current kinetic energy spectrum, there are notable power density variations at different frequencies (Fig. 5b, c). In winter, the energy at the diurnal frequency is higher in winter than in summer by about roughly a half of an order of magnitude (1.5 10^{-2} and 6 10^{-3} m^2 s^{-2} cph^{-1} respectively) (Fig. 5b, c), whereas opposite

Table 1 Results of comparison of HFR velocities processed by three different methods and in situ velocity measurements at AWAC mooring. The period of measurements spans from October 17 to October 29, 2015

Method	Correlation		BIAS (m s^{-1})		RMSE (m s^{-1})		α	θ
	U	*V*	*U*	*V*	*U*	*V*		
HFR OMA vs AWAC	0.66	0.82	−0.04	0.06	0.14	0.12	0.74	−2.57°
HFR OMA + Gap filling vs AWAC	0.70	0.84	−0.03	0.04	0.14	0.10	0.75	−1.06°
HFR 2dVar + gap filling vs AWAC	0.78	0.85	−0.03	0.03	0.12	0.10	0.79	−0.93°

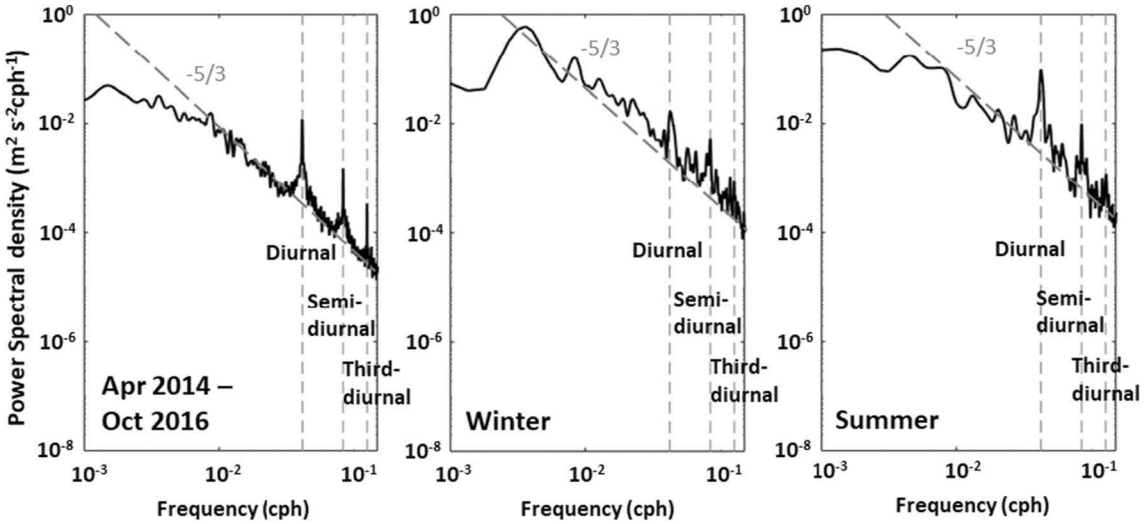

Fig. 4 Basin-wide average power spectral density for reanalyzed wind speed for the whole 2.5-year-long period of analysis from April 2014 to October 2016 (**a**), for the winter period (November 2014 to January 2015) (**b**), and summer period (June to August 2015) (**c**)

distribution is observed in the wind spectra where the peak at the diurnal frequency in summer is higher than in winter by half an order of magnitude (5 10^{-2} and 1 10^{-2} m^2 s^{-2} cph^{-1} respectively) (Fig. 4b, c). Contrarily, the inertial peak in the PSD of the currents in winter becomes less significant and shifts toward the sub-inertial band (less than 0.026 cph). The variability of the current velocities with a period of 2–5 days (Fig. 5b) is similar to that of the wind also observed in winter (Fig. 4b).

3.2 Tidal currents

3.2.1 Space-time variation of the tidal currents

The PCA method was used to analyze hourly velocities recorded by HFR for 17 days, from October 13, 2015, to October 31, 2015. This period corresponds to the period of AWAC measurements (Fig. 6). The evolution of tidal currents in both the space and time domain is quantified using the synthesized ellipses derived from the PCA and rotary spectral analysis.

The tidal wave propagating southward is controlled by the topography and is characterized by the lower eccentricity of tidal ellipses (flatter tidal ellipses) oriented parallel to the shoreline. The magnitude of the tidal currents, as presented by the length of current ellipses, is high at the southern entrance, with values ranging from 0.4 to 0.6 m s^{-1}, then decreases (0.05 to 0.2 m s^{-1}) in the northern part. A major branch of tidal energy enters the gulf through the southern entrance, and a large part of incoming tidal flux tends to be deflected to the right along the Hainan Island (Nguyen et al. 2014). Subsequently, the tidal magnitude near the gulf entrance is slightly higher in the offshore zone (0.5 to 0.6 m s^{-1},

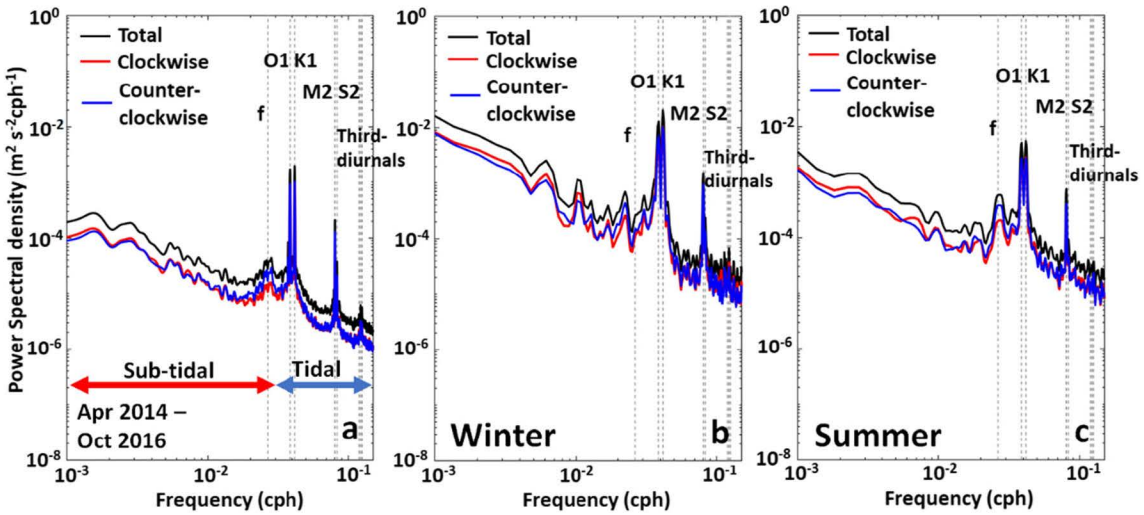

Fig. 5 Basin-wide average power spectral density for surface current velocities for the whole 2.5-year-long period from April 2014 to October 2016 (**a**), in winter (November 2014 to January 2015) (**b**), and in summer (June to August 2015) (**c**)

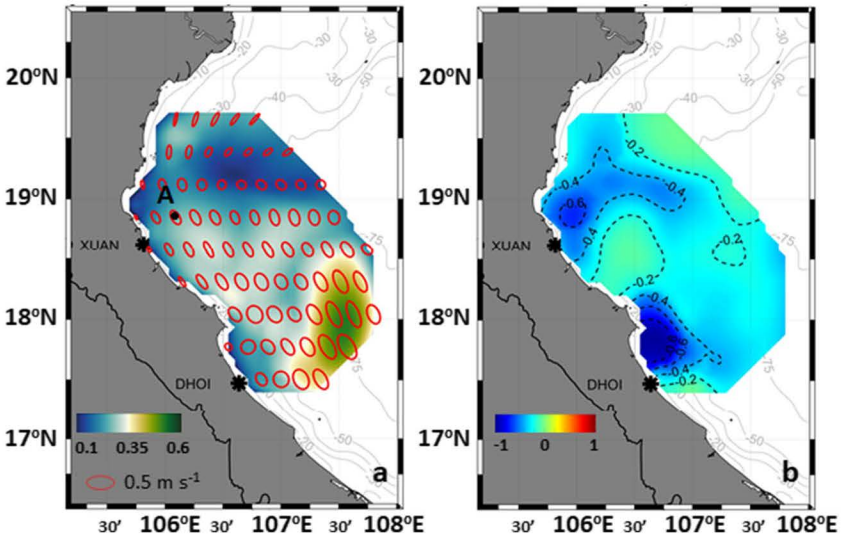

Fig. 6 **a** PCA-derived tidal ellipses during a 17-day period from October 13, 2015, to Oct 31, 2015. Tidal ellipses are plotted every tenth grid points. Red ellipses denote the clockwise rotating current vectors. The major axis of the ellipses indicates the tidal magnitude in m s^{-1} (color shading). **b** Rotary coefficient of surface current velocities during the same period (color shading and contour lines). Black point A corresponds to the AWAC mooring location

Fig. 6a). The energy of the tidal wave traveling in the gulf dissipates due to the effect of bottom friction, and the resulting amplitude of tidal currents gradually decreases with decreasing depth in the northern sector (Fig. 6a).

The spatial distribution of the rotary coefficient (Fig. 6b) exhibits a complex pattern. The tidal current vectors in the GoT are dominated by the cw rotation, with the average value of rotary coefficient ranging from − 0.1 to − 0.3 in the middle part of the gulf. Lower values (from − 0.6 to − 0.4) are observed in the shallow water area along the Vietnamese coast and in the region located between the two radar sites.

PCA was also applied to evaluate the temporal variability of the tidal currents at the location of the AWAC mooring (point A in Fig. 6a) during a whole tidal cycle from October 13, 2015, to November 08, 2015. During this period, a fortnightly variation of tidal current occurs, and both the primary and secondary spring tides are observed in the time series of the tidal ellipse evolution (Fig. 7). The tidal amplitude increases from 0.07 m s^{-1}, on October 13, to 0.36 m s^{-1}, on October 20. The comparison suggests that both the HFR-derived and AWAC-derived ellipses exhibit similar magnitudes and shapes. The mean bias in the magnitude of the AWAC- and HFR-derived tidal current is 3 cm s^{-1}. In spite of a good overall agreement, a larger discrepancy of about 10 cm s^{-1} between HFR- and AWAC-derived tidal ellipse magnitude is observed on October 26, 2015. On this day, the radar measurements showed a stronger southward current than that observed AWAC (Fig. 15). The difference can arise from the scale of motions resolved by two measurement techniques: point measurements by AWAC and spatial averaged velocity obtained by HFR. It can also result from technical problems of data acquisition by HFR on this particular day.

3.2.2 Tidal harmonic analysis

Figure 8 presents the results of the harmonic analysis of the tidal current velocities. The spatial distribution of the total velocity variance indicates that tidal motions account for a large percentage of surface current variability in the GoT. This contribution ranges from 20% in the shallow water zone near the Red River mouth and in the middle of the domain to 70% at the southern entrance of the gulf. The mean tidal contribution to the total surface variability is 60%, which is obtained by averaging the percentages over the study region. Typically, the variability of the velocity is much larger in the north-south direction (V-component) than in the east-west direction (U-component) as the tides enter the gulf mainly through the southern open boundary.

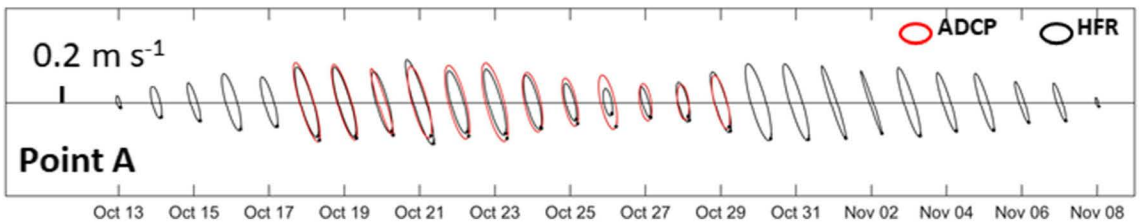

Fig. 7 Time evolution of tidal current ellipses at point A (at the AWAC mooring location) from October 13, 2015, to November 08, 2015. HFR-derived current ellipses are shown in black and ellipses from ADCP measurements are shown in red. The major axis of ellipses denotes the tidal current magnitude. The scale of the tidal ellipses is shown on the left side

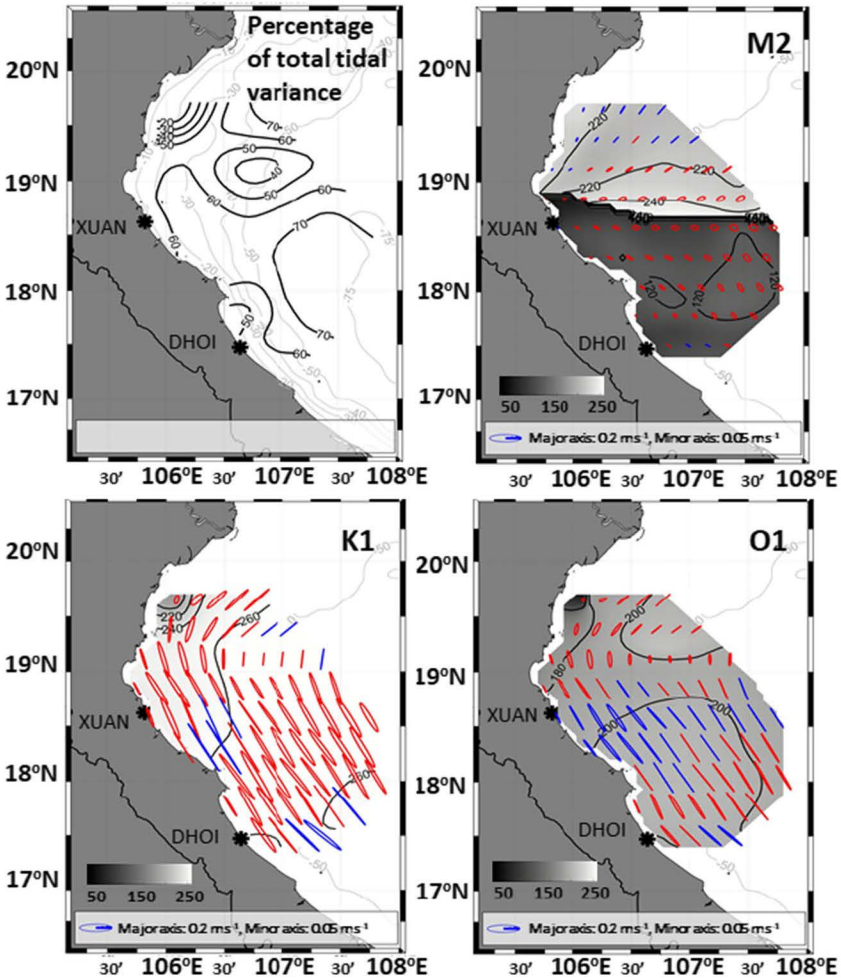

Fig. 8 Contribution of tidal motions to the total variance of surface current velocities (left top panel). Tidal current ellipses and corresponding phase distribution (gray shading and contour lines) for three dominant tidal constituents (O1, K1, and M2) were derived from the tidal harmonic analysis. The current vector rotation is shown in blue for ccw and in red for cw rotating currents

The spatial patterns of the tidal ellipses of the predominant diurnal constituents (K1 and O1) are quite similar in terms of structure. The cw motion of the K1 constituent dominates most of the domain, whereas the ccw motions of the O1 constituent are concentrated in the middle of the domain. The tidal ellipses are tightened and strongly controlled by the basin configuration. The tidal magnitude ranges from 0.05 m s^{-1}, near the river mouth and in the middle of the gulf, to 0.2 m s^{-1}, at the southern limit of the gulf. A comparison of the phase distribution for the tidal elevation and the tidal currents indicates a combination of standing wave and progressive wave motions. The phase of surface elevation for predominant diurnal tidal constituents ranges from 100° to 120° for the K1 constituent and from 30° to 40° for the O1 constituent (Nguyen et al. 2014; Piton et al. 2020), whereas the phases of tidal currents are about 260° for the K1 constituent and 200° for the O1 constituent on average. The footprint of a standing wave in the northeast-southwest direction can be inferred from the difference in the phase of tidal current and elevation (close to quadrature) near the coast in the northern part of the gulf. Thus, the tidal dynamics in the northern gulf is similar to that of the standing wave (Nguyen et al. 2014).

The amplitude and phase distribution of the semi-diurnal tidal current constituents are quite complex. The magnitude of the M2 constituent, which ranges from 0.02 to 0.05 m s^{-1}, is lower than the diurnal tides by a factor of 4. The phase distribution of the M2 constituent rapidly changes from 220° in the northern sector to 120° in the southern sector (Fig. 8b). The spatial distribution of phase lags and tidal ellipses orientation suggest that a tidal wave has the form of a progressive Kelvin wave and travels in the southwest direction along the coast of Vietnam. The shape of the tidal ellipses and phase distribution of S2 (not shown) tidal ellipses and phases are almost identical to those of M2. However, the magnitude of S2 harmonic, which ranges from 0.01 to 0.02 m s^{-1}, is lower than that of the diurnal tidal harmonics by a factor of 8. A combination of the major tidal constituents gives the total tidal ellipse a more circular shape in the southern part of the domain (Fig. 6a).

3.3 Sub-tidal variability of the surface currents

The sub-tidal variability of the surface currents was evaluated after applying to HFR-derived velocities a low-pass filter with a 38-h cutoff. The pl66tn (Beardsley and Rosenfeld 1981)

low-pass filter was used to create hourly filtered data. The same filter was also applied to wind data.

3.3.1 Annual mean surface flow and seasonal variability

The mean velocity distributions derived from the HFR measurements indicate a prominent southward flow along the coast of Vietnam (Fig. 9). The flow originates from the northern part of the gulf, follows the 30-m isobath, and experiences intensification between 18° N and 19° N. In the southern part, a separation of the coastal current into two branches is observed: one branch keeps flowing southward and the other changes the direction to offshore and then merges with the northward flow from the SCS. The annual mean circulation pattern is thus cyclonic.

The time series of the hourly current speed in 2015 were extracted at two points, one near the shoreline and another in the offshore region (point A and point B in Fig. 9), to assess the annual variability compared with the wind stress variability. In winter, the current magnitudes are stronger than in other seasons (at an average of 0.3 to 0.5 m s^{-1}), which is influenced by periodic strong northeasterly winds. Near the shore, the current speeds occasionally reach 0.8 to 1.0 m s^{-1} during strong wind (Fig. 10, middle panel) and can exceed the offshore current speed (the highest speed is about 0.6 m s^{-1}). A large difference in the nearshore and offshore current magnitudes, which could exceed 0.4 m s^{-1}, is observed from late September to early March, whereas from May to August, the difference is less significant (Fig. 10).

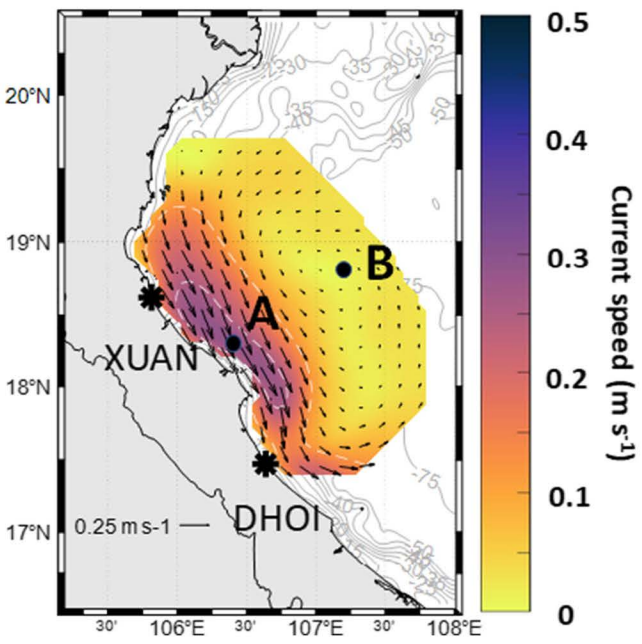

Fig. 9 Mean surface current velocity field during the period from April 2014 to October 2016. Surface velocities are plotted every 15 km. Points A and B correspond to the nearshore and offshore location selected for further assessment

Figure 11 a and b present the mean surface current fields for July (summer) and December (winter). The current velocity variance is estimated and presented as ellipses. From winter to summer with the wind direction reversal, the current speed gradually decreases from 0.4 to 0.2 m s^{-1}. Near the shoreline, the current speeds are stronger (0.3–0.5 m s^{-1}) than in the middle of the gulf (0.1–0.3 m s^{-1}). The mean values and variability presented in Fig. 11b suggest that the currents in winter are stronger and experience less variation than during other periods.

A Hovmoller diagram was used to better understand the seasonal evolution of surface circulation in the GoT (Fig. 11c, d). Monthly surface current data were extracted along the line perpendicular to the shoreline. The velocity vectors were projected onto two directions, normal and parallel to the cross section, thus providing two velocity components: along-shore and cross-shore. Negative along-shore velocities match the current directed southwestward. Positive cross-shore velocities match the offshore flow. The cross-section spans from the shoreline to approximately 150-km offshore. The same goes for the wind stresses extracted along the cross section (Fig. 11e).

As can be seen from the diagram, an annual cycle is observed for both the cross-shore and along-shore velocity components, which correspond to the wind forcing reversal. In the offshore zone, the velocity component normal to the cross-section line is quite low, with the value ranging from − 0.1 to less than 0.1 m s^{-1}. In winter, the prevailing direction of the current is southward (Fig. 11c). Starting from April to the end of summer, the direction of the currents changes under the influence of prevailing southwesterly wind. A much stronger variability is observed in the nearshore zone. The along-shore current persists throughout the whole year, with a large amplitude of seasonal variability (from − 0.25 m s^{-1} during winter to close to 0 during summer). The offshore extension of the area with a velocity larger than 0.1 m s^{-1} varies widely: 25–75 km. During the dry season (from September to February), a strong coastal jet with a velocity of more than 0.25 m s^{-1} is observed at a large distance from the shore (Fig. 11c).

From May to August, the velocity decreases to 0.1 m s^{-1}, and the spatial extension of the jet does not exceed 25 km from the shore. What is more surprising is the duration of the weak-strong stages of the coastal jet. Compared with the variations of the cross-shore velocity component (Fig. 11d), which is strictly periodic and associated with the wind variation, the modulation of the along-shore component appears different. The stage of a strong coastal jet lasts 8 to 9 months, whereas the stage of a weak jet lasts only 3 months (from June to August). Contrarily, the seasonal variability of the cross-shore velocity component follows the low-frequency variations of the wind.

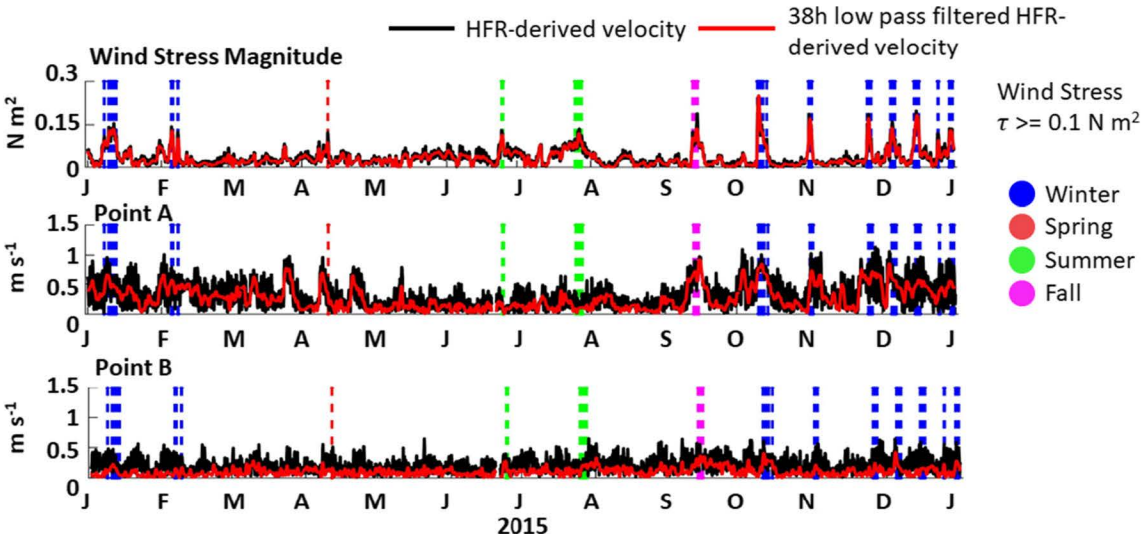

Fig. 10 Time series of spatial mean wind stress magnitude (top), the hourly current velocities (black line), and 38-h low-pass filtered velocities (red line) from the nearshore area at point A (middle), and from the offshore area at point B (bottom) in 2015. The color vertical lines mark the events of strong wind (wind stress magnitude greater than 0.1 N m^2)

3.3.2 Wind/current coherence analysis

To evaluate in detail the wind-current interactions and their spatial variability, we conducted a joint analysis of the wind stress and the observed current field. The obtained current velocities and wind stresses were projected on the cross-shore and along-shore directions (given by line A orientation in Fig. 11). Spatially averaged current velocities and wind stresses were considered after the spatial averaging of both the current and wind stress components at all data points and for each single time step. The analysis was performed, taking into consideration the 95% confidence level.

The first order of wind-current relationship is quantified by the lagged vector correlation (Kundu 1976) for the total time series and shows a significant correlation between the HFR-derived current and wind data (Fig. 12), with an absolute complex correlation value of 0.69 (Table 2). The spatial distribution of the correlation values shows an area of high values (0.5–0.6) in the northeast part of the domain, and an area of a lower correlation (0.3–0.4) near the shoreline. The distribution

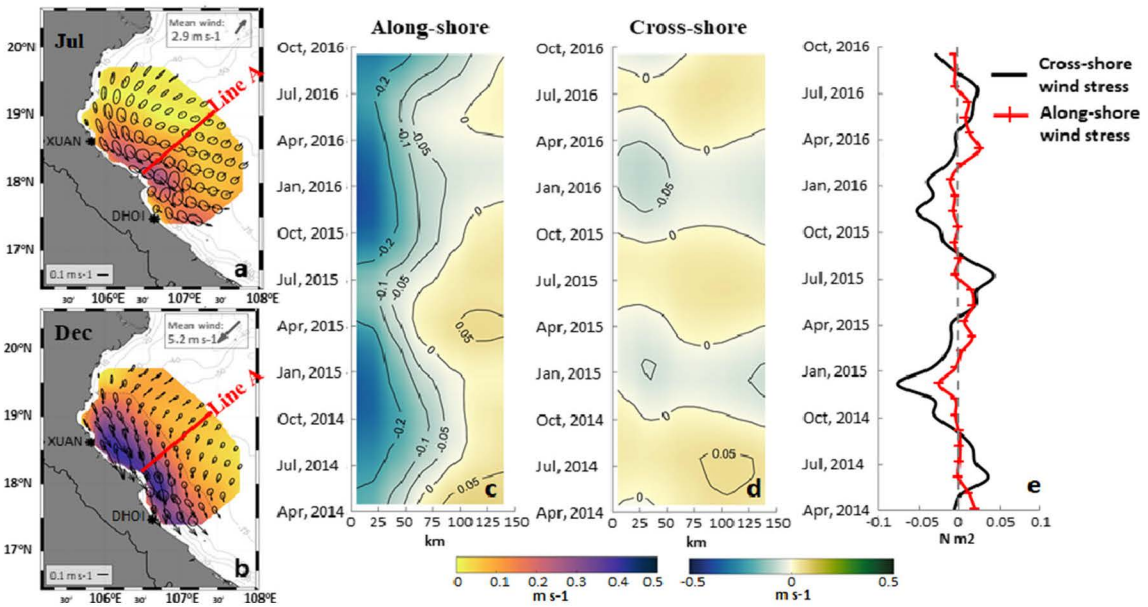

Fig. 11 Mean surface current magnitude (color shading) in summer (**a**) and in winter (**b**). Ellipses in **a** and **b** show the variance of the low-pass filtered current velocities. Space-time evolution of the along-shore and cross-shore surface current velocities along the transect A is shown in **c** and **d** by color shading. Monthly mean along and cross-shore components of the wind stress (**e**). Negative velocities indicate the southeastward and onshore current directions for the along-shore and cross-shore components respectively

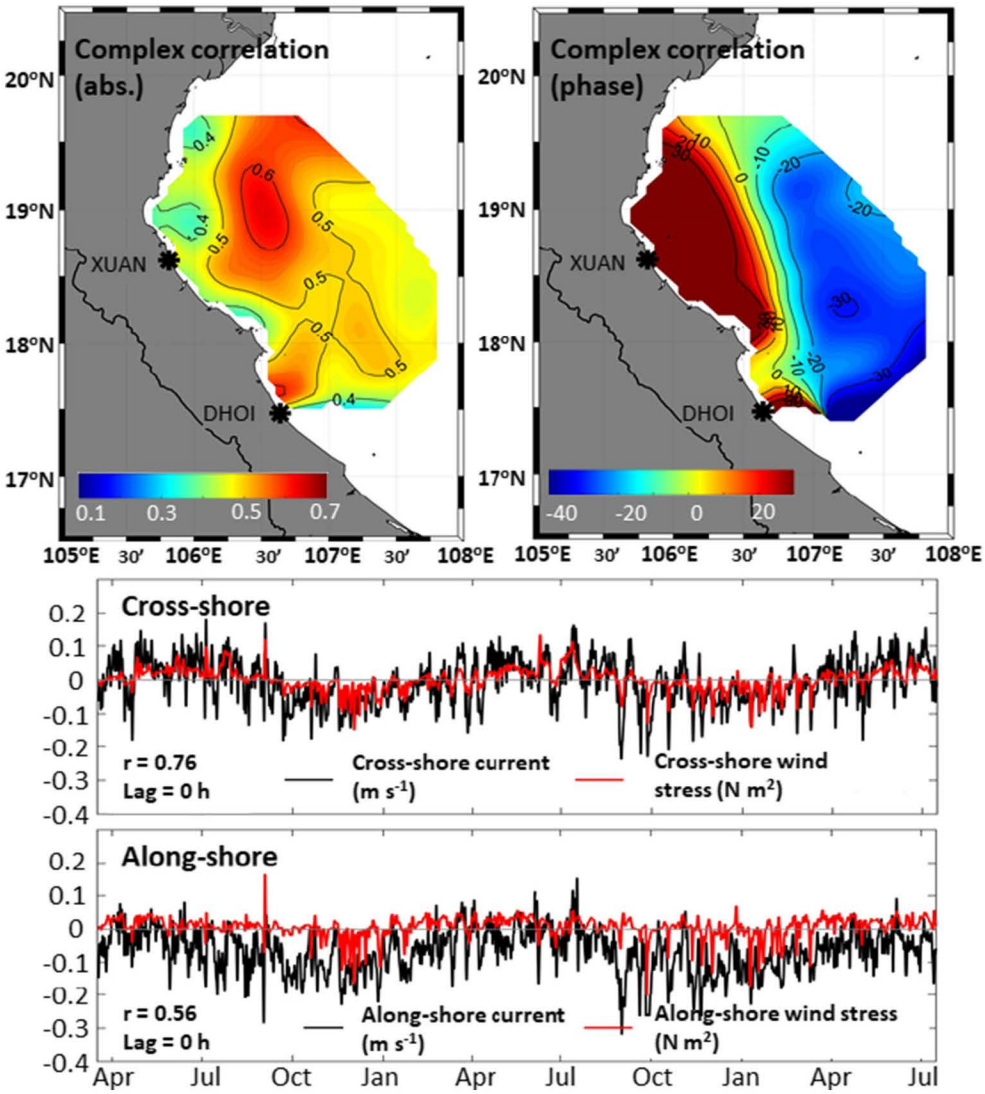

Fig. 12 Complex correlation between sub-tidal current velocities and wind stress. Contours are absolute values (left) and veering angles in degrees (right), negative values of veering angles mean that the current rotates clockwise from the wind. Time series of sub-tidal current velocity and wind stress components, from April 2014 to July 2016, are shown at two bottom sub-plots

of the phase correlation is complex, with negative values (− 30° to − 10°) overwhelming in the offshore area, whereas the positive values (10° to 35°) are found near the shoreline. The negative values in the offshore region reflect the tendency of the current to rotate clockwise with respect to the wind, which agrees with the Ekman theory. Positive veering angles near the shoreline are clearly related to the coastal currents previously mentioned. In addition, the time series of the domain-wide average exhibits a high correlation (0.76) between the wind stress and surface current for the cross-shore components, whereas, for the along-shore components, the correlation is significantly less (0.56). The seasonal cycle of the

Table 2 Correlations between the wind and surface current velocity components for different seasons and stratification conditions

		Cross-shore current vs. cross-shore wind	Along-shore current vs. along-shore wind	Complex correlation value	Complex correlation phase
Total		0.76 (lag=0 h)	0.56 (lag=0 h)	0.69 (lag=0 h)	−0.7° (lag=0 h)
Northeasterly wind	November 2014–January 2015	0.84 (lag=0 h)	0.68 (lag=0 h)	0.77 (lag=0 h)	5.7° (lag=0 h)
(well-mixed condition)	November 2015–January 2016	0.76 (lag=0 h)	0.50 (lag=0 h)	0.67 (lag=0 h)	3.2° (lag=0 h)
Southwesterly wind	June 2015–August 2015	0.55 (lag=6 h)	0.39 (lag=6 h)	0.48 (lag=6 h)	−35° (lag=6 h)
(weak stratified condition)	June 2016–August 2016	0.45 (lag=6 h)	0.50 (lag=6 h)	0.42 (lag=6 h)	−27° (lag=6 h)
Southwesterly wind	June 2015–July 2015	0.70 (lag=6 h)	0.53 (lag=6 h)	0.61 (lag=6 h)	−27.3° (lag=6 h)
(temporary mixed condition)	June 2016–July 2016	0.61 (lag=6 h)	0.32 (lag=6 h)	0.47 (lag=6 h)	−33.1° (lag=6 h)

current due to the wind reversal can be clearly observed in the cross-shore time series (mostly positive through April to August and vice versa). In addition, minimal lag at 0 h of both the time series indicates the nearly immediate response of the surface layer to the wind.

While the high correlation of the wind and surface current was obtained on average, there were some differences in the seasonal responses. To further evaluate the seasonal differences in wind-surface current responses, we extracted the data in the middle of two distinct periods: during the northeasterly (winter) and southwesterly wind (summer) conditions. After the seasonal separation, the high correlations (0.67 to 0.77) and small phase differences between wind and current vectors (5.7° and 3.2°) are observed between the surface current and wind data during winter (Table 2). The correlation between the cross-shore wind and current velocities is high (0.84) at the lag of 0 h, whereas a slightly lower correlation is observed for the along-shore components (0.68- at 0-h lag). High correlation and small phase differences indicate that the surface currents rapidly respond to the strong wind in winter. Under the strong wind, the surface currents are pushed onshore and travel southward along the coastline. The wind-induced current, thus, significantly contributes to the sub-tidal current variability during winter.

The correlation between the wind and current in summer is presented in Table 2. The surface current shifts toward the offshore direction following the change in the wind direction. The phase difference of − 35° indicates that the current vectors veer to the right of the wind direction. This is in agreement with the Ekman transport theory. In summer, the southwesterly wind is weaker than the northeasterly wind. The complex correlation is found to be significantly low (the highest is 0.48). Both along-shore and cross-shore components (the highest correlations are 0.55 and 0.50 respectively) exhibit a larger response time of 6 h. In addition, we analyzed the weakly stratified condition in mid-summer (approximately from mid-June to mid-July). After the freshwater was "trapped," the surface current somehow appears to be in phase with the variation of the wind as shown by the slight increases in the wind-current correlation (the highest complex correlation is 0.61 compares to 0.48 in this season) and the cross-shore components (0.70 compares to 0.55 respectively). From August toward the end of summer, the freshwater is released again thus inducing stratification and results in a decrease in the wind-current correlation.

3.4 Influence of freshwater discharge on surface currents

3.4.1 River plume variability

During the year, a large amount of riverine freshwater is discharged from July to September and the lowest is in mid-winter. The typical discharge in the Ba Lat station is at a rate of 1200 m^3 s^{-1}. The highest discharge in August is at a rate of 1400 m^3 s^{-1} whereas in January, the average discharge is low, typically around 500 m^3 s^{-1} (Fig. 13e). The monthly CTD transect survey data from the cross-shore transects (red line in Fig. 1) were analyzed to study the evolution of the Red River plume. While the monthly temperature transects allow the characterization of the seasonal cycle of the surface heat flux into the water column (results not shown), the salinity distribution helps understand the variability of the Red River coastal plume (Fig. 13a–d). Using the same data, Rogowski et al. (2019) demonstrated the seasonal variability of the Red River plume in the coastal zone. The freshwater plume, which is confined to the surface layer (about 5-m thick) and advected southward along the Vietnam coast at the end of summer, extends deeper into the water column from October onward (the observed fresher water is about 10-m deep and spreads outward to the sea beyond the survey line), thus inducing stratification (Fig. 13a). In winter, the decrease in the riverine discharge and the cooling of the seawater favors the mixing of the coastal water. The water column becomes well mixed in the middle of January (Fig. 13b), which coincides with the minimal discharge from the Red River. In April, the thin layer of freshwater observed on the surface suggests that the river plume continued to evolve (Fig. 13c). In mid-summer (late June), the transect data shows that the water became saltier, indicating that the river plume was trapped at the mouth of the Red River under southwesterly wind conditions and the denser water from the open ocean intruded into the shallow water zone (Fig. 13d).

Figure 13e presents the monthly variation of the PEA index ϕ which is calculated from the CTD transect survey data. From September to October, as the river plume is developed and advected southward, the water column is found to be highly stratified (the value of ϕ is 13 to 18 J m^{-3}). In winter, a decrease in the river discharge causes a decrease in ϕ, which matches the well-mixed conditions generally observed in December and January (the value of ϕ is 2 to 4.5 J m^{-3}). The second cycle of stratification increase starts in March and lasts until May. It is related to the southward advection of the freshwater coming from the river mouth. Mid-summer, which spans from June to July, is considered as the second mixed period. During these months, the coastal currents reverse, and the river plume is transported eastward. The decrease in the freshwater discharge influence on the southern coast of Vietnam creates favorable conditions for water mixing. This is supported by a local minimum of ϕ in June (the value of ϕ is 5.7 J m^{-3}).

3.4.2 River discharge and tidal straining

The PSD of the current velocities indicates that the power density at the diurnal and semi-diurnal frequencies changes

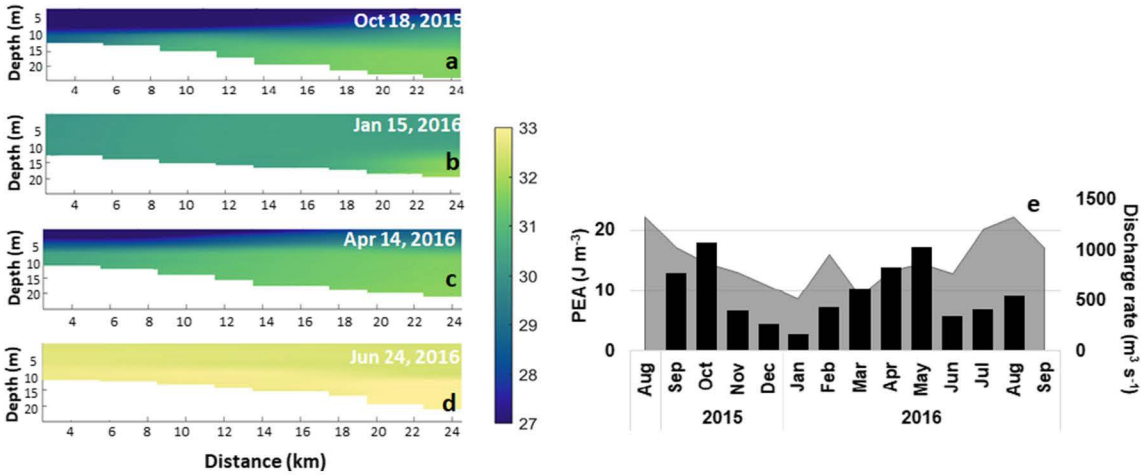

Fig. 13 Salinity variations along the cross-shore transect off XUAN site in October 2015 (stratified condition) (**a**), January (well-mixed condition) (**b**), April (**c**) and June 2016 (weakly stratified condition) (**d**). The climatological discharge in the Ba Lat station (gray shade area) overlaid by the time evolution of the potential energy anomaly (PEA) index ϕ (**e**)

during the year and appears higher in winter by approximately half an order of magnitude (Fig. 5b, c). At the same time, the PCA-derived current ellipses did not exhibit noticeable changes in the tidal current magnitude between seasons. However, there were significant differences in the shape of the tidal ellipses under stratified and mixed conditions, revealing a large variability of the cross-shore tidal shear (Fig. 14). The HFR-derived velocities on October 18–25, 2015 and January 03–10, 2016 corresponding to the stratified and mixed conditions were selected for the assessment of the influence of the river discharge on the tidal current ellipses. Figure 14 demonstrates that the tidal current ellipses close to the XUAN radar site are flattened in January when the water is well mixed. On the contrary, the ellipses within roughly 40 km in the coastal zone are more circular in October and exhibit a greater tendency toward the cw motions (rotary coefficients range from 0.4 to 0.6). This phenomenon is called "tidal cross-shore straining" (Simpson and Sharples 2012).

To further investigate the role of freshwater discharge in the polarization of the tidal ellipses, we used the current profiles obtained from the AWAC meter in October 2015 (Fig. 15). During this highly stratified period, the coastal current is characterized by a two-layer circulation, with the surface flow detached from the bottom layer flow (Mazzini et al. 2014; Rogowski et al. 2019). The important feature of the tidal circulation is the difference in the current vector rotations between the surface and bottom layers (Fig. 15). Current vectors rotate cw in the surface layer (up to 6 m below the surface), with a corresponding r value of approximately −0.4, whereas in the lower half of the water column, the currents

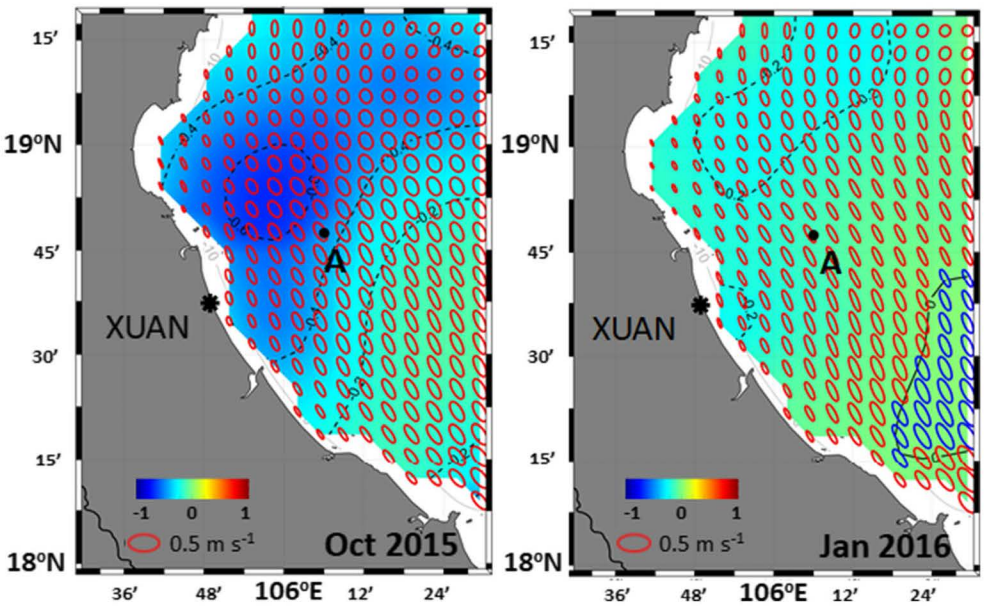

Fig. 14 PCA-derived tidal current ellipses, averaged during 7 days of spring tide in October 2015 (October 18–25, stratified condition) and in January 2016 (January 03–10, well-mixed condition). The rotary coefficient of tidal ellipses is shown by color shading. The current vector rotation is shown in blue for ccw and in red for cw rotating currents

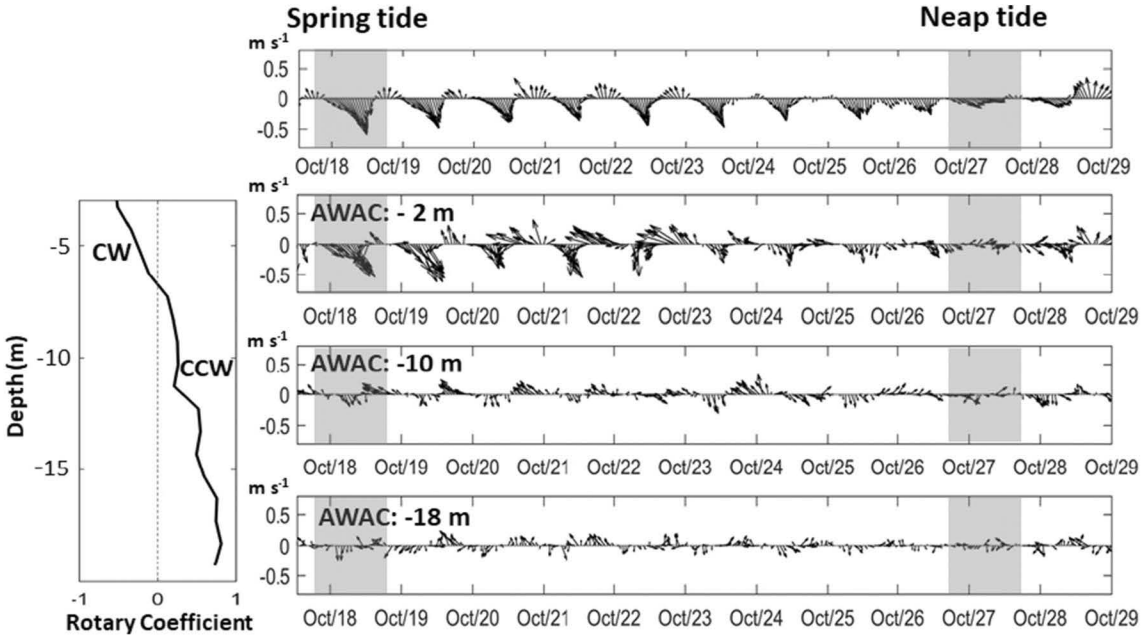

Fig. 15 Time series of HFR-derived current velocities and observed velocities at AWAC mooring location in October 2015 at different depth levels: surface layer (− 2 m), mid-depth (− 10 m), and bottom layer (− 18 m) (right). Vertical profile of the rotary coefficient from measured velocities (left). Gray shading shows the peak spring tide and neap tide periods

achieve a ccw rotation with $r > 0.6$. A separation between two layers is clearly observed at a depth of 7 m, as presented in Fig. 15 (left panel). The maximum current velocities in the surface layer (up to 6 m below the surface) vary from 0.3 m s^{-1} on the neap tide to 0.6 m s^{-1} on a spring tide, and the current direction matches the advection of the river plume along the coast. Lower velocities are observed below that depth, with maximum values ranging from 0.1 to 0.4 m s^{-1}. The current velocity profile is highly sheared and shows a direction reversal in certain periods (Fig. 15, right panel).

The spatial distribution of the rotary coefficients also indicates variations between stratified and mixed periods (Fig. 14). In the stratified period, due to the detachment of the surface layer from the less mobile bottom layer (trapped layer), the cw rotation is more pronounced (the rotary coefficient is about − 0.6). Under a well-mixed condition in January, the tides act in the whole water column, which results in more rectilinear current vectors. The rotary coefficients range from 0 to − 0.2, indicating a low clockwise rotation.

4 Discussion

The analysis reported in this paper is primarily based on the observation by HFR, which is located in the southern GoT. Two radar systems were selected for the analysis of the surface circulation in a region with complicated dynamics associated with the domination of the East Asian monsoon. HFR-derived currents were obtained at high resolution (6 km in a rectangular grid and 1-h time step) using the 2dVar-EOF method. The comparison of the HFR observations and the data from AWAC mooring yields a good correlation (0.7) with acceptable RMSE differences (less than 0.12 m s^{-1}). In our opinion, the variational interpolation of the HFR data (EOF/2dVar) applied to the radial velocity measurements in the GoT provides slightly better results compared with the OMA technique in this region (Table 1). A comparison of two interpolation techniques performed in Bodega Bays, USA (Yaremchuk and Sentchev 2009), supports our conclusion.

The tides in the GoT can be described as a progressive tidal wave propagating northward along the eastern coast (Hainan coast) and propagating southward along the western side (Vietnamese coast) (Nguyen et al. 2014). By analyzing the HFR-derived current in this study, we observed the propagation of the tidal wave more clearly. The tidal wave enters the gulf mainly through the southern entrance and bounds to the east (Hainan Island coast) as a progressive Kelvin wave under the Coriolis forcing effect. The energy of diurnal tides here is already stronger than the semi-diurnal tides (Zu et al. 2008; Chen et al. 2009; Nguyen et al. 2014). The length of the gulf (approximately 500 km) is comparable with the Rossby radius of deformation $\frac{\sqrt{gD}}{f}$, which yields a value of about 400 km (at a latitude of 19° N with a depth of 40 m). Subsequently, the Coriolis force affects the tidal propagation in the GoT. Within the gulf, the tidal wave propagates much slower than in the open ocean, and its energy partly dissipates due to the bottom friction. However, the slow propagation of the tidal wave and

the basin geometry cause the diurnal tides to be resonant and reflected at the northern enclosure of the gulf. The tidal wave then behaves as a combination of the standing wave and progressive wave motions, which is balanced by the Coriolis force, and bounds to the Vietnamese coast in the west and exits the gulf. Consequently, this makes the anticlockwise propagation dominant while the tidal wave propagates along the coasts. The results of the PCA analysis of the current velocities derived from the radar measurements support this consideration.

The result from the tidal harmonic analysis in Section 3.2.2 revealed that tidal motions account for a large percentage of the overall velocity variability. The contribution of the tidal current velocity variability in the GoT is approximately 60%. Therefore, it could be deduced that the residual currents, which includes wind, buoyancy, and, to a minor extent, remote forcing, account for the remaining 40% of the total velocity variability in the GoT.

Seasonal differences in the tidal current amplitudes in summer have been documented by Ding et al. (2013). From the mooring data analysis, the authors revealed that both the diurnal and semi-diurnal tidal ellipse major axes in northern GoT are larger in summer. In our study, the tidal current ellipses provided by the PCA of the velocity measurements did not exhibit noticeable changes in the tidal current amplitude other than the "tidal cross-shore straining" phenomenon due to the stratification of the water column. At the same time, the spectral analysis of basin-wide average HFR-derived current velocities indeed reveals an increase in energy by roughly a half of an order of magnitude at the diurnal and semi-diurnal frequencies during winter. This is contradictory to the finding of Ding et al. (2013) in the northern gulf. The seasonal variability of the tidal currents could be due to the adjustment of the currents to the wind (i.e., sea breeze). In summer, under the effects of the wind, the spectral energy at the diurnal and semi-diurnal frequencies is found to be spread toward lower frequencies. The inertial motions in summer are more energetic due to persistent southwesterly wind in summer, indicating an adjustment of wind-driven currents to wind forcing (Fig. 5c). Contrarily, the inertial peak in the PSD of the currents in winter becomes less significant and shifts toward the sub-inertial band, implying that the inertial oscillations are insignificant during this period.

The large seasonal variability of sea surface currents is associated with the monsoon wind. Wind-driven currents largely contribute to the surface circulation variability in the GoT, as shown by the wind-current correlation analysis. During winter, the northeast wind drives the surface current onshore. In summer, the wind changes to the offshore direction, thus pushing the water offshore. The surface currents veer to the right of the wind, which is in agreement with the Ekman theory, and the water flow is directed eastward to the Hainan coast. The correlation coefficient of the wind and HFR-derived current is found to be high in winter and low in summer. Based on this analysis, we can conclude that the residual current in the southern gulf in winter is primarily generated by strong northeasterly wind. Typically, the response time of the current to the wind is slower under mixed conditions since the flux of the momentum from the atmosphere requires more time to be transferred vertically inside the water column (Dzwonkowski et al. 2009). The zero lag, which is found in the analysis of the wind-surface current correlation in winter, could be the result of the strong wind effect. In the middle of winter (December to January), strong northeasterly wind, which occasionally exceeds 0.1 N m^2, immediately drives the surface current. Contrary to mid-summer, the higher response time (6-h lag) of the surface current to the wind is observed when the freshwater is trapped at the mouth of the Red River (Table 2).

Our analyses revealed a cyclonic circulation structure in the southern gulf throughout the year. Considering the surface current magnitude, the average surface current velocities are generally larger during fall and winter under the effects of strong northeasterly wind than during summer and spring. Moreover, in our analyses, nearshore current velocities observed by HFR are often much larger than those in the middle gulf throughout the whole year. The southward coastal current along the coast is assumed to be a particular feature of the circulation pattern, which was demonstrated in the recent study of the GoT circulation by Rogowski et al. (2019). Also, Manh and Yanagi (2000) had shown that in summer, the tide-induced and density-driven currents have the same southward direction in the southern gulf.

The freshwater discharge from the Red River affects the coastal dynamics and increases the complexity of the current patterns. A portion of the plume in the surface layer (about 5 m thick) is detached from the bottom layer. The coastal current is described as a surface-advected river plume (Mazzini et al. 2014; Mulligan and Perrie 2019). The detached surface velocities are generally larger than those of the bottom layer (Fig. 15). Associated with the down-coast river plume, a frictionless water body, which is forced by the river flow and the strong northeasterly wind, is responsible for the intensification of the coastal current. We demonstrated that the seasonal variability of the nearshore-offshore currents (the coastal current intensity and the asymmetry in Fig. 11) is related to the coupling between wind forcing and freshwater input from rivers along the Vietnamese coast. The onshore flow induced by the NE wind (negative cross-shore velocity) contributes to the intensification of the coastal jet. However, wind forcing alone cannot account for the whole variation of the coastal flow.

The northeasterly wind drives the freshwater plume from the Red River southward during the end of summer to early winter, resulting in the high stratification of the region. Conversely, mixed conditions occur during mid-winter, which coincides with the minimum discharge from the Red River and cooler surface temperature. The large variability of cross-shore tidal shear in the coastal area is observed under

stratified and mixed conditions in October and January, respectively. As the tide takes the form of a progressive Kelvin wave propagating parallel to the shoreline, the tidal currents are rectilinear. The stratification induced from the Red River plume modified the tidal current ellipses polarizations. During the stratified period, the cw rotation of the surface current vectors is enhanced while in the bottom layer, the current vectors rotate ccw. The horizontal tidal shear weakens when mixing occurs and is enhanced under stratified conditions. During mid-winter, the mixing increases due to the strong wind and surface waves, thus tightening the tidal ellipses. Schematically, the mean stratification under low-power-steering input (weaker wind) modifies the polarization of the tidal ellipses and generates a strong cross-shore tidal shear (Souza and Simpson 1996; Simpson and Sharples 2012).

Furthermore, the discharge from the Red River carries large quantities of nutrients and controls the interannual variation of nutrient supply along the coast of GoT (Chen et al. 2009; Loisel et al. 2017). Moreover, it provides large sediment flux into the gulf (Vinh et al. 2014). Knowledge of how freshwater interacts with the coastal circulation in this area and its variation is important to understand the coastal dynamics and thus requires thorough assessment in future studies.

5 Concluding remarks

The spatial and temporal variabilities of the surface circulation in the southern Gulf of Tonkin were assessed using the continuous velocity time series obtained by HFRs during the period of 2014–2016. The large length of the time series and spatial coverage by radar observations, resulting from the application of the variational approach of data processing (EOF/2dVar), enabled the characterization of the current variability spanning from the tidal and sub-tidal frequencies to the annual scale.

Spectral analysis of the velocity time series revealed a pronounced seasonal variability and an energy transfer from large-scale (low-frequency) variability in winter to low-scale (higher frequency) variability in summer. For instance, the wind-induced variability of the surface currents at the diurnal frequency was found to be amplified in summer. The temporal variability of the kinetic energy of the surface currents was found to be tightly correlated with the wind forcing variations.

Our analyses revealed that tidal motions account for a large percentage of surface current variability in the GoT, which is approximately 60% of the overall surface velocity variability. Stratification induced by freshwater input from the Red River affects the tidal currents by modifying the polarization of the tidal ellipses. Moreover, it generates tidal straining within a wide (~ 40 km) coastal region located south of the Red River mouth.

The coastal flow is a prominent feature of the general circulation in the southern GoT. Its width, strength, and mode of variability are largely governed by a combination of freshwater input and wind forcing, particularly the cross-shore wind component. Remote forcing can also affect the coastal current variability, as suggested by Rogowski et al. (2019). However, we did not capture its effect on our observation-based study. The annual variability of the coastal current does not follow a seasonal cycle. The stage of current intensification lasts 8 to 9 months, with larger velocities and seaward extension observed in late fall (September to October) and weaker current (lower velocities) occurring in mid-summer (June to July). It was found that the monsoon atmospheric circulation contributes to the temporal variations of the coastal flow in two ways. The zonal wind component experiences a closely harmonic seasonal variability and induces the cross-shore mass exchange, thus affecting the coastal flow speed and seaward extension. Contrarily, the meridional (along shore) wind component causes a weak modulation of the along-shore current. The Red River discharge, which is characterized by bimodal temporal evolution, affects the coastal current variability and enhances the asymmetry in the current velocity variations.

The obtained data and the results from the database analysis are thought to be useful for further studies of coastal circulation in the GoT, i.e., for the improvement of numerical models and for practical applications related to marine biology, ocean color remote sensing, Search and Rescue (SaR) operations, and management of the marine environment.

Acknowledgments This study was supported by the University of Littoral Côte d'Opale and the Région "Hauts-de-France" PhD fellowship. The study was also partly supported by the Vietnam state-level project KC09.14/16-20. The data set used in this study has been collected in the framework of the US-Vietnam collaboration project: "Gulf of Tonkin Circulation study" (NICOP N62909-15-1-2018), financed by the Office of Naval Research (ONR). We also thank the field team of the CFO for technical assistance. We appreciate the valuable comments from two anonymous reviewers for helping in improving the paper.

Authors' contributions M.C.T. performed the data analysis and wrote the original version of the manuscript. A.S. proposed the ideas and was deeply involved in the analysis, manuscript organization, and co-writing. K.C.N. gave valuable comments and revised the manuscript.

Funding This study was funded by Université du Littoral-Côte d'Opale for PhD scholarship fellowship and partly supported by Vietnam state-level project KC09.14/16-20.

Compliance with ethical standards

Conflict of interest The authors declare that they have no conflict of interest.

References

Bassin CJ, Washburn L, Brzezinski M, McPhee-Shaw E (2005) Submesoscale coastal eddies observed by high frequency radar: a new mechanism for delivering nutrients to kelp forests in the Southern

California Bight. Geophys Res Lett 32(12). https://doi.org/10.1029/2005GL023017

Beardsley RC, & Rosenfeld LK (1981) Introduction to the CODE-1 moored array and large-scale data report, in CODE-1: Moored Array and Large-Scale Data Report

Chen C, Gao G, Qi J, Proshutinsky A, Beardsley RC, Kowalik Z, Lin H, Cowles G (2009) A new high-resolution unstructured grid finite volume Arctic Ocean model (AO-FVCOM): an application for tidal studies. J Geophys Res Oceans 114(C8). https://doi.org/10.1029/2008JC004941

Chen C, Lai Z, Beardsley RC, Xu Q, Lin H, Viet NT (2012) Current separation and upwelling over the southeast shelf of Vietnam in the South China Sea. J Geophys Res Oceans 117(C3). https://doi.org/10.1029/2011JC007150

Chern C-S, Jan S, Wang J (2010) Numerical study of mean flow patterns in the South China Sea and the Luzon Strait. Ocean Dyn 60(5): 1047–1059. https://doi.org/10.1007/s10236-010-0305-3

Ding Y, Chen C, Beardsley RC, Bao X, Shi M, Zhang Y, Lai Z, Li R, Lin H, Viet NT (2013) Observational and model studies of the circulation in the Gulf of Tonkin, South China Sea. J Geophys Res Oceans 118(12):6495–6510. https://doi.org/10.1002/2013JC009455

Dzwonkowski B, Kohut JT, Yan X-H (2009) Sub-inertial characteristics of the surface flow field over the shelf of the central Mid-Atlantic Bight. Cont Shelf Res 29(15):1873–1886. https://doi.org/10.1016/j.csr.2009.07.005

Fujii S, Heron M, Kim K, Lai J-W, Lee S-H, Wu X, Wu X, Wyatt L, Yang W-C (2013) An overview of developments and applications of oceanographic radar networks in Asia and Oceania countries. Ocean Sci J 48:69–97. https://doi.org/10.1007/s12601-013-0007-0

Furgerot L, Sentchev A, Bailly du Bois P, Lopez G, Morillon M, Poizot E, Méar Y, Bennis AC (2020) One year of measurements in Alderney Race: preliminary results from database analysis. Phil Trans R Soc A 378(2178):20190625

Gan J, Li H, Curchitser EN, Haidvogel DB (2006) Modeling South China Sea circulation: response to seasonal forcing regimes. J Geophys Res Oceans 111(C6). https://doi.org/10.1029/2005JC003298

Gao J, Xue H, Chai F, Shi M (2013) Modeling the circulation in the Gulf of Tonkin, South China Sea. Ocean Dyn 63(8):979–993. https://doi.org/10.1007/s10236-013-0636-y

Gao JS, Chen B, Shi MC (2015) Summer circulation structure and formation mechanism in the Beibu Gulf. Sci China Ser D-Earth Sci 58: 286–299

Gao J, Wu G, Ya H (2017) Review of the circulation in the Beibu Gulf, South China Sea. Cont Shelf Res 138:106–119. https://doi.org/10.1016/j.csr.2017.02.009

IMHEN & UNDP (2015) Vietnam special report on managing the risks of extreme events and disasters to advance climate change adaptation (VN-SREX). Website: http://www.imh.ac.vn/. ISBN 978-604-904-623-0

Kaplan DM, Lekien F (2007) Spatial interpolation and filtering of surface current data based on open-boundary modal analysis. J Geophys Res Oceans 112(C12). https://doi.org/10.1029/2006JC003984

Kim SY, Terrill EJ, Cornuelle BD (2008) Mapping surface currents from HF radar radial velocity measurements using optimal interpolation. J Geophys Res Oceans 113(C10). https://doi.org/10.1029/2007JC004244

Kundu PK (1976) Ekman veering observed near the ocean bottom. J Phys Oceanogr 6(2):238–242. https://doi.org/10.1175/1520-0485(1976)006<0238:EVONTO>2.0.CO;2

Large WG, Pond S (1981) Open Ocean momentum flux measurements in moderate to strong winds. J Phys Oceanogr 11(3):324–336. https://doi.org/10.1175/1520-0485(1981)011<0324:OOMFMI>2.0.CO;2

Liu FS, Yu TC (1980) Preliminary study on the oceanic circulation in Beibu Bay. Trans Oceanol Limnol 1, 9–15, (in Chinese with English abstract)

Liu Y, Weisberg RH, Merz CR (2014) Assessment of CODAR SeaSonde and WERA HF radars in mapping surface currents on the West Florida Shelf. J Atmos Ocean Technol 31(6):1363–1382. https://doi.org/10.1175/JTECH-D-13-00107.1

Loisel H, Vantrepotte V, Ouillon S, Ngoc DD, Herrmann M, Tran V, Mériaux X, Dessailly D, Jamet C, Duhaut T, Nguyen HH, Van Nguyen T (2017) Assessment and analysis of the chlorophyll-a concentration variability over the Vietnamese coastal waters from the MERIS ocean color sensor (2002–2012). Remote Sens Environ 190:217–232. https://doi.org/10.1016/j.rse.2016.12.016

Lopez G, Bennis A-C, Barbin Y, Sentchev A, Benoit L, Marié L (2020) Surface currents in the Alderney race from high-frequency radar measurements and three-dimensional modelling. Philos Trans R Soc A Math Phys Eng Sci 378(2178):20190494. https://doi.org/10.1098/rsta.2019.0494

Manh D-V, Yanagi T (2000) A study on residual flow in the Gulf of Tongking. J Oceanogr 56(1):59–68. https://doi.org/10.1023/A:1011162524466

Mazzini PLF, Barth JA, Shearman RK, Erofeev A (2014) Buoyancy-driven coastal currents off Oregon during fall and winter. J Phys Oceanogr 44(11):2854–2876. https://doi.org/10.1175/JPO-D-14-0012.1

Mulligan RP, Perrie W (2019) Circulation and structure of the Mackenzie River plume in the coastal Arctic Ocean. Cont Shelf Res 177:59–68. https://doi.org/10.1016/j.csr.2019.03.006

Nguyen NM, Patrick M, Florent L, Sylvain O, Gildas C, Damien A, Van Uu D (2014) Tidal characteristics of the gulf of Tonkin. Cont Shelf Res 91:37–56. https://doi.org/10.1016/j.csr.2014.08.003

Paduan JD, Washburn L (2013) High-frequency radar observations of ocean surface currents. Annu Rev Mar Sci 5(1):115–136. https://doi.org/10.1146/annurev-marine-121211-172315

Pawlowicz R, Beardsley B, Lentz S (2002) Classical tidal harmonic analysis including error estimates in MATLAB using T_TIDE. Comput Geosci 28(8):929–937. https://doi.org/10.1016/S0098-3004(02)00013-4

Piton V, Herrmann M, Lyard F, Marsaleix P, Duhaut T, Allain D, Ouillon S (2020) Sensitivity study on the main tidal constituents of the Gulf of Tonkin by using the frequency-domain tidal solver in T-UGOm. Geosci Model Dev 13(3):1583–1607. https://doi.org/10.5194/gmd-13-1583-2020

Rogowski P, Zavala-Garay J, Shearman K, Terrill E, Wilkin J, Tran HL (2019) Air-sea-land forcing in the Gulf of Tonkin: assessing seasonal variability using modern tools. Oceanography 32(2):150–161

Sentchev A, Forget P, Barbin Y (2009) Residual and tidal circulation revealed by VHF radar surface current measurements in the southern Channel Isles region (English Channel). Estuar Coast Shelf Sci 82(2):180–192. https://doi.org/10.1016/j.ecss.2008.12.003

Sentchev A, Forget P, Barbin Y, Yaremchuk M (2013) Surface circulation in the Iroise Sea (W. Brittany) from high resolution HF radar mapping. J Mar Syst 109–110:S153–S168. https://doi.org/10.1016/j.jmarsys.2011.11.024

Simpson JH, Sharples J (2012) Introduction to the physical and biological oceanography of shelf seas. Cambridge University Press, Cambridge Core. https://doi.org/10.1017/CBO9781139034098

Simpson JH, Brown J, Matthews J, Allen G (1990) Tidal straining, density currents, and stirring in the control of estuarine stratification. Estuaries 13(2):125–132. https://doi.org/10.2307/1351581

Souza AJ, Simpson JH (1996) The modification of tidal ellipses by stratification in the Rhine ROFI. Cont Shelf Res 16(8):997–1007. https://doi.org/10.1016/0278-4343(95)00042-9

Stewart RH, Joy JW (1974) HF radio measurements of surface currents. Deep-Sea Res Oceanogr Abstr 21(12):1039–1049. https://doi.org/10.1016/0011-7471(74)90066-7

Thiébaut M, Sentchev A (2017) Asymmetry of tidal currents off the W.Brittany coast and assessment of tidal energy resource around

the Ushant Island. Renew Energy 105:735–747. https://doi.org/10.1016/j.renene.2016.12.082

Vinh, V. D., Ouillon, S., Thanh, T. D., & Chu, L. V. (2014). Impact of the Hoa Binh dam (Vietnam) on water and sediment budgets in the Red River basin and delta. Hydrology and Earth System Sciences, 18(10), 3987–4005. https://doi.org/10.5194/hess-18-3987-2014

Yaremchuk M, Sentchev A (2009) Mapping radar-derived sea surface currents with a variational method. Cont Shelf Res 29(14):1711–1722. https://doi.org/10.1016/j.csr.2009.05.016

Yaremchuk M, Sentchev A (2011) A combined EOF/variational approach for mapping radar-derived sea surface currents. Cont Shelf Res 31(7–8):758–768. https://doi.org/10.1016/j.csr.2011.01.009

Ye AL, Robinson IS (1983) Tidal dynamics in the South China Sea. Geophys J Int 72(3):691–707. https://doi.org/10.1111/j.1365-246X.1983.tb02827.x

Yoshikawa Y, Matsuno T, Marubayashi K, Fukudome K (2007) A surface velocity spiral observed with ADCP and HF radar in the Tsushima Strait. J Geophys Res Oceans 112(C6). https://doi.org/10.1029/2006JC003625

Zu, T., Gan, J., & Erofeeva, S. Y. (2008). Numerical study of the tide and tidal dynamics in the South China Sea. Deep Sea Research Part I: Oceanographic Research Papers, 55(2), 137–154. https://doi.org/10.1016/j.dsr.2007.10.007

Chapter IV. Transport processes and turbulent dispersion in the Gulf of Tonkin

4.1. Introduction

Motivation for the article

Mapping the transport pathway of particulate materials floating with the ocean currents, dispersion of pollutants, micro-plastics, and other tracers, etc., is a great challenge in oceanography since the oceanic flows are turbulent on many levels. Turbulent motions, arising from the interaction of different physical processes and spanning a wide range of spatial and temporal scales, govern the transport of oceanic tracers. In the coastal regions with more complex bathymetry and shoreline, turbulent motions can be significantly amplified, thus, affecting the spatial distribution of tracers. Therefore, understanding how the distribution of materials varies in space and time in the flow field is important for a number of practical applications, for example, oil spills, transport of larvae or marine debris, etc.

This issue is naturally approached using the Lagrangian framework, i.e., by analyzing the trajectories of ocean fluid parcels or real drifters, both considered as "particles" evolving in the water media. From the Lagrangian point of view, the relative separation of the particle pairs is an important quantity that can describe the rate of mixing of tracers in a turbulent flow field. The assessment of relative dispersion can be also used to inspect the flow field variability in a wide range of scales and shed light on the dominant physical process behind certain scales of motions (Berti et al., 2011; Haza et al., 2008; LaCasce, 2008; Meyerjürgens et al., 2020; Ohlmann et al., 2012; Poje et al., 2010). In addition, to the best of our knowledge, the issue of relative dispersion at regional scale has not been addressed yet in this part of the VNES/SCS.

Therefore, we addressed this issue and performed the assessment of turbulent properties of the flow field using radar measurements and a realistic numerical model, both coupled with a Lagrangian transport model. These tools (described in detail in section 2.3.2) provided a number of Lagrangian diagnostics used for characterizing the transport patterns and dispersal of materials in this region. Three main objectives were identified in this chapter: (i) Assessment of the capability of the numerical model (SYMPHONIE model) to represent fine-scale dynamic processes in the GoT, (ii) Estimation of scaling properties of particle pairs separation for a better understanding of the scale of motions and

dispersion regimes and (iii) Characterization of the physical processes that significantly impact the turbulent dispersion in the GoT.

Methods of analysis

In practice, a fully experimental assessment of turbulent dispersion at regional scales is difficult to realize due to the cost of such experiments (deployment and localization of hundreds of drifters for a long period of time). In this work, we investigated the transport patterns of materials and turbulent dispersion using synthetic drifters advected in the velocity field derived from the HF radar measurements and high-resolution numerical model. Compared to radar measurements, the numerical model provides the velocity field in the whole GoT, with higher resolution (300 m), close to the Vietnamese coast, and overcomes the limitations of radar measurements (limited space coverage and coarse (~6 km) resolution). In the first step, the model simulations were extensively validated using the available HF radar measurements, historical *in-situ* data, and satellite observations. Details of the validation are given in Piton et al. (2021) and Nguyen-Duy et al. (2021).

The Lagrangian approach, based on two-particle statistics, is used to assess the dispersion properties and to investigate the interaction between different scales of motions in the GoT: from small scale (sub-mesoscale) to large scale (mesoscale). The Lagrangian quantities that we analyzed include the relative dispersion, relative diffusivity and Finite Size Lyapunov Exponent (FSLE) estimates. The particle tracking experiments were performed during two periods, August and November 2015, which represent two monsoon seasons, summer and winter characterized by a significant freshwater discharge.

Results

Regarding the quantification of the dispersion regime at scales larger than 20 km, the results revealed a good consistency for both types of velocity fields available in the GoT (radar-derived and model velocity field). This proves the model capability to reproduce turbulent motions and generate turbulent dispersion in the mesoscale range. However, the exploration of smaller scale motions in the region is prohibited by too coarse resolution of the radar velocity fields (~6 km). The dispersion rate estimated using the radar velocities was two times lower than that obtained from the model in this part of the GoT.

In the second step, particle tracking experiments using numerical simulations only were performed for further characterization of seasonal variability in transport patterns and dispersion regimes in the whole gulf. The results revealed the Richardson super diffusion regime in summer, and ballistic regime in winter. Both regimes characterize the local dispersion dominating in the mesoscale range,

i.e., dispersion generated by eddies of size lying in the range from 20 to 70 km. The change in dispersion regime was tightly correlated to a combined effect of river discharge and summer monsoon wind which enlarges the river plume area and enhances stirring in the coastal region extending up to 100 km offshore. On the other hand, during winter, the coastal current was active and strengthened the local dispersion in the nearshore region. Additionally, our analysis revealed four regions of high dispersion level (and large horizontal mixing) that should be considered as hotspots where the local hydrodynamics and velocity variability have a strong influence on the particulate material distribution, and therefore on marine ecology. We consider that our results provided a reference for further analysis of turbulent dispersion regimes in this geographic region, poorly covered by observations and in other coastal regions.

The results of the study are presented in the research article: "Assessment of relative dispersion in the Gulf of Tonkin using numerical modeling and HF radar observations of surface currents" published in Continental Shelf Research journals. https://doi.org/10.1016/j.csr.2022.104784.

Additionally, a part of the work was integrated to the papers published in 2021:

Piton, V., Herrmann, M., Marsaleix, P., Duhaut, T., Ngoc, T. B., Tran, M. C., Shearman, K., & Ouillon, S. (2021). Influence of winds, geostrophy and typhoons on the seasonal variability of the circulation in the Gulf of Tonkin: A high-resolution 3D regional modeling study. *Regional Studies in Marine Science*, *45*, 101849. https://doi.org/10.1016/j.rsma.2021.101849

Nguyen-Duy, T., Ayoub, N. K., Marsaleix, P., Toublanc, F., De Mey-Frémaux, P., Piton, V., Herrmann, M., Duhaut, T., Tran, M. C., & Ngo-Duc, T. (2021). Variability of the Red River Plume in the Gulf of Tonkin as Revealed by Numerical Modeling and Clustering Analysis. In *Frontiers in Marine Science* (Vol. 8, p. 1636). https://www.frontiersin.org/article/10.3389/fmars.2021.772139

4.2. The article

Continental Shelf Research 245 (2022) 104784

Contents lists available at ScienceDirect

Continental Shelf Research

journal homepage: www.elsevier.com/locate/csr

Assessment of relative dispersion in the Gulf of Tonkin using numerical modeling and HF radar observations of surface currents

Manh Cuong Tran [a,b,e,*], Alexei Sentchev [a,e], Stefano Berti [c], Nadia K. Ayoub [d,e], Tung Nguyen-Duy [d,e], Nguyen Kim Cuong [f]

[a] Laboratory of Oceanology and Geosciences, UMR 8187, CNRS, Univ. Littoral Côte d'Opale, Univ. Lille, IRD, 62930, Wimereux, France
[b] Center for Oceanography (CFO), Vietnam Administration of Seas and Islands (VASI), 8 Phao Dai Lang, Dong Da, Hanoi, Viet Nam
[c] Univ. Lille, ULR 7512, Unité de Mécanique de Lille Joseph Boussinesq (UML), 59000, Lille, France
[d] LEGOS, UMR5566, IRD, CNES, CNRS, Université de Toulouse, 31400, Toulouse, France
[e] LOTUS Laboratory, University of Science and Technology of Hanoi, Vietnam Academy of Science and Technology, Hanoi, Viet Nam
[f] VNU University of Science, Vietnam National University, 334 Nguyen Trai, Thanh Xuan, Hanoi, Viet Nam

ARTICLE INFO

Keywords:
Relative dispersion
Scale of motion
HF radar measurements
Numerical modeling
Gulf of Tokin

ABSTRACT

Particle pair statistics from synthetic drifter trajectories reconstructed from realistic, high-resolution numerical simulations (SYMPHONIE model) and HF radar velocity measurements are used to investigate the dispersion properties in the Gulf of Tonkin (GoT). This study takes an approach based on two-particles statistics providing the relative dispersion, relative diffusivity and Finite Size Lyapunov Exponent (FSLE) estimates. In the GoT, the relative dispersion follows the predictions from the theory of two-dimensional turbulence with two inertial subranges identified in the kinetic energy spectrum with the spectral slopes −5/3 and −3. The time evolution of dispersion shows an exponential growth during 5–8 days, followed by a power law regime during the next 6–20 days. Fixed-length indicators from the relative diffusivity and the FSLE reveal a local dispersion at large and intermediate scales (above Rossby radius of deformation) and non-local dispersion in sub-mesoscale range (below Rossby radius of deformation). The effect of river runoff on the local hydrodynamics and dispersion processes is assessed using the numerical model simulations without river discharge. The results show that in the model, the river plume, when present, highly impacts the Lagrangian statistics. High gradients of buoyancy reinforce the sub-mesoscale circulation in a large region along the Vietnamese coast and modify the scales and intensity of turbulent dispersion. However, a clear change of dispersion regime in the sub-mesoscale range is not identified, suggesting that the mesoscale circulation in the GoT largely governs particle spreading even at small scale.

1. Introduction

Transport and dispersion processes in the ocean have practical importance since they play a major role in the functioning of marine ecosystems by carrying physical and chemical quantities such as heat, salt, nutrients, as well as biological relevant tracers, matter and marine debris. For example, in the North Sea, the transport of the flatfish larvae from the spawning areas to the nurseries and mortality rate are heavily impacted by the hydrodynamics processes and the environmental factors (Lacroix et al., 2013). In the coastal zone, the knowledge of transport properties is even more important for assessing the dispersal of anthropogenic pollutant tracers released accidently (Corrado et al., 2017). Mapping the transport pathways of materials advected by ocean currents is of great interest for understanding the interconnection between geographical regions (Haza et al., 2010; van Sebille et al., 2011, 2015), physical and relevant biogeochemical processes (d'Ovidio et al., 2015). However, prediction of the Lagrangian transport remains challenging since the oceanic flow is turbulent in a wide range of spatial and temporal scales. The oceanic coherent structures, which we refer to as jets, eddies, fronts, arise from multi-scale interactions of physical processes in the ocean and at its interfaces with the atmosphere and the continent. The instabilities of these structures, due to the flow turbulence or episodic forcing (e.g., wind), result in chaotic motions and may dictate the transport statistics (Haza et al., 2016).

* Corresponding author. Laboratory of Oceanology and Geosciences, UMR 8187, CNRS, Univ. Littoral Côte d'Opale, Univ. Lille, IRD, 62930, Wimereux, France.
E-mail address: manh-cuong.tran@univ-littoral.fr (M.C. Tran).

https://doi.org/10.1016/j.csr.2022.104784
Received 9 March 2022; Received in revised form 26 May 2022; Accepted 9 June 2022
Available online 11 June 2022
0278-4343/© 2022 Elsevier Ltd. All rights reserved.

Lagrangian framework is naturally linked to the investigation of transport since the Lagrangian observations track the fluid parcels and sample the spatiotemporal evolution of their properties rather than measuring them at a fixed point in the Eulerian approach (Essink et al., 2019). Trajectory maps can provide the details of the circulation and dispersion of materials in the flow field. Since an individual trajectory in the turbulent flow field is largely unpredictable and depends strongly on the initial conditions, the ensemble average over many trajectories is needed to provide the statistical description of the flow field (LaCasce, 2008; Essink et al., 2019).

Characteristics of the oceanic turbulent flow based on the Lagrangian approach have been described in many studies, e.g., in the North Atlantic (Lumpkin & Elipot, 2010), in the South Atlantic, (Berti et al., 2011), in the Nordic Seas (Koszalka et al., 2009), in the Gulf of Mexico (LaCasce & Ohlmann, 2003; D'Asaro et al., 2018), and in the Mediterranean Sea (Haza et al., 2010; Schroeder et al., 2011, 2012; Hernández-Carrasco et al., 2018a). These studies aimed to explore how pollutants or biological tracers disperse in the marine environment and how the energy is transferred across scales of motion. The relative dispersion, which might be estimated from the mean squared separation of particle pairs, is used to characterize the underlying turbulent flow field. Among the Lagrangian statistics, pair dispersion gains importance since the spreading rate of pairs of particles is sensitive to the amount of energy distribution within different scales. The spreading of particle pairs depends, in principle, on the velocity difference at the length scale corresponding to the pair separation distance (Lumpkin & Elipot, 2010). Therefore, the statistics based on relative dispersion are useful for the assessment of mixing in the turbulent flow field at small and intermediate scales and can characterize the most important physical processes controlling the underlying fluid motions (Meyerjürgens et al., 2020).

The relationship between the oceanic turbulent flow and the relative dispersion statistics has been extensively discussed (see, e.g., LaCasce, 2008; Foussard et al., 2017; Berti and Lapeyre, 2021). It was shown that the dispersion properties can be theoretically predicted from the kinetic energy spectrum, $E(k) \sim k^{-\beta}$, of the underlying flow field. Specifically, the relative dispersion can be either local if $1 < \beta < 3$, or non-local, in the case of $\beta \geq 3$. In a number of studies using the relative dispersion statistics (Koszalka et al., 2009; Lumpkin & Elipot, 2010; Poje et al., 2014; van Sebille et al., 2015; Sansón et al., 2016; Beron-Vera and LaCasce 2016; Corrado et al., 2017; Essink et al., 2019), the geographic dependency of the stirring regime is found across different ocean regions. Contradictory results in some regions have been reported revealing a non-local dispersion regime at scales below the Rossby radius of deformation and local dispersion in the same scale range. For example, Meyerjürgens et al. (2020) identified significantly different dispersion regimes in the vicinity of the tidal front in the North Sea. Scaling of the relative dispersion indicated a non-local dispersion regime while the Finite Size Lyapunov Exponent (FSLE) showed a local dispersion. At large spatial scales, the existence of different dispersion regimes was revealed. In some studies (e.g., Schroeder et al., 2011), a transition to the diffusive regime was identified in the Liguro-Provençal basin, whereas other studies indicated a Richardson-like dispersion, most likely due to the effect of large-scale velocity shear observed in the Gulf of Mexico (e.g., LaCasce & Ohlmann, 2003). In addition, characterization of the dispersion regime based on the observations from drifting buoys alone is practically difficult and requires many pairs of Lagrangian drifters whose number is always limited in ocean regions. The lack of observations leads to differences in assessment of the dispersion regime in the world oceans (i.e., Haza et al., 2008; Schroeder et al., 2012). Recently, advances in observations of ocean dynamics by remote sensing techniques such as altimetry, coastal radars, etc., and the improvement in the ocean modeling accuracy have opened new opportunities for assessment of the oceanic dispersion properties (using synthetic drifters).

The present study is performed in the Gulf of Tonkin (GoT), a shallow, semi-isolated gulf, located in the northwestern part of the South China Sea (Fig. 1). As demonstrated in recent studies, the hydrodynamics in the GoT is controlled by the Asian monsoon system, complex bathymetry and exchanges with the South China Sea in the south and through the Hainan Strait (e.g., Tran et al., 2021; Piton et al., 2021; Rogowski et al., 2019). The freshwater input from the Red River impacts the hydrology and circulation along the Vietnamese coast with a strong seasonality as shown recently for instance by Nguyen-Duy et al. (2021). In coastal and shallow-water seas, a combination of tidal and wind forcing, in conjunction with complex topography, can lead to the formation of sub-mesoscale eddies (e.g., Zimmerman, 1981). Additionally, large freshwater discharge enhances the density gradients and can also generate sub-mesoscale motions that play an important role in organizing the flow structures and material transport.

In this work, we employ the realistic, high-resolution numerical model SYMPHONIE and velocity measurements by high-frequency radars to investigate the dispersion properties of the flow field. We adopt an approach based on particle pairs statistics to quantify different scales of the flow field variability and associated dispersion regimes, in the GoT. This article is organized as follows. In section 2, we briefly describe the data and methods used for dispersion quantification. The description of the flow fields during two selected periods is given in section 3. In section 4, results of the assessment of the turbulent dispersion based on the coastal radar velocity measurements and the numerical model simulations are presented. We also assess the effect of river discharge on the Lagrangian statistics. We discuss the results in section 5 and summarize them in section 6.

2. Materials and methods

2.1. HF radar velocity measurements

The velocity data were acquired at two radar sites, Nghi Xuan (XUAN, 105.82 °E, 18.62 °N) and Dong Hoi (DHOI, 106.64 °E, 17.47 °N), which have been operating within the GoT since 2012 (Fig. 1). The radar network was configured to operate at a frequency of 4.625 MHz (which was changed to 5.25 MHz in 2018). The radial velocity component is measured by the radars at the effective depth of ~2 m with an instrumental error of ~0.07 m s^{-1}. The following configuration has been

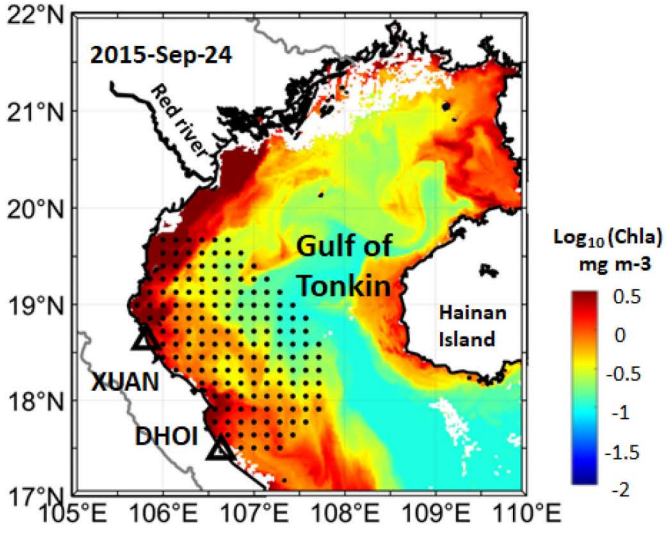

Fig. 1. Study region – the Gulf of Tonkin. Location of HF radars sites is indicated by triangles. Black dots show the radar coverage adopted in the study. The dot spacing is 12 km. Color shading represents a snapshot of Chl-a concentrations (in $\log_{10}$ scale) obtained from the Aqua/MODIS sensor on September 24, 2015. High Chl-a concentration patterns, extending from the nearshore blooming region seaward, are visible through the elongated filaments and small eddies.

used at each radar site to retrieve the radial velocities of the surface currents: 5.8 km along the beam and azimuthal spacing 5°. The temporal resolution was set to 1 h. The HFR total velocities were mapped using EOF/Variational interpolation method (Yaremchuk and Sentchev, 2011). The resulting product consists of hourly maps of two current velocity components (zonal and meridional) on a regular 6-km grid as described in Tran et al. (2021).

2.2. Numerical model configuration

We use the numerical simulations of Nguyen-Duy et al. (2021) made with SYMPHONIE model. SYMPHONIE is a hydrostatic numerical model which solves the primitive equations on a curvilinear bipolar Arakawa C-grid with regular sigma vertical levels (Marsaleix et al., 2006, 2008). A description of the model configuration is given in Nguyen-Duy et al. (2021) and we only recall here the characteristics relevant to this study. The grid covers the whole GoT with a highly variable horizontal resolution, from ~300 m along the Vietnamese coast and the Red River delta region, to about 1.5–2 km in the middle Gulf, and reaching the maximum, 4.5 km, at the southern open boundary (see Fig. 2A in Nguyen-Duy et al., 2021). The water column is discretized onto 20 sigma levels.

The bathymetry is reconstructed from GEBCO 2014 combined with other sources and field surveys in order to characterize the complex topography, with many islands and islets located within the region and especially the coastal area adjacent to the Red River delta (Piton et al., 2020). Intertidal areas are simulated with a wetting and drying scheme. The k-ε turbulence closure scheme is implemented as in Michaud et al. (2012).

Tidal motions at the open boundaries are prescribed from the sea surface elevation and barotropic currents of 9 tidal constituents from the FES2014 atlas (Lyard et al., 2021). The tidal astronomical potential is also considered at every grid point of the model. In addition, the 1/12° spatial resolution, daily averaged sea surface height (SSH), velocity components, temperature and salinity provided by the Copernicus Marine Systems (CMEMS) global model are also used at the boundaries.

At the sea surface, the boundary conditions include the 3-hourly data for wind, precipitation, solar energy, atmospheric temperature and pressure from the Operational ECMWF product. The fluxes of momentum, heat, and freshwater are computed internally in the model using the bulk formulae of Large and Yeager (2004).

In the reference simulation (hereafter GoT-Ref), the river discharge from 16 rivers is introduced in the model and configured as realistically as possible according to the method described in Nguyen-Duy et al. (2021). Daily freshwater runoff is used from the main seven distributaries of the Red River. For other rivers, climatological data are used. An additional configuration without the river discharge (GoT-noriv configuration, see Nguyen-Duy et al., 2021) is used to assess the effect of rivers discharge on the dispersion properties.

The model was extensively validated over the period 2011–2016 and the results of the validation are given in Piton et al. (2021) and Nguyen-Duy et al. (2021). In our study, we performed an additional comparison of the model simulation with the current velocity derived from HFR measurements for two periods: August and November 2015 (Fig. 2). The correlation between the current velocity derived from both data sources remains larger than 0.7 with a slightly higher value obtained in November (0.85). A relative difference of about 6–10% quantifies the disagreement between the HFR data and the numerical simulations, for both the latitudinal (u) and longitudinal (v) velocity components. The model velocities were found to be slightly smaller than those derived from HFR measurements.

2.3. Lagrangian diagnostics

In this study, we used the velocity data from the model simulation covering one-year long period in 2015. Virtual particles organized in clusters were advected using OceanParcels Lagrangian framework (https://oceanparcels.org) by the velocity field from the model at 1 h resolution. These Lagrangian tracers were uniformly distributed in the surface layer at 2 m depth. Each cluster included one center particle and two satellite pairs along x- (longitude) and y-axis (latitude) with the initial separation $\delta_0 = 0.5$ km. The clusters were seeded every 2 km

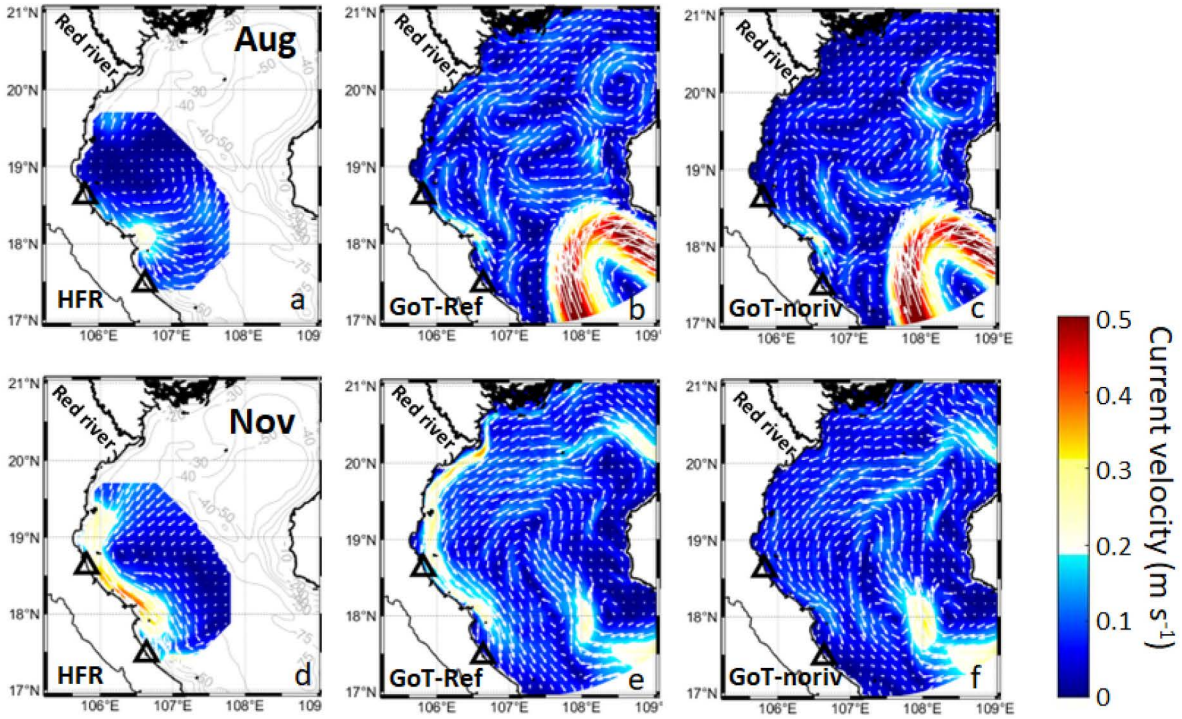

Fig. 2. 30-day mean surface currents in the GoT from HFR measurements (a, d) and numerical model in two configurations: with river discharge (b, e) and without river discharge (c, f) in August and November 2015. The current vectors are interpolated on a regular grid and plotted every 15 km.

across the domain in order to keep the initial pair separation as low as possible and not to exceed a reasonable computational cost. The particles are advected horizontally using the 4th order Runge-Kutta scheme.

In this study, we focus on assessing the statistics of Lagrangian particle pairs advected in the flow fields derived from the HFR measurements and the model simulation during two seasons (summer and late fall). The Lagrangian quantities analyzed include the relative dispersion, relative diffusivity and Finite Size Lyapunov Exponent (FSLE).

The relative dispersion is a common metric for assessing the dispersion of tracers. It is defined as the average, over all particle pairs, of the squared separation between particles i and j in a pair at time t:

$$\delta^2(t) = \frac{1}{N(N-1)} \sum_{ij}^{N} \left\| \overrightarrow{x_i}(t) - \overrightarrow{x_j}(t) \right\|^2 \quad (1)$$

where N is the number of particles. The pairs were identified using the particles with initial separations below 2 km. The relative dispersion behavior depends on the level of turbulence in the flow field. The latter is reflected in the kinetic energy spectrum which shows a power law distribution as a function of the (horizontal) wavenumber $k = |\overrightarrow{k}|$: $E(k) \simeq k^{-\beta}$. At the early stage, when the pair separation is small, the particle pair velocities are close and the growth of relative dispersion follows a ballistic behavior, $\delta^2 \sim t^2$. At larger time scales, relative dispersion grows exponentially in the case of non-local dispersion, when $\beta > 3$. Otherwise, if $1 < \beta < 3$, relative dispersion is local and scales as a power law $\delta^2 \simeq t^{\frac{4}{(3-\beta)}}$ (Foussard et al., 2017). Richardson super diffusive regime corresponds to $\delta^2 \sim t^3$ where the pair separation is controlled by eddies with a size similar to the separation distance of particles. When the particle separation reaches scales much larger than the largest characteristic flow scale, the pair velocities are considered uncorrelated. Relative dispersion in this case is expected to scale as $\delta^2 \simeq t$, corresponding to a diffusive behavior.

In addition, we diagnose the relative diffusivity κ, which represents the growth rate of the average squared separation. This quantity is defined as the time derivative of relative dispersion,

$$\kappa = \frac{1}{2} \frac{d\delta^2(t)}{dt} \quad (2)$$

and it can be useful to assess the mixing properties and the corresponding spreading regime. For this purpose, it is often interesting to consider κ as a function of the separation distance δ, rather than of time. Depending on the shape of the given kinetic energy spectrum, $\kappa(\delta)$ scales as δ^2 for the non-local dispersion regime and as $\delta^{4/3}$ (when $\beta = 5/3$) for the local dispersion one.

The third quantity, the Finite Size Lyapunov Exponent (FSLE), is estimated by measuring the time τ, averaged over all particle pairs, needed to separate particles in a pair from a distance δ_k to a distance $\delta_{k+1} = r\,\delta_k$, with $r > 1$ ($k = 1, \ldots, N_k$ and N_k is the number of bins chosen in a way to span the relevant range of scales):

$$\lambda = \frac{ln(r)}{\tau} \quad (3)$$

Values of FSLE can be used to distinguish a local regime of dispersion from a non-local one (Schroeder et al., 2011). Compared to relative dispersion, the FSLE, being a fixed-length (instead of fixed-time) indicator, better allows to disentangle contributions from turbulent features of different size (Artale et al., 1997). We implemented a method called fastest-crossing for the computation of the FSLE (Lumpkin & Elipot, 2010). A sensitivity study of the results to the choice of r was performed with the fixed number of particles in the area. It was found that varying r from 1.2 to 1.6 does not change the FSLE slope considerably (Poje et al., 2014) and the value of $r = 1.4$ was chosen. The Lyapunov exponent quantifies the exponential rate of separation and is often used for the identification of the non-local regime of pair separation (Haller and Yuan, 2000). At very small separations, the FSLE is expected to recover such, scale-independent, value. The behavior of the FSLE in a turbulent flow field with spectrum $E(k) = k^{-5/3}$ typically is as follows: $\lambda \simeq$ constant (exponential growth and non-local dispersion regime) at very small scales, $\lambda \simeq \delta^{-2/3}$ for local dispersion (Richardson regime) in the inertial range and $\lambda \simeq \delta^{-2}$ for the diffusive regime expected at separations much larger than the largest flow scales (Berti et al., 2011; Corrado et al., 2017). A ballistic regime $\lambda \sim \delta^{-1}$ can also be expected in the presence of intense mean currents.

2.4. Horizontal stirring from FSLE maps

In addition, the spatial distribution of FSLEs has been obtained for two selected periods representing two seasons (in August and November). The backward FSLE calculations were performed for 30 days with a time step of 1 h, following the method proposed by d'Ovidio et al. (2004). The advantage of this technique is to restrict the analysis of dispersion within relevant structures among selected length scales. The optimum choice for the spatial FSLE amplification factor δ_f/δ_i was discussed several times in previous studies Haza et al. (2010); Berta et al. (2014). We compute the exponential growth rate, $\lambda(x)$:

$$\lambda(x) = \frac{1}{\tau(x)} ln\left(\frac{\delta_f}{\delta_i}\right) \quad (4)$$

in analogy with Eq. (3), with $\delta_i \simeq 1.86$ km and $\delta_f = 13$ km. Such values of δ_i and δ_f allow to adequately visualize the relevant coherent structures and transport patterns associated with small-scale processes.

3. Description of the Eulerian flow fields

Fig. 2 shows the 30-days averaged surface current fields from the HF radar measurements and from model simulations in August and November. During summer, the prevailing wind is from the southwest direction and remains persistent until September 12 when a typhoon hits the region. Interestingly, during August, the surface currents from the model show a pronounced northeast flow in the northern part of the gulf above 19°N roughly follows the 50 m isobath. This flow is partly captured in the northern part of the radar field (Fig. 2a). During November, the wind changes to northeasterly with larger speed. The surface currents demonstrate a typical winter pattern with a gulf-scale cyclonic circulation, an intense coastal current in the western part (Fig. 2 d, e), and several energetic jets with mean velocity of 0.3 m s^{-1}. The lack of river discharge in the model leads to the decrease of the surface current velocity (by roughly 0.1 m s^{-1}) in the vicinity of the Red river mouth in August (Fig. 2b and c) and large reduction of the southward coastal jet in November (Fig. 2f).

While the mean current patterns look similar for the three velocity fields, the gradients of the flow field, which control the separation process of the advected Lagrangian particles, appear different. The horizontal flow field and its small-scale content can be inspected from the snapshots of relative vorticity, $\zeta = \frac{\partial v}{\partial x} - \frac{\partial u}{\partial y}$, normalized by the Coriolis frequency f (Fig. 3). A comparison with the Okubo-Weiss parameter, which is also commonly used to quantify the regions dominated by either strain or vorticity reveals that the two quantities are similar (not shown). However, relative vorticity is more suitable to present a larger number of coherent structures of different size in the flow field: from a large-scale structure induced by the incoming current from the open sea that occupies the southern area in August, to abundant thin filaments and small vortices across the gulf with the size from few to tens of km. Additionally, the vorticity distribution in the GoT was compared to the normalized divergence, div/f, which also controls the separation of drifting particles by enhancing vertical motions and generating clustering effects. Globally, the spatial distribution of both quantities reveals a similarity. However, much weaker values of the divergence field, more affected by noise, make the results difficult to interpret (not shown).

The magnitude of vorticity field shown in Fig. 3 can reach values of

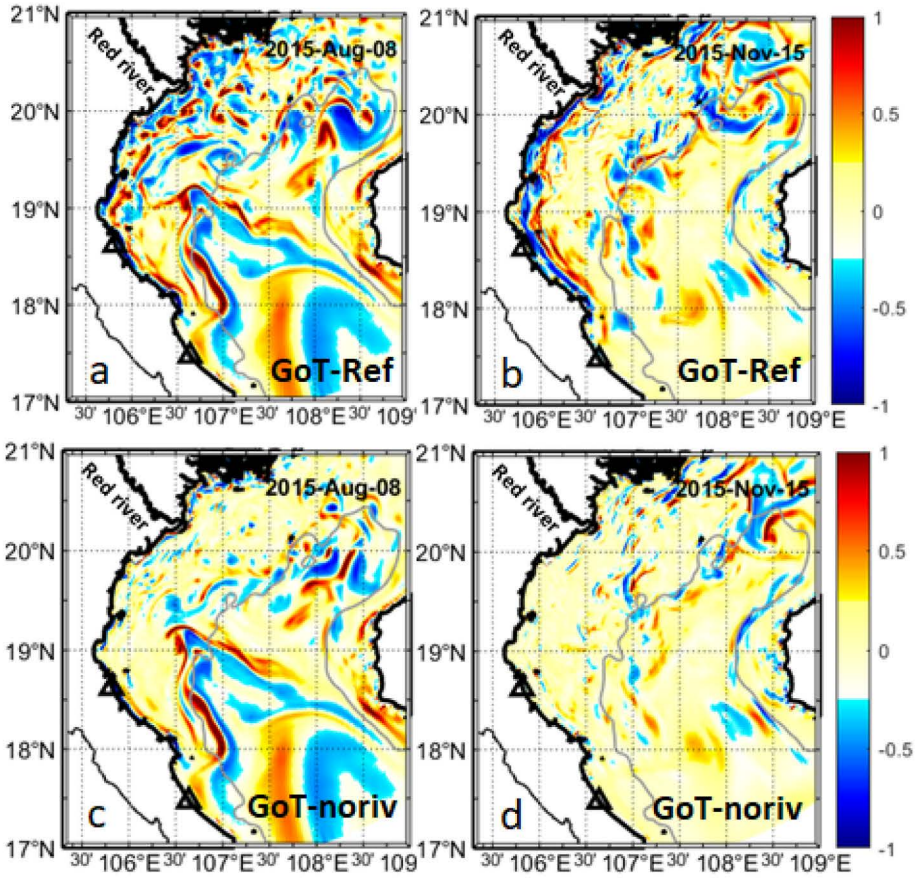

Fig. 3. Snapshots of the relative vorticity normalized by the Coriolis frequency in August and November 2015 from model simulation with (a, b) and without river discharge (c, d). Gray line shows 50 m isobath.

the order of f. When the Rossby number $R_o = \zeta/f \sim O(1)$, a departure from the geostrophic equilibrium in the flow is expected and smaller-scale processes can come into play, such as frontogenesis, mixed-layer instability (Zhong and Bracco, 2013).

Consequently, these sub-mesoscale structures of the velocity fields can directly impact the dispersion process by increasing the rate of dispersion by an order of magnitude compared to the geostrophic turbulence (Berta et al., 2020). A significant difference in velocity gradients between the full model and the model without river discharge is the lack of a number of structures with high vorticity which are observed better in the vicinity of the Red river mouth in August and in November (Fig. 3b, d). Due to the coarse resolution of the HFR measurements, the vorticity field is much smoother, its magnitude is drastically reduced, and small-scale coherent structures are almost vanishing (results not shown).

The statistical characterization of the velocity field variability can be obtained from the surface turbulent kinetic energy spectrum, E(k) (Fig. 4). The spectra indicate a wide range of motions: from geostrophic and wind driven circulation at large scale to sub-mesoscale turbulent motions. The energy distribution appears different between the two periods and higher for the GoT-Ref model configuration than for the GoT-noriv case. In both models, the kinetic energy is concentrated at large scales (roughly at a length scale of about 60 km) and decays more rapidly (steeper spectral slope $\sim k^{-3}$) at scales below 20 km. In the range roughly above 20 km, despite some noise, the energy distribution follows $k^{-5/3}$ law in both seasons. While the difference in energy distribution between the two seasons is rather small, a significant difference is observed for model simulations with and without river forcing. In the

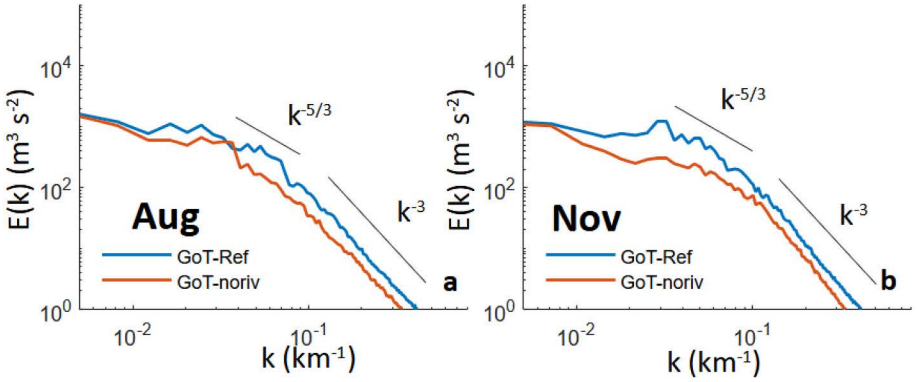

Fig. 4. Power spectra of surface horizontal turbulence kinetic energy in August (a) and November (b) for two model configurations: with and without river input.

latter case, the spectral slope from GoT-noriv model in summer appears steeper in a wide range of scales, 8–70 km, indicating a nonlocal dispersion regime from a Lagrangian perspective (Fig. 4a). In November, the spectrum is flatter and close to the $k^{-5/3}$ law in the scales 10–30 km (k ~ 0.03–0.1), thus suggesting that the dispersion is local and scale dependent (Fig. 4b).

4. Lagrangian pair dispersion

4.1. Lagrangian dispersion from HFR measurements and model simulation

In order to assess the turbulent dispersion in the vicinity of the Vietnamese coast, a first Lagrangian tracking experiment was conducted. A total of 2800 particles were uniformly seeded in a rectangular area of the size 30 × 30 km^2. Fig. 5 shows the trajectories of particles advected in the velocity field derived from HFR measurements and in the model velocity field. The drifting time of each particle is shown in color. Two releases were performed, one on August 3 and another on November 10, with a tracking time of 30 days. During the first tracking period, the surface currents are driven by the southwest monsoon while during the second period, the winter cyclonic circulation is formed, and the coastal current is reinforced as described in the previous section.

For particles released in August, trajectories are globally controlled by the cyclonic eddy located at the latitude 19°N which "trapped" the particles during the first 10 days. The effect of particle trapping is clearly seen in trajectories from the model and radar velocity fields (Fig. 5a and b). Ten days after the release when the eddy is weakened, particles formed groups drifting in different directions in the model simulations. One group of particles remains within the coastal zone close to XUAN radar site while another group is transported by the coastal buoyant jet southward, down to the gulf entrance (Fig. 5a). The direction of particle advection in the radar-derived velocity field is also southward for days 10–20, then it changes to eastward and northward (Fig. 5b). Agreement between the two transport patterns is found only for the first 15–20 days of tracking.

In November, a much better agreement in advection pathways in both HFR-derived and model velocity fields is found. In both cases, the trajectories of particles are related to the cyclonic circulation responsible for their transport southward. At the early stages, most of the particles are advected southward by the coastal jet. Later in time (roughly 10 days after the release), the particle drift direction changed to offshore, then reversed to northward after 15 days before continuing to the south after day 20. Regarding the number of particles remaining within the radar coverage area, 30% of particles left the area covered by HF radar measurements while this number is 10% for particles advected by the model velocity fields. The final location of the particles is shown in Fig. 5 in red color. At the end of the 30 days period, the particles advected in the radar velocity field show a more uniform distribution, while in the model simulation, the particles are separated into a number of distant groups (Fig. 5c). It is possible that larger dispersion in the model simulation is caused by irregularities in the velocity fields since the sub-mesoscale motions are better resolved in the high-resolution model. The coarser resolution of radar measurements somehow has an effect on the mean transport and also on the dispersion rate.

To quantify the dispersion regime, we used relative dispersion and the FSLE. In the subsequent analysis of the turbulent dispersion, we used the estimation of the Rossby radius R_d performed by Nguyen-Duy et al. (2021). In summer (April to September), large river discharge and thermal exchange with the atmosphere lead to the increase of stratification and R_d ranges from 10 to 15 km. During winter (Oct to Mar), strong wind and waves increase mixing in the water column. As a consequence, R_d has values of about 4–8 km and is even smaller in the shallow water area (see Fig. 4 in Nguyen-Duy et al., 2021). Therefore, in this study, the value of 8 km in November and 15 km in August are adopted for R_d.

Despite the differences in advection pathways, the relative dispersion regimes appear rather similar (Fig. 6). For the cluster released in

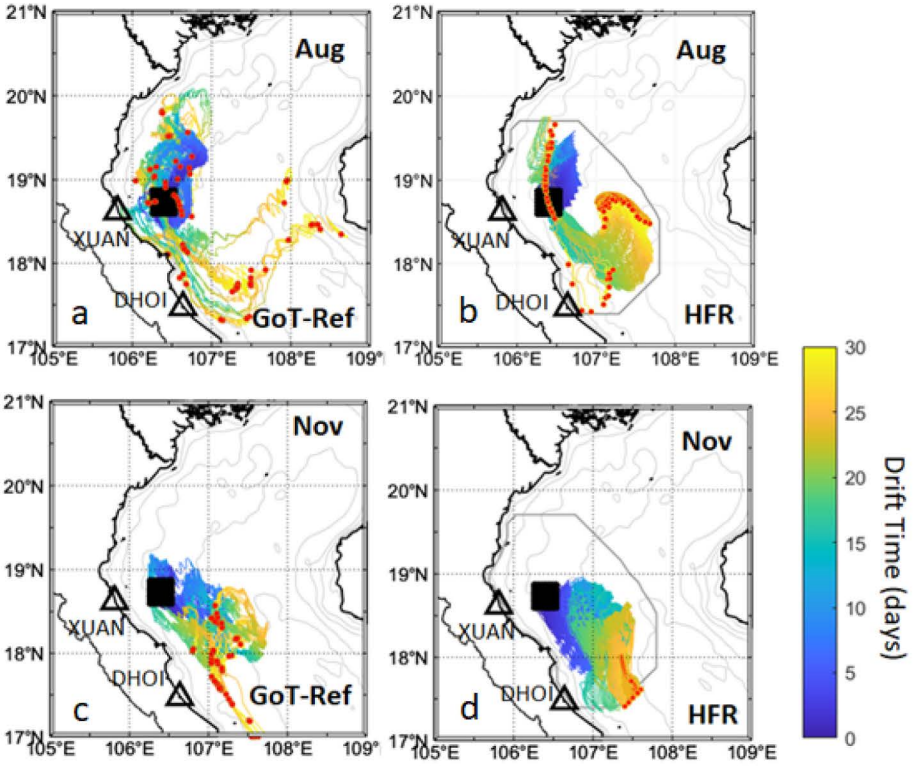

Fig. 5. Trajectories of a subset of particles released close to the XUAN radar site (black square) during both periods of study from the model (a, c) and from the HFR data (b, d) for 30 days since release. The drift time is color-coded. The particle final positions correspond to the red points.

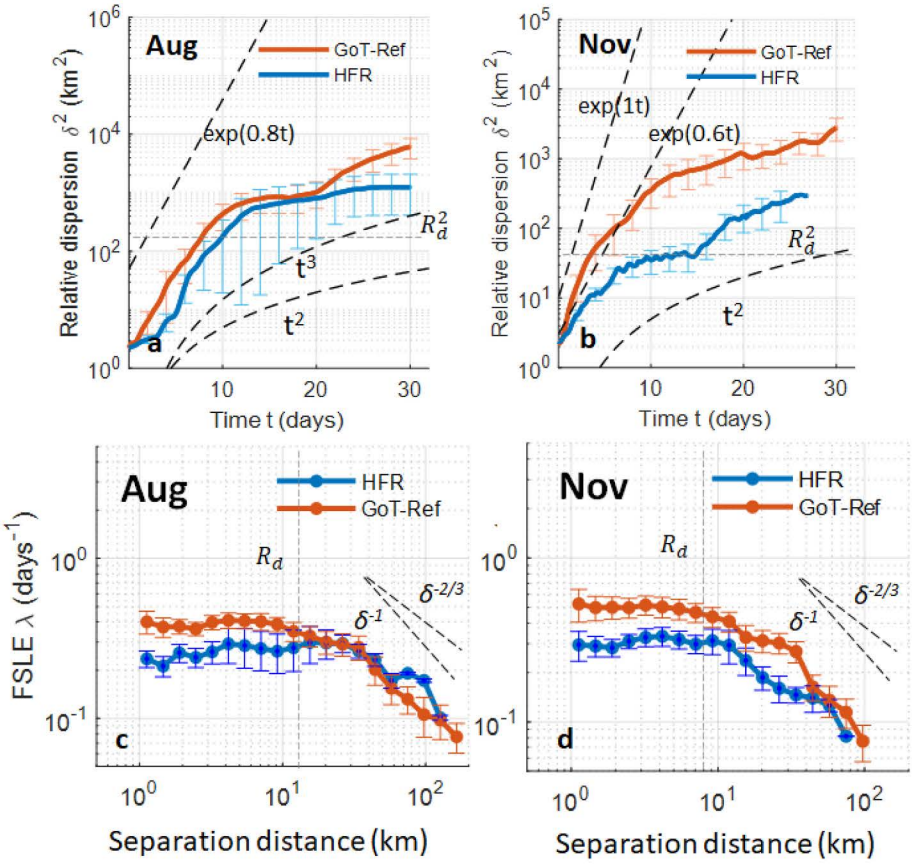

Fig. 6. Scaling properties from relative dispersion (a, b) and FSLE (c, d) for particles advected by model and HFR-derived velocity field in August and November. The horizontal (a, b) and vertical (c, d) lines correspond to separation distances equal to the Rossby radius R_d.

August, for both radar and model fields, relative dispersion indicates an exponential regime (exp (0.8t)) occurring during the first 10 days. It should be noted that in the case of the radar field, the pair separation grows slowly during the first 3 days, which can be explained by the coarser resolution of the HFR measurements (~6 km) that is larger than the initial separation (~2 km). During the next few days, the dispersion rapidly increases until reaching the distance equal to the grid resolution. The similarity in the exponential growth shown in Fig. 6a for both the HFR and the model indicates that relative dispersion during this initial period is dominated by processes with length-scale larger than the pair separation distance. On day 15, both curves flatten, suggesting that the particle pairs possibly reached eddies with typical length scale of about (20–30) km and larger (at later times). The evolution of relative dispersion follows a power-law behavior not far from Richardson regime for the model ($\delta^2 \sim t^3$) and ballistic regime for the radar ($\delta^2 \sim t^2$). The latter result is affected by larger statistical errors (Fig. 6a).

In November, the relative dispersion shows larger differences (Fig. 6b). Although the particles were released at the coastal current boundary, which can rapidly separate the particles pairs, only the model indicates a high rate of exponential growth (exp(t)). This exponential phase is short and lasts approximately 4 days. Compared to the model, the exponential growth in the HFR measurement is lower. After 10–15 days, both curves display a separation growth that is intermediate between a ballistic (t^2) and Richardson (t^3) regime. The characterization of the separation growth from HFR data is more difficult but, globally, the ballistic regime appears dominant at timescale larger than 4–5 days.

Another approach used for the identification of dispersion regimes involves the FSLE analysis (Fig. 6c and d). The FSLE uses the pair separation distance as an independent variable. Thus, it is less affected by an interfering contribution from pairs evolving under different dispersion regimes at the same time. This methodology, involving HF radar measurements, has been recently applied by Hernández-Carrasco et al. (2018a, 2018b) to assess dispersion processes in two European coastal regions – the Ibiza channel in the western Mediterranean and in the south-east Bay of Biscay. In agreement with relative dispersion, the FSLE curves demonstrate a non-local dispersion regime for the scale range below 10 km, where the FSLE is constant, $\lambda(\delta) \simeq \lambda_L$, with λ_L the maximum Lagrangian Lyapunov exponent (Fig. 6c and d). In this range, the associated e-folding time ($T = 1/(2\lambda_L)$) is close to the values found in Fig. 6a, b, i.e., from 1 to 1.25 days in the model and from 1.25 to 1.6 days in the HFR velocity fields. The increase in exponential growth rate in correspondence with increased grid resolution (model vs HFR data) is consistent with previous works (Poje et al., 2010) as pair dispersion at small separation is affected by small-scale motions resolved by the model.

At larger scales, a somewhat common behavior can be recognized. In August, a transition of the dispersion regime is observed at the scale of about 30 km. Above this scale, the FSLE indicates a regime of dispersion close to Richardson one ($\lambda(\delta) \sim \delta^{-2/3}$) for both velocity fields. A similar change of dispersion behavior is observed in November, but now at a scale of roughly 10 km, beyond which the FSLE is somehow steeper than in the Richardson regime and approaches the scaling ($\lambda(\delta) \sim \delta^{-1}$) typical of a ballistic regime.

4.2. *Transport and dispersion of particles in the GoT from model simulations*

Besides the coarse resolution of the HFR-derived velocity field, another weakness of the HFR measurements is the limited coverage which prevents the assessment of dispersion properties in an area in which the dynamics are strongly dominated by large-scale circulation features (gulf-scale eddy, coastal jet, etc.). Thus, to extend the study area

to the whole region, we resort to numerical simulations. In particular, we are interested in assessing the effect of the river discharge which can rapidly generate sub-mesoscale structures and largely affect the dispersion in the small-scale range. A series of Lagrangian tracking experiments were performed during the same two periods (August and November) with particles seeded uniformly, with a total number of 24065 particles, in the whole domain of model simulation. The average density of particle distribution at the release is 1.25 particles/km^2. Two model configurations were used to assess the Lagrangian transport: the model with all forcings including the river discharge (GoT-Ref) and without river discharge (GoT-noriv). Fig. 7 shows the spatial distribution of particles 30 days after the release on August 3 (a, c) and November 10 (c, d) and their concentration per km^2. In all cases, the spatial distribution of particles is found to be controlled by the flow field forced by the monsoon system. The particle distribution reveals a large difference between seasons. In August, the synthetic drifters are scattered throughout the gulf with a high density of particles observed in the middle and the northern gulf, while in November, most of the particles are located in the western gulf (Fig. 7b, d). At the end of the 30-day period, roughly 75% and 90% of particles released in August and November, respectively, remain inside the gulf. This suggests that the hydrodynamics of the gulf is quite local and the exchange with the open sea is limited.

Regarding the impact of the river discharge, the model simulation revealed that the distribution in August is quite similar in the southern gulf, whose dynamics is dominated by the inflow through the southern boundary (Fig. 7a, c). A much larger difference can be seen in the northern gulf. In the GoT-Ref case, the particles are organized into long filaments and wrapped around different eddies. Two regions of high density of particles are found there. The shape of the particle spatial distribution mimics the eddy-like structures with sizes that can reach 100 km. In the Got-Ref simulation, the spatial distribution of particles in August reveals that mesoscale motions are largely enhanced by the river discharge which increases the number of well-organized structures, such as eddies and filaments, with large concentration of particles there (Fig. 7a). The results of simulations without river discharge showed that the maximum concentration of particles per km^2 appears similar but the spatial patterns of particle distribution are less sharp (Fig. 7c).

In November, both models show a large number of elongated structures in particle distribution field. These structures are associated with the unstable manifolds (attracting the materials drifting with currents) and thus structuring the transport of particles. They also indicate a cyclonic pattern in the GoT winter circulation (Fig. 7b, d). Moreover, the particle distribution in both model simulations shows higher concentrations along the middle Vietnamese coast, between 18°–20° N. In the GoT-Ref case, the lines of high-density particle distribution extend toward the south, demonstrating a tendency of particle alignment along the outer edge of the coastal current that carries them southward. In addition to the rapid southward transport, the fluctuation of the jet can facilitate the formation of eddies at the jet boundary, as described via idealized model (Poje et al., 2010) which contribute to the enhancement of particle spreading.

In the GoT-noriv case, the majority of particles are concentrated along a line located roughly 50 km offshore in the northern part and in the southwestern part of the gulf, with large density (~5 particles per km^2) observed in the vicinity of the shoreline between latitudes 18°N and 19°N (Fig. 7d).

Fig. 8 helps to characterize the relative dispersion regime in the GoT during the two periods of interest. In August, relative dispersion shows an exponential regime exp(0.8t) in the GoT-Ref case while it grows a bit more slowly in the GoT-noriv case (~exp(0.6t)) (Fig. 8a). A change in dispersion regime occurs after 8 days when the average squared separation exceeds 8 km, a scale close to R_d. The exponential regime indicates non-local dispersion which can be expected at sufficiently small scales, where the flow is smooth. In our case, the separation (δ ~10 km) at which dispersion changes behavior is larger than the model resolution. This suggests that dispersion is driven by eddies of larger size, at least of $O(R_d)$. At intermediate times, roughly from 10 days onward,

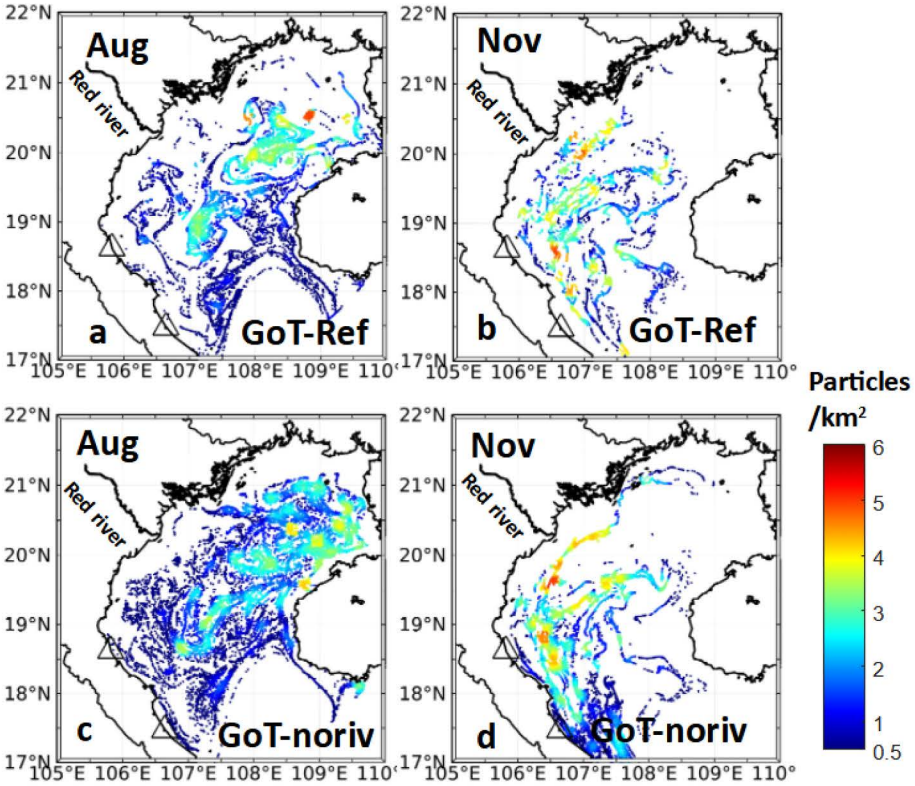

Fig. 7. Particle distribution in August and November, 30 days after the release, from the full model (GoT-Ref) (a, b) and without river discharge (GoT-noriv) (c, d) (unit: number of particles per km^2).

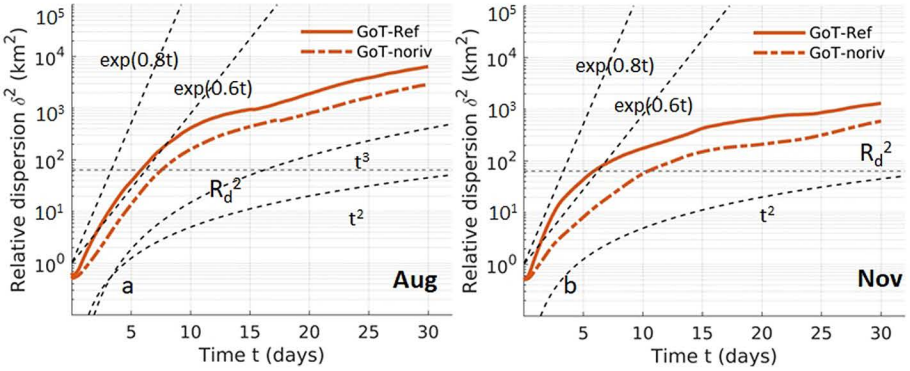

Fig. 8. Relative dispersion as a function of time (in linear-log scale) from the release in August (a) and November (b) in linear-log scale. In this case, particles were released uniformly in the GoT domain. The horizontal line in light black shows a separation distance corresponding to the Rossby radius R_d.

relative dispersion displays a power-law dependency close to a local Richardson regime ($\delta^2 \sim t^3$) at scales larger than 40 km (Fig. 8a).

In November, exponential growth in the GoT-Ref case with a similar rate occurs for a shorter timescale of 3 days (Fig. 8b) then quickly changes to a regime closer to the ballistic ($\delta^2 \sim t^2$) than to Richardson ($\delta^2 \sim t^3$), hinting to particles separating due to the coastal buoyant jet. The ballistic regime holds until the end of the tracking period, when the largest separation of roughly 30 km is reached. The estimated slope for this period is 2.2. In the GoT-noriv case, exponential growth is observed in a short early period, but with a smaller rate (~exp(0.6t)). The general features of the evolution of dispersion are not very different from those of the previous cases. The ballistic regime occurs after 5 days of drift. A possible explanation for the change to the ballistic regime in both configurations seems to be related to the particle entrainment inside the coastal current where the velocity shear causes a rapid separation in the cross-jet direction. On the whole, the rate of dispersion in the GoT-Ref case appears larger than that in the GoT-noriv simulation. The difference is caused by the presence of fine motions generated by the river plume advection where particles are stirred more effectively in the area that is not controlled by the mesoscale motions.

Fig. 9 shows relative diffusivity κ as a function of the separation distance δ in August and November respectively. The variability of this quantity is more affected by noise as κ is the time-derivative of relative dispersion. Thus, following Koszalka et al. (2009), we binned $\kappa(\delta)$ in such a way that a given value of δ is a multiple of the previous one, as one would do for the computation of the FSLE. Only the values with more than 50 data points for each bin are considered in the analysis. Despite some wiggles, the scaling properties of κ are consistent with the relative dispersion ones. During August and November, κ scales as δ^2 in the range below R_d. This indicates the dominance of non-local dispersion at these scales. The transition from the non-local to the local regime ($\kappa \sim \delta^{4/3}$) is observed for scales close to R_d (and in fact slightly smaller). The estimated exponent ranges from 1.2 to 1.5 (Fig. 9), and it is smaller in November. The comparison of diffusivity demonstrates that the freshwater runoff increases the diffusivity in the whole domain.

The FSLE curves λ as a function of δ shown in Fig. 10 reveal a larger difference in dispersion scaling behaviors between the two periods of the study. A common feature for both seasons is a transition from a non-local dispersion regime to a local dispersion one, occurring at a separation distance close to the Rossby radius R_d. The exponential growth of separation distance below R_d gives an e-folding time of 1.2–1.3 days for the GoT-Ref model and 1.7–2.2 days for the GoT-noriv configuration (Fig. 10), in fair agreement with the corresponding estimate obtained from relative dispersion (Fig. 8).

At larger scales (above R_d), a scaling slightly less steep than $\delta^{-2/3}$ and close to $\delta^{-1/2}$ is observed in August, likely due to relatively small-scale coherent structures that steepen the kinetic energy spectrum to k^{-2} (see, e.g., Capet et al., 2008). Note that in the GoT-noriv case the corresponding curve is less steep. Therefore, these results point to the enhancement of the particle spreading at scales comparable or smaller than R_d, in the simulation including the river discharge. The largest difference between the two configurations is observed at small scales. It appears that including the river contributions enhances stirring and shortens the dispersion time by a factor of two in this range of scales (Fig. 10a).

The FSLE curves in November show rather different behavior. Above 20 km, the FSLE in both GoT-Ref and GoT-noriv cases indicates a scale dependent dispersion rate in a broad range of scales. In GoT-Ref case, the FSLE scales as δ^{-1} (ballistic regime) until $\delta \sim 70$ km, which reveals a strong shear dispersion. This can be explained by the tendency of

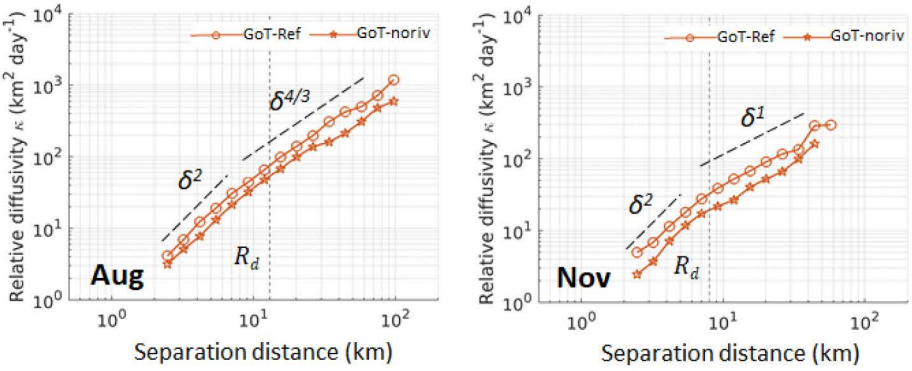

Fig. 9. Relative diffusivity as a function of the separation distance for the two tracking periods in August (a) and November (b) and for the two model configurations (with and without river discharge). In this case, particles were released uniformly in the GoT domain. The vertical lines correspond to separation distances equal to the Rossby radius R_d.

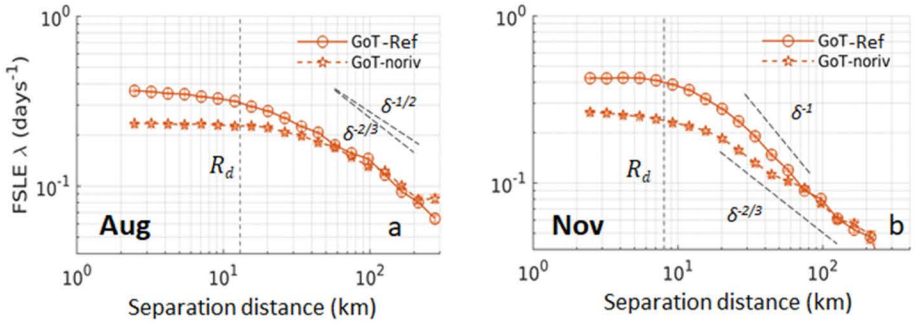

Fig. 10. FSLE $\lambda(\delta)$ versus the separation distance δ in August (a) and November 2015 (b), for particles released uniformly in the GoT domain. The vertical lines correspond to separation distances equal to the Rossby radius R_d.

particles to be concentrated in the western gulf where the coastal current contributes to the rapid southward transport. At scales above 70 km, for both the full model and the GoT-noriv one, the FSLE is perhaps closer to $\delta^{-2/3}$. In the larger scale ranges, the dispersion rate in November is on average slightly lower than in August (Fig. 10b).

4.3. Lagrangian Coherent structures in the GoT

Among different Lagrangian diagnostics, FSLE spatial distributions have been widely used in the analysis of ocean transport and mixing since they can reveal the hidden transport structures of the flow field. The characteristic lines with large FSLE values can show the location of Lagrangian coherent structures (LCS) organizing the transport processes in the GoT. They are sought as the barriers along which the advected particles are concentrated. Here, we analyze FSLE maps after 30 days of backward integration using the model simulation. In Fig. 11, the FSLE distribution is shown for two particular dates, September 02 and December 10. The figure demonstrates the complexity of the transport and turbulent dispersion. The FSLE fields are organized in thin filament-like features with high values (0.6–1.2 days^{-1}). The LCSs shaped by these lines reveal a frontal zone of 25 km wide along the Vietnamese shore in both periods. Long and highly tangled ridge lines evidence the variability of the flow field there (Fig. 11a). Another region showing a large number of FSLE ridge lines is located further (~100 km) offshore. Most of the ridge lines in this region seem to be aligned along 50 m isobath (Fig. 11b).

In contrast to the full model, the LCSs derived from the GoT-noriv model simulation clearly lack many small-scale features in the coastal region. In addition, they indicate much weaker transport barriers (convergence zones) in the offshore region. FSLE ridge lines appear sparse and characterized by lower values compared to the full model simulation at the same period (Fig. 11c and d).

Each map of FSLE provides information on short-lived processes. The temporal average of the FSLE maps over different periods contains a

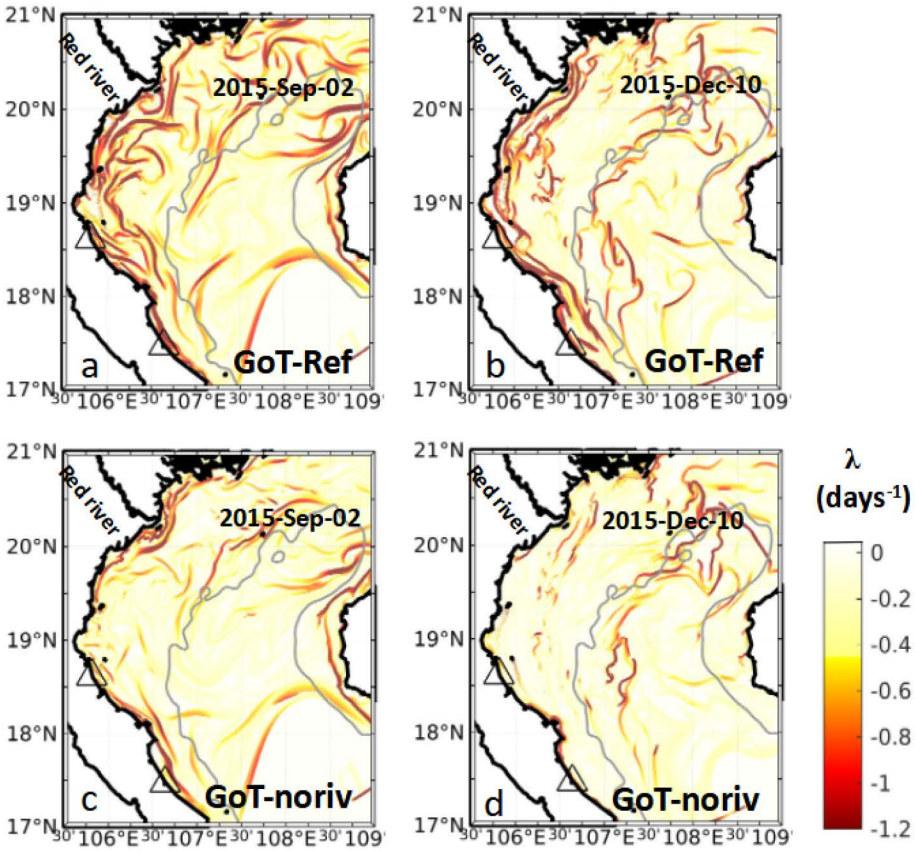

Fig. 11. FSLE distribution for two particular dates on September 02 and December 10 using two model simulations. Gray line shows 50 m isobath.

signature of the low-frequency and longer-lived processes. In addition, such FSLEs provide information on the dispersion time scale. In other terms, the areas with high FSLE values are characterized by more intense horizontal stirring (Hernandez-Carrasco et al., 2012). We assessed the spatial variability of dispersion in the GoT by time averaging thirty FSLE maps for two periods. Several regions of high density of ridge lines can be seen in both seasons with the values of λ ranging from 0.2 to 0.6 days^{-1}. Here we focus on four geographical regions: the northern gulf (A), the southern gulf (B), nearshore (C) and middle gulf region (D). It can be seen that regions of intense dispersion ($\lambda = 0.6$ days^{-1}) are found in the northern gulf (location A) and along the shore (location B), both characterized also by the largest number of filaments and eddies (Fig. 12).

In August, thin ridge lines also indicate an intense dispersion in the north and middle regions (location A and C). Another interesting feature is a quasi-permanent ridge line with $\lambda = 0.6$ days^{-1} (location B) matching the location of a loop in the flow incoming from the southern boundary (Fig. 2b).

In November, the FSLE maps reveal two regions of intense dispersion located along the middle of the Vietnam coast (region C) and further offshore (region D) with λ ranging from 0.5 to 0.6 days^{-1}. The ridge lines in these two regions indicate the effect of the coastal jet and the branch of the current, originating from Hainan strait (Fig. 2e), on horizontal dispersion. Moreover, spreading of the ridge lines in location D (Fig. 12b) reveals large spatial variability of the dispersion rate within an offshore band of 25–50 km large. LCSs can persist for up to several days thus limiting the exchange between the coastal and offshore regions located west and east of the ridge lines concentrated in sector D (Fig. 12b).

The intensity of stirring, which can be identified by taking the spatial average of the FSLEs over the whole area (d'Ovidio et al., 2004), is approximately 0.4 days^{-1} in the GoT-ref model. In the absence of the river discharge, the intensity of stirring decreases by roughly two times on average, down to 0.2 days^{-1}. These average values are reasonably in agreement with the FSLE plateau values λ_L at small scales from Fig. 10.

5. Discussion

In this study, we focus on the analysis of turbulent dispersion regimes and on the identification of LCSs in the GoT from realistic simulations using an approach based on particle pair dispersion. The analysis of relative dispersion is of great importance for the assessment of turbulent stirring in the open and coastal ocean at different spatial and temporal scales. Thus, the main objective of this study was to quantify the turbulent dispersion in the GoT, which is characterized by complex and multiscale dynamics, modulated by the monsoon wind and large buoyant input from a number of rivers (the largest being from the Red River). To the best of our knowledge, this problem has not been addressed yet in this region. Recent advances in the realism of the coastal modeling and observations using coastal radars allow the investigation of the turbulent dispersion using synthetic drifters advected in the radar and model velocity fields. Analysis of turbulent dispersion is performed for two periods, August and November 2015, representing typical summer and winter weather and river discharge conditions. Compared to other velocity data such as geostrophic currents from AVISO products, HFR measurements provide a near-real time, higher space-time resolution (6 km resolution, hourly data compared to roughly 27 km spatial resolution, daily data from AVISO). These data are more suitable for the quantification of the dispersion processes in the GoT. Our results indicate that relative dispersion statistics derived from the HFR tracking of particles are comparable to those obtained from the model. However, the spatial resolution of the HFR-derived velocity fields is still low compared to that of the model. As the short time and small-scale dispersion are sensitive to the details of the flow field, the coarse resolution of the HFR data makes the exploration of small-scale features difficult. In the small-scale range, the dispersion rate estimated from the radar measurements is significantly lower than the one from the model simulations in November (e-folding

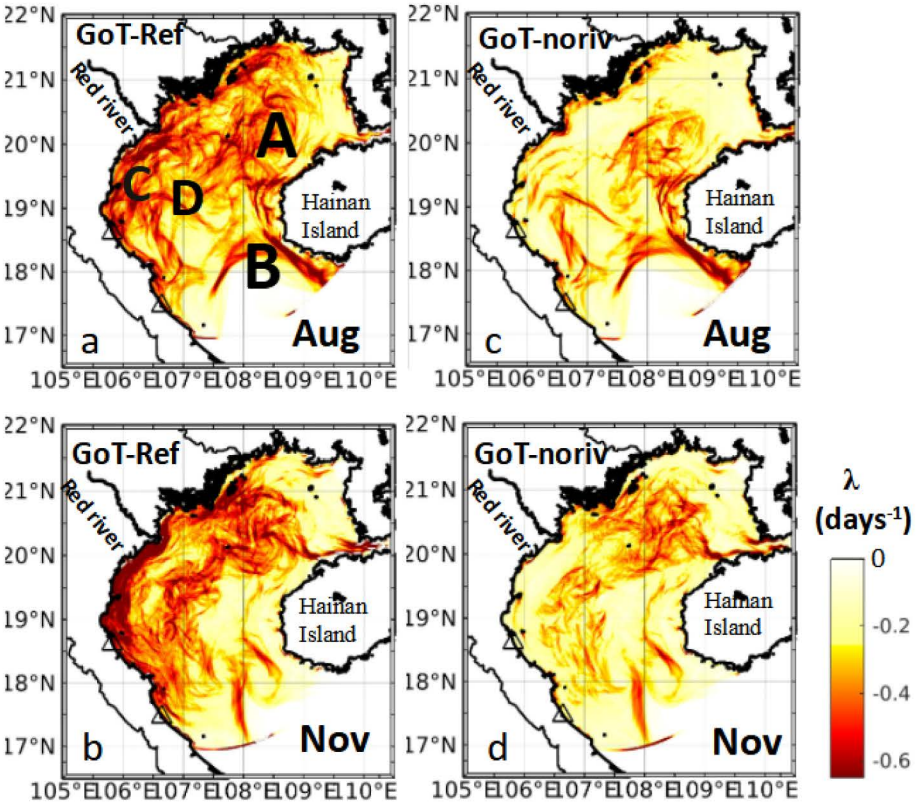

Fig. 12. 30-day mean FSLEs for the period of August and November from the two model simulations: GoT-Ref (a, b) and GoT-noriv (c, d).

time of approximately 2 and 1 days, respectively).

Analysis of relative dispersion, relative diffusivity and FSLE from the numerical model indicated an exponential regime at sub-mesoscale which is consistent with estimations of these quantities for other ocean basins (Beron-Vera and LaCasce, 2016; Berti et al., 2011; Essink et al., 2019; van Sebille et al., 2015). At this scale, the e-folding time estimated using the relative dispersion and the FSLE is similar for both seasons but appears strongly dependent on the river runoff (e-folding time of roughly 1.25 days for the full model and 2.5 days in the GoT-noriv model simulation). At larger scales, the dispersion exhibits a scale-dependent behavior indicative of either Richardson local dispersion or ballistic separation, controlled by strong mean currents. Such a transition between regimes occurs at scales close to the Rossby radius of deformation. In general, the pair dispersion properties in the GoT, obtained from the analysis of three Lagrangian diagnostics (relative dispersion, relative diffusivity and FSLE), are consistent with the results of previous studies, based on the analysis of the global drifter dataset (Corrado et al., 2017).

It is argued that a super diffusive regime can occur in the presence of strong shear and is characterized by the power law behavior $t^{\gamma}(\gamma > 1)$, as reported in some other studies performed in different regions: in the Adriatic Sea, γ is found ~1.8 (Haza et al., 2008), in the Gulf of California, γ ~1.9 (Zavala Sansón, 2015). In our case, γ is found larger, ~2.2. However, rather clear hints to Richardson regime $(\gamma = 3)$ are also found over some scale subranges for both model configurations, with and without river discharge.

In regions characterized by strong sub-mesoscale dynamics, different limiting FSLE values were found for scales $\delta < 10$ km: λ_L, ~1–1.1 days^{-1} in the Gulf of Mexico, (Choi et al., 2017), or $\lambda_L \sim 0.6$ days^{-1} in the Liguro basin (Schroeder et al., 2011). In the Gulf of La Spezia, the value of λ_L can readily reach 2.5 days^{-1} (Haza et al., 2010). In our case, the value of λ_L for the same scales ($\delta < 10$ km) is clearly weaker, ranging from 0.3 to 0.4 days^{-1}. In addition, the FSLE slopes, both from the radar data and the model, do not show a scale-dependent dispersion regime in the sub-mesoscale range, typically O(1–10 km), which is different from the one found in the well-known regions of strong sub-mesoscale dynamics such as in Ibiza channel (Hernández-Carrasco et al., 2018a) or the Gulf of Mexico (Choi et al., 2017; Poje et al., 2014). This indicates that the contribution of sub-mesoscale motions in turbulent dispersion in the Gulf of Tonkin is weak. This seems reasonable because the GoT is a quite shallow basin with limited potential energy which can be stored in the mixed layer where small eddies can be hashed by the wind. Our results are in agreement with some previous studies, which reported and demonstrated that dispersion at the sub-mesoscale can be induced non-locally by mesoscale motions (e.g., Haza et al., 2008; Poje et al., 2010). However, it should be noted that the variable model resolution, ranging from 0.3 km near the shore to 1.5–2 km in the middle gulf, likely prohibits the exploration of the local stirring generated by small-scale turbulent motions. Assuming that the effective scale of motions resolved in the model is roughly between four to six times the numerical grid resolution, only the upper range of sub-mesoscale variability (scale 1.5–10 km) can be properly identified and assessed. In this regard, HFR measurements in the GoT, with spatial resolution of 6 km, do not allow quantification of surface current velocity variability and dispersion at sub-mesoscale. Moreover, it was demonstrated by Hernández-Carrasco et al. (2018b) that different current mapping techniques, used in radar data processing, can affect the characterization of dispersion regimes based on particle pair statistics.

The impact of the river discharge on the surface dynamics of the GoT is explored using the model simulation with and without rivers runoff. During both periods considered, the river input in the model enhances the dispersion in a wide range of scales, from sub-mesoscale up to 50 km. The river discharge causes a significant change of e-folding time, which decreases from roughly 2.5 days to 1.25 days. The river discharge (when introduced in the model) creates buoyancy gradients and enhances the sub-mesoscale dynamics which in turn modifies the Lagrangian statistics. However, the difference between two numerical experiments, with and without river discharge, was not found to significantly alter the dispersion scaling behaviors. A possible reason could be that we examined statistics averaged over all particle pairs in the whole domain, while the river discharge primarily enhances the dispersion of particles in the western part of the gulf.

Lastly, we quantified the horizontal stirring caused by small-scale motions using the spatial distribution of FSLEs in different seasons. The LCSs, identified from backward FSLEs using the model velocity field, were analyzed to assess the horizontal stirring by small-scale processes, and appear to be very sensitive to the river forcing. Moreover, the FSLE maps clearly show the regionality of small-scale motions and their impact on dispersion processes. In August, a large concentration of FSLE ridge lines is found in the northern gulf and in the southern gulf where the transport and dispersion are strongly influenced by the incoming flow from the southern open boundary. During August, when the river discharge is at its peak, the river plume is driven northward and can detach from the coast due to the persistent southwest wind (Nguyen-Duy et al., 2021). The surface layer is then decoupled from the subsurface layer. This creates favorable conditions for the development of sub-mesoscale motions via roll-up instabilities of larger scale structures (Klein et al., 2011; Roullet et al., 2012; Berti and Lapeyre, 2021). Alternatively, sub-mesoscale motions could be also generated by a complex topography in the northern gulf (small islands, complex bathymetry, etc.). This can explain a high concentration of large FSLE values in the vicinity of the Red river in the GoT-Ref model (location C in Fig. 12a). In winter, the spatial distribution of FSLEs reveals the existence of another region of high concentration of FSLE ridge lines matching the outer limit of the coastal current which strongly affects the dispersion processes by organizing the particle distribution.

6. Summary

Relative dispersion in the coastal ocean environment, characterized by a wide range of scales of flow variability is still largely unknown. At scales less than a few km, the dispersion processes have been experimentally investigated using surface drifters in a number of limited size coastal regions. The experimental assessment of turbulent dispersion at larger scales is difficult to realize due to the cost of such experiments. In the present study, we adopted an alternative approach and investigated the turbulent dispersion and transport pathways in the GoT by using a large number of virtual drifters advected in the velocity fields derived from a high-resolution numerical model and HFR measurements.

For both types of fields, the results revealed a high degree of consistency regarding the dispersion regime at scales larger than 20 km. At smaller scales, the dispersion rate in the radar velocity field appeared two times lower, which is explained by the comparatively low spatial resolution of radar measurements.

The Rossby radius of deformation, R_d, is a key lengthscale that separates the regimes of turbulent dispersion. It was estimated from numerical simulations in the GoT performed by Nguyen-Duy et al. (2021). Our results revealed a non-local dispersion regime at scales below R_d and local dispersion at larger scales, which is in agreement with the results of earlier investigations performed in different regions of the world oceans (e.g., Haza et al., 2008; Corrado et al., 2017).

The seasonal variability in transport patterns and dispersion regimes was further characterized. The time evolution of dispersion showed an exponential growth during the first 5–8 days of drift for both seasons, followed by a power law regime during the next 6–20 days. The ballistic regime was found to dominate the dispersion at mesoscales in winter while Richardson super diffusion regime was diagnosed in summer. This change in regime is mainly related to a combined effect of river discharge and summer monsoon wind which enlarges the river plume area and enhances stirring in the coastal region extending up to 100 km offshore. In November, the ballistic regime is probably induced by strong northeastern monsoon wind providing the coastal current

strengthening and local shear dispersion intensification. The local dispersion regime (in the sub-mesoscale range) was not clearly identified, suggesting that the mesoscale circulation in the GoT largely governs the dispersion at small scales.

Four regions with high level of dispersion were identified in the GoT: a nearshore region under the fresh-water influence, an offshore region distant by ~100 km from the coast, a central part of the northern gulf, and a region close to the southern gulf entrance. Seasonality in dispersion strength caused by the variability of wind forcing and freshwater input from the Red river were identified and quantified.

Finally, this study provided a reference for further analysis of turbulent dispersion regimes in this geographic region, poorly covered by observations. It highlighted the capability of high-resolution model in reconstructing the circulation patterns and assessing the impact of the monsoon wind and river runoff on turbulent dispersion and transport of passive tracers. This is of primary importance for applications involving multi-scale interactions in the coastal ocean, the transport of particulate biological or anthropogenic material.

Authors' contributions

M.C.T, A.S, S.B contributed to the conception and scientific design of the study. M.C.T performed the data analysis and wrote the original version of the manuscript. A.S, S.B and N.A were deeply involved in the analysis, manuscript organization, and co-writing. N.A and T.ND developed and provided the numerical model results. All authors actively contributed to the revision of the manuscript.

Funding

This study was funded by the Université du Littoral-Côte d'Opale and the Région "Hauts-de-France" PhD fellowship.

Declaration of competing interest

The authors declare that they have no known competing financial interests or personal relationships that could have appeared to influence the work reported in this paper.

Acknowledgments

This study was supported by the University of Littoral Côte d'Opale and the Région "Hauts-de-France" PhD fellowship. Chl-a data were provided by ACRI, GlobColour products (https://hermes.acri.fr/). We would like to thank Tran Trung Kien for help with Chl-a data processing. The SYMPHONIE code is available at the SIROCCO French national service website (https://sirocco.obs-mip.fr/). CALMIP facilities (Toulouse, France) were used to run the model. We acknowledge the anonymous Reviewers for the constructive comments which helped to improve the scientific quality of the paper.

References

Artale, V., Boffetta, G., Celani, A., Cencini, M., Vulpiani, A., 1997. Dispersion of passive tracers in closed basins: beyond the diffusion coefficient. Phys. Fluids 9 (11), 3162–3171. https://doi.org/10.1063/1.869433.

Beron-Vera, F.J., LaCasce, J.H., 2016. Statistics of simulated and observed pair separations in the Gulf of Mexico. J. Phys. Oceanogr. 46 (7), 2183–2199. https://doi.org/10.1175/JPO-D-15-0127.1.

Berta, M., Ursella, L., Nencioli, F., Doglioli, A.M., Petrenko, A.A., Cosoli, S., 2014. Surface transport in the Northeastern Adriatic Sea from FSLE analysis of HF radar measurements. Continent. Shelf Res. 77, 14–23. https://doi.org/10.1016/j.csr.2014.01.016.

Berta, M., Griffa, A., Haza, A.C., Horstmann, J., Huntley, H.S., Ibrahim, R., Lund, B., Özgökmen, T.M., Poje, A.C., 2020. Submesoscale kinematic properties in summer and winter surface flows in the Northern Gulf of Mexico. J. Geophys. Res.: Oceans 125 (10). https://doi.org/10.1029/2020JC016085.

Berti, S., Lapeyre, G., 2021. Lagrangian pair dispersion in upper-ocean turbulence in the presence of mixed-layer instabilities. Phys. Fluids 33 (3), 036603. https://doi.org/10.1063/5.0041036.

Berti, S., Dos Santos, F.A., Lacorata, G., Vulpiani, A., 2011. Lagrangian drifter dispersion in the Southwestern Atlantic Ocean. J. Phys. Oceanogr. 41 (9), 1659–1672. https://doi.org/10.1175/2011JPO4541.1.

Capet, X., McWilliams, J.C., Molemaker, M.J., Shchepetkin, A.F., 2008. Mesoscale to submesoscale transition in the California current system. Part I: flow structure, eddy flux, and observational tests. J. Phys. Oceanogr. 38, 29–43. https://doi.org/10.1175/2007JPO3671.1.

Choi, J., Bracco, A., Barkan, R., Shchepetkin, A.F., McWilliams, J.C., Molemaker, J.M., 2017. Submesoscale dynamics in the Northern Gulf of Mexico. Part III: Lagrangian implications. J. Phys. Oceanogr. 47 (9), 2361–2376. https://doi.org/10.1175/JPO-D-17-0036.1.

Corrado, R., Lacorata, G., Palatella, L., Santoleri, R., Zambianchi, E., 2017. General characteristics of relative dispersion in the ocean. Sci. Rep. 7 (1), 46291 https://doi.org/10.1038/srep46291.

d'Ovidio, F., Fernández, V., Hernández-García, E., López, C., 2004. Mixing structures in the Mediterranean Sea from finite-size Lyapunov exponents. Geophys. Res. Lett. 31 (17), 1–4. https://doi.org/10.1029/2004GL020328.

D'Asaro, E.A., Shcherbina, A.Y., Klymak, J.M., Molemaker, J., Novelli, G., Guigand, C. M., Haza, A.C., Haus, B.K., Ryan, E.H., Jacobs, G.A., Huntley, H.S., Laxague, N.J.M., Chen, S., Judt, F., McWilliams, J.C., Barkan, R., Kirwan, A.D., Poje, A.C., Özgökmen, T.M., 2018. Ocean convergence and the dispersion of flotsam. Proc. Natl. Acad. Sci. USA 115 (6), 1162–1167. https://doi.org/10.1073/PNAS.1718453115.

d'Ovidio, F., Della Penna, A., Trull, T.W., Nencioli, F., Pujol, M.-I., Rio, M.-H., Park, Y.-H., Cotté, C., Zhou, M., Blain, S., 2015. The biogeochemical structuring role of horizontal stirring: Lagrangian perspectives on iron delivery downstream of the Kerguelen Plateau. Biogeosciences 12 (19), 5567–5581. https://doi.org/10.5194/bg-12-5567-2015.

Essink, S., Hormann, V., Centurioni, L.R., Mahadevan, A., 2019. Can we detect submesoscale motions in drifter pair dispersion? J. Phys. Oceanogr. 49 (9), 2237–2254. https://doi.org/10.1175/JPO-D-18-0181.1.

Foussard, A., Berti, S., Perrot, X., Lapeyre, G., 2017. Relative dispersion in generalized two-dimensional turbulence. J. Fluid Mech. 821, 358–383. https://doi.org/10.1017/jfm.2017.253.

Haller, G., Yuan, G., 2000. Lagrangian coherent structures and mixing in two-dimensional turbulence. Phys. Nonlinear Phenom. 147 (3–4), 352–370. https://doi.org/10.1016/S0167-2789(00)00142-1.

Haza, A.C., Poje, A.C., Özgökmen, T.M., Martin, P., 2008. Relative dispersion from a high-resolution coastal model of the Adriatic Sea. Ocean Model. 22 (1–2), 48–65. https://doi.org/10.1016/j.ocemod.2008.01.006.

Haza, A.C., Özgökmen, T.M., Griffa, A., Molcard, A., Poulain, P.-M., Peggion, G., 2010. Transport properties in small-scale coastal flows: relative dispersion from VHF radar measurements in the Gulf of La Spezia. Ocean Dynam. 60 (4), 861–882. https://doi.org/10.1007/s10236-010-0301-7.

Haza, A.C., Özgökmen, T.M., Hogan, P., 2016. Impact of submesoscales on surface material distribution in a gulf of Mexico mesoscale eddy. Ocean Model. 107, 28–47. https://doi.org/10.1016/j.ocemod.2016.10.002.

Hernandez-Carrasco, I., López, C., Hernandez-García, E., Turiel, A., 2012. Seasonal and regional characterization of horizontal stirring in the global ocean. J. Geophys. Res.: Oceans 117 (10), 1–12. https://doi.org/10.1029/2012JC008222.

Hernández-Carrasco, I., Orfila, A., Rossi, V., Garçon, V., 2018a. Effect of small scale transport processes on phytoplankton distribution in coastal seas. Sci. Rep. 8 (1), 1–13. https://doi.org/10.1038/s41598-018-26857-9.

Hernández-Carrasco, I., Solabarrieta, L., Rubio, A., Esnaola, G., Reyes, E., Orfila, A., 2018b. Impact of HF radar current gap-filling methodologies on the Lagrangian assessment of coastal dynamics. Ocean Sci. 14 (4), 827–847. https://doi.org/10.5194/os-14-827-2018.

Klein, P., Lapeyre, G., Roullet, G., Le Gentil, S., Sasaki, H., 2011. Ocean turbulence at meso and submesoscales: connection between surface and interior dynamics. Geophys. Astrophys. Fluid Dyn. 105 (4–5), 421–437. https://doi.org/10.1080/03091929.2010.532498.

Koszalka, I., LaCasce, J.H., Orvik, K.A., 2009. Relative dispersion in the Nordic Seas. J. Mar. Res. 67 (4), 411–433. https://doi.org/10.1357/002224009790741102.

LaCasce, J.H., 2008. Statistics from Lagrangian observations. Prog. Oceanogr. 77 (1), 1–29. https://doi.org/10.1016/j.pocean.2008.02.002.

LaCasce, J.H., Ohlmann, C., 2003. Relative dispersion at the surface of the Gulf of Mexico. J. Mar. Res. 61 (3), 285–312. https://doi.org/10.1357/002224003322201205.

Lacroix, G., Maes, G.E., Bolle, L.J., Volckaert, F.A.M., 2013. Modelling dispersal dynamics of the early life stages of a marine flatfish (Solea solea L.), pp. 13–25. https://doi.org/10.1029/2010JC006338. J. Sea Res. 84, 13 25.

Large, W.G., Yeager, S., 2004. Diurnal to Decadal Global Forcing for Ocean and Sea–Ice Models: The Data Sets and Flux Climatologies. NCAR Technical Note, NCAR/TN-460+STR. Boulder, CO: National Center for Atmospheric Research. https://doi.org/10.5065/D6KK98Q6.

Lumpkin, Rick, Elipot, Shane, 2010. Surface drifter pair spreading in the North Atlantic. J. Geophys. Res. 115 (c12) https://doi.org/10.1029/2010JC006338.

Lyard, F.H., Allain, D.J., Cancet, M., Carrère, L., Picot, N., 2021. FES2014 global ocean tide atlas: design and performance. Ocean Sci. 17 (3), 615–649. https://doi.org/10.5194/os-17-615-2021.

Marsaleix, P., Auclair, F., Estournel, C., 2006. Considerations on open boundary conditions for regional and coastal ocean models. J. Atmos. Ocean. Technol. 23 (11), 1604–1613. https://doi.org/10.1175/JTECH1930.1.

Marsaleix, P., Auclair, F., Floor, J.W., Herrmann, M.J., Estournel, C., Pairaud, I., Ulses, C., 2008. Energy conservation issues in sigma-coordinate free-surface ocean models. Ocean Model. 20 (1), 61–89. https://doi.org/10.1016/j.ocemod.2007.07.005.

Meyerjürgens, J., Ricker, M., Schakau, V., Badewien, T.H., Stanev, E.V., 2020. Relative dispersion of surface drifters in the North Sea: the effect of tides on mesoscale diffusivity. J. Geophys. Res.: Oceans 125 (8). https://doi.org/10.1029/2019JC015925.

Michaud, H., Marsaleix, P., Leredde, Y., Estournel, C., Bourrin, F., Lyard, F., Mayet, C., Ardhuin, F., 2012. Three-dimensional modelling of wave-induced current from the surf zone to the inner shelf. Ocean Sci. 8 (4), 657–681. https://doi.org/10.5194/os-8-657-2012.

Nguyen-Duy, T., Ayoub, N.K., Marsaleix, P., Toublanc, F., De Mey-Frémaux, P., Piton, V., Herrmann, M., Duhaut, T., Tran, M.C., Ngo-Duc, T., 2021. Variability of the Red River Plume in the Gulf of Tonkin as revealed by numerical modeling and clustering analysis. Front. Mar. Sci. 8, 1636. https://www.frontiersin.org/article/10.3389/fmars.2021.772139.

Piton, V., Ouillon, S., Vinh, V.D., Many, G., Herrmann, M., Marsaleix, P., 2020. Seasonal and tidal variability of the hydrology and suspended particulate matter in the Van Uc estuary, Red River, Vietnam. J. Mar. Syst. 211, 103403 https://doi.org/10.1016/j.jmarsys.2020.103403.

Piton, V., Herrmann, M., Marsaleix, P., Duhaut, T., Ngoc, T.B., Tran, M.C., Shearman, K., Ouillon, S., 2021. Influence of winds, geostrophy and typhoons on the seasonal variability of the circulation in the Gulf of Tonkin: a high-resolution 3D regional modeling study. Reg. Stud. Mar. Sci. 45, 101849 https://doi.org/10.1016/j.rsma.2021.101849.

Poje, A.C., Haza, A.C., Özgökmen, T.M., Magaldi, M.G., Garraffo, Z.D., 2010. Resolution dependent relative dispersion statistics in a hierarchy of ocean models. Ocean Model. 31 (1–2), 36–50. https://doi.org/10.1016/j.ocemod.2009.09.002.

Poje, A.C., Özgökmen, T.M., Lipphardt, B.L., Haus, B.K., Ryan, E.H., Haza, A.C., Jacobs, G.A., Reniers, A.J.H.M., Olascoaga, M.J., Novelli, G., Griffa, A., Beron-Vera, F.J., Chen, S.S., Coelho, E., Hogan, P.J., Kirwan, A.D., Huntley, H.S., Mariano, A.J., 2014. Submesoscale dispersion in the vicinity of the Deepwater Horizon spill. Proc. Natl. Acad. Sci. U.S.A. 111 (35), 12693–12698. https://doi.org/10.1073/pnas.1402452111.

Rogowski, P., Zavala-Garay, J., Shearman, K., Terrill, E., Wilkin, J., Lam, T.H., 2019. Air-sea-land forcing in the Gulf of Tonkin: assessing seasonal variability using modern tools. Oceanography 32 (2), 150–161. https://doi.org/10.5670/oceanog.2019.223.

Roullet, G., Mcwilliams, J.C., Capet, X., Molemaker, M.J., 2012. Properties of steady geostrophic turbulence with isopycnal outcropping. J. Phys. Oceanogr. 42 (1), 18–38. https://doi.org/10.1175/JPO-D-11-09.1.

Sansón, L.Z., Pérez-Brunius, P., Sheinbaum, J., 2016. Surface relative dispersion in the Southwestern Gulf of Mexico. J. Phys. Oceanogr. 47 (2), 387–403. https://doi.org/10.1175/JPO-D-16-0105.1.

Schroeder, K., Haza, A.C., Griffa, A., Özgökmen, T.M., Poulain, P.M., Gerin, R., Peggion, G., Rixen, M., 2011. Relative dispersion in the Liguro-Provençal basin: from sub-mesoscale to mesoscale. Deep Sea Res. Oceanogr. Res. Pap. 58 (3), 209–228. https://doi.org/10.1016/j.dsr.2010.11.004.

Schroeder, K., Chiggiato, J., Haza, A.C., Griffa, A., Zgkmen, T.M., Zanasca, P., Molcard, A., Borghini, M., Poulain, P.M., Gerin, R., Zambianchi, E., Falco, P., Trees, C., 2012. Targeted Lagrangian sampling of submesoscale dispersion at a coastal frontal zone. Geophys. Res. Lett. 39 (11), 4–9. https://doi.org/10.1029/2012GL051879.

Tran, M.C., Sentchev, A., Nguyen, K.C., 2021. Multi-scale variability of circulation in the Gulf of Tonkin from remote sensing of surface currents by high-frequency radars. Ocean Dynam. 71 (2), 175–194. https://doi.org/10.1007/s10236-020-01440-x.

van Sebille, Erik, Beal, Lisa M., Johns, William E., 2011. Advective time scales of Agulhas Leakage to the North Atlantic in surface drifter observations and the 3D OFES model. J. Phys. Oceanogr. 41 (5), 1026–1034. https://doi.org/10.1175/2010JPO4602.1.

van Sebille, E., Waterman, S., Barthel, A., Lumpkin, R., Keating, S.R., Fogwill, C., Turney, C., 2015. Pairwise surface drifter separation in the western Pacific sector of the Southern Ocean. J. Geophys. Res.: Oceans 120 (10), 6769–6781. https://doi.org/10.1002/2015JC010972.

Yaremchuk, M., Sentchev, A., 2011. A combined EOF/variational approach for mapping radar-derived sea surface currents. Continent. Shelf Res. 31 (7–8), 758–768. https://doi.org/10.1016/j.csr.2011.01.009.

Zavala Sansón, L., 2015. Surface dispersion in the Gulf of California. Prog. Oceanogr. 137, 24–37. https://doi.org/10.1016/j.pocean.2015.04.008.

Zhong, Y., Bracco, A., 2013. Submesoscale impacts on horizontal and vertical transport in the Gulf of Mexico. J. Geophys. Res.: Oceans 118 (10), 5651–5668. https://doi.org/10.1002/jgrc.20402.

Zimmerman, J.T.F., 1981. Dynamics, diffusion and geomorphological significance of tidal residual eddies. Nature 290 (5807), 549–555. https://doi.org/10.1038/290549a0.

Chapter V. Turbulence and spatial distribution of phytoplankton

5.1. Introduction

Coastal zones are dynamically active regions in the ocean that largely contribute to the global budget of carbon and host many biogeochemical processes (Jahnke, 2010). Their dynamics is characterized by a complex interaction of multiple processes that significantly increase the growth of phytoplankton and contribute to the primary production. Due to their importance, the role of these multiscale dynamical processes in regulating marine ecosystems has attracted the attention of many studies in the last decades aiming at a better understanding of the marine bio-physical interactions (Hernández-Carrasco et al., 2018, Lévy et al., 2014).

In the past few years, the data from ocean color satellite radiometry have allowed deriving a number of biogeochemical parameters from space. In particular, chlorophyll-a concentration (Chl-a) fields have been used to study the ocean primary production (e.g., Loisel et al., 2016). Patchiness of Chl-a observed from the ocean color satellite products enabled assessing the stirring processes by mesoscale motions (Lehahn et al., 2018). Using the ocean color archive data, spatio-temporal variability of Chl-a in the GoT was analyzed revealing a strong seasonality caused by the East Asian Monsoon cycle (Tang et al., 2003; Ha et al., 2014, Loisel et al., 2016). Using satellite data from 2002-2012, Loisel et al. (2016) also demonstrated a high correlation of the observed Chl-a concentrations with the intensity of turbulent activity along the Vietnamese coast. The relationship between Chl-a fields and turbulence quantities is complex and involves mechanisms depending on the region and period of time under consideration.

When studying the effect of physical factors on biogeochemical processes, the ocean dynamics variability is often characterized by spatial scales of motions of roughly 1-100 km and temporal scales of days to weeks, referred to as “fine scales” or (sub)mesoscale motions. In the ocean, these motions, though having relatively short time scales, contain much of energy in the ocean turbulence spectrum and crucially affect ocean physics and ecology up to the climate scale (Ferrari & Wunsch 2009). The enhancement of primary production is often associated with the presence of mesoscale eddies affecting the marine environment in different ways, i.e., via the water pumping in cyclonic vortices

(McGillicuddy et al., 1999; Gaube et al., 2015) or trapping water of mesotrophic waters (Brzezinski and Washburn, 2011; Huntley et al., 2000) or the entrainment of nutrient-rich water into the depleted region through horizontal advection patterns and small-scale filaments (Lehahn et al., 2007). Additionally, the fronts that emerged from energetic mesoscale eddies induce a strong vertical motion that connects the surface to its interior and favors the increase of vertical mixing (D'Asaro et al., 2018; Klein et al., 2011). Although it is relatively well known in the open ocean, the role of these motions in structuring the coastal marine communities requires further investigation due to the complex interactions of different oceanic processes. In some studies, it was found a negative response of the presence of mesoscale eddies to primary production near the shore, i.e., mesoscale eddies enhance cross-shore exchange, thus, transporting the nutrients from the nearshore environment to the offshore region (e.g., Gruber et al., 2011, Rubio et al., 2018).

In the present work, our main aim is to assess the variability of biological quantities in the GoT and from that, we discuss the role of (sub)mesoscale dynamics in structuring the spatial distribution of biological fields, namely Chl-a concentration. We study this problem using the modeling approach in combination with the remote sensing of ocean color (MODIS/AQUA Chl-a product). As the identification of fine-scale features in spatial distribution of tracers naturally involves Lagrangian methods of analysis, the Lagrangian framework is used to investigate the transport pathways and turbulent mixing in the GoT in conjunction with analysis of Chl-a concentrations.

5.2. Data and methods

5.2.1. Satellite ocean color data

Chl-a concentrations are an indicator of phytoplankton abundance and biomass in coastal and estuarine waters and can be observed from the satellite. In this study, daily MODIS/AQUA Chl-a distributions at 4 km resolution from GlobColour archive (https://hermes.acri.fr/) in the GoT during the period 2010 – 2020 were used (Fig. 5.1). However, since the model simulation presented in Chapter IV was limited to the year 2015, the comparison between the hydrodynamic model and the satellite data is carried out only during this year. The data used in this study were processed by the OC5 algorithm (Gohin et al., 2002) since this algorithm can produce the lowest bias for the satellite-derived Chl-a in the coastal waters. The method was used to assess the Chl-a variability in the Vietnamese waters by Loisel et al. (2016) during the period 2002 – 2012.

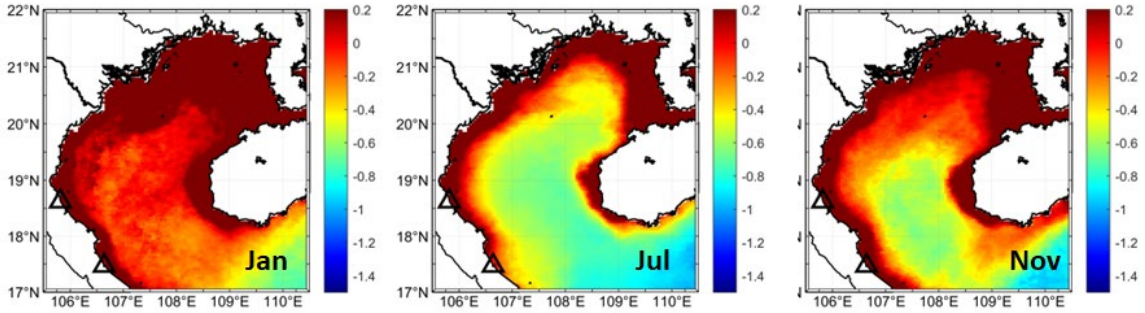

Figure 5.1: Climatology of Chl-a distribution in the GoT: Monthly mean Chl-a concentrations for January, July and November averaged over the period from 2010 to 2020 from MODIS satellite dataset.

To analyze the spatio-temporal variations of Chl-a, the Census X-11 method (Pezzulli, Stephenson, and Hannachi, 2005) was applied to the monthly Chl-a data for 10 years. A pre-processing is applied to the time series in each grid point. Calendar months that are underrepresented (less than 50% of coverage by the data) in the series are excluded. This method allows separating the analyzed time series X(t) into three modes of variability: the seasonal cycle (S), trend (T), and residual (or irregular) variation (I):

$$X(t) = S(t) + T(t) + I(t) \qquad \text{(Eq. 5.1)}$$

The X-11 method is useful in identifying the magnitude of variation and the contribution of each component to the total variance. Based on this, maps of the relative contribution of S(t), I(t), and T(t) components to the variability contained in the initial series can be computed. The technique defines the shape of the seasonal cycle, thus, distinguishing the other terms (trend T(t) and irregular I(t) variation) from the bias of inter-annual variation (Vantrepotte & Mélin, 2009). A detailed description of the method is given in Vantrepotte & Mélin (2009).

5.2.2. Horizontal stirring assessment from FSLE

The Finite-Size Lyapunov Exponent (FSLE) method allows the identification of manifolds of relevant hyperbolic points of the flow field, or so-called Lagrangian Coherent Structures (LCSs), that constrain the fluid motions and ocean transport (Artale et al., 1997; Boffetta et al., 2001; Siegelman et al., 2020). The method is often used for assessing the coherent structures (jets, eddies, fronts, etc.), thus, helping to inspect the horizontal stirring and mixing properties of the flow field (D'Ovidio et al., 2004; Hernandez-Carrasco et al., 2012; Hernández-Carrasco & Orfila, 2018; Nencioli et al., 2011). It appears very effective for localizing the regions with enhanced mesoscale dynamics. The FSLEs are computed from the minimum time, τ, required for two-particle separation from an initial distance δ_i to a final distance δ_f(Section 2.3.2). The following values were attributed to these parameters $\delta_i \approx$1.86 km

and δ_f = 13 km. Such values allow us to adequately visualize the relevant coherent structures and transport patterns associated with small-scale motions in the GoT.

The spatial distribution of time-averaged FSLE values indicates the location of regions with different mixing activities (Fig. 5.2b). Larger (absolute) FSLE values correspond to the areas with high EKE levels (Fig. 5.2a). Compared with the Eulerian view, the Lagrangian approach gives an extensive picture of stirring processes since it allows assessing smaller scales, often looking as filaments-like or eddies, which are induced by the interaction of large-scale flow structures (mesoscale). The standard deviation of the monthly FSLE during the year 2015 shows the regions of strong turbulence activity and large horizontal mixing (Fig. 5.2c).

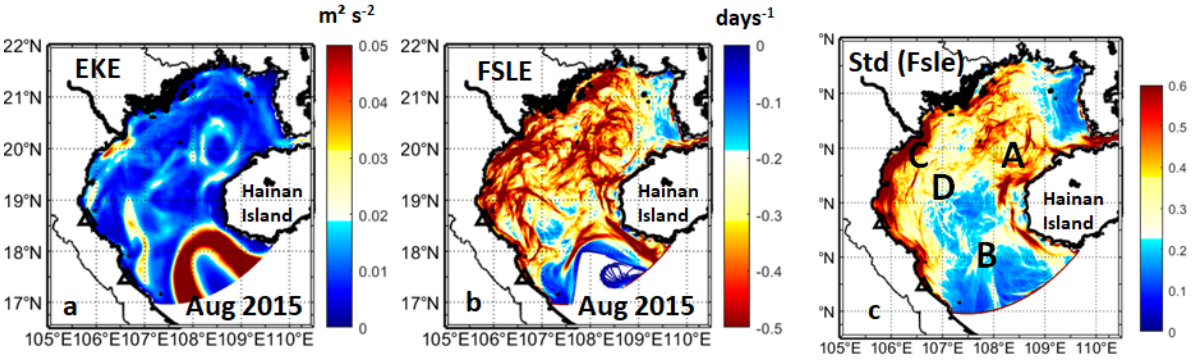

Figure 5.2: Monthly averaged Eddy Kinetic Energy (EKE) (a), FSLE (b) of the surface flow field in the GoT in August 2015, and the standard deviation of monthly FSLE in the year 2015 (c). Four regions of high stirring are denoted by letters in (c).

5.3. Results and discussion

5.3.1. Temporal variability of Chl-a concentrations in the GoT

In the GoT, the Chl-a concentrations demonstrate a strong variability during a year (Fig. 5.1). Applying the Census X-11 method, the temporal patterns of Chl-a variability can be identified (Fig. 5.3). The magnitude of Chl-a variation (variation coefficient), which is computed as (the standard deviation/mean) x 100, indicates a large temporal variation within the gulf (on average, 50% of the total variance) (Fig. 5.3a). The pattern of high Chl-a variability (variation coefficient can attain 80% of the total variance) matches well regions of strong turbulence shown in Fig. 5.2c. They are co-located along the Vietnamese coast (region C, Fig. 5.2c), in the middle of the gulf (region A, Fig. 5.2c). Another region of strong Chl-a variability is observed along the southern gulf entrance which exceeds the boundary of the model. On the contrary, the regions of low Chl-a variability can be found near the Red River delta, north and west of Hainan Island, and along the Hainan strait. The magnitude of Chl-a variations is less than 20% there. In these areas, the Chl-a concentrations are high and stable around the whole year due to the input of a large amount of nutrients (Fig. 5.3a).

Accounting for about 80% (can be up to 90% in some regions) of the total variance, the seasonal cycle provides the largest contribution to the Chl-a variation in the offshore region and in the vicinity of the southern entrance to the gulf (Fig. 5.3b). This high variability results from the difference in winter/summer conditions. During summer, the warm weather and large freshwater flux cause a stable stratification of the water column and limit the nutrients supply to the surface layer where they are quickly consumed. As the result, low Chl-a concentrations are observed in summer. In winter, the Chl-a concentrations of the whole gulf are the highest due to the enhancement of vertical mixing. During this period, cold weather and strong wind induce a vast cooling and densification of the water in the surface layer in the whole gulf, thus, leading to the extension of the mixed layer depth down to the bottom (Loisel et al., 2017; Tang et al., 2003).

In addition to the seasonal cycle, a relatively high contribution of the irregular component can be found across the gulf. It represents up to 20 – 30% of the total Chl-a variability. Its contribution can reach ~ 40% in several places, e.g., north and west of Hainan Island (Fig. 5.3c). North of Hainan Island, the strong residual current through the Hainan strait occurs during the whole year. Moreover, the Chl-a variation west of Hainan Island is related to tidal mixing (Lü et al., 2008) which can explain the high contribution of the residual (irregular) component there.

Along the Vietnamese coast below the Red River delta, the spatial pattern of irregular component fairly well matches the location of the river plume and associated frontal zones identified in FSLE maps in Chapter IV. Lines of high FSLE values mark the region of river plume fronts which not only act as a barrier preventing the cross-shore exchange but possibly trigger the upwelling mechanism at the frontal zone that enhancing the Chl-a variation.

Along the shoreline, the Chl-a concentrations are higher than that of the offshore region (Fig. 5.1). As a matter of fact, the high concentration of the Chl-a near the shore can be explained by strong mixing, nutrients supplied from the mainland, and the presence of frontal zones. However, little is known about the sources of the nutrients that govern the blooming processes in the center of the gulf (Minh et al., 2014; Tang et al., 2003).

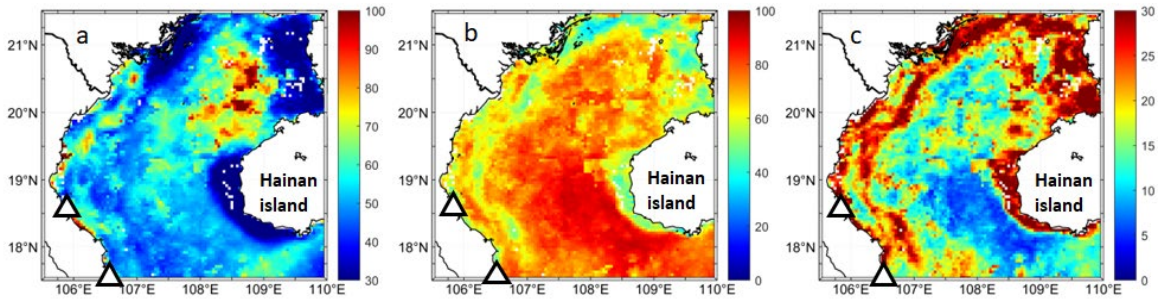

Figure 5.3: Variation coefficient of Chl-a during 2010 – 2020 (unit: %) (a). Relative contribution of the seasonal (b) and non-seasonal components (c) in the total Chl-a variance as estimated by X-11 method. Triangles mark the location of the radar sites.

5.3.2. Impact of horizontal stirring on the Chl-a distribution

In the ocean, turbulent mixing is recognized as a critical factor for the growth of the phytoplankton populations. At the seasonal scale, the heating/cooling cycle strongly drives the turbulent mixing across the water column. At smaller scales (days to months), mesoscale motions provide the energy for generating submesoscale fronts, separating the water of different densities (Siegelman et al., 2020) and smaller-scale motions via turbulence energy cascade. Therefore, ocean turbulence plays a certain role in setting patterns of phytoplankton diversity (Lévy et al., 2014). One of the quantities used for turbulence characterization is the backward FSLE, which provides a measure of lateral stirring in the flow field and can be quantified by the backward integration of the separation distance of particle pairs. Schematically, the tracer distributions in turbulent flow are stretched and largely concentrated along the lines of local maxima of FSLE value, λ. These lines of high values of λ (the ridge lines) are associated with the regions of large strain or the horizontal buoyancy fronts at the edge of the mesoscale eddies and in between them. In many studies, the distribution of Chl-a and the location of local maxima of FSLEs was shown highly correlated (i.e., Hernández-Carrasco et al., 2014, 2018; Lehahn et al., 2007; Nencioli et al., 2013).

Fig. 5.4 shows a snapshot of the Chl-a field during the autumn bloom in 2015 together with the FSLEs field computed during the same period. The local maximum of the Chl-a in several places (i.e., at the location marked by the letters A and B, Fig. 5.4a) is collocated with the eddy-like structures in the FSLEs field obtained from the model simulations (Fig. 5.4c). Additionally, the horizontal gradient of Chl-a (Fig. 5.4b), estimated as a bidirectional gradient norm of the daily Chl-a, $\nabla Chla = \sqrt{\left(\frac{\partial Chla}{\partial x}\right)^2 + \left(\frac{\partial Chla}{\partial y}\right)^2}$, is often used as an indicator of ocean productivity fronts (i.e., Kouketsu et al. 2016, Druon et al., 2019). Visual inspection of the Chl-a gradients and the FSLEs reveals a quite similar patterns and demonstrates that high concentrations of Chl-a are confined to the zones of large stirring, i.e., their spatial extension and shape mimic the ridge lines distribution. Therefore, the

inherent features of ocean turbulence, delivered from the numerical model, are assumed to control the spatial distribution of biological materials.

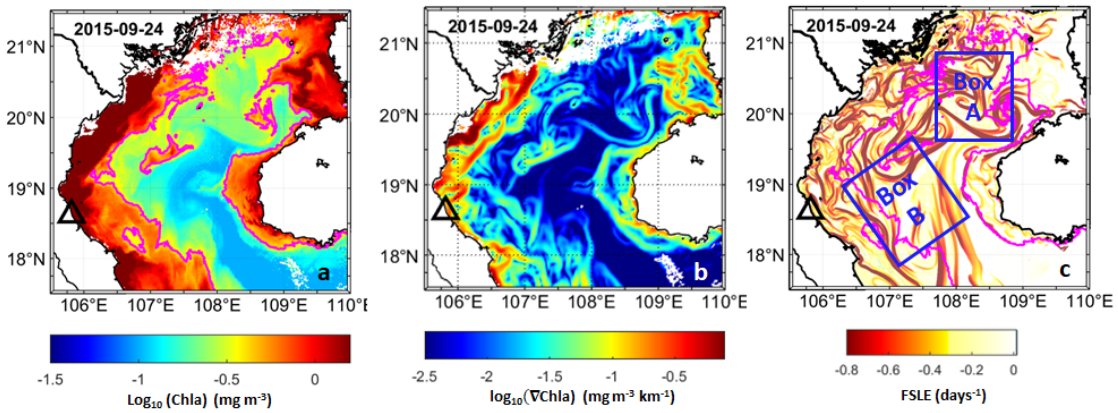

Figure 5.4: Chl-a concentrations in the GoT on 24-September-2015 (a), gradients of Chl-a field indicating the productivity frontal zones (b) and the distribution of FSLEs from numerical simulations (c). Magenta lines mark the regions of high Chl-a concentrations. Rectangles show the location of northern (box A) and southern region (box B) identified for detailed analysis.

Fig. 5.5 shows three snapshots representing the time evolution of small-scale turbulent structures identified in the FSLE fields and the Chl-a concentrations for the same period spanning from the end of October to mid-November. From Fig. 5.5a, it is seen that high concentrations of Chl-a are found in the northern gulf (region A) and along the Vietnamese coast (region C) where they exhibit a large stirring (as inferred from the large density of FSLEs in these regions). Moreover, the minimum of Chl-a concentrations is located in the middle gulf below 19.5°N in correlation with the region of low FSLEs. Therefore, it can be said that the high stirring in the northern gulf and along the coast acts as barrier between these regions and the middle and southern gulf.

At the beginning of November, a zone of high stirring is found in region D (Fig. 5.5b). It matches the location of the slope current running along 50 m isobath (as shown in the chapter IV). Along the front of the slope current, the small-scale eddies are generated by high strain in velocity field and instabilities of currents. These small-scale eddies are effective in strengthening the horizontal advection and diffusion of the nutrients and phytoplankton (Capet et al., 2008a). The high concentrations of Chl-a observed in the northern gulf are stirred and stretched along the high-value FSLE ridge lines toward the southern gulf (Fig. 5.5b). However, the barrier between the offshore (location D, ~150 km offshore) and nearshore region (location C) is still maintained by this vigorous stirring and locally traps the biomass between the coastal zone and the offshore region (Fig. 5.5b, c). These results suggest that the horizontal mixing induced by the small scales thereby could affect phytoplankton growth in the GoT.

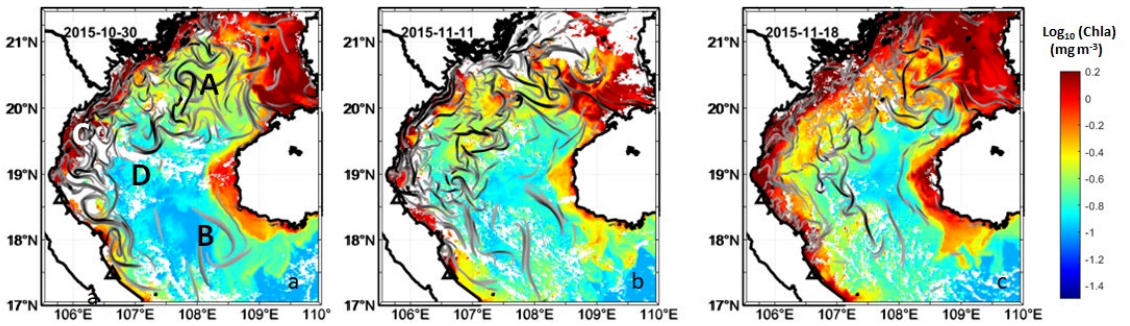

Figure 5.5: Snapshots of Chl-a concentrations from 30-October-2015 to 18-November-2015 superimposed on the FSLEs map computed from numerical model

5.3.3. Co-variation of biomass concentration and FSLEs

As an indicator of turbulent mixing, FSLEs can be used to inspect the turbulence level in the flow field. Taking the spatial average of the daily FSLEs in the northern gulf (box A) and the southern gulf (box B), a proxy of the horizontal turbulence level can be defined for two regions (Fig. 5.6). A common feature between the two regions is a decrease of mixing intensity during winter and an increase in summer and autumn. It suggests that the small-scale features in the GoT are not populated during the cold winter (averaged FSLE values less than 0.2 $days^{-1}$) and this period can last from the beginning of winter until April (in box A) or even until July (in box B). Although during this period, the mixed layer depth, which supplies the energy to form small-scale motions, can extend toward the bottom, the presence of the strong northeast wind can break the geostrophic balance and quickly wash away the small-scale structures of regional circulation.

In box A, the phase of high turbulence lasts from May until November. As noted, this period of time coincides with the phase of high river discharge that is favoring the formation of small-scale motions. The period from August to October marks the transition from southwest to northeast monsoon. The combination of intense northeast wind and water flow from the VNES/SCS via the Hainan strait intensifies the turbulent motions in this energetic area (Zavala-Garay et al., 2022).

On the other hand in summer, the southeast wind is less intense than in winter and the river discharge in the southern gulf is much lower than in the northern gulf. Thus, the turbulence in box B during summer is mostly caused by the intrusion of the VNES/SCS boundary current that flows northeastward around the shelf break (Fang et al., 2012). Under the effect of the northeast monsoon, the fresh water from the Red River is transported southward within a buoyancy-driven flow along the Vietnamese coast. This coastal current is reinforced by the southward flow in the deeper part of the northern gulf leading to an enhancement of turbulent motions in a wide region extending from the shore by ~100 km.

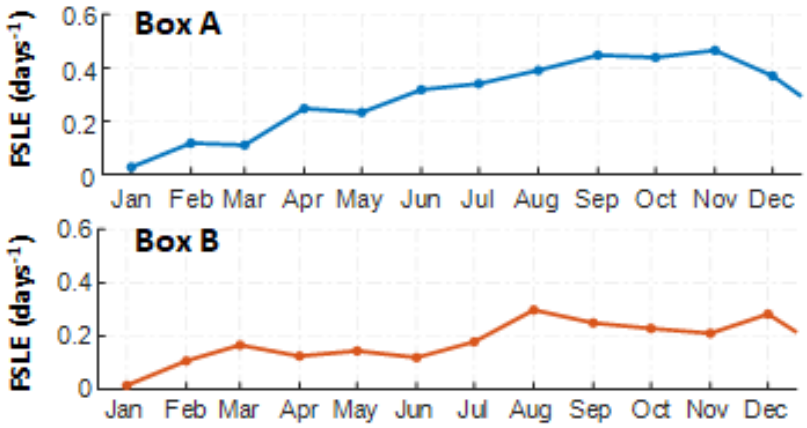

Figure 5.6: Temporal evolution of monthly mean, space averaged FSLEs during the year 2015 in two regions: A (blue) and B (orange).

In order to further investigate the relationship between the biological processes and turbulent motions, we analyzed a co-variation of daily mean FSLEs and Chl-a concentrations in each of two regions and for two periods of the year – winter-spring and summer-autumn. The former period is characterized by a relatively low intensity of turbulent motions: the mean λ is equal to 0.3 (region A) and 0.2 $days^{-1}$ (region B) with the maximum value not exceeding 0.5 $days^{-1}$. At the same time, the Chl-a shows large variability in the range 0.1 to 1 mg/ m^{-3} (Fig. 5.7a). The low correlations were found between FSLEs and Chl-a in both regions (0.39 and 0.2 respectively). Therefore, it could be said that the limited horizontal stirring is unlikely to have effect on Chl-a concentrations increase during this period.

During summer and autumn, the turbulence activity is higher, however, it coincides with the period of lower Chl-a concentrations averaged over each region, with the mean Chl-a values of 0.3 and 0.17 mg m^{-3} for box A and box B respectively. The positive correlations (0.45 and 0.51) between FSLEs and Chl-a emerge in both regions: larger is the surface stirring/mixing, larger is the Chl-a concentration (Fig. 5.7b). Moreover, Fig. 7b suggests that the increase of Chl-a concentrations in the northern gulf during the oligotrophic summer/autumn period is more likely favored by the stirring and turbulent mixing, which are much weaker in the southern gulf. Also, it is worth noting that the flatter trend observed in the southern gulf could highlight the fact that a water body with low nutrient concentrations is trapped within the large-scale circulation structure there. It maintains the Chl-a concentration low during summer/autumn which can be observed in the climatological field (Fig. 5.1).

In addition, the highest correlation between Chl-a and FSLE time series is obtained for a time lag of 7 days. The period of 7-days is longer than a typical period of most of oceanic motions (e.g., internal gravity waves, near-inertial waves, and tidal motions) (Zhang et al., 2019). This time lag could be related to a characteristic timescale for bringing unused nutrients into the oligotrophic area and possibly boost the phytoplankton growth (Zhang et al., 2019).

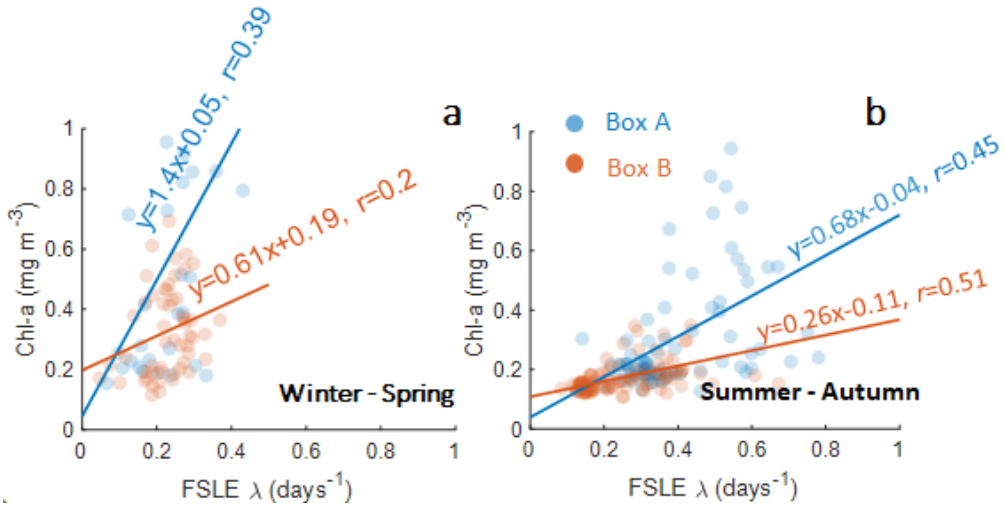

Figure 5.7: Scatter plots of spatially averaged daily Chl-a concentrations and daily FSLE values in box A (blue dots) and box B (orange dots) for two periods of the year: winter-spring (December - April) and summer-autumn (May-November) characterized by different level of horizontal mixing.

5.4. Summary

In this chapter, we investigated the role of (sub)mesoscale motions in structuring the spatial distribution of biological fields by examining the variation of Chl-a distribution in space and time (seasonal variation). The level of horizontal stirring in the flow field was estimated using FSLE, obtained from the Lagrangian tracking experiments. The results of Lagrangian tracking model provided the locations of regions with high horizontal stirring which were found to be positively correlated with the spatial distribution of the phytoplankton. The horizontal mixing shows an increase in intensity during summer and autumn. Two-dimensional advection processes revealed from FSLE maps largely contribute to structuring the distribution of biomass during the same period of time when the major biological drivers are weak (i.e., increase in stratification due to temperature rise and decrease of vertical mixing). Our findings indicate that the vigorous stirring induced by fine-scale motions has a dual role. On the one hand, it acts as a barrier that blocks the exchange of water between the coastal and offshore regions and between the northern and the southern gulf in autumn - when a larger level of turbulence in the flow is observed. On the other hand, an episodic increase of turbulent motions in the mean flow induces entrainment of the water rich in nutrients to the oligotrophic offshore areas, thus, boosting the primary production. The areas with high Chl-a concentrations appear to be delimited by the LCSs, which locations were distinctly identified using a numerical model coupled with a Lagrangian transport model.

Chapter VI. General Conclusions and Perspectives

The hydrodynamics of the Gulf of Tonkin, situated in the northwestern part of the Vietnam East Sea (or the South China Sea), was documented only in a limited number of publications (in English) and was mostly based on modeling studies. The complex hydrodynamics of the GoT is a result of a macro tidal regime, significant river freshwater discharge, and strong seasonal variability of atmospheric forcing. However, the response of the GoT circulation to these forcings remains poorly understood. The lack of systematic observations in the region is assumed to be the main reason that prevents further analysis of the overall scheme of the water dynamics in this basin, especially leading to the debate on the seasonal variability of the flow field (e.g., cyclonic/anti-cyclonic circulation in summer) and the role of physical processes controlling this variability.

In this context, the main objective of the present study was to improve the knowledge of the coastal water dynamics in the GoT. To reach this objective, we took advantage of the continuous measurements from coastal HF radars operating in the GoT. The radar data can be potentially used for assessing the hydrodynamical model performance and analyzing the surface current variability in the region. In my PhD thesis the data of a 2.5-year-long period (April 2014 – October 2016) were used because, during this period, the radars performed rather stable and provided the largest coverage. Long-time series of surface current velocities allowed assessment of the spatio-temporal variability of the surface circulation in the study area at different scales, spanning from the tidal and sub-tidal frequencies to the annual scale.

Characterization of ocean currents is important as it provides valuable information for many aspects of human activities including marine ecology, economics, water management, etc. In this regard, high-performance technology of surface current monitoring (HF radars), which are set up along the coast of Vietnam, appears to be useful for assessing the coastal circulation, the transport and dispersion of materials in the water, or evaluation of the potential of marine renewable energy and validation of hydrodynamic models. Additionally, the HF radar observations in Vietnam will possibly integrate the emerging international network aiming at environmental monitoring of the coastal regions.

Despite the undeniable capability of the HF radar system to provide nearly real-time observations of surface circulation at large spatial scales, the measurements are always affected by the uncertainty related to the observational coverage decrease with distance, hardware failure, etc. To acquire the most accurate current velocity maps from the radar measurements, we implemented the variational approach (EOF/2dVar), proposed by Yaremchuk & Sentchev (2011) for radar data processing. This non-local, kinematically constrained interpolation method is capable of producing a continuous, gap-free dataset and particularly effective in case of radar failure during short periods (1 ~ 2 days of one radar malfunction). The performance of the EOF/2dVar method was evaluated by comparison with the *in-situ* measurements of surface current velocities and Lagrangian drifter trajectories available in the study area. A good agreement is found between different sources of data and the results of the comparison are quite consistent with those documented in previous studies performed in other coastal ocean regions (e.g., Liu et al., 2014; Molcard et al., 2009; Yaremchuk et al., 2016). This increases our confidence in using HF radar data for the analysis *of the surface circulation in the GoT.*

Characterization of the surface circulation in the GoT – the added value of HF radar measurements

In the first part of the study, the data from two radar sites (XUAN and DHOI) were reprocessed by the EOF/2dVar interpolation method to obtain the gap-free 2.5-year-long velocity time series. This extended dataset enables the assessment of the surface current velocity variability in the data-poor region of the southern GoT.

The results of the HFR data analysis revealed the dominant role of tides and monsoon wind in the variability of circulation. At high frequency, fortnightly variation of the current velocity is shown to be consistent with individual velocity measurement by AWAC while at a lower frequency (monthly to seasonal scale), the current velocities were closely correlated with the surface wind. Though this has been documented in several modeling studies, the radar-derived velocity data revealed the flow complexity and variability at a level of detail that was not previously available.

Different scales of space-time variation of circulation in the GoT have been quantified. The results revealed that the contribution of tides to the total velocity variability is close to 60%. The circulation in the GoT is primarily driven by the diurnal tidal regime. The spatial patterns of tidal ellipses demonstrated the propagation of the tidal wave parallels the coast. The current velocity magnitudes were found larger (~0.6 m s^{-1}) in the southern gulf entrance while they decrease gradually to ~0.2 m s^{-1} toward the middle gulf (~19°N) due to the bottom friction. Regarding the velocity magnitude of tidal components, the velocity of diurnal tidal constituents (K1 and O1) was found 4 and 8 times larger than that of semi-diurnal, M2 and S2 constituents, respectively. These results are consistent with the

previous modeling-based study of Minh et al. (2014) focusing on analysis of the tidal circulation in the GoT.

The contributions of different forcing terms to the total variability of the surface circulation were also quantified. The results revealed the energy transfer from large-scale (low-frequency) variability of currents, in winter, to their low-scale (higher frequency) variability, in summer. In winter, the surface currents are mostly driven by the wind. High correlation (~0.8) was found between the radar-derived velocities and the reanalyzed wind stress. During the summer period, smaller correlation (~0.5) suggests a possible contribution of other factors, e.g., sea-breeze motions capable to amplify the current variability at diurnal frequency. Buoyancy forcing, mesoscale motions, or possibly the effects of remote forcing (i.e., typhoons), can also contribute to high-frequency variability of surface circulation in summer.

Lastly, the role of freshwater discharge, mainly from the Red River, in modulation of coastal circulation was assessed as it enhances the complexity of current patterns. The low salinity, surface advected water body (about 5 m thick) appears practically detached from the bottom layer. Extending southward along the coast, a frictionless water body, forced by the strong northeasterly wind, causes the near-shore current intensification. We found that the speed of nearshore flow, induced by the southward advection of buoyancy in combination with the intense NE wind, can readily exceed 1 m s^{-1}. The period of nearshore current intensification lasts 8 to 9 months corresponding to the maximum extension of the river plume observed in late fall (September to October) while the period of weaker flow intensity (lower velocities) occurs in mid-summer (June to July).

The zonal wind component experiences a closely harmonic seasonal variation and induces a cross-shore mass exchange, thus affecting the coastal flow speed and seaward extension. On the contrary, the meridional (along shore) wind component variability causes only a weak modulation of the coastal current.

Assessment of Lagrangian transport and dispersion properties in the GoT using the radar data and high-resolution numerical model

In the second part of the study, we characterized the transport patterns and assessed the turbulent dispersion in the GoT using the Lagrangian framework. This implied the advection of virtual particles (water parcels) in the radar-derived velocity fields and also using the high-resolution numerical model (SYMPHONIE model). The regional model, which was developed for the GoT (Piton et al., 2020, 2021) and extensively improved in Nguyen-Duy et al. (2021), allows identifying fine-scale structures in the flow field. These structures, with spatial scales from one to a hundred km and temporal scales from days to weeks, largely affect the transport patterns and dispersion properties. To the best of our knowledge, the problem of turbulent dispersion has not been addressed yet in this region. The analysis

was performed for two periods, August and November 2015, representing the typical summer and winter conditions.

In the first step, a comparison of Lagrangian statistics was done using virtual particles advected in the radar-derived velocity field and then using the numerical model velocities. While the particle distribution 30-days after the release diverges significantly in both cases, the particle trajectories look rather similar, especially for the first 15 days. Lagrangian statistics (relative dispersion and FSLE) estimated by using two velocity fields (radar-derived and numerical model) indicated a similar change in dispersion regime for scales above 20 km. Therefore, it suggests an acceptable accuracy of the model and its capability in reproducing large-scale, low-frequency variability of the regional dynamics and transport patterns. However, the difference in dispersion statistics at smaller scales indicated that the coarse resolution of the HFR data limits the exploration of small-scale turbulent dispersion. In the small-scale range, the dispersion rate estimation based on radar measurements is significantly lower than that obtained in the model simulations, e.g., in November, the rate of dispersion was found two times smaller. This explains the difference in the spatial distribution of advected particles in two velocity fields. The model advected particles are stirred more effectively and appear clustered in several distinct locations.

After that, we moved further and employed only the numerical model for the assessment of transport and dispersion statistics at the scale of the whole GoT. From that, the seasonal variability in transport patterns and dispersion regimes was characterized. As the GoT circulation is largely driven by the monsoon wind, the final distribution of particles after 30 days of tracking showed significant differences in August and November. In August, the advected particles are more scattered around the gulf and a large portion of them are concentrated in several eddy-like structures in the middle and northern gulf. Whereas in November, the advected particles are confined to the western part of the gulf and are mostly organized within long filaments. The turbulent dispersion regimes in the two seasons also appear different revealing a change from the Richardson super-diffusive regime to the ballistic regime for the scales of motions above 20 km.

It is worth noting that the first baroclinic Rossby radius of deformation, R_d, appears to be a key length scale that plays a role in separating different regimes of dispersion. In our study, a non-local dispersion regime is found at scales below R_d while a local dispersion is observed at larger scales, which is in agreement with the results of earlier investigations performed in different regions of the world ocean (e.g., Haza et al., 2008; R. Corrado et al., 2017). The value of R_d in the GoT varies from season to season, and it is smaller in winter due to stronger vertical mixing and larger in summer when the water column is more stratified. R_d also varies in space, from the coastal to the open sea region. The smaller value of R_d, ~1 km, is obtained near the coast and the larger value, ~16 km, is found in the deeper water near the southern entrance (see Nguyen-Duy et al., 2021, their Fig. 4).

Additionally, the effect of river discharge on turbulent dispersion is also examined in this study. By turning on and off the river discharge in the model, its relative contribution to the dispersion of tracers can be quantified. During both periods considered, the river input in the model enhances the dispersion in a wide range of scales, from sub-mesoscale to ~50 km. The river discharge causes a significant decrease in e-folding time (the time interval in which the particle separation increases by a factor of e) from roughly 2.5 days to 1.25 days, evidencing a much larger rate of dispersion in the sub-mesoscale range (at the scale below 15 km). The river discharge (when introduced in the model) creates buoyancy gradients and enhances the sub-mesoscale dynamics which in turn increases the dispersion and affects significantly the Lagrangian statistics, especially during the rainy season.

Studying the transport pathways in the GoT involves the characterization of turbulent coherent structures (such as jets and eddies), which dictate much of the transport patterns. These dynamical structures are driven by intrinsic spatio-temporal variability of the flow field and also by the external forcing (such as wind, buoyancy, etc.) that exerts on the flow. In the shallow water region, these structures experience large variability and are prone to the interaction of intense wind and large riverine input which can be identified by the adequate settings of the FSLE method (i.e., the initial and final separation of the particle set). The Lagrangian Coherent Structures (LCSs), identified from the FSLE method, give the location of regions with strong stretching and dispersion of materials, i.e., areas of strong stirring in the flow. By analyzing the spatial variability of FSLEs fields, four regions with a high level of dispersion were identified in the GoT: a nearshore region under the fresh-water influence, an offshore region distant by ~100 km from the coast, a central part of the northern gulf, and a region close to the southern gulf entrance. These regions should be considered as hotspots with enhanced influence of hydrodynamics on particulate distribution as well as on marine ecology. We clearly demonstrated that areas with high concentration of Chl-a coincide with those of large stirring. Spatial organization of Chl-a distribution and its temporal variability appears to be significantly affected by turbulence which generates stirring and imposes natural barriers for phyplankton distribution (results presented in Chapter V). In addition, the wind forcing and the freshwater discharge, both largest during autumn, modulate the Chl-a variability in low-frequency band.

Perspectives

The results obtained in this study provide insight into the complexity of surface circulation in the GoT. However, several limitations would be worth addressing as they prevent improving the knowledge of the GoT dynamics. The first limitation comes from the short duration of the analysis. As mentioned previously, the analyses performed in this study are mostly based on 2.5-year data (from 2014 to 2016) provided by the radar measurements. Therefore, a longer dataset covering more years would be useful for assessing the long-term variability of the surface circulation in the GoT (e.g., inter-annual

variability related to ENSO phenomena) and the analysis of additional processes such as the response of the GoT circulation to remote forcing from the VNES/SCS basin.

Future directions of the research will include the application of the regional hydrodynamic model, which allows a three-dimensional description of the circulation in the GoT, and the operational forecasting system with data assimilation capability. Indeed, it still exists many uncertainties in the use of a numerical model which may come from the parameterization of forcing and the use of different turbulent mixing schemes. Therefore, a large and reliable coastal radar dataset can be used for improving the numerical model in long term. Assimilation of the near-real-time radar data in a model is a good way to provide more accurate boundary conditions at the sea surface and improve the surface current fields. Therefore, this direction of research can help to improve the representation of the circulation in this region.

Further investigations using Lagrangian observations (drifter observations) are necessary as the Lagrangian approach can be used to address the fundamental problems of ocean dynamics. Lagrangian observations are valuable in oceanographic applications related to particulate material transport, dispersion, and marine biology. However, at the present stage, the number of real drifter observations in the GoT is highly insufficient as highlighted by Gao et al. (2017). Given the lack of Lagrangian observations, HF radar measurements, and modeling appear as appropriate tools for the analysis of turbulent dispersion. The Lagrangian instruments are categorized into two types: a) drifters, which follow the water in the surface layer, and b) floats, which can sink to a specific depth (D'Asaro et al., 2020). Both of them will be useful not only in validating the oceanic numerical circulation model and radar measurements but also enable detailed studies of turbulent dispersion at different levels.

The current convergence and divergence are viewed as the physical processes that are tightly related to vertical motions and a possible clustering of particulate materials in the ocean. For example, sub-mesoscale structures (spatial scales of hundreds of meters to tens of km) associated with horizontal density fronts with strong surface convergences and downwelling, may lead to three-dimensional patterns of particle distribution (e.g., D'Asaro et al. (2018); Essink et al. (2018). These processes can be important for biogeochemical activities as the enhancement of vertical mixing in the frontal zone sweeps floating material to the front and controls the supply of nutrients necessary for marine organism growth. Also, toxic materials, such as oil spills, can be driven down to depth by downwelling motions, thus, amplifying their impacts on the ocean (D'Asaro et al., 2018). In our opinion, this subject would deserve a separate, more thorough investigation in the nearest future.

Conclusion Générale

L'hydrodynamisme dans le Golfe du Tonkin (GoT), situé dans la partie nord-ouest de la mer Orientale du Vietnam (mer de Chine Méridionale), n'a été documenté que dans très peu d'études, basées principalement sur la modélisation. La circulation complexe dans le golfe résulte d'un forçage macro-tidale, d'un important apport d'eau douce des fleuves et d'une forte variabilité saisonnière des forçages atmosphériques. La réponse de la circulation régionale à ces forçages reste mal comprise.

Le manque d'observations systématiques est probablement la principale raison qui empêche une bonne compréhension du schéma global de la dynamique dans ce bassin. Cela induit notamment le débat sur la variabilité saisonnière de la circulation (par exemple, circulation cyclonique ou anticyclonique en été) et sur rôle des processus physiques contrôlant cette variabilité. Dans ce contexte, l'objectif principal de ce travail de thèse était d'améliorer la connaissance de la dynamique côtière dans le GoT en utilisant un outil très puissant de télédétection des courants superficiels par radars océanographiques Haute Fréquence (radars HF), installés depuis 2012 sur la côte dans la partie nord du Vietnam.

L'application de méthodes performantes de traitement de données a rendu possible la constitution des séries longues de vitesse des courants de surface, l'analyse de la variabilité des courants ainsi que l'évaluation des performances d'un modèle de circulation régionale. Dans ce travail de thèse, les données d'une période de deux ans et demi (avril 2014 - octobre 2016) ont été utilisées car, pendant cette période, les radars avaient un fonctionnement plutôt stable et la couverture spatiale par des mesures était plus grande. Des séries longues de vitesse, à haute fréquence d'échantillonnage et d'une couverture spatiale étendue, ont servi pour évaluer la variabilité des courants dans une large gamme d'échelles allant de la fréquence de marée à l'échelle annuelle.

La caractérisation des courants océaniques est importante car les informations obtenues sont utilisées ensuite dans de nombreux domaines d'activités humaines, à savoir l'écologie marine, l'économie, la gestion de l'eau, etc. Elles s'avèrent cruciales en cas de gestion de crises liés aux catastrophes survenues en mer ou prêt des côtes (naturelles ou causées par des acticités humaines), pour l'évaluation du transport et de la dispersion des matières polluantes en dérive avec les coutants, ou encore pour l'évaluation du potentiel des énergies marines renouvelables. Le réseau radar HF existant au Vietnam intégrera prochainement un réseau international, en constitution depuis les dernières années, qui vise à surveiller continuellement l'environnement marin des régions côtières.

Malgré la capacité d'un réseau radar HF à fournir des observations de la circulation océanique côtière à de grandes échelles spatiales et presque en temps réel, les mesures radar sont toujours affectées par une incertitude liée à la diminution de la portée, à des pannes matérielles, etc.

Pour gérer le problème d'incertitudes, et tirer le meilleur profit de la mesure, nous avons implémenté une technique variationnelle (EOF/2dVar) pour le traitement des données radar. Proposée par Yaremchuk et Sentchev (2011), cette technique d'interpolation non-locale, intégrant des contraintes dynamiques, est capable de générer des séries longues et continues de vitesse. Elle s'est avérée particulièrement efficace en cas de pannes ou dysfonctionnements de radars pendant de courtes périodes (1 ~ 2 jours). Les performances de la méthode EOF/2dVar ont été évaluées par comparaison avec d'autres mesures in-situ de vitesses de courants de surface et avec des trajectoires de bouées lagrangiennes disponibles dans la zone d'étude. Un bon accord a été trouvé entre les différentes sources de données et les résultats de la comparaison ont été trouvés cohérents avec ceux documentés dans les études précédentes réalisées dans d'autres régions océaniques côtières (e.g., Liu et al., 2014 ; Molcard et al., 2009 ; Yaremchuk et al., 2016). Les résultats de cette évaluation ont renforcé notre confiance dans les données radars HF et leur utilisation pour l'analyse de la circulation de surface dans le GoT.

Caractérisation de la circulation superficielle dans le Golfe du Tonkin – la valeur ajoutée des mesures radar HF

Dans la première partie de l'étude, les données en provenance de deux sites radar (XUAN et DHOI) ont été retraitées par la méthode EOF/2dVar pour obtenir des séries continues de vitesses. Ces données, couvrant une période de temps assez étendue (deux ans et demi), ont servi à l'évaluation de la variabilité des courants de surface dans la partie sud du golfe du Tonkin –la région dépourvue d'observations.

Les résultats de l'analyse ont révélé le rôle dominant de la marée et du vent saisonnier (la mousson de l'Asie du sud-est) dans la variabilité de la circulation. Aux échelles inférieures à un mois, les variations de la vitesse de courants sont essentiellement dues à la marée, ce qui est cohérent avec les observations indépendantes réalisées par AWAC. En revanche, de l'échelle mensuelle à l'échelle saisonnière, la vitesse de courants a été étroitement corrélée avec le vent de surface. Bien que cela ait été documenté dans plusieurs études de modélisation, les données de vitesse issues de la télédétection radar ont révélé la complexité de l'écoulement et de ses variations à un niveau de précision qui n'était pas disponible auparavant.

Les différentes échelles de variabilité spatio-temporelle de la circulation ont été quantifiées. Les résultats ont révélé que la marée contribue à la hauteur de 60% dans la variation totale des vitesses. La circulation dans le GoT est principalement dominée par le régime des marées diurnes. La

représentation spatiale des ellipses de marée a montré la propagation de l'onde de marée parallèlement à la côte. La vitesse des courants de marée a été trouvée plus grande (~0,6 m s-1) dans le sud du golfe et au voisinage de la frontière ouverte, alors qu'elle diminue progressivement, jusqu'à ~0,2 m s-1 , vers le milieu du golfe (~19°N), en raison du frottement sur le fond. En ce qui concerne l'amplitude de la vitesse des composantes dominantes, elle a été trouvée 4 et 8 fois plus grande pour les composantes diurnes (K1 et O1) que pour les composantes semi-diurnes (M2 et S2) de la marée. Nos résultats sont cohérents avec ceux rapportés par Minh et al. (2014), issus de la modélisation de la circulation de marée dans le golfe.

La contribution de différents termes de forçage dans la variabilité totale de la circulation de surface a également été quantifiée. Les résultats ont révélé le transfert d'énergie de la variabilité à grande échelle (basse fréquence), en hiver, vers la variabilité à petite échelle (fréquence plus élevée), en été. En hiver, les courants de surface sont principalement générés par le vent. Une corrélation élevée (~0,8) a été obtenue entre les vitesses mesurées par radar et la tension du vent. Pendant la période estivale, une plus petite corrélation (~0,5) suggère que d'autres processus apportent leur contribution à la variabilité: par exemple, la brise marine amplifie les variations des courants à la fréquence diurne. Les flux de flottabilité depuis des estuaires vers la mer, la dynamique à fine échelle ou éventuellement les forçages distants (par exemple, les cyclones tropicaux) peuvent engendrer les variations à haute fréquence de la circulation de surface en été.

Enfin, le rôle des apports d'eau douce par des rivières, principalement par le fleuve Rouge, dans la modulation de la circulation côtière a été étudié car ces apports augmentent la complexité de la dynamique dans cette région. Une couche d'eau, d'environ 5 m d'épaisseur, de faible salinité, se trouve pratiquement détachée de la couche inférieure et advectée par le vent en surface. S'écoulant vers le sud le long des côtes vietnamiennes sans frottement, ce grand volume d'eau, forcé par le vent soutenu du nord-est, génère l'intensification du courant côtier. Nous avons démontré que la vitesse peut dépasser 1 m s-1 dans cet écoulement côtier, intensifié par les apports fluviaux et le vent du nord-est, soufflant pendant la mousson d'été. La période d'intensification de ce courant côtier dure de 8 à 9 mois et correspond à l'extension maximale du panache fluvial se produisant généralement vers le milieu de l'automne (de septembre à octobre). En revanche, la plus faible intensité du courant est observée en été (de juin à juillet).

La composante zonale du vent, qui suit une variation saisonnière quasi harmonique, induit un transfert de masse et de quantité de mouvement en direction perpendiculaire à la côte (échange côte-large). C'est cette composante qui contrôle les variations de la vitesse du courant côtier et son extension vers la mer. Au contraire, la variabilité de la composante méridienne du vent (orientée le long des côtes) ne crée qu'une faible modulation du courant côtier.

Caractérisation du transport et de la dispersion lagrangienne dans le Golfe du Tonkin à partir des mesures radar et de la modélisation à haute résolution

Dans la deuxième partie de la thèse, nous avons abordé la problématique de la caractérisation du transport et de la dispersion turbulente dans le GoT en utilisant une approche lagrangienne. Cette approche fait intervenir des particules virtuelles (petits volumes d'eau étiquetés) advectées dans le champ de vitesse des courants mesurés par radar et également issues d'un modèle numérique à haute résolution (modèle SYMPHONIE). Ce modèle de circulation régionale a été mis en œuvre dans le GoT pour la première fois par Piton et al. (2020, 2021). Puis il a été beaucoup amélioré par Nguyen-Duy et al. (2021), dans le cadre de sa thèse au LEGOS. Ces améliorations et un raffinement du maillage du modèle ont permis de reproduire des structures dynamiques à fines échelles dans l'écoulement et plus particulièrement au voisinage des côtes vietnamiennes. Ces structures, caractérisées par des échelles spatiales allant d'un à cent km et des échelles temporelles allant du jour à la semaine, affectent fortement le transfert d'eau et de matière via le mécanisme de dispersion turbulente. A notre connaissance, cette problématique scientifique n'a pas encore été abordée dans cette région géographique et même dans la région plus vaste de l'Asie du sud-est.

Nous avons procédé à l'évaluation des caractéristiques du transport lagrangien et de la dispersion turbulente en se focalisant sur deux périodes de l'année 2015, août et novembre, représentant les conditions typiques d'été et d'hiver. Dans un premier temps, une comparaison des statistiques lagrangiennes a été effectuée en utilisant des de trajectoires de particules virtuelles advectées dans le champ de vitesse issue de la télédétection des courants par radar, puis en utilisant les vitesses du modèle.

Alors que la distribution spatiale des particules, lâchées au même endroit et suivies pendant 30 jours, a montré une différence notable à la fin de la période en fonction des champs de vitesse utilisés, les trajectoires de déplacement des particules ont parues assez similaires pendant les 15 premiers jours de suivi. Les diagnostiques lagrangiens (dispersion relative et FSLE) obtenus pour ces deux champs de vitesse (radar et modèle) ont clairement montré une similitude quant au changement du régime de dispersion aux échelles supérieures à 20 km.

Cela nous a convaincu dans la capacité du modèle SYMPHONIE à reproduire assez fidèlement la variabilité de la dynamique régionale à grande échelle et basse fréquence et avec une précision acceptable. En revanche, la différence relevée dans les statistiques de la dispersion à des échelles plus petites a indiqué que la résolution spatiale assez basse des mesures radar (~6 km) rend difficile, voir impossible, la caractérisation de la dispersion turbulente à cette échelle. Dans cette gamme d'échelles, l'estimation du taux de dispersion obtenue à partir des mesures radar a été nettement inférieure à celle obtenue à partir des simulations numériques. Par exemple, en novembre, le taux de dispersion

turbulente a été deux fois plus petit. Ceci permet d'expliquer une plus grande différence dans la distribution spatiale des particules à la fin du suivi en novembre. Lorsque les particules sont advectées dans le champ du modèle, leur dispersion se révèle beaucoup plus grande et elles apparaissent regroupées en clusters, assez éloignés les uns des autres.

Après cette étude préliminaire, nous sommes allés encore plus loin dans l'utilisation du modèle pour l'évaluation des propriétés de transport et de dispersion à l'échelle de tout le golfe du Tonkin. La variabilité saisonnière des schémas de circulation, du transport et des régimes de dispersion turbulente a été caractérisée. Comme la circulation superficielle dans le GoT est largement contrôlée par le vent de mousson, la distribution finale des particules après 30 jours de suivi a montré des différences notables entre les deux saisons, plus précisément entre le mois d'août et le mois de novembre. En août, les particules sont plus dispersées au sein du golfe et une grande partie d'elles se trouvent regroupée dans plusieurs structures tourbillonnantes situées au centre et dans le nord du golfe. Alors qu'en novembre, les particules se trouvent confinées dans une large partie ouest du golfe et s'organisent majoritairement en longs filaments longeant les côtes vietnamiennes. Les régimes de dispersion turbulente au cours des deux saisons apparaissent également différents et montrent une évolution du régime super-diffusif (régime de Richardson) vers le régime balistique, et ceci pour les échelles spatiales supérieures à 20 km.

Il convient de préciser que le rayon barocline de déformation de Rossby, Rd, représente une grandeur clé dans le spectre d'échelles de mouvements et joue un rôle déterminant dans la séparation des différents régimes de dispersion. Nous avons mis en évidence le fait que le régime de dispersion était non-local aux échelles inférieures à Rd , tandis que la dispersion a été diagnostiquée locale aux échelles plus grandes (supérieures à Rd). Nos conclusions confirment les résultats d'autres études réalisées antérieurement dans de différentes régions océaniques (e.g., Haza et al ., 2008 ; R. Corrado et al., 2017). La valeur de Rd varie dans le golfe en fonction de la saison: elle est plus petite en hiver, en raison d'un mélange vertical plus intense, et plus grande en été, lorsque la colonne d'eau est beaucoup plus stratifiée. Le rayon de déformation varie également dans l'espace, principalement de la côte vers le large. La plus petite valeur de Rd, ~1 km, est obtenue au voisinage des côtes et la plus grande valeur, ~16 km, dans la partie profonde du golfe - près de la frontière sud (voir Nguyen-Duy et al., 2021, Fig. 4).

En outre, l'effet des apports d'eau douce des fleuves sur la dispersion turbulente a été évalué dans cette partie de l'étude. En activant ou désactivant le débit des fleuves dans le modèle, son impact sur la dispersion turbulente de traceurs passifs pourrait être quantifiée. Nous avons démontré que les apports d'eau douce, pris en compte dans le modèle, augmentent la dispersion dans une large gamme d'échelles - de la sous-mésoéchelle jusqu'à ~ 50 km, et ce pour les deux périodes considérées. Le débit des fleuves, introduit dans le modèle de manière réaliste, conduit à une diminution significative de la

constante de temps de croissance exponentielle: de 2,5 à 1,25 jours (il s'agit de l'intervalle de temps pendant lequel la séparation des particules augmente d'un facteur e). Cela se traduit par un taux de dispersion beaucoup plus élevé aux échelles inférieures à 15 km (la gamme de sous-mésoéchelle). Les apports d'eau douce créent les gradients de salinité et facilitent la génération de structures dynamiques à sous-méso-échelle ce qui affecte de manière significative la dispersion et les statistiques lagrangiennes, en particulier en été, pendant la saison de pluies.

L'étude du transport d'eau et de matière à l'intérieur du bassin implique la caractérisation des structures dynamiques cohérentes, telles que des jets et des tourbillons, sans lesquels il est difficile d'établir des schémas de transfert réalistes. Ces structures dynamiques sont régies par les variations intrinsèques de la vitesse de l'écoulement et également des forçages externes (vent, apports d'eau douce, etc.) qui contrôlent l'écoulement. Dans le Golfe du Tonkin, région peu profonde, ces structures sont particulièrement sensibles aux variations du vent et des apports fluviaux et par conséquent peuvent facilement changer la forme et la localisation ou interagir entre elles, ce qui accroit davantage leur variabilité.

L'approche lagrangienne et plus particulièrement l'utilisation des exposants de Lyapounov (FSLE) permet la caractérisation de ces structures et leur variabilité spatiale et temporelle. Ces structures cohérentes lagrangiennes (LCS), identifiées à partir de la méthode FSLE, nous renseignent sur la nature turbulente de l'écoulement et indiquent la localisation des régions à forte intensité de dispersion de matière ou à fort entrainement de matière.

En analysant les variations spatiale et temporelle de la distribution des FSLE, quatre régions à haut niveau de dispersion turbulente ont été identifiées dans le GoT : une région côtière sous l'influence des apports fluviaux, une région située au large et distante d'environ 100 km de la côte, une troisième située au centre de la partie nord du golfe et une région proche de l'entrée sud du golfe. Elles indiquent les lieux où l'hydrodynamisme exerce une forte influence sur la distribution spatiale de matière (traceurs passifs ou matériel particulaire) et donc peut avoir une importance considérable pour la biologie marine et écologie. Nous avons clairement démontré que les régions de forte concentration de phytoplancton, donc de forte productivité, sont celles où la dispersion turbulente et le mélange horizontal sont les plus forts. L'organisation spatiale du champ de Chl-a et sa variabilité temporelle semble être significativement affectée par la turbulence marine qui génère un brassage d'eau et de matière et crée des barrières naturelles qui structurent la distribution spatiale du phytoplancton. Ces résultats ont été présentés dans le chapitre V de la thèse. Nous avons pu également constater que le forçage éolien et les apports d'eau douce, tous deux plus importants en automne, créent une modulation basse fréquence de la variabilité de Chl-a dans le golfe.

Perspectives

Les résultats obtenus dans cette étude donnent un aperçu de la complexité de la circulation de surface dans le Golfe du Tonkin. En même temps, des limitations liées à l'utilisation de données et des méthodes mériteraient d'être mentionnées.

La première limitation concerne la durée des séries temporelles de vitesses utilisées dans l'analyse. Nous avons spécifié que l'analyse de données radar HF couvre la période de deux ans et demi (de 2014 à 2016) durant laquelle la performance du système de télédétection des courants et la couverture spatiale étaient optimales. Par conséquent, les séries temporelles plus longues, couvrant des périodes plus récentes (au delà de 2016), auraient été utiles pour l'évaluation de la variabilité des courants de surface à plus long terme. Elles permettraient d'accéder à la description de la variabilité interannuelle, évaluer l'impact du phénomène ENSO sur la dynamique ou encore discerner la réponse de la circulation dans le golfe aux forçages distants exercés depuis le bassin VNES/SCS.

Les futures recherches devraient intégrer l'utilisation du modèle hydrodynamique régional, qui permet une description tridimensionnelle de la circulation dans le GoT. Ce modèle (SYMPHONIE), dont les performances ont été mises en avant et quantifiées dans notre étude, est disponible dans des structures de recherche au Vietnam (LMI LOTUS) et en France (LEGOS). Un système opérationnel de prévision, basé sur l'utilisation de ce modèle avec les fonctionnalités d'assimilation de données, apparait comme indispensable dans les années à venir. En effet, des incertitudes persistent dans la modélisation, liées à l'intégration et au paramétrage des forçages et à l'utilisation de différents schémas du mélange turbulent. Par conséquent, les données radar HF, fiables et à haute fréquence d'échantillonnage (une heure), peuvent apporter une amélioration notable de la modélisation numérique à plus long terme. L'assimilation de données radar en temps quasi réel dans un modèle de circulation permettrait l'optimisation des conditions aux limites et par conséquent et l'amélioration des résultats de la modélisation. Cette perspective de recherche peut donc aider à améliorer notre connaissance de la circulation dans cette région et sa représentation fidèle dans les modèles.

Des actions supplémentaires dans la recherche sont nécessaires dans lesquelles l'accent est mis sur l'utilisant des observations lagrangiennes. L'approche lagrangienne est très efficace, et nous l'avons démontrée, pour la recherche des solutions aux problèmes fondamentaux de la dynamique océanique et la dynamique côtière. Les observations lagrangiennes sont indispensables pour des applications océanographiques liées au transport et à la dispersion de matière, à la biologie marine, l'écologie, la gestion de l'eau, etc. Cependant, le nombre d'observations lagrangiennes réelles (par bouées dérivantes) actuellement disponibles dans le golfe est très insuffisant, comme c'est souligné dans (Gao et al., 2017). En l'absence d'observations lagrangiennes, les mesures radar HF et la modélisation apparaissent comme des outils de premier plan, indispensables pour l'étude de la turbulence marine, la dispersion turbulente et la dynamique à sous-mésoéchelle. Les instruments lagrangiens sont classés en deux catégories : a) les bouées dérivantes qui suivent l'écoulement dans la couche de surface et b) les

flotteurs dériveurs qui peuvent couler pour atteindre une profondeur spécifique et se déplacer à cette profondeur (D'Asaro et al., 2020). Les deux seront utiles non seulement pour valider les performances d'un modèle numérique de circulation ou des mesures radar, mais également pour pouvoir réaliser des études plus détaillées sur la dispersion turbulente à différents niveaux verticaux.

La convergence et la divergence des courants sont considérées actuellement comme des processus physiques étroitement liés aux mouvements verticaux d'eau et à une éventuelle répartition de matières au sein de clasters (regroupement ou assemblage) dans la colonne d'eau. Par exemple, les structures à sous-mésoéchelle (échelles spatiales de centaines de mètres à dizaines de km) associées à des gradients horizontaux de densité (zones frontales) avec une forte convergence en surface et une subsidence de l'eau, peuvent facilement générer une répartition tridimensionnelle du matériel dérivant initialement en surface (e.g., D'Asaro et al., 2018; Essink et al., 2018). Ces processus de transfert d'eau et de matière peuvent être importants pour des activités biogéochimiques, car ils créent le mélange vertical et peuvent ainsi contrôler l'apport de nutriments nécessaires à la croissance des organismes marins. D'autre part, des matières toxiques, telles que des hydrocarbures, déversées accidentellement dans la mer, peuvent être entraînées en profondeur par des mouvements descendants, amplifiant ainsi leur impact sur l'écosystème (D'Asaro et al., 2018). C'est un autre sujet attractif et très d'actualité que nous pouvons aborder dans un avenir proche.

APPENDIX

Appendix A. Statistical metrics

Statistical measures for both scalar and vector correlations are used in the present study. The scalar correlation measures include the correlation coefficient (r^2), root mean squared error (*rmse*), mean absolute error (*mse*), mean, standard deviation. The scalar correlation measures between any two data sets $x = x_1, x_2, x_3 \ldots\ldots\ldots, x_n$ and $y = y_1, y_2, y_3 \ldots\ldots\ldots\ldots, y_n$ are given below:

The mean is defined as: $$\overline{x} = \frac{1}{n}\sum_{i=1}^{n} x_i \quad \text{(A.1)}$$

The mean absolute error is defined as: $$mse = \frac{1}{n}\sum_{i=1}^{n} |x_i - y_i| \quad \text{(A.2)}$$

The standard deviation is defined as: $$\sigma_x = \sqrt{\sum_{i=1}^{n} (x_i - \overline{x})^2} \quad \text{(A.3)}$$

The correlation coefficient is defined as: $$r = \frac{1}{n-1}\sum_{i=1}^{n} \left[\left(\frac{x_i - \overline{x}}{\sigma_x}\right)\left(\frac{y - \overline{y}}{\sigma_y}\right)\right] \quad \text{(A.4)}$$

The root mean squared error is defined as: $$rmse = \sqrt{\frac{1}{n}\sum_{i=1}^{n} (x_i - y_i)^2} \quad \text{(A.5)}$$

The expected error *e* is defined as the mean absolute difference between the interpolated value x^{interp} and the true value *x* normalized by the mean absolute error:

$$e = \frac{\langle |x^{interp} - x| \rangle}{\langle |x - \langle x \rangle| \rangle} \quad \text{(A.6)}$$

Where < > denotes the average.

The vector correlation between any two vector fields is computed following the formulations of complex correlation suggested by Kundu (1976). The complex correlation coefficient between two vectors $\vec{x} = u_x + iv_x$ and $\vec{y} = u_y + iv_y$ is defined as:

$$\alpha = \frac{\langle u_x u_y + v_x v_y \rangle - \langle u_x v_y + u_y v_x \rangle}{\sqrt{\langle u_x^2 + v_x^2 \rangle}\sqrt{\langle u_y^2 + v_y^2 \rangle}} \quad \text{(A.6)}$$

$$\theta = tan^{-1} \frac{\langle u_x v_y - u_y v_x \rangle}{\langle u_x u_y - v_x v_y \rangle} \quad \text{(A.7)}$$

Where α represents the magnitude of the complex correlation while θ represents the phase of the complex correlation, representing the average veering of second vector with respect to the first vector. The positive value of θ shows that the second vector veers to the right of the first vector and vice versa. The phase correlation is meaningful only if the magnitude of the correlation is high. The values of $\alpha \sim 1$ and $\theta \sim 0°$ denotes an excellent comparison between the two-vector series.

Appendix B: Variational interpolation with gap-filling capability for mapping the ocean surface circulation remotely sensed by HF radar

B.1. The radial velocity gap filling

The data interpolating EOF is an iterative methodology for interpolation of gaps and missing data in geophysical data. The technique is applied to the 3-d radial data matrix spanning both space and time dimensions.

Before the analysis, the outliers of velocity measurements were identified. This is important because such outliers can result in large errors in the total velocity field as well as in the comparison statistics. The basic criteria to identify erroneous information was based on the statistical study of the radial data and from the experience in regional dynamics. In the preliminary step, the velocity exceeding 1.5 m s^{-1} was removed from the data since the current velocity in the GoT rarely exceeds this value. Then the temporal and spatial gradient of radial speeds were inspected. Gaussian filter was applied to the entire dataset to detect the trends in the data. The differences between filtered data with the raw velocities can be compared and it is possible to eliminate a large part of the abrupt change by setting acceptable temporal and spatial gradient threshold. In the present study, this threshold value is practically chosen as 2 times standard deviation of the current velocity. The data points were discarded if the change in velocity gradient becomes larger than two times the standard deviation. After running the outlier removal, roughly 10% more of the data was removed from the dataset.

In the first step, anomalies of non-missing data were computed at each location then the gaps or missing data were marked and set to zeros. The covariance matrix C can be implicitly drawn from the velocity field. This covariance matrix is represented by the spectral decomposition:

$$C = U\Lambda U^T$$

where U is the rectangular matrix whose column contains the eigenvectors e_k (EOFs) of C corresponding to the eigenvalues λ_k, Λ = diag(λ_k). The radial velocities are roughly estimated from the sum of finite number N of orthogonal modes which are "fixed" in spatial patterns and evolve in time domain:

$$v = \sum_{k=1}^{N} \alpha_k \, e_k$$

where α_k is the expansion coefficient of each mode. The missing data, initially set at zeros, were filled in by the EOF modes computed based on the original data. After this stage, a new set of EOF expansion was computed by the filled data and this computation was iteratively improved until the lowest error ε between the reconstructed and the original dataset was found (Yaremchuk & Sentchev, 2011).

$$\varepsilon^2 = \sum_{x_i \in \omega_c} \left[v(x_i) - \sum \alpha_k \, e_k(x_i) \right]^2 \rightarrow min(\varepsilon^2)$$

B.2. Implementation of radial data gap filling technique.

From this stage, the finite expanse EOF modes were then employed to reconstruct the data. The gap-free velocity fields were rebuilt from a different number of EOFs until a minimum expected error was found with the cross-validated dataset. From the assessment, 86 EOF modes, responsible for 90% of explained variability of the initial data, were used to build the reconstructed data (Fig. B.1).

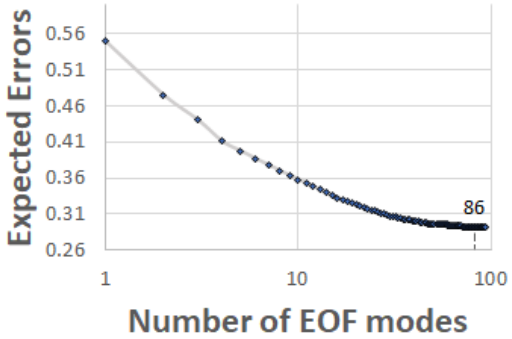

Figure B.1: Interpolation error e as a function of the number of modes

In order to avoid the strong seasonal variation of the GoT circulation, we used a 4-month moving average for the application of the EOF gap-filling method in our study. For testing the gap-filling application, the iterative EOF method was applied for four months of hourly data from September to December 2015, which corresponded to 2928-time instances and the mean standard deviation of about

0.19 m s^{-1}. In the reconstruction, the grid points with valid data less than 30% of operating time were not considered. The gaps were randomly added in 435 snapshots of the hourly data. In this way, 27646 points were removed which accounted for roughly 20% of data loss in the region. The data with removed points were then reconstructed by employing the EOF decomposition technique. The withheld data are used for a cross-validation of final results.

To assess the accuracy of interpolation, difference between the cross-validation and the original data points was computed (Figure B.2). The histogram of scaled errors normalized by the standard deviation is shifted to the negative mean at about 0.013 and the std of 0.73. Thus, it indicates that the reconstructed field is lower than the original data (mean bias 2.7 cm s^{-1}) and underestimates the expected error by roughly 18%. Figure A4 shows reconstructed data for the day 13 October 2015 for two sites and the mean RMSE for the cross-validations. In general, the reconstructed fields are reasonable with the original data (Figure B.3). Being reconstructed from truncated EOF modes, the obtained results obviously are smoother than the original ones and indicate some artifacts in the result. The spatial variability of the mean RMSE indicates the reconstructions are better (less than 5 cm s^{-1}) in the middle field with large coverage (more than 60% of the data availability), however, at the edges of each site, the RMSE is found up to more than 13 cm s^{-1}. Therefore, a second spike removal technique was applied to the reconstructed velocities in order to remove the erroneous points prior to obtaining the final dataset.

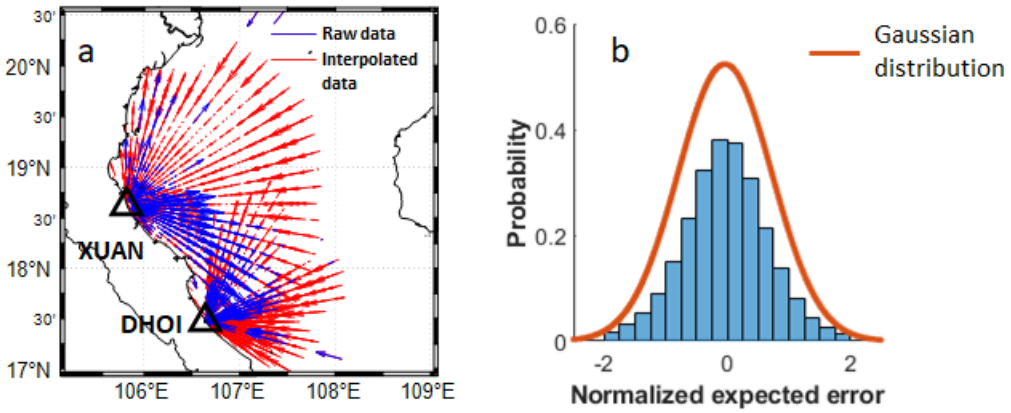

Figure B.2: Result of the reconstructed radial velocities using the iterative EOF-based gap-filling (a) and errors between the the reconstructed and cross-validated dataset normalized by the standard deviation (b).

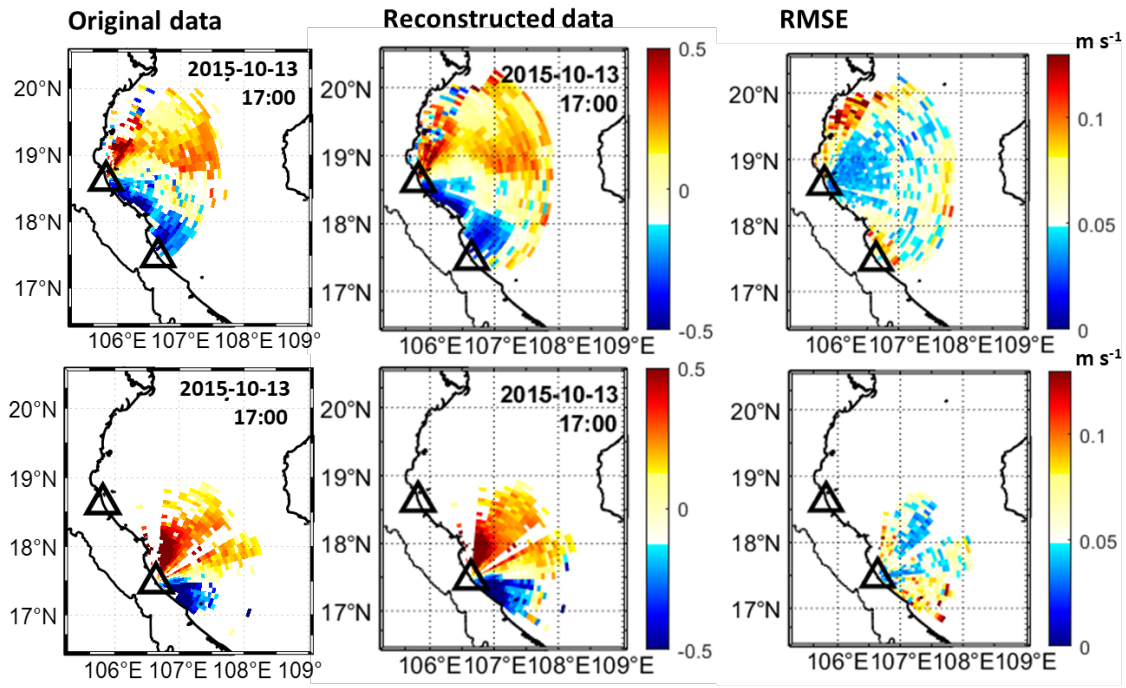

Figure B.3: Snapshot of the raw data (left panel), the reconstructed radial data (middle column) and the mean RMS errors (right panel column) between the reconstructed and the cross-validated dataset for two radar sites.

Appendix C: Assessment of velocity vectors reconstruction techniques

C.1. Mapping surface current from the EOF/2dVar method

Conceptually, surface velocity v is determined by the standard methodology of variational interpolation which minimizes the quadratic cost function $\boldsymbol{J}$ over the oceanic domain $\boldsymbol{\Omega}$. Our goal is to obtain a best estimated v at every grid point k with their observation error σ_k. The first term in the Eq. 1 indicates the regularization of projected velocity v on the radial beam $\boldsymbol{r}$. Additionally, the expression in the second term requires the penalizing the small-scale variability (or enforcing smoothness of the interpolated fields) via justifying the velocity gradient pattern, $\nabla v = \partial_x u + \partial_y v$, $curl v = \partial_x v - \partial_y u$ and an additional smoothness for velocity field Δv. This approach maintains the extraction of important physical features in the flow field while reducing the number of artifacts from the interpolation. Along with the Eulerian view, a better Lagrangian Prediction (LP) skill is obtained with a more accurate reconstruction of the geostrophic component, which in turns, reduce the presence of higher frequency variation components (tides, wave-induced, etc.) and smoother the flow field (Yaremchuk et al., 2016). The 2dVar method proposes a more flexible choice in terms of regularization, thus, the exercise of fine-tuning the 2dVar method via the comparison with the in-situ measurement and the drifter observations helps to provide an accurate radar-derived velocity field. Assuming the flow field is non-divergence, the dimensionless weight factor values are chosen as W_d = $1e^2$, W_c = $5e^0$ and W_u = 1 respectively.

$$J = \frac{1}{2K}\sum_{k=1}^{k} \sigma_k^{-2}\left[\left(\hat{P}_k v\right)\cdot r_k\right]^2 + \frac{1}{2A}\int_{\Omega}\left[W_d(\Delta divv)^2 + W_c(\Delta curlv)^2 + W_u(\Delta v)^2\right] d\Omega$$

C.2. Comparison between radar-derived velocities and in-situ measurement

The 30-minutes data series from two moored AWACs during two periods October 17 – 29, 2015 (P1) and June 02 – 17, 2020 (P2) (Fig. 2.10, chapter II) were used for comparison with the radar measurements.

Here we compared the performance of two techniques 2dVar and the commonly used OMA method which were both non-local interpolation methods with the surface current velocity processed by a

traditional method, the Least Squared fit (LS). OMA utilizes a set of linearly independent eigenfunctions or modes (boundary, incompressible or irrotational) that can be used for interpolation and extrapolation of the flows on the pre-defined domain (Kaplan & Lekien, 2007). In terms of adjustable parameters, OMA provides two choices for regularization: the minimum mode cutoff length scale which was chosen as 10 km, and the corresponding regularization weighting constant κ. The velocities were generated by 96 modes which creates a gaps-free surface current map.

We investigated both the differences between the AWAC current meters and the HFR total current velocity processed using OMA solution and EOF/2dVar method. Three sets of radar-derived velocity were compared with the AWAC data: (1) the radial velocities reprocessed by the OMA method; (2) the velocities after the gap-filling by EOF and reprocessed by the OMA method; and (3) the velocities reprocessed by the EOF/2dVar with gap-filling capability.

The results, which are presented in Fig. C.1, revealed that all methods provide a good complex correlation between the AWAC and radar velocities, and the use of iterative EOF to fill the gap in radial velocity benefits the overall outcomes. For a detailed comparison, the absolute correlation values (α) are larger than 0.7. The phase difference (θ) for each of the three cases is less than 3° and demonstrated a rotation of the HFR-derived current vector to the right of the AWAC-derived current vector. Quantitatively, the bias between the AWAC and HFR is about 0.03 m s^{-1} for the zonal components for the three cases and less than 0.06 m s^{-1} for the meridional component. In terms of RMSE, the differences are found to be less than 0.14 m s^{-1} for both components. Generally, the radar-derived velocities processed by EOF/2dVar exhibit a slightly better agreement with the AWAC measurements than those processed by the OMA method (Fig. C.1).

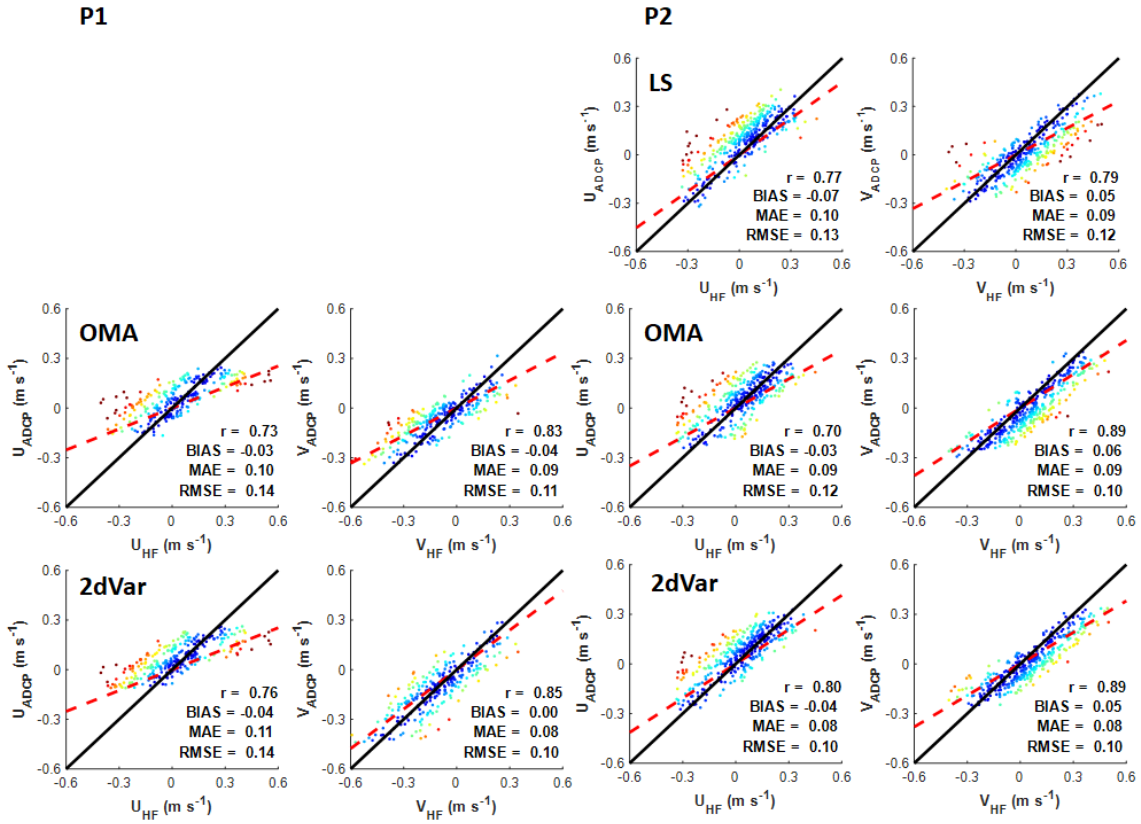

Figure C.1: The comparison of surface current velocities measured from AWAC and HFR data processed by three methods of interpolation (LS, OMA and 2dVar) in P1 (upper panel) and P2 (lower panel).

Since the in-situ measurements by AWAC only provides the data in one point and in a limited time period, an additional analysis is implemented to assess the total surface current velocity reprocessed from two gap-filling methods: OMA and 2dVar compared with the widely used LS method. In this way, we selected several snapshots (~ 400 snapshots) with good coverage data and considered them as the "reference" data. The comparison was done for 4 variables: u- and v-components, divergence and vorticity of the total current velocity field. The results, which are presented in Fig. C.3 and Table C.1, demonstrated that the velocity field reprocessed from 2dVar method appears to be closer to the "true" field.

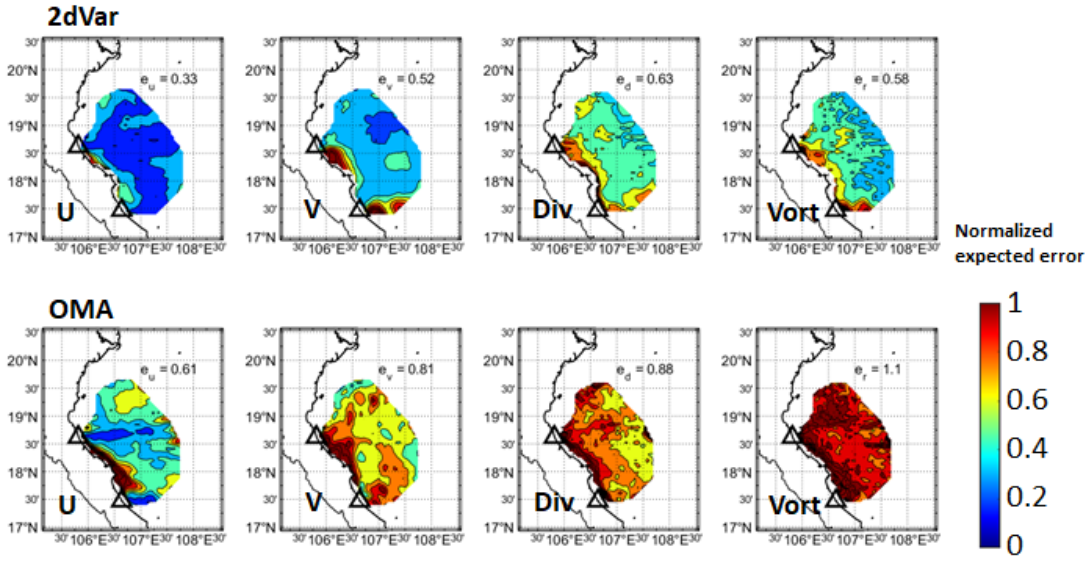

Figure C.2: Comparison between two methods of interpolation (2dVar and OMA) with the surface velocity field processed from the LS method

Table C.1: Comparison of expected error between two methods of interpolation (2dVar and OMA) with the velocity field processed by LS method in current velocity u-component (e_u), v-component (e_v), horizontal divergence (e_d) and curl (e_r) (lower values are better)

Time	Method	e_U	e_V	e_d	e_r
October 17 – 29, 2015	2dVar	0.33	0.52	0.63	0.58
	OMA	0.61	0.81	0.88	1.1
June 02 – 17, 2020	2dVar	0.29	0.4	0.57	0.58
	OMA	0.49	0.65	0.84	0.93

C.3. Lagrangian tracking assessment

In this study, seven surface drifters released close to the XUAN radar site also were used to assess the Lagrangian tracking ability by the HFR-derived velocity. Table C.2 provides the number, time, and tracks of each drifter being used in this study from April 2017 to January 2018. We started with the analysis focusing on the accuracy of single trajectory computed by HFR and the real drifters. In order to do that, the HFR-advected drifters were computed from fourth order Runge-Kutta integration scheme with a timestep of 30 minutes. We initially placed the virtual drifters surrounds the position of the real ones and then the distance between both virtual and real drifters are computed. Following other authors (Berta et al., 2014a; Hernández-Carrasco et al., 2018; Enrile, et al., 2018), we also reinitialized the virtual drifters at the position of the real ones every 6h during the calculation since this time window is relevant for Search and Rescue operation (SAR).

Table C.2: The drifting buoys used in the study during the period 2017 – 2018

Drifter number	Lifetime within the study domain		Number of days in the GoT	Season
	Start	End		
454	03/11/2017	03/27/2017	16	Spring
455	29/07/2017	04/08/2017	7	Summer
529	08/23/2017	09/26/2017	33	Summer
530	11/28/2017	12/12/2017	14	Winter
531	09/20/2017	10/01/2017	11	Fall
532	23/10/2017	28/10/2017	6	Fall
534	18/01/2018	02/04/2018	17	Winter

Fig. C.3 gives three examples comparing the real drifter and the synthetic drifter trajectories advected by 2dVar and OMA-derived velocity fields. The synthetic drifters demonstrated the tendency of southern transport of the real ones as well. Generally, the synthetic trajectories advected by HFR velocities processed by 2 methods (OMA and 2dVar) followed closely to their real counterparts though some discrepancies can be noticed. Regarding the synthetic trajectories processed by individual methods, during the first 12 hours both of them perform similarly and remain quite close with the drifter. However, the trajectory reproduced by 2dVar adequately captured the drifter pathway while the one from OMA departs significantly (Fig. C.3a, c). For the example in Fig. C.3a, the drifter deployed in the area was covered by only one radar site, thus, an accurate surface current velocity was hard to estimate. As in this case, the 2dVar appeared to produce an estimation quite close to the real drifter. In addition, the flexible choices of regularization from 2dVar allow correcting the artifacts in the reconstructed velocity field than OMA. Fig. C.3c indicated the case that the velocity field from OMA overestimates an artificial eddy that was not captured in the real counterpart.

Another one that can be noticed is a striking difference in the pattern of the drifter no. 531 which was deployed in September 2017 (Fig. C.3b). After the first two days, the drifter moved southward along the coast and then remained "trapped" close to the southern radar site for about 3 – 4 days representing a small-scale clockwise eddy pattern. Although the separation between the real and the synthetic drifter remained low in this case (less than 8 km/48 h), the synthetic drifters advected from both methods failed to reproduce such a complex trajectory. However, it should be noted that the spatial resolution of the HFR-derived velocities of about 6 km possibly prohibited resolving structures smaller than this size.

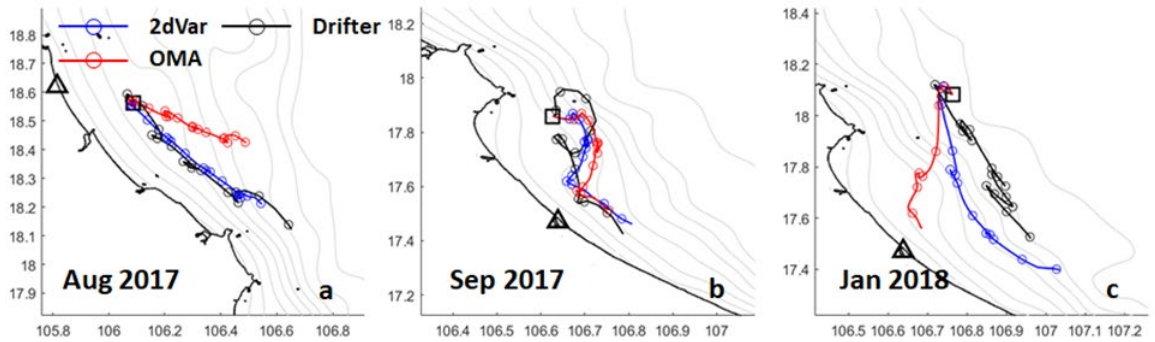

Figure C.3: Real drifter trajectories (black lines) and synthetic drifter positions advected by HFR-derived velocities processed from 2dVar (blue lines) and OMA (red lines). The drifter positions every 6h are shown. The bathymetry contour is plotted every 5 m

BIBLIOGRAPHY

Abascal, A. J., Castanedo, S., Medina, R., Losada, I. J., & Alvarez-Fanjul, E. (2009). Application of HF radar currents to oil spill modelling. *Marine Pollution Bulletin*, *58*(2), 238–248. https://doi.org/10.1016/j.marpolbul.2008.09.020

Alvera-Azcárate, A., Barth, A., Rixen, M., and Beckers, J.- M.: Reconstruction of incomplete oceanographic data sets us- ing Empirical Orthogonal Functions. Application to the Adri- atic Sea Surface Temperature, Ocean Model., 9, 325–346, https://doi.org/10.1016/j.ocemod.2004.08.001, 2005

Aoki, K., & Kataoka, T. (2018). High-frequency ocean radar derived characteristics of sea surface currents in the Ariake Sea, Japan. *Journal of Oceanography*, *74*(4), 431–437. https://doi.org/10.1007/s10872-018-0464-2

Artale, V., Boffetta, G., Celani, A., Cencini, M., & Vulpiani, A. (1997). Dispersion of passive tracers in closed basins: Beyond the diffusion coefficient. *Physics of Fluids*, *9*(11), 3162–3171. https://doi.org/10.1063/1.869433

Balwada, D., LaCasce, J. H., Speer, K. G., & Ferrari, R. (2020). Relative Dispersion in the Antarctic Circumpolar Current. *Journal of Physical Oceanography*, *51*(2), 553–574. https://doi.org/10.1175/jpo-d-19-0243.1

Barrick DE.1971a. Theory of HF and VHF propagation across the rough sea, 1: the effective surface impedance for a slightly rough highly conducting medium at grazing incidence. Radio Sci. 6:517–26

Barrick DE. 1971b. Theory of HF and VHF propagation across the rough sea, 2: application to HF and VHF propagation above the sea. Radio Sci. 6:527–33

Barrick DE. 1972. First-order theory and analysis of MF/HF/VHF scatter from the sea. IEEE Trans. Antennas Propag. 20:2–10

Barrick, D. E., Evans, M. W., & Weber, B. L. (1978). Ocean Surface Currents Mapped by Radar. *Science*, *198*(4313), 138–144. https://doi.org/10.1126/science.198.4313.138

Barrick, D. E., and Lipa, B. J. (1985). "Mapping surface currents with codar." Sea Technol. 26, 43–48

Barrick, D., and Lipa, B. (2011). Japan tsunami detected by HF radars on two continents. in Proceedings of the OCEANS'11 MTS/IEEE KONA. (Waikoloa, HI: IEEE)

Barth, A., Alvera-Azcárate, A., Licer, M., & Beckers, J.-M. (2020). DINCAE 1.0: a convolutional neural network with error estimates to reconstruct sea surface temperature satellite observations. *Geoscientific Model Development*, *13*(3), 1609–1622. https://doi.org/10.5194/gmd-13-1609-2020

Bassin, C. J., Washburn, L., Brzezinski, M., & McPhee-Shaw, E. (2005). Sub-mesoscale coastal eddies observed by high frequency radar: A new mechanism for delivering nutrients to kelp forests in the Southern California Bight. *Geophysical Research Letters*, *32*(12). https://doi.org/10.1029/2005GL023017

Beron-Vera, F. J., & LaCasce, J. H. (2016). Statistics of simulated and observed pair separations in the Gulf of Mexico. *Journal of Physical Oceanography*, *46*(7), 2183–2199. https://doi.org/10.1175/JPO-D-15-0127.1

Berta, M., Griffa, A., Haza, A. C., Horstmann, J., Huntley, H. S., Ibrahim, R., Lund, B., Özgökmen, T. M., & Poje, A. C. (2020). Submesoscale Kinematic Properties in Summer and Winter Surface Flows in the Northern Gulf of Mexico. *Journal of Geophysical Research: Oceans*, *125*(10). https://doi.org/10.1029/2020JC016085

Berta, M., Ursella, L., Nencioli, F., Doglioli, A. M., Petrenko, A. A., & Cosoli, S. (2014). Surface transport in the Northeastern Adriatic Sea from FSLE analysis of HF radar measurements. *Continental Shelf Research*, *77*, 14–23. https://doi.org/10.1016/j.csr.2014.01.016

Berti, S., Dos Santos, F. A., Lacorata, G., & Vulpiani, A. (2011). Lagrangian drifter dispersion in the southwestern Atlantic Ocean. *Journal of Physical Oceanography*, *41*(9), 1659–1672. https://doi.org/10.1175/2011JPO4541.1

Berti, S., & Lapeyre, G. (2021). Lagrangian pair dispersion in upper-ocean turbulence in the presence of mixed-layer instabilities. *Physics of Fluids*, *33*(3), 036603. https://doi.org/10.1063/5.0041036

Brzezinski, M.A., Washburn, L., 2011. Phytoplankton primary productivity in the Santa Barbara Channel: effects of wind-driven upwelling and mesoscale eddies. J. Geophys. Res. 116, C12013.

Camargo S. J., Sobel A. H. (2005) Western North Pacific Tropical Cyclone Intensity and ENSO. Amer. Meteor. Soc., 18: 2996-3006., doi:10.1175/JCLI3457.1

Cai, S., Long, X., Wu, R., & Wang, S. (2008). Geographical and monthly variability of the first baroclinic Rossby radius of deformation in the South China Sea. *Journal of Marine Systems*, *74*(1–2), 711–720. https://doi.org/10.1016/j.jmarsys.2007.12.008

Camargo, S.J., Sobel, A.H., 2005. Western north Pacific tropical cyclone intensity and ENSO. Amer. Meteor. Soc. 18, 2996–3006. http://dx.doi.org/10.1175/ JCLI3457.1

Capet, X., McWilliams, J. C., Molemaker, M. J., & Shchepetkin, A. F. (2008). Mesoscale to submesoscale transition in the California Current system. Part I: Flow structure, eddy flux, and observational tests. *Journal of Physical Oceanography*, *38*(1), 29–43. https://doi.org/10.1175/2007JPO3671.1

Chant, R., Wilkin, J., Zhang, W., Choi, B.J., Hunter, E., Castelao, R., Glenn, S., Jurisa, J., Schofield, O., 818 Houghton, R., Kohut, J., Frazer, T. and Moline, M., Dispersal of the Hudson River Plume in the New York 819 Bight: Synthesis of Observational and Numerical Studies During LaTTE. Biol. Sci., 2008, 21

Chen, C., Gao, G., Qi, J., Proshutinsky, A., Beardsley, R. C., Kowalik, Z., Lin, H., & Cowles, G. (2009). A new high-resolution unstructured grid finite volume Arctic Ocean model (AO-FVCOM): An application for tidal studies. *Journal of Geophysical Research: Oceans*, *114*(C8). https://doi.org/10.1029/2008JC004941

Chen, C., Lai, Z., Beardsley, R. C., Xu, Q., Lin, H., & Viet, N. T. (2012a). Current separation and upwelling over the southeast shelf of Vietnam in the South China Sea. *Journal of Geophysical Research: Oceans*, *117*(C3). https://doi.org/10.1029/2011JC007150

Chen, C., Limeburner, R., Gao, G., Xu, Q., Qi, J., Xue, P., Lai, Z., Lin, H., Beardsley, R., Owens, B., Carlson, B., Group, and members of the U.-D. F., & Group, and members of the W. F. M. (2012b). FVCOM model estimate of the location of Air France 447. *Ocean Dynamics*, *62*(6), 943–952. https://doi.org/10.1007/s10236-012-0537-5

Chern, C.-S., Jan, S., & Wang, J. (2010). Numerical study of mean flow patterns in the South China Sea and the Luzon Strait. *Ocean Dynamics*, *60*(5), 1047–1059. https://doi.org/10.1007/s10236-010-0305-3

Chou C., Tu J. Y., Yu J. Y. (2003) Interannual variability of the Western North Pacific summer monsoon: Differences between ENSO and non-ENSO years, J. Clim., 16(13), 2275-2287, doi: 10.1175/2761.1

Chu, P.C., Li, R., 2000. South China sea isopycnal-surface circulation. J. Phys. Oceanogr. 30 (9), 2419–2438. http://dx.doi.org/10.1175/1520-0485(2000) 030<2419:SCSISC>2.0.CO;2

Cianelli, D., D'Alelio, D., Uttieri, M. *et al.* Disentangling physical and biological drivers of phytoplankton dynamics in a coastal system. *Sci Rep* **7**, 15868 (2017). https://doi.org/10.1038/s41598-017-15880-x

Corrado, R., Lacorata, G., Palatella, L., Santoleri, R., & Zambianchi, E. (2017). General characteristics of relative dispersion in the ocean. *Scientific Reports*, *7*(1), 46291. https://doi.org/10.1038/srep46291

Da, N. D., Herrmann, M., Morrow, R., Niño, F., Huan, N. M., & Trinh, N. Q. (2019). Contributions of Wind, Ocean Intrinsic Variability, and ENSO to the Interannual Variability of the South Vietnam Upwelling: A Modeling Study. *Journal of Geophysical Research: Oceans*, *124*(9), 6545–6574. https://doi.org/10.1029/2018JC014647

Da Silva, R. C. Q., Miranda, W. L., Chacra, A. R., & Dib, S. A. (2005). Metabolic syndrome and insulin resistance in normal glucose tolerant Brazilian adolescents with family history of type 2 diabetes. *Diabetes Care*, *28*(3), 716–718. https://doi.org/10.2337/diacare.28.3.716

Ding, Y., Chen, C., Beardsley, R. C., Bao, X., Shi, M., Zhang, Y., Lai, Z., Li, R., Lin, H., & Viet, N. T. (2013). Observational and model studies of the circulation in the Gulf of Tonkin, South China Sea. *Journal of Geophysical Research: Oceans*, *118*(12), 6495–6510. https://doi.org/10.1002/2013JC009455

Dippner J. W., Bombar D., Loick-Wilde N., Voss M., Subramaniam A. (2013a), Comment on "current separation upwelling over the southeast shelf of Vietnam in the South China Sea" by Chen et al., J. Geophys. Res. Ocean., 118(3), 1618-1623, doi: 10.1002/jgrc.20118

D'Asaro, E. A., Carlson, D. F., Chamecki, M., Harcourt, R. R., Haus, B. K., Fox-Kemper, B., Molemaker, M. J., Poje, A. C., & Yang, D. (2020). Advances in Observing and Understanding Small-Scale Open Ocean Circulation During the Gulf of Mexico Research Initiative Era. *Frontiers in Marine Science*, *7*(May), 1–23. https://doi.org/10.3389/fmars.2020.00349

D'Asaro, E. A., Shcherbina, A. Y., Klymak, J. M., Molemaker, J., Novelli, G., Guigand, C. M., Haza, A. C., Haus, B. K., Ryan, E. H., Jacobs, G. A., Huntley, H. S., Laxague, N. J. M., Chen, S., Judt, F., McWilliams, J. C., Barkan, R., Kirwan, A. D., Poje, A. C., & Özgökmen, T. M. (2018). Ocean convergence and the dispersion of flotsam. *Proceedings of the National Academy of Sciences*, *115*(6), 1162–1167. https://doi.org/10.1073/PNAS.1718453115

d'Ovidio, F., Della Penna, A., Trull, T. W., Nencioli, F., Pujol, M.-I., Rio, M.-H., Park, Y.-H., Cotté, C., Zhou, M., & Blain, S. (2015). The biogeochemical structuring role of horizontal stirring: Lagrangian perspectives on iron delivery downstream of the Kerguelen Plateau. *Biogeosciences*, *12*(19), 5567–5581. https://doi.org/10.5194/bg-12-5567-2015

D'Ovidio, F., Fernández, V., Hernández-García, E., & López, C. (2004). Mixing structures in the Mediterranean Sea from finite-size Lyapunov exponents. *Geophysical Research Letters*, *31*(17), 1–4. https://doi.org/10.1029/2004GL020328

Dzwonkowski, B., Kohut, J. T., & Yan, X.-H. H. (2009). Sub-inertial characteristics of the surface flow field over the shelf of the central Mid-Atlantic Bight. *Continental Shelf Research*, *29*(15), 1873–1886. https://doi.org/https://doi.org/10.1016/j.csr.2009.07.005

Ebuchi N, Fukamachi Y, Oshima K, Shirasawa K, Ishikawa M, Takatsuka T, Daibo T, Wakatsuchi M (2006) Observation of the Soya warm current using HF ocean radar. J Oceanogr 62(1):47-61

Emery, B. M., Washburn, L., & Harlan, J. A. (2004). Evaluating Radial Current Measurements from CODAR High-Frequency Radars with Moored Current Meters*. *Journal of Atmospheric and Oceanic Technology*, *21*(8), 1259–1271. https://doi.org/10.1175/1520-0426(2004)021<1259:ERCMFC>2.0.CO;2

Emery, B., & Washburn, L. (2019). Uncertainty Estimates for SeaSonde HF Radar Ocean Current Observations. *Journal of Atmospheric and Oceanic Technology*, *36*(2), 231–247. https://doi.org/10.1175/JTECH-D-18-0104.1

Essen H-H, G¨urgel K-W. 2000. On the accuracy of current measurements by means of HF radar. IEEE J. Ocean. Eng. 25:472–80

Essink, S., Hormann, V., Centurioni, L. R., & Mahadevan, A. (2019). Can we detect submesoscale motions in drifter pair dispersion? *Journal of Physical Oceanography*, *49*(9), 2237–2254. https://doi.org/10.1175/JPO-D-18-0181.1

Fang G. (1986) Tide and tidal current charts for the marginal seas adjacent to China, Chin. J. Oceanol. Limnol., 4, 1-16, https://doi.org/10.1007/BF02850393.

Fang G., Kwok Y. K., Yu K., Zhu Y. (1999) Numerical simulation of principal tidal constituents in the South China Sea, Gulf of Tonkin and Gulf of Thailand, Cont. Shelf Res., 19(7), 845-869, https://doi.org/10.1016/S0278-4343(99)00002-3.

Fang W. (2002) Seasonal structure of upper layer circulation in the southern South China Sea from in situ observations, J. Geophys. Res., 107(C11), 3202, doi: 10.1029/2002JC001343

Ferrari R, Wunsch C. 2009. Ocean circulation kinetic energy: reservoirs, sources, and sinks. Annu. Rev. Fluid Mech. 41:253–82

Foussard, A., Berti, S., Perrot, X., & Lapeyre, G. (2017). Relative dispersion in generalized two-dimensional turbulence. *Journal of Fluid Mechanics*, *821*, 358–383. https://doi.org/10.1017/jfm.2017.253

Fujii, S., Heron, M. L., Kim, K., Lai, J.-W., Lee, S.-H., Wu, X. X., Wu, X. X., Wyatt, L. R., & Yang, W.-C. (2013). An overview of developments and applications of oceanographic radar networks in Asia and Oceania countries. *Ocean Science Journal*, *48*(1), 69–97. https://doi.org/10.1007/s12601-013-0007-0

Gan, J., Li, H., Curchitser, E. N., & Haidvogel, D. B. (2006). Modeling South China Sea circulation: Response to seasonal forcing regimes. *Journal of Geophysical Research: Oceans*, *111*(C6). https://doi.org/10.1029/2005JC003298

Gao, J.S., Chen, B., He, X.Y., et al., 2014. Responses of the circulation and water mass in the Beibu Gulf to the seasonal forcing regime. Acta Oceanol. Sin. 33 (7), 1–11

Gao, J. S., Chen, B., & Shi, M. C. (2015). Summer circulation structure and formation mechanism in the Beibu Gulf. *Science China Earth Sciences*, *58*(2), 286–299. https://doi.org/10.1007/s11430-014-4916-2

Gao, J., Wu, G., & Ya, H. (2017). Review of the circulation in the Beibu Gulf, South China Sea. *Continental Shelf Research*, *138*, 106–119. https://doi.org/10.1016/j.csr.2017.02.009

Gao, J., Xue, H., Chai, F., & Shi, M. (2013). Modeling the circulation in the Gulf of Tonkin, South China Sea. *Ocean Dynamics*, *63*(8), 979–993. https://doi.org/10.1007/s10236-013-0636-y

García-Reyes, Marisol & Largier, John. (2012). Seasonality of coastal upwelling off central and Northern California: New insights, including temporal and spatial variability. Journal of Geophysical Research. 117. 10.1029/2011JC007629.

Gaube, P., Chelton, D.B., Samelson, R.M., Schlax, M.G., O'Neill, L.W., 2015. Satellite observations of mesoscale eddy-induced Ekman pumping. J. Phys. Oceanogr. 45, 104–132. http://dx.doi.org/10.1175/JPO-D-14-0032.1

Gohin, F., Druon, J.N., Lampert, L., 2002. A five channel chlorophyll concentration algo- rithm applied to SeaWiFS data processed by Seadas in coastal waters. Int. J. Remote Sens. 23:1639–1661. http://dx.doi.org/10.1080/01431160110071879

Gürgel K-W, Antonischki G, Essen H-H, Schlick T. 1999a. Wellen Radar (WERA): a new ground-wave HF radar for ocean remote sensing. Coast. Eng. 37:219–34

Gürgel K-W, Essen H-H, Kingsley SP. 1999b. High-frequency radars: physical limitations and recent devel- opments. Coast. Eng. 37:201–18

Griffies, S. M., Winton, M., & Samuels, B. L. (2004). The Large and Yeager (2004) dataset and CORE. *NCAR Tech. Note*, *TN--460+ST*(2004), 1–5.

Grilli, S. T., Guérin, C.-A., Shelby, M., Grilli, A. R., Moran, P., Grosdidier, S., Insua, T. L. (2017) "Tsunami detection by high frequency radar beyond the continental shelf: ii. extension of time correlation algorithm and validation on realistic case studies". Pure Appl. Geophys. 174, 3003–3028. doi: 10.1007/s00024-017-1619-6

Grosdidier, Samuel & Baussard, Alexandre. (2012). Ship detection based on morphological component analysis of high-frequency surface wave radar images. Radar, Sonar & Navigation, IET. 6. 813-821. 10.1049/iet-rsn.2012.0062.

Gruber, N., Lachkar, Z., Frenzel, H., Marchesiello, P., Münnich, M., McWilliams, J. C., Nagai, T., & Plattner, G. K. (2011). Eddy-induced reduction of biological production in eastern boundary upwelling systems. Nature Geoscience, 4(11), 787–792. https://doi.org/10.1038/ngeo1273

Guérin, C.-A., Grilli, S. T., Moran, P., Grilli, A. R., Insua, T. L. (2018). "Tsunami detection by high-frequency radar in British Columbia: performance assessment of the time-correlation algorithm for synthetic and real events". Ocean Dynam. 68, 423–438. doi: 10.1007/s10236-018-1139-7

Ha, N.T.T., Koike, K., Nhuan, M.T., 2014. Improved accuracy ofchlorophyll-a concentration estimates fromMODIS imagery using a two-band ratio algorithmand geostatistics: as applied to the monitoring of eutrophication processes over Tien Yen Bay (northern Vietnam). Remote Sens. 6:421–442. http://dx.doi.org/10.3390/rs6010421

Haza, A. C., Özgökmen, T. M., & Hogan, P. (2016). Impact of submesoscales on surface material distribution in a gulf of Mexico mesoscale eddy. *Ocean Modelling*, *107*, 28–47. https://doi.org/10.1016/j.ocemod.2016.10.002

Haza, A. C., Poje, A. C., Özgökmen, T. M., & Martin, P. (2008). Relative dispersion from a high-resolution coastal model of the Adriatic Sea. *Ocean Modelling*, *22*(1–2), 48–65. https://doi.org/10.1016/j.ocemod.2008.01.006

Haza, A. C., Özgökmen, T. M., Griffa, A., Molcard, A., Poulain, P.-M., & Peggion, G. (2010). Transport properties in small-scale coastal flows: relative dispersion from VHF radar measurements in the Gulf of La Spezia. *Ocean Dynamics*, *60*(4), 861–882. https://doi.org/10.1007/s10236-010-0301-7

Helzel, T., Kniephoff, M., & Petersen, L. (2006). WERA: Remote ocean sensing for current, wave and wind direction. *2006 IEEE US/EU Baltic International Symposium*, 1–8. https://doi.org/10.1109/BALTIC.2006.7266143

Herrmann, M. J., & Somot, S. (2008). Relevance of ERA40 dynamical downscaling for modeling deep convection in the Mediterranean Sea. *Geophysical Research Letters*, *35*(4), L04607. https://doi.org/10.1029/2007GL032442

Hernandez-Carrasco, I., López, C., Hernandez-García, E., & Turiel, A. (2012). Seasonal and regional characterization of horizontal stirring in the global ocean. *Journal of Geophysical Research: Oceans*, *117*(10), 1–12. https://doi.org/10.1029/2012JC008222

Hernández-Carrasco, I., Rossi, V., Hernández-García, E., Garçon, V., & López, C. (2014). The reduction of plankton biomass induced by mesoscale stirring: A modeling study in the Benguela upwelling. *Deep-Sea Research Part I: Oceanographic Research Papers*, *83*, 65–80. https://doi.org/10.1016/j.dsr.2013.09.003

Hernández-Carrasco, I., Solabarrieta, L., Rubio, A., Esnaola, G., Reyes, E., & Orfila, A. (2018a). Impact of HF radar current gap-filling methodologies on the Lagrangian assessment of coastal dynamics. *Ocean Science*, *14*(4), 827–847. https://doi.org/10.5194/os-14-827-2018

Hernández-Carrasco, I., Orfila, A., Rossi, V., & Garçon, V. (2018b). Effect of small scale transport processes on phytoplankton distribution in coastal seas. *Scientific Reports*, *8*(1), 1–13. https://doi.org/10.1038/s41598-018-26857-9

Hu J. Y., Kawamura H., Hong H. S., Kobashi F., Xie Q. (2001) Tidal features in the China Seas and their adjacent areas derives from TOPEX/Poseidon altimeter data, Chin. J. Oceanol. Limnol., 19, 293-305, https://doi.org/10.1007/BF02850732

Hu, J. Y., Kawamura, H., & Tang, D. L. (2003). Tidal front around the Hainan Island, northwest of the South China Sea. *Journal of Geophysical Research: Oceans*, *108*(11), 1–9. https://doi.org/10.1029/2003jc001883

Huntley, H.S., Lipphardt, B.L., Kirwan, A.D., 2011. Lagrangian predictability assessed in the East China Sea. Ocean Model. 36, 163–178.

Huynh H.-N., Alvera-Azcarate A., Barth A., Beckers J.-M. (2016) Reconstruction and analysis of long-term satellite-derived sea surface temperature for the South China Sea, J. Oceanogr., 1-20, doi: 10.1007/s10872-016-0365-1

Jahnke, R. A. (2010). *Global Synthesis1 BT - Carbon and Nutrient Fluxes in Continental Margins: A Global Synthesis* (K.-K. Liu, L. Atkinson, R. Quiñones, & L. Talaue-McManus (eds.); pp. 597–615). Springer Berlin Heidelberg. https://doi.org/10.1007/978-3-540-92735-8_16

Julien Marmain. Circulation côtière en Méditerranée Nord Occidentale: courantométrie par radar HF et couplage avec un modèle numérique. Autre [cond-mat.other]. Université de Toulon, 2013. Français. NNT: 2013TOUL0015. tel-00994937

Juneng L., Tangang F. T. (2005) Evolution of ENSO-related rainfall anomalies in Southeast Asia region and its relationship with atmosphere-ocean variations in Indo-Pacific sector, Clim. Dynam., 25: 337-350, doi: 10.1007/s00382-005-0031-6.

Kaplan, D. M., Largier, J., & Botsford, L. W. (2005). HF radar observations of surface circulation off Bodega Bay (northern California, USA). *Journal of Geophysical Research: Oceans*, *110*(C10). https://doi.org/10.1029/2005JC002959

Kim, S. Y., Terrill, E. J., & Cornuelle, B. D. (2008). Mapping surface currents from HF radar radial velocity measurements using optimal interpolation. *Journal of Geophysical Research: Oceans*, *113*(C10). https://doi.org/10.1029/2007JC004244

Kim, S. Y. (2010). Observations of submesoscale eddies using high-frequency radar-derived kinematic and dynamic quantities. *Continental Shelf Research*, *30*(15), 1639–1655. https://doi.org/10.1016/j.csr.2010.06.011

Kim, S. Y., & Kosro, P. M. (2013). Observations of near-inertial surface currents off Oregon: Decorrelation time and length scales. *Journal of Geophysical Research: Oceans*, *118*(7), 3723–3736. https://doi.org/10.1002/jgrc.20235

Klein, P., Lapeyre, G., Roullet, G., Le Gentil, S., & Sasaki, H. (2011). Ocean turbulence at meso and submesoscales: connection between surface and interior dynamics. *Geophysical & Astrophysical Fluid Dynamics*, *105*(4–5), 421–437. https://doi.org/10.1080/03091929.2010.532498

Kohut, J. T., & Glenn, S. M. (2003). Improving HF Radar Surface Current Measurements with Measured Antenna Beam Patterns. *Journal of Atmospheric and Oceanic Technology*, *20*(9), 1303–1316. https://doi.org/10.1175/1520-0426(2003)020<1303:IHRSCM>2.0.CO;2

Kohut JT, Glenn SM, Paduan JD. 2006. Inner-shelf response to tropical storm Floyd. J. Geophys. Res. 111:C09S91

Kokkini, Z., Potiris, M., Kalampokis, A., & Zervakis, V. (2014). HF Radar observations of the Dardanelles outflow current in North Eastern Aegean using validated WERA HF radar data. *Mediterranean Marine Science*, *15*(4), 753. https://doi.org/10.12681/mms.938

Kolmogorov, A., “The Local Structure of Turbulence in Incompressible Viscous Fluid for Very Large Reynolds' Numbers”, Akademiia Nauk SSSR Doklady, vol. 30, pp. 301–305, 1941

Koszalka, I., LaCasce, J. H., & Orvik, K. A. (2009). Relative dispersion in the Nordic Seas. *Journal of Marine Research*, *67*(4), 411–433. https://doi.org/10.1357/002224009790741102

Kundu, P. K. (1976). Ekman Veering Observed near the Ocean Bottom. *Journal of Physical Oceanography*, *6*(2), 238–242. https://doi.org/10.1175/1520-0485(1976)006<0238:EVONTO>2.0.CO;2

LaCasce, J. H. (2008). Statistics from Lagrangian observations. *Progress in Oceanography*, *77*(1), 1–29. https://doi.org/10.1016/j.pocean.2008.02.002

LaCasce, J. H., & Ohlmann, C. (2003). Relative dispersion at the surface of the Gulf of Mexico. *Journal of Marine Research*, *61*(3), 285–312. https://doi.org/10.1357/002224003322201205

Lacroix, G., Maes, G. E., Bolle, L. J., & Volckaert, F. A. M. (2013). Modelling dispersal dynamics of the early life stages of a marine flatfish (Solea solea L.). *Journal of Sea Research*, *84*, 13–25. https://doi.org/10.1016/j.seares.2012.07.010

Large, W. G., and Yeager, S. (2004). Diurnal to Decadal Global Forcing for Ocean and Sea–Ice Models: The Data Sets and Flux Climatologies, NCAR Technical Note, NCAR/TN-460+STR. Boulder, CO: National Center for Atmospheric Research. doi: 10.5065/D6KK98Q6

Lehahn, Y., d'Ovidio, F., Lévy, M., & Heifetz, E. (2007). Stirring of the northeast Atlantic spring bloom: A Lagrangian analysis based on multisatellite data. *Journal of Geophysical Research: Oceans*, *112*(8), C08005. https://doi.org/10.1029/2006JC003927

Lehahn, Y., D'Ovidio, F., & Koren, I. (2018). A Satellite-Based Lagrangian View on Phytoplankton Dynamics. *Annual Review of Marine Science*, *10*(1), 99–119. https://doi.org/10.1146/annurev-marine-121916-063204

Lekien, F., Coulliette, C., Mariano, A. J., Ryan, E. H., Shay, L. K., Haller, G., & Marsden, J. (2005). Pollution release tied to invariant manifolds: A case study for the coast of Florida. *Physica D: Nonlinear Phenomena*, *210*(1–2), 1–20. https://doi.org/10.1016/j.physd.2005.06.023

Lévy, M., Franks, P. J. S., & Smith, K. S. (2018). The role of submesoscale currents in structuring marine ecosystems. *Nature Communications*, *9*(1), 1–16. https://doi.org/10.1038/s41467-018-07059-3

Lentz, S. J., & Helfrich, K. R. (2002). Buoyant gravity currents along a sloping bottom in a rotating fluid. *Journal of Fluid Mechanics*, *464*, 251–278.

Li, R., Chen, C., Xia, H., Beardsley, R. C., Shi, M., Lai, Z., Lin, H., Feng, Y., Liu, C., Xu, Q., Ding, Y., & Zhang, Y. (2014). Observed wintertime tidal and subtidal currents over the continental shelf in the northern South China Sea. *Journal of Geophysical Research: Oceans*, *119*(8), 5289–5310. https://doi.org/10.1002/2014JC009931

Lipa BJ, Barrick DE. 1983. Least-squares method for the extraction of surface currents fromCODAR crossed- loop data: application at ARSLOE. IEEE J. Ocean. Eng. 8:226–53

Lipa, B. J. (2005): "Directional Wave Information from the Seasonde", *IEEE J. Oceanic Eng.*, OE-30

Liu, S., Cai, S., Wang, S., 2011. Observations of strong near-bottom current after the passage of Typhoon Pabuk in the South China Sea. J. Mar. Syst. 87 (1), 102–108. http://dx.doi.org/10.1016/j.jmarsys.2011.02.023

Liu, Y., Weisberg, R. H., Merz, C. R., Lichtenwalner, S., & Kirkpatrick, G. J. (2010). HF radar performance in a low-energy environment: CODAR seasonde experience on the West Florida shelf. Journal of Atmospheric and Oceanic Technology, 27(10), 1689–1710. https://doi.org/10.1175/2010JTECHO720.1

Liu, Yonggang & Merz, Clifford & Weisberg, Robert. (2008). HF Radar Performance on a Low Energy Environment as Found Using CODAR SeaSonde on the West Florida Shelf. AGU Fall Meeting Abstracts.

Liu, Y., Weisberg, R. H., & Merz, C. R. (2014). Assessment of CODAR SeaSonde and WERA HF Radars in Mapping Surface Currents on the West Florida Shelf*. *Journal of Atmospheric and Oceanic Technology*, *31*(6), 1363–1382. https://doi.org/10.1175/JTECH-D-13-00107.1

Liu Q., Jiang X., Xie S.-P., Liu W. T. (2014) A gap in the Indo-Pacific warm pool over the South China Sea in boreal winter: Seasonal development and interannual variability, J. Geophys. Res., 109(C07012), doi:10.1029/2003JC002179

Loisel, H., Vantrepotte, V., Ouillon, S., Ngoc, D. D., Herrmann, M., Tran, V., Mériaux, X., Dessailly, D., Jamet, C., Duhaut, T., Nguyen, H. H., & Van Nguyen, T. (2017). Assessment and analysis of the chlorophyll-a concentration variability over the Vietnamese coastal waters from the MERIS ocean color sensor (2002–2012). *Remote Sensing of Environment*, *190*, 217–232. https://doi.org/10.1016/j.rse.2016.12.016

Loo, Y. Y., Billa, L., & Singh, A. (2015). Effect of climate change on seasonal monsoon in Asia and its impact on the variability of monsoon rainfall in Southeast Asia. *Geoscience Frontiers*, *6*(6), 817–823. https://doi.org/10.1016/j.gsf.2014.02.009

Lopez, G., Bennis, A.-C., Barbin, Y., Sentchev, A., Benoit, L., & Marié, L. (2020). Surface currents in the Alderney Race from high-frequency radar measurements and three-dimensional modelling. *Philosophical Transactions of the Royal Society A: Mathematical, Physical and Engineering Sciences*, *378*(2178), 20190494. https://doi.org/10.1098/rsta.2019.0494

Lumpkin, R., & Elipot, S. (2010). Surface drifter pair spreading in the North Atlantic. *Journal of Geophysical Research*, *115*(C12), C12017. https://doi.org/10.1029/2010JC006338

Lumpkin, R., Maximenko, N., & Pazos, M. (2012). Evaluating where and why drifters die. *Journal of Atmospheric and Oceanic Technology*, *29*(2), 300–308. https://doi.org/10.1175/JTECH-D-11-00100.1

Lumpkin, R., Özgökmen, T., & Centurioni, L. (2017). Advances in the Application of Surface Drifters. *Annual Review of Marine Science*, *9*(1), 59–81. https://doi.org/10.1146/annurev-marine-010816-060641

Lyard, F. H., Allain, D. J., Cancet, M., Carrère, L., and Picot, N. (2021). FES2014 global ocean tide atlas: design and performance. Ocean Sci. 17, 615–649. doi: 10.5194/os-17-615-2021

Manh, D.-V. Van, & Yanagi, T. (2000). A study on residual flow in the Gulf of Tongking. *Journal of Oceanography*, *56*(1), 59–68. https://doi.org/10.1023/A:1011162524466

Marsaleix, P., Auclair, F., and Estournel, C. (2006). Considerations on open boundary conditions for regional and coastal ocean models. J. Atmos. Ocean. Technol. 23, 1604–1613. doi: 10.1175/JTECH1930.1

Marsaleix, P., Auclair, F., Floor, J. W., Herrmann, M. J., Estournel, C., Pairaud, I., et al. (2008). Energy conservation issues in sigma–coordinate free–surface ocean models. Ocean Model. 20, 61–89. doi: 10.1016/j.ocemod.2007.07.005

Mazzini, P. L. F., & Chant, R. J. (2016). Two-dimensional circulation and mixing in the far field of a surface-advected river plume. *Journal of Geophysical Research: Oceans*, *121*(6), 3757–3776. https://doi.org/10.1002/2015JC011059

Mazzini, P. L. F. F., Barth, J. A., Shearman, R. K., Erofeev, A., Kipp Shearman, R., & Erofeev, A. (2014). Buoyancy-Driven Coastal Currents off Oregon during Fall and Winter. *Journal of Physical Oceanography*, *44*(11), 2854–2876. https://doi.org/10.1175/JPO-D-14-0012.1

McGillicuddy, D.J., Johnson, R., Siegel, D.A., Michaels, A.F., Bates, N.R., Knap, A.H., 1999. Mesoscale variations of biogeochemical properties in the Sargasso Sea. J. Geophys. Res. 104 (C6), 13381–13394

Meyerjürgens, J., Ricker, M., Schakau, V., Badewien, T. H., & Stanev, E. V. (2020). Relative Dispersion of Surface Drifters in the North Sea: The Effect of Tides on Mesoscale Diffusivity. *Journal of Geophysical Research: Oceans*, *125*(8). https://doi.org/10.1029/2019JC015925

Michaud, H., Marsaleix, P., Leredde, Y., Estournel, C., Bourrin, F., Lyard, F., Mayet, C., & Ardhuin, F. (2012). Three-dimensional modelling of wave-induced current from the surf zone to the inner shelf. *Ocean Science*, *8*(4), 657–681. https://doi.org/10.5194/os-8-657-2012

Miles, T., G. Seroka, and S. Glenn, 2017: Coastal ocean circulation during Hurricane Sandy. *J. Geophys. Res. Oceans*, **122**, 7095–7114, https://doi.org/10.1002/2017JC013031

Minh, N. N., Patrick, M., Florent, L., Sylvain, O., Gildas, C., Damien, A., & Van Uu, D. (2014). Tidal characteristics of the gulf of Tonkin. *Continental Shelf Research*, *91*, 37–56. https://doi.org/https://doi.org/10.1016/j.csr.2014.08.003

Molcard, A., Poulain, P. M., Forget, P., Griffa, A., Barbin, Y., Gaggelli, J., De Maistre, J. C., & Rixen, M. (2009). Comparison between VHF radar observations and data from drifter clusters in the Gulf of La Spezia (Mediterranean Sea). *Journal of Marine Systems*, *78*(SUPPL. 1), S79–S89. https://doi.org/10.1016/j.jmarsys.2009.01.012

Mork, M., 1981: Circulation phenomena and frontal dynamics of the Norwegian Coastal Current. Philos. Trans. Roy. Soc., A302, 635–648, doi:10.1098/rsta.1981.0188

Münchow, A., and R. Garvine, 1993: Buoyancy and wind forcing of a coastal current. J. Mar. Res., 51, 293–322, doi:10.1357/ 0022240933223747

N. Ebuchi *et al*., "Observation of the Soya warm current using HF ocean radar," *IGARSS 2004. 2004 IEEE International Geoscience and Remote Sensing Symposium*, 2004, pp. 1175-1178, doi: 10.1109/IGARSS.2004.1368624.

Nguyen Ngoc Thuy, 1984: Thủy triều vùng biển ViệtNam. Nxb KHKT, Hà Nội

Nguyen, K.-A., Liou, Y.-A., & Terry, J. P. (2019). Vulnerability of Vietnam to typhoons: A spatial assessment based on hazards, exposure and adaptive capacity. *Science of The Total Environment*, *682*, 31–46. https://doi.org/10.1016/j.scitotenv.2019.04.069

Nguyen-Duy, T., Ayoub, N. K., Marsaleix, P., Toublanc, F., De Mey-Frémaux, P., Piton, V., Herrmann, M., Duhaut, T., Tran, M. C., & Ngo-Duc, T. (2021). Variability of the Red River Plume in the Gulf of Tonkin as Revealed by Numerical Modeling and Clustering Analysis. In *Frontiers in Marine Science* (Vol. 8, p. 1636). https://www.frontiersin.org/article/10.3389/fmars.2021.772139

Paduan, J.D., and H.C. Graber. 1997. Introduction to high-frequency radar: Reality and myth. *Oceanography* 10(2):36–39, https://doi.org/10.5670/oceanog.1997.18.

Paduan, J. D., & Washburn, L. (2013). High-Frequency Radar Observations of Ocean Surface Currents. *Annual Review of Marine Science*, *5*(1), 115–136. https://doi.org/10.1146/annurev-marine-121211-172315

Pawlowicz, R., Beardsley, B., & Lentz, S. (2002). Classical tidal harmonic analysis including error estimates in MATLAB using T_TIDE. *Computers & Geosciences*, *28*(8), 929–937. https://doi.org/https://doi.org/10.1016/S0098-3004(02)00013-4

Peng D., Palanisamy H., Cazenave A., Meyssignac B. (2013), Interannual Sea Level Variations in the South China Sea over 1950-2009, Mar. Geod., 36: 164-182, doi: http://dx.doi.org/ 10.1080/01490419.2013.771595

Piton, V., Herrmann, M., Lyard, F., Marsaleix, P., Duhaut, T., Allain, D., & Ouillon, S. (2020). Sensitivity study on the main tidal constituents of the Gulf of Tonkin by using the frequency-domain tidal solver in T-UGOm. *Geoscientific Model Development*, *13*(3), 1583–1607. https://doi.org/10.5194/gmd-13-1583-2020

Piton, V., Herrmann, M., Marsaleix, P., Duhaut, T., Ngoc, T. B., Tran, M. C., Shearman, K., & Ouillon, S. (2021). Influence of winds, geostrophy and typhoons on the seasonal variability of the circulation in the Gulf of Tonkin: A high-resolution 3D regional modeling study. *Regional Studies in Marine Science*, *45*, 101849. https://doi.org/10.1016/j.rsma.2021.101849

Poje, A. C., Haza, A. C., Özgökmen, T. M., Magaldi, M. G., & Garraffo, Z. D. (2010). Resolution dependent relative dispersion statistics in a hierarchy of ocean models. *Ocean Modelling*, *31*(1–2), 36–50. https://doi.org/10.1016/j.ocemod.2009.09.002

Poje, A. C., Özgökmen, T. M., Lipphardt, B. L., Haus, B. K., Ryan, E. H., Haza, A. C., Jacobs, G. A., Reniers, A. J. H. M., Olascoaga, M. J., Novelli, G., Griffa, A., Beron-Vera, F. J., Chen, S. S., Coelho, E., Hogan, P. J., Kirwan, A. D., Huntley, H. S., & Mariano, A. J. (2014). Submesoscale dispersion in

the vicinity of the Deepwater Horizon spill. *Proceedings of the National Academy of Sciences of the United States of America*, *111*(35), 12693–12698. https://doi.org/10.1073/pnas.1402452111

Qu, T., & Song, Y. T. (2009). Mindoro Strait and Sibutu Passage transports estimated from satellite data. *Geophysical Research Letters*, *36*(9), 1–5. https://doi.org/10.1029/2009GL037314

Räsänen T. A., Kummu M. (2013) Spatiotemporal influences of ENSO on precipitation and flood pulse in the Mekong River Basin, J of Hydrol., 476, 154-168, doi: http://dx.doi.org/10.1016/j.hydrol.2012.10.028

Räsänen T. A., Lindgren V., Guillaume J. H. A., Buckley B. M., Kummu M. (2016) On the spatial and temporal variability of ENSO precipitation and drought teleconnection in mainland Southeast Asia, Clim. Past., 12, 1889-1905, doi: 10.5194/cp-12-1889-2016

Reffray, G., Fraunié, P., andMarsaleix, P. (2004). Secondary flows induced by wind forcing in the Rhône region of freshwater influence. Ocean Dyn. 54, 179–196. doi: 10.1007/s10236-003-0079-y

Rétif, Fabien & Bouchette, Frédéric & Marsaleix, Patrick & Liou, Jiing-Yih & Meulé, Samuel & Michaud, Héloïse & Lin, Li-Ching & Hwang, Kao & Bujan, Nans & Hwung, Hwung-Hweng & Team, SIROCCO. (2014). REALISTIC SIMULATION OF INSTANTANEOUS NEARSHORE WATER LEVELS DURING TYPHOONS. Coastal Engineering Proceedings. 1. 17. 10.9753/icce.v34.waves.17.

Roarty, Hugh & Smith, Michael & Glenn, Scott & Barrick, Donald. (2013). Real-Time Beyond the Horizon Vessel Detection. Proceedings of SPIE - The International Society for Optical Engineering. 8714. 87140Z. 10.1117/12.2015871.

Roarty, H., Cook, T. T., Hazard, L., George, D., Harlan, J., Cosoli, S., Wyatt, L., Alvarez Fanjul, E., Terrill, E., Otero, M., Largier, J., Glenn, S., Ebuchi, N., Whitehouse, B., Bartlett, K., Mader, J., Rubio, A., Corgnati, L. P., Mantovani, C., … Matta, K. S. (2019). The Global High Frequency Radar Network. Frontiers in Marine Science, 6(MAR). https://doi.org/10.3389/fmars.2019.00164

Rogowski, P., Zavala-Garay, J., Shearman, K., Terrill, E., Wilkin, J., & Lam, T. H. (2019). Air-Sea-Land Forcing in the Gulf of Tonkin: Assessing Seasonal Variability Using Modern Tools. *Oceanography*, *32*(2), 150–161. https://doi.org/10.5670/oceanog.2019.223

Rong Z., Liu Y., Zong H., Cheng Y. (2007) Interannual sea level variability in the South China Sea and its response to ENSO, Glob. Planet. Change, 55, 257-272, doi: http://dx.doi.org/10.1016/j.gloplacha.2006.08.001

Rubio, A., Caballero, A., Orfila, A., Hernández-Carrasco, I., Ferrer, L., González, M., Solabarrieta, L., & Mader, J. (2018). Eddy-induced cross-shelf export of high Chl-a coastal waters in the SE Bay of Biscay. *Remote Sensing of Environment*, *205*, 290–304. https://doi.org/10.1016/j.rse.2017.10.037

Rypina, I. I., Kirincich, A., Lentz, S., & Sundermeyer, M. (2016). Investigating the eddy diffusivity concept in the coastal ocean. *Journal of Physical Oceanography*, *46*(7), 2201–2218. https://doi.org/10.1175/JPO-D-16-0020.1

Roullet, G., Mcwilliams, J. C., Capet, X., & Molemaker, M. J. (2012). Properties of steady geostrophic turbulence with isopycnal outcropping. *Journal of Physical Oceanography*, *42*(1), 18–38. https://doi.org/10.1175/JPO-D-11-09.1

Sansón, L. Z., Pérez-Brunius, P., & Sheinbaum, J. (2017). Surface Relative Dispersion in the Southwestern Gulf of Mexico. *Journal of Physical Oceanography*, *47*(2), 387–403. https://doi.org/10.1175/jpo-d-16-0105.1

Schroeder, K., Chiggiato, J., Haza, A. C., Griffa, A., Özgökmen, T. M., Zanasca, P., Molcard, A., Borghini, M., Poulain, P. M., Gerin, R., Zambianchi, E., Falco, P., & Trees, C. (2012). Targeted Lagrangian sampling of submesoscale dispersion at a coastal frontal zone. *Geophysical Research Letters*, *39*(11), n/a-n/a. https://doi.org/10.1029/2012GL051879

Schroeder, K., Haza, A. C., Griffa, A., Özgökmen, T. M., Poulain, P. M., Gerin, R., Peggion, G., & Rixen, M. (2011). Relative dispersion in the Liguro-Provençal basin: From sub-mesoscale to mesoscale. *Deep Sea Research Part I: Oceanographic Research Papers*, *58*(3), 209–228. https://doi.org/10.1016/j.dsr.2010.11.004

Lekien, F., Coulliette, C., Mariano, A. J., Ryan, E. H., Shay, L. K., Haller, G., & Marsden, J. (2005). Pollution release tied to invariant manifolds: A case study for the coast of Florida. *Physica D: Nonlinear Phenomena*, *210*(1–2), 1–20. https://doi.org/10.1016/j.physd.2005.06.023

Sentchev, A., Forget, P., & Barbin, Y. (2009). Residual and tidal circulation revealed by VHF radar surface current measurements in the southern Channel Isles region (English Channel). *Estuarine, Coastal and Shelf Science*, *82*(2), 180–192. https://doi.org/10.1016/j.ecss.2008.12.003

Sentchev, A., Forget, P., Barbin, Y., & Yaremchuk, M. (2013). Surface circulation in the Iroise Sea (W. Brittany) from high resolution HF radar mapping. *Journal of Marine Systems*, *109–110*, S153–S168. https://doi.org/10.1016/j.jmarsys.2011.11.024

Shadden, S. C., Lekien, F., Paduan, J. D., Chavez, F. P., & Marsden, J. E. (2009). The correlation between surface drifters and coherent structures based on high-frequency radar data in Monterey Bay. *Deep Sea Research Part II: Topical Studies in Oceanography*, *56*(3), 161–172. https://doi.org/https://doi.org/10.1016/j.dsr2.2008.08.008

Shen, Wei & Gurgel, Klaus-Werner & Voulgaris, George & Schlick, Thomas & Stammer, Detlef. (2012). Wind-speed inversion from HF radar first-order backscatter signal. Ocean Dynamics - OCEAN DYN. 62. 10.1007/s10236-011-0465-9.

Shi, M.C., Chen, C.S., Xu, Q., et al., 2001. The role of Qionqzhou Strait in the seasonal variation of the South China Sea circulation. J. Phys. Oceanogr. 32, 103– 121. http://dx.doi.org/10.1175/1520-0485(2002)032%3C0103:TROQSI%3E2.0. CO;2

Siegelman, L., O'toole, M., Flexas, M., Rivière, P., & Klein, P. (2019). Submesoscale ocean fronts act as biological hotspot for southern elephant seal. *Scientific Reports*, *9*(1), 1-13

Simpson, J. H., Crisp, D. J., & Hearn, C. (1981). The Shelf-Sea Fronts: Implications of their Existence and Behaviour [and Discussion]. *Philosophical Transactions of the Royal Society of London. Series A, Mathematical and Physical Sciences*, *302*(1472), 531–546. http://www.jstor.org/stable/37036

Simpson, J. H., & Sharples, J. (2012). *Introduction to the Physical and Biological Oceanography of Shelf Seas*. Cambridge University Press. https://doi.org/DOI: 10.1017/CBO9781139034098

Stewart, R. H., & Joy, J. W. (1974). HF radio measurements of surface currents. *Deep Sea Research and Oceanographic Abstracts*, *21*(12), 1039–1049. https://doi.org/https://doi.org/10.1016/0011-7471(74)90066-7

Sun, H., Huang, W., Zhao, J.S., 2001. Three-dimensional numerical simulation for tide and tidal current in the Beibu Gulf. Acta Oceanol. Sinica 23 (2), 1–8

Tan, C.H., 1987. Preliminary analysis of hydrologic structure and hydrologic feature in the sea region of the Beibu Gulf. Trans. Oceanol. Limnol. 4, 7–15

Tang, D. L., Kawamura, H., Lee, M. A., & Van Dien, T. (2003). Seasonal and spatial distribution of chlorophyll-a concentrations and water conditions in the Gulf of Tonkin, South China Sea. *Remote Sensing of Environment*, *85*(4), 475–483. https://doi.org/10.1016/S0034-4257(03)00049-X

Taylor, G. I.: Tidal oscillations in gulfs and rectangular basins. Proc. London Math. Soc., Ser. 2, 20, 148-181, https://doi.org/10.1112/plms/s2-20.1.148, 1922.

Tran, M. C., Sentchev, A., & Nguyen, K. C. (2021). Multi-scale variability of circulation in the Gulf of Tonkin from remote sensing of surface currents by high-frequency radars. *Ocean Dynamics*, *71*(2), 175–194. https://doi.org/10.1007/s10236-020-01440-x

Ullman, D.S., O, Donnell, J., Kohut, J., Fake, T., Allen, A., 2006. Trajectory prediction using HF radar surface currents: Monte Carlo simulations of prediction uncertainties. J. Geophys. Res. 111, C12005. doi:10.1029/2006JC003715

Ulses, C., Estournel, C., Bonnin, J., Durrieu de Madron, X., & Marsalei, P. (2008). Impact of storms and dense water cascading on shelf-slope exchanges in the Gulf of Lion (NW Mediterranean). *Journal of Geophysical Research: Oceans*, *113*(2), 1–18. https://doi.org/10.1029/2006JC003795

van Maren D. S., Hoekstra P.: Seasonal variation of hydrodynamics and sediment dynamics in a shallow subtropical estuary: the Ba Lat River, Vietnam, Estuar. Coastal Shelf Sci., 60(3), 529-540, 2004

van Sebille, E., Beal, L. M., & Johns, W. E. (2011). Advective Time Scales of Agulhas Leakage to the North Atlantic in Surface Drifter Observations and the 3D OFES Model. *Journal of Physical Oceanography*, *41*(5), 1026–1034. https://doi.org/10.1175/2010JPO4602.1

van Sebille, E., Griffies, S. M., Abernathey, R., Adams, T. P., Berloff, P., Biastoch, A., Blanke, B., Chassignet, E. P., Cheng, Y., Cotter, C. J., Deleersnijder, E., Döös, K., Drake, H. F., Drijfhout, S., Gary, S. F., Heemink, A. W., Kjellsson, J., Koszalka, I. M., Lange, M., … Zika, J. D. (2018). Lagrangian ocean analysis: Fundamentals and practices. *Ocean Modelling*, *121*(October 2017), 49–75. https://doi.org/10.1016/j.ocemod.2017.11.008

van Sebille, E., Waterman, S., Barthel, A., Lumpkin, R., Keating, S. R., Fogwill, C., & Turney, C. (2015). Pairwise surface drifter separation in the western Pacific sector of the Southern Ocean. *Journal of Geophysical Research: Oceans*, *120*(10), 6769–6781. https://doi.org/10.1002/2015JC010972

Vantrepotte, V., & Mélin, F. (2009). Temporal variability of 10-year global SeaWiFS time-series of phytoplankton chlorophyll a concentration. *ICES Journal of Marine Science*, *66*(7), 1547–1556. https://doi.org/10.1093/icesjms/fsp107

Vinh, V. D., Ouillon, S., Thanh, T. D., & Chu, L. V. (2014). Impact of the Hoa Binh dam (Vietnam) on water and sediment budgets in the Red River basin and delta. *Hydrology and Earth System Sciences*, *18*(10), 3987–4005. https://doi.org/10.5194/hess-18-3987-2014

Wang, D.R., 1998. Study of the Dynamic-Thermodynamic Mechanic of Beibu Bay Cool Water Masses (Doctoral dissertation). Ocean University of China, Qingdao, (in Chinese with English abstract).

Wang C., Wang W., Wang D., Wang Q. (2006), Interannual variability of the South China Sea associated with El Niño, J. Geophys. Res., 111: C03023, doi: 10.1029/2005JC003333

Wang, L., Li, J., Lu, H., Gu, Z., Rioual, P., Hao, Q., Mackay, A. W., Jiang, W., Cai, B., Xu, B., Han, J., & Chu, G. (2012). The East Asian winter monsoon over the last 15,000 years: Its links to high-latitudes and tropical climate systems and complex correlation to the summer monsoon. *Quaternary Science Reviews*, *32*, 131–142. https://doi.org/10.1016/j.quascirev.2011.11.003

Wang, W., & Gill, E. W. (2016). Evaluation of Beamforming and Direction Finding for a Phased Array HF Ocean Current Radar. *Journal of Atmospheric and Oceanic Technology*, *33*(12), 2599–2613. https://doi.org/10.1175/JTECH-D-15-0181.1

Wang, X., Wang, C., Han, G., Li, W., Wu, X., 2014. Effects of tropical cyclones on large-scale circulation and ocean heat transport in the South China Sea. Clim. Dyn. 43, 3351–3366. http://dx.doi.org/10.1007/s00382-014-2109-5

Wu C. R., Chang C. W. K. (2005) Interannual variability of the South China Sea in a data assimilation model, Geophys. Res. Lett., 32(17),1-4, doi: 10.1029/2005GL023798

Wyatt, Lucy & Robinson, A. & Howarth, M.J.. (2011). Wind farm impacts on HF radar current and wave measurements in Liverpool Bay. OCEANS 2011 IEEE - Spain. 10.1109/Oceans-Spain.2011.6003418.

Wyrtki, K. (1961). *Physical Oceanography of the Southeast Asian waters*. https://escholarship.org/uc/item/49n9x3t4

Xia, H.Y., Li, S.H., Shi, M.C., 2001. Three-D numerical simulation of wind-driven current and density current in the Beibu Gulf. Acta Oceanol. Sin. 20, 455–472

Xu X. (1982) The general descriptions of the horizontal circulation in the South China Sea, in Proceedings of the 1980 Symposium on Hydrometeorology, Chinese Society of Oceanology and Limnology, pp. 137-145, Science Press

Xue Z., Liu J. P., Ge Q. (2011) Changes in hydrology and sediment delivery of the Mekong River in the last 50 years: connection to damming, monsoon, and ENSO, Earth Surf. Proc. Land., 36: 296-308, doi: 10.1002/esp.2036

Yaremchuk, M., & Sentchev, A. (2011). A combined EOF/variational approach for mapping radar-derived sea surface currents. *Continental Shelf Research*, *31*(7–8), 758–768. https://doi.org/10.1016/j.csr.2011.01.009

Yaremchuk, M., & Sentchev, A. (2009). Mapping radar-derived sea surface currents with a variational method. *Continental Shelf Research*, *29*(14), 1711–1722. https://doi.org/10.1016/j.csr.2009.05.016

Yang, S.Y., Bao, X.W., Chen, C.S., et al., 2003. Analysis on characteristics and mechanism of current system in west coast of Guangdong Province in the summer. Acta Oceanol. Sin. 25 (6), 1–8, (in Chinese with English abstract)

Yang Y., Xie S.-P., Du Y., Tokinaga H. (2015) Interdecadal difference of interannual variability characteristics of South China Sea SSTs associated with ENSO, Amer. Meteor. Soc. 28: 7145-7160, doi:10.1175/JCLI-D-15-0057.1

Ye, A. L., & Robinson, I. S. (1983). Tidal dynamics in the South China Sea. *Geophysical Journal International*, *72*(3), 691–707. https://doi.org/10.1111/j.1365-246X.1983.tb02827.x

Yoshikawa, Y., Matsuno, T., Marubayashi, K., & Fukudome, K. (2007). A surface velocity spiral observed with ADCP and HF radar in the Tsushima Strait. *Journal of Geophysical Research: Oceans*, *112*(C6). https://doi.org/10.1029/2006JC003625

Yuan, S.Y., Deng, J.Z., 1999. Numerical research in the circulation in the Beibu Gulf. Nanhai Yanjiu Yu Kaifa 2, 41–46, (in Chinese with English abstract).

Yuan Y., Yang H., Zhou W., Li C. (2008) Influences of the Indian Ocean Dipole on the asian summer monsoon in the following year, Int. J. Climatol., 28(14),1849-1859, doi:10.1002/joc.1678

Yu, M.G., Liu, J.F., 1993. South China Sea circulation system and situation. Mar. Forecasts 10, 13–17

Yu, Y., Xing, X., Liu, H., Yuan, Y., Wang, Y., & Chai, F. (2019). The variability of chlorophyll-a and its relationship with dynamic factors in the basin of the South China Sea. *Journal of Marine Systems*, *200*(June), 103230. https://doi.org/10.1016/j.jmarsys.2019.103230

Zavala Sansón, L. (2015). Surface dispersion in the Gulf of California. *Progress in Oceanography*, *137*, 24–37. https://doi.org/10.1016/j.pocean.2015.04.008

Zavala-Garay, J., Rogowski, P., Wilkin, J., Terrill, E., Shearman, R. K., & Tran, L. H. (2022). An Integral View of the Gulf of Tonkin Seasonal Dynamics. *Journal of Geophysical Research: Oceans*, *127*(5). https://doi.org/10.1029/2021JC018125

Zhang L., Wang B., Zeng Q. (2009) Impact of the Madden-Julian oscillation on summer rainfall in the Southeast China, J. Clim., 22(2), 201-216, doi: 10.1175/2008JCLI1959.1

Zhang, Z., Qiu, B., Klein, P., & Travis, S. (2019). The influence of geostrophic strain on oceanic ageostrophic motion and surface chlorophyll. *Nature Communications*, *10*(1), 1–11. https://doi.org/10.1038/s41467-019-10883-w

Zhong, Y., & Bracco, A. (2013). Submesoscale impacts on horizontal and vertical transport in the Gulf of Mexico. *Journal of Geophysical Research: Oceans*, *118*(10), 5651–5668. https://doi.org/10.1002/jgrc.20402

Zimmerman, J. T. F. (1981). Dynamics, diffusion and geomorphological significance of tidal residual eddies. *Nature*, *290*(5807), 549–555. https://doi.org/10.1038/290549a0

Zu, T.T., 2005. Analysis of the Current and Its Mechanism in the Gulf of Beibu (Master dissertation). Ocean University of China, Qingdao, (in Chinese with English abstract).